UNIVERSITY OF CAPE TOWN
IYUNIVESITHI YASEKAPA • UNIVERSITEIT VAN KAAPSTAD

Development of an Intermediate Strain Rate Compression Testing Machine

Submitted to the University of Cape Town in partial fulfilment
for the degree of MSc. in Mechanical Engineering

Melchior Stander

Supervisor:
Mr. T.J. Cloete

May 2014

Blast Impact and Survivability Research Centre
Department of Mechanical Engineering
University of Cape Town

Abstract

The further development of the wedge bar Intermediate Strain rate Tester (IST) presented by Cloete and Oxtoby [1] is presented in this dissertation. The concept uses a wedge mechanism to deform 5 mm diameter, 5 mm long specimens at strain rates in the region of 10 s^{-1}, up to strains of 30%. As impact principles are used to start and stop the experiment, it takes less than 1% of the testing duration to reach testing speed and to stop the experiment. The kinetic energy stored in the wedge bar helps ensure a near constant loading rate over the duration of the experiment. The yield stress is captured at above 80% of the average strain rate for the experiment for most of the materials investigated. The design work focuses primarily around the design of the new load-frame, load-cell, loading platforms and wedge bar displacement sensor. Finite Element Analysis (FEA) was used to investigate the dynamic response of the IST and modify the design of components where necessary. The modifications made the load-frame and load-cell result in a significant improvement in the quality of the measured signals. The wedge bar displacement sensor performed well. The back pressure driven loading concept shows potential but needs more development before it is suitable for routine testing. A range of common engineering materials was tested at quasi static, intermediate and high strain rates and compared to the results found in the literature. The results match well, however, friction effects dominate the large strain response of the metal specimens. In its current configuration the IST is used effective for testing polymers up to large strains as well as yield stress and small strain measurement of metals. For materials for which specimen friction effects are a problem, interrupted tests can be used to extend the maximum strain achievable.

Acknowledgements

There have been many people who have helped and contributed to this dissertation in some way. I would like to draw special attention to and thank the following

- Mr T.J Cloete: Thank you for the input you have given me over the years. I have learnt a lot from you about thinking out of the box and you have always challenged me to improve my work. You have always been willing to give input to your students and it has appreciated. Good luck with finishing your PHD over the next couple of months.

- G Neuric: Thank you for the work you have put into BISRU over the years. The culture you have managed to create at BISRU makes it a great place to do research.

- Mr G Newins and the workshop staff: Thank you for the many hours you spent machining the components required for my project. It is appreciated.

- Mom and Dad: I would like to thank you for all the love and support you have given me over the years. It has meant a lot to me. Thanks especially for your continual encouragement to get my dissertation done. Thanks mom for your help proof reading.

- To all my friends: Thanks for your encouragement and support it has meant a lot to me over the years. A special thanks to Neil and Duncan in this regard. To Wesley, thanks for all the nights we spent working on our projects together, it helped a lot. To Lee-Anne, thanks for letting me invade your house and all the suppers you provided while me and Wesley were working. To Kath a BIG thanks for all your help proof reading.

Thank you

Declaration

1. I know that plagiarism is wrong. Plagiarism is to use anothers work and to pretend it is one's own.

2. Each significant contribution to, and quotation in, this report from the work, or works of other people has been attributed and has cited and referenced.

3. This dissertation is my own work

4. I have not allowed and will not allow anyone to copy my work with the intention of passing it off as his or her own.

Name: Melchior Stander Signature: ..... Date: .....

Contents

List of Figures

List of Tables

Nomenclature

BISRU Blast Impact and Survivability Research Unit

CG Centre of Gravity

DIC Digital Image Correlation

EPP Elastic Perfectly Plastic

FEA Finite Element Analysis

HFLF High Frequency Load-Frame

HPB Hopkinson Pressure Bar

ISR Intermediate Strain Rate

IST Intermediate Strain rate Tester

MLF Monolithic Load-Frame

PMMA Polymethyl Methacrylate

QS Quasi Static

ROS Reflective Object Sensor

SHPB Split Hopkinson Pressure Bar

UCS Ultimate Compressive Strength

Chapter 1

Introduction

Materials testing and characterisation is a critical component of mechanical design. It is difficult to make informed design choices without a proper understanding of the materials to be used. For this reason materials testing is regularly performed.

Most of the materials testing done is Quasi Static (QS) testing. The tests are done slowly enough to assume the specimen and testing machine are in equilibrium. QS testing is a well-established field with a wealth of information available in the literature. Testing is done on commercially available testing machines of either the electro-servohydraulic or screw driven type. The testing procedures are governed by standards [2].

However, it is well established that the mechanical properties of many materials are rate dependent [3, 4], meaning that their yield stress and flow stress vary depending on the rate of deformation. Therefore, when loading rates other than QS are expected, it is useful to know the material response at these rates. High strain rate testing is a less mature field than QS testing. High strain rate testing is typically done using a Split Hopkinson Pressure Bar (SHPB) [5]. SHPB testing is not governed by standards, but a large body of literature covering this testing method exists [5, 6].

A considerable amount of literature has been published on the QS and high strain rate material properties. However, there has been relatively little literature published on Intermediate Strain Rate (ISR) properties of materials. ISR testing is regularly omitted due to the experimental difficulties associated with testing in this range [7, 8]. ISR testing provides many challenges as it falls below the strain rates achievable using the SHPB and above the strain rate achievable on universal testing machines. The limitations of these testing methods are discussed in more detail in Sections 2.2.1 and 2.2.2. Furthermore, no international standards appear to exist governing ISR testing.

However, despite the lack of ISR data available in the literature the ISR properties of materials are important. Materials are deformed at intermediate strain rates in many everyday engineering applications such as vehicle crash protection, high-speed forming operations and low velocity projectile impacts [8–11].

Currently the need for ISR data is driven largely by the requirements of computational modelling [3, 12, 13]. When using Finite Element Analysis (FEA) to model a complex problem, such as a crash simulation, it is critical to have an accurate material model. The material model used can have a large effect on the analysis results [14]. If only quasi static and high strain rate testing data is available, the ISR data needs to be inferred from these results. This can result in the material model not accurately describing the material response at intermediate strain rates [7]. Inferring the ISR properties has

provided satisfactory results for some traditional engineering materials, such as metals. This is due to the relatively low rate dependence of metals, at rates below 100 s^{-1} [15] and the smooth transition in material properties seen between low and high rate tests.

Polymers and biological materials have shown significant rate dependence at QS, ISR and high strain rates [1, 15, 16]. For non-linear viscoelastic materials, such as bone, composites and polymers it is not known what the intermediate rate response will be. Unlike with metals, interpolating from the QS and SHPB data will not necessarily provide accurate results in the ISR regime for these materials. Furthermore, the lack of information in the literature makes it difficult to justify any assumptions made about the intermediate rate response of these newer materials.

Therefore, the author believes intermediate strain rate testing is an important component of the material characterisation process and that developments allowing routine testing at intermediate strain rates will help improve the understanding of material properties under different loading conditions.

This dissertation builds on the wedge bar Intermediate Strain rate Testing machine (IST) presented by Cloete and Oxtoby [1]. The majority of the design work focuses on the development of a new load-frame, load-cell and loading platform to improve on the force measurement capabilities of the IST as well as the development of a new displacement sensor. FEA is used to analyse the dynamic response of the IST to inform design changes required to minimise noise on the measured signals.

Chapter 2

Literature Review

In this chapter the literature relating to Intermediate Strain Rate (ISR) material testing is reviewed. First, material testing data is presented from tests performed at Quasi Static (QS), high strain rate and ISR (where available). A brief review of established QS and high strain rate testing methods is then presented, followed by the work of various authors who have modified these testing methods in an attempt to extend their usable testing range into the ISR regime. Testing techniques that use energy storage devices such as flywheels and drop towers to store the energy required for testing are then presented. The final testing techniques covered are the custom-built machines designed specifically for ISR testing. This review focuses primarily on the different techniques used for ISR testing and discusses their strengths and weaknesses, with the view of drawing up design specifications for a new IST.

2.1 Rate Sensitivity Of Material Properties

The materials selected to be tested using the IST are steel, copper, aluminium, nylon and PMMA. These materials are selected as the mechanical properties are well documented and cover a wide range of properties. Some of the materials have no distinct yield point while others have clearly defined yield points, the ultimate strengths varies from around 70 MPa to a few hundred MPa and the rate sensitivity varies from rate insensitive to highly rate sensitive. Testing these materials allows the response of the IST to be evaluated over a wide range of operating conditions.

In this section a selection of results found in the literature are presented showing the effect of strain rate on mechanical properties of these materials. These results show the rate sensitivity of the materials and highlight the scarcity of ISR data available in the literature. The results are used in Chapter 6 to compare with the experimental results of the new Intermediate Strain rate Tester (IST) . The testing techniques used by the authors that present ISR data are discussed in more detail in sections 2.3 to 2.6.2

2.1.1 Steel

The QS and dynamic material properties of annealed mild steel are well reported in the literature. However, ISR data is still scarce [6]. Intermediate strain rate results for mild steel presented by Zhao and Gary [11, 17] and Campbell and Ferguson [18] and Manjoine [4] are presented.

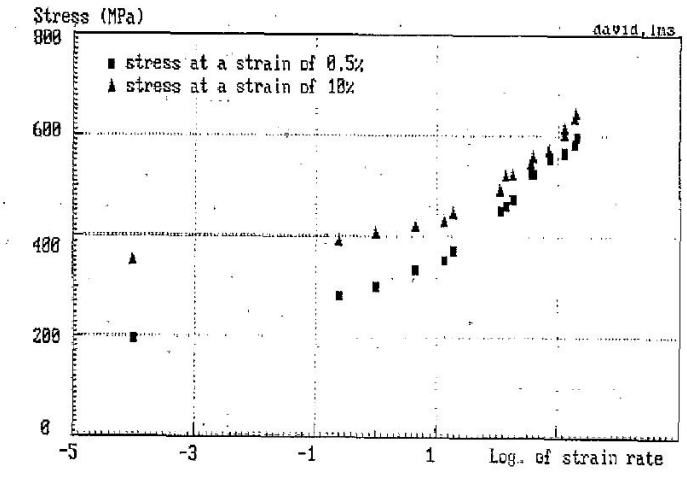

(a) Results presented by Zhao and Gary for mild steel [11]

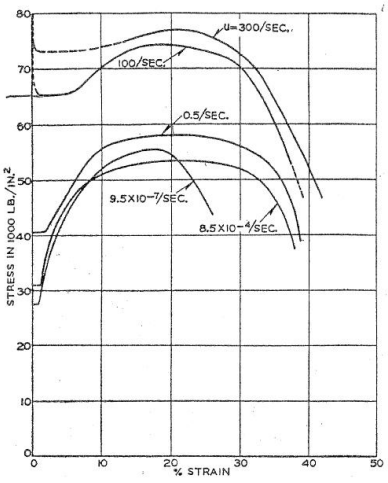

(b) Results presented by Manjoine for mild steel [19]

Figure 2.1: Mild steel results

Zhao and Gary [11, 17] presented results for uni-axial QS and SHPB tests at rates from 10^{-4} $s^{-1}$to 3000 s^{-1}as shown in Figure 2.1(a). The low rate test results are obtained using a hydraulic testing machine and the high strain rate tests are performed using a SHPB and a sandwich specimen consisting of four sheets of sheet metal cemented together. No information is given on how the intermediate rate tests are performed.

Manjoine investigated the influence of strain rate and temperature on the yield stress of mild steel [4]. Tensile tests are performed at rates from 10^{-6} $s^{-1}$to 10^{3} $s^{-1}$and temperatures from room temperature to 600 °C. The high strain rate tests are performed on a high speed tension machine and a constant strain rate machine is used for the intermediate and slow rate tests. The results for room temperature tests are presented in Figure 2.1(b). Note no ISR data is presented.

Campbell and Ferguson [18] published the results shown in Figure 2.2 comparing the results of tensile tests and punch tests performed at various strain rates presented by Campbell and Cooper [18] and Dowling and Harding [20].

The test results presented show that the material properties of steel are highly rate dependant. The the yield stress increases by a factor of between 2.5 to 3 times over the strain rate range covered. These results are compared to the test results used to benchmark the new IST in Figure 6.1.

2.1.2 Aluminium

Smerd et al. [21] performed quasi static and high strain rate tensile tests on two aluminium alloys commonly used in the automotive industry, AA5182 and AA5754. The QS tests are performed on an Instron servo-electric testing machine while the high strain rate tests are performed on a tensile SHPB. The results shown in Figure 2.3 show no significant increase in flow stress for aluminium AA5182. However, the aluminium AA5754 shows an initial increase in flow stress between the QS and 600 s^{-1} tests, with no further increase seen after this point.

Oosterkamp et al. [22] performed uniaxial compression tests at varying strain rates and temperatures on AA6082 aluminium in T6 temper. QS and intermediate rate tests are performed on a servo hydraulic test machine and high strain rate tests are performed on a SHPB. The results showing the

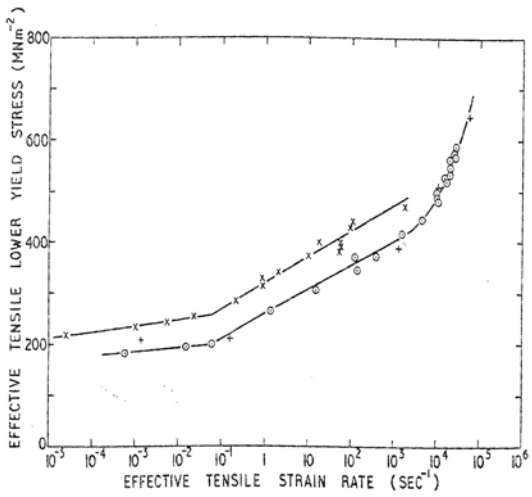

Figure 2.2: Results presented by Campbell and Ferguson for mild steel [18]

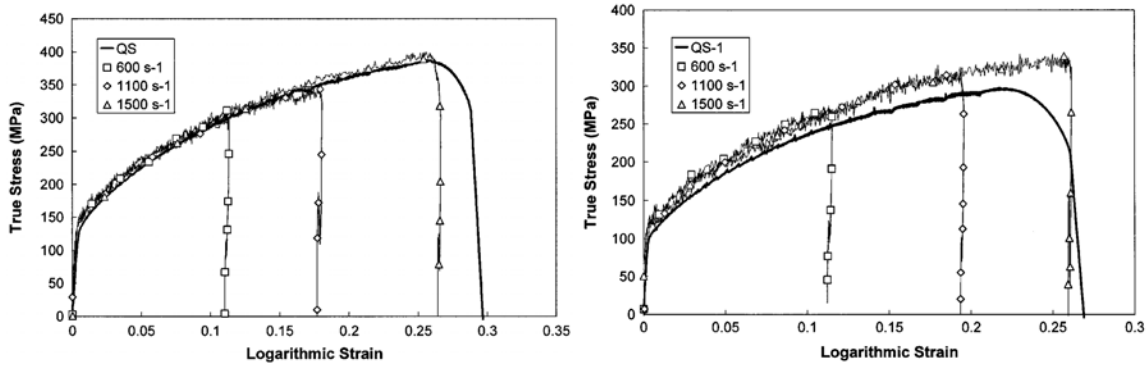

(a) Aluminium AA5182 [21]

(b) Aluminium AA5754[21]

Figure 2.3: QS and SHPB results for aluminium presented by Smerd et al.

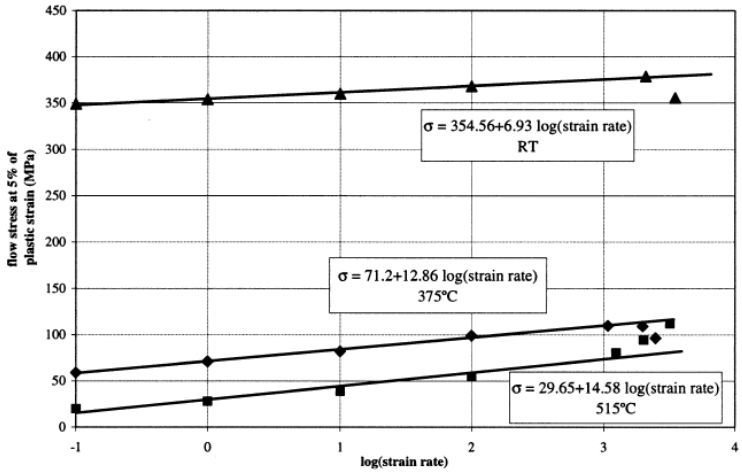

Figure 2.4: Flow stress of AA6082 aluminium at T6 temper and 5% plastic strain presented by Oosterkamp [22]

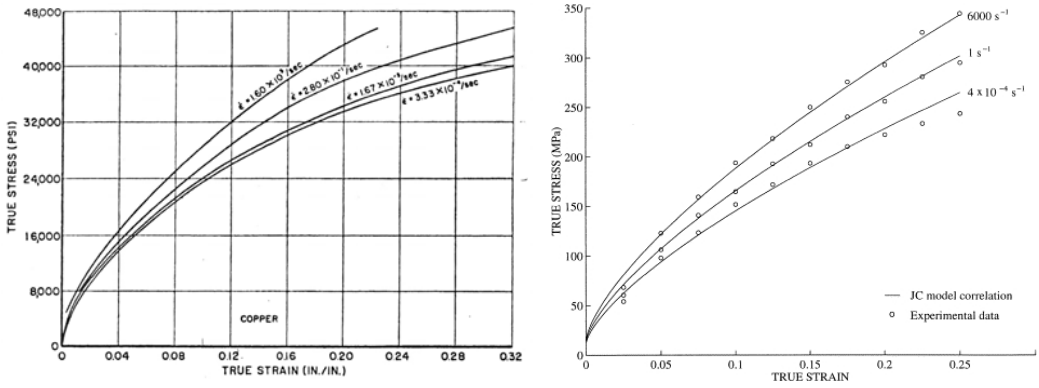

(a) Results for copper presented by Lindholm [6]

(b) Results for OFCH copper presented by Liang and Khan [23]

Figure 2.5: The effects of strain rate on copper

flow stress at 5% strain are shown in Figure 2.4. These results show aluminium to be mildly rate sensitive with an increase of approximately 10% in the flow stress between the QS and high strain rate tests at 1500 s^{-1}.

The test results presented show that aluminium tends to vary between rate insensitive to mildly rate sensitive depending on the grade of aluminium tested. These results are compared to the test results used to benchmark the new IST in Figure 6.2.

2.1.3 Copper

U.S. Lindholm presented results for commercially pure copper at quasi static and dynamic rates [6]. The QS tests are done using a Baldwin-Emery SR4 universal testing machine while the high strain rate tests are done using a SHPB [6]. Specimen of 1/2 inch diameter and 1/4 inch length are used for all the experiments. The results presented in Figure 2.5(a) show an increase in flow stress of approximately 30% between strain rates of 10^{-4} s^{-1} to 1600 s^{-1}.

Liang and Khan [23] compare four constitutive material models to experimental data reported by others to investigate the limitations of the models. The Johnson-Cooke model is compared to experimental results presented by Follansbey [24] and Tanner [25] for OFHC copper, see Figure 2.5(b). The results show an increase of approximately 45% between the QS and dynamic tests, 4×10^{-4} s^{-1} to 6000 s^{-1}. Note, once again, no intermediate rate tests are performed.

The test results presented show that copper tends to be mildly rate sensitive with an increase in flow stress between 30% and 45% expected from QS to high strain rate tests. These results are compared to the test results used to benchmark the new IST in Figure 6.3.

2.1.4 Polymethyl Methacrylate

Segreti et al. investigated the puncture resistance of Polymethyl Methacrylate (PMMA) at low and high impact velocities. Compression tests and impact tests are performed. An ESH testing machine is used for tests up to rates of 10 s^{-1} and a compression SHPB is used for the high strain rate tests [26], the results are shown in Figure 2.6(a). Note the large increase in flow stress between the tests performed at 10 s^{-1} and 200 s^{-1}.

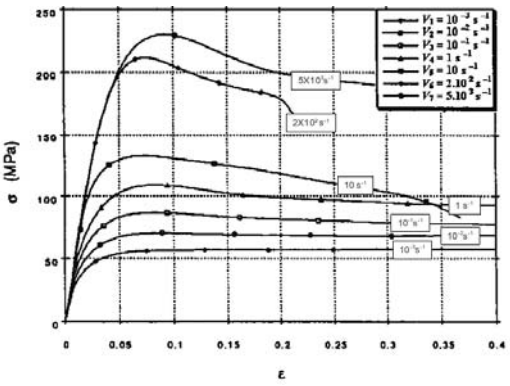

(a) Results for PMMA presented by Segreti [26]

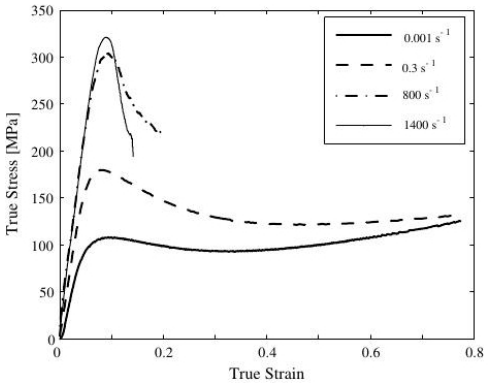

(b) Results for PMMA presented by Mulliken and Boyce [27]

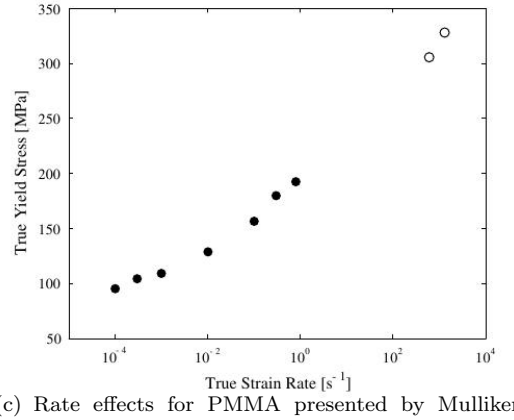

(c) Rate effects for PMMA presented by Mulliken and Boyce [27]

Figure 2.6: The effects of strain rate on PMMA

Mulliken and Boyce [27] investigated the mechanical behaviour of polymers. Test results are presented for PMMA (Plexiglas G) at strain rates ranging from 10^{-4} s^{-1} to 10^4 s^{-1}. A uniaxial tension and compression testing machine is used for the QS tests and an aluminium SHPB is used for the high rate tests. The results are shown in Figure 2.6. Note the gap in data for rates between 0.3 s^{-1} and 800 s^{-1}.

The test results presented show PMMA to be highly rate sensitive with the Ultimate Compressive Strength (UCS) increasing by a factor of between 3.5-4 over the strain rate range of 1×10^{-3} s^{-1} to 5×10^3 s^{-1}. This is greater than the rate sensitivity of steel. These results are compared to the test results used to benchmark the new IST in Figure 6.5.

2.1.5 Nylon

Farrokh and Khan [28, 29] investigated the rate sensitivity of the yield stress and the thermo-mechanical response of nylon 101. QS tests are performed on an ESH testing machine and high strain rate tests are performed on a SHPB. The results in Figure 2.7(a) and Figure 2.7(b) show that the yield stress increases by a factor of approximately 2 over the strain rate range of 10^{-5} s^{-1} to 3.6×10^3 s^{-1}.

Pouriayevali et al. [30] developed a visco-hyperelastic constitutive equation to describe the behaviour of visco elastic polymers. Testing is done at QS and high strain rates using a universal testing machine

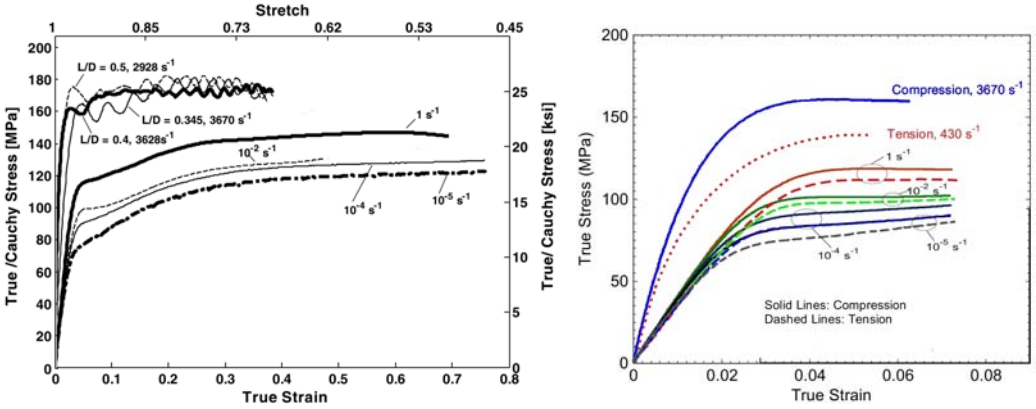

(a) Quasi static and high strain rate tests for nylon 101 [29]

(b) Quasi static tension and compression tests for nylon 101 [28]

Figure 2.7: The effect of strain rate on nylon 101

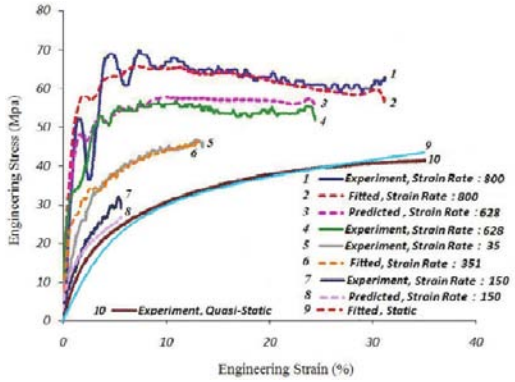

Figure 2.8: The effect of strain rate on nylon 6 [30]

and SHPB to provide data to validate the material model for nylon 6. The results for the QS, ISR and high strain rate tests are shown in Figure 2.8[1]. No ISR testing was performed.

These results show that the UCS of nylon increases by a factor of between 1.7 to 2 over the strain rate range of 10^{-5} s^{-1} to 3.6×10^{3} s^{-1}. Nylon is approximately half as rate sensitive as PMMA. As with the PMMA note the large jump in flow stress between the QS and SHPB tests and the lack of ISR data. These results are compared to the test results used to benchmark the new IST in Figure 6.4.

2.1.6 Evaluation of Published Data

Intermediate strain rate testing is regularly excluded from the material characterisation process, and as a result, ISR data available in the literature is scarce compared to QS and high strain rate data. Of the materials investigated, the mild steel and polymers have the highest rate sensitivity. An increase in flow stress of between 250% and 400% is seen between the QS and high strain rate tests. Due to this large increase in material properties over the ISR region, it is important that the material response is properly understood in this range.

[1]The strain rate of 35 s^{-1} given for test 5 appears to be a misprint. It is assumed that the strain rate for this test is 350 s^{-1}.

2.2 Established Testing Methods

Quasi static materials testing is a mature field with the testing procedures governed by testing standards [2]. By comparison, SHPB testing is not as mature a field but is well established and is the preferred method of performing high strain rate tests [2, 5]. However, each technique has physical limitations preventing its use in the ISR regime. In this section the capabilities and limitations of the classic SHPB and ESH testing methods are discussed.

2.2.1 Universal Testing Machines

Universal testing machines are regularly used for tensile and compressive testing at low rates [31]. The key components of the testing machines are the frame, a movable cross head, displacement measurement, load-cell and specimen grips. The cross head is normally either driven by power screws or electro servo hydraulic actuators. These testing machines are typically manufactured with strong heavy components to resist reduce flexing during testing. This helps ensure accurate displacement measurement during QS testing. Conventional quasi-static machines typically yield useful results for strain rates in the range of 10^{-3} to 10^{-1} s^{-1} [31] while some can test at rates approaching 1 s^{-1} [1].

Universal testing machines are typically equipped with a built in cross head displacement sensor, a cross head displacement transducer is often used. Using the cross head displacement data for displacement measurement of the specimen yields accurate results for tests with low loads and high displacements. However, for tests involving high loads and low displacements the error introduced due to machine compliance becomes significant. Under these conditions and extensometer is sometimes used. However, none of the authors discussed in Section 2.4 who modify ESH testing machines for ISR testing use extensometers.

Although ESH machines are capable of the velocities required for ISR testing [32] they are generally not suitable for testing at these rates. Two key factors plague ESH testing machines when used for ISR testing. First, the initiation of the experiment often leads to ringing in the load-frame and load-cell [8, 33]. Second, the inertial forces increase with the increasing velocity to the point that they are no longer insignificant and need to be corrected for [1, 34].

The initiation of the experiment often excites resonance in ESH testers as the loading duration is close to the natural period of the load-frame, load-cell or both. Resonance in the load-frame and load-cell can present as ringing in the output signal [8, 33]. These oscillations can present in both the force time and displacement time signals and can obscure the specimen response. Furthermore, stress wave oscillation can lead to non-uniform load distribution in the load-frame, violating the assumption that the specimen and load-cell are in equilibrium [1].

During quasi static tests the velocities are low, < 0.01 m/s [34] and therefore the inertial forces are negligible [31]. However, as the testing velocities increase, so do inertial forces. The oscillations in the measured signal caused by the inertial effects can account for as much as 50% of the measured signal [8]. These oscillations often obscure the specimen response and make it difficult or impossible to determine key material properties, such as yield stress, accurately. Oscillations in ISR data often require significant numerical smoothing after the experiment and therefore these results must be interpreted with care [8, 34]. Significant inertial forces also violate the assumption that the specimen and load-cell are in equilibrium [8].

Some authors have attempted to correct for the inertial effects, either by measuring the acceleration of the moving components with accelerometers and then subtracting the inertial forces from the measured force or by characterising the dynamic response of the system [9, 34]. Any error in the inertial correction process can lead to large errors in the results as the inertial forces account for

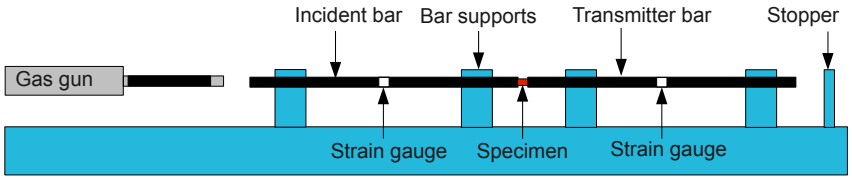

Figure 2.9: Classic SHPB configuration

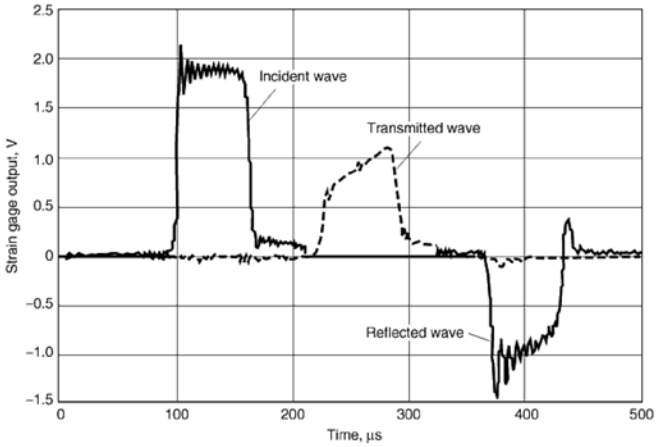

Figure 2.10: Raw signals from a classic SHPB setup [5]

as much as 50% of the measured signal [34]. Owing to the complex geometries found in most ESH machines, simplifications and assumptions are made during the correction for inertial effects. These assumptions introduce errors into the inertial correction process which are visible as oscillations in the signal after the corrections are made.

Owing to their large mass, ESH testing machines are relatively slow to accelerate up to test speed. For quasi static tests this is not a problem as the required velocities are low. However, for ISR tests this results in a large variation in strain rate over the duration of the experiment which is undesirable.

2.2.2 Hopkinson Pressure Bar

The use of the SHPB for high strain rate testing is a well-established field with a large body of supporting data available in the literature [5]. The classic SHPB layout used for high strain rate compressive testing is shown in Figure 2.9 with typical recorded signals shown in Figure 2.10.

The specimen is placed between the incident and transmitter bars. When the striker impacts the incident bar it generates a stress wave (the incident wave) that travels down the bar towards the specimen. A portion of the stress wave is transmitted through the specimen into the transmitter bar (the transmitted wave) and a portion is reflected back up the incident bar as a tensile wave (the reflected wave). The stress waves are recorded at the strain gauges on each bar. The incident, reflected and transmitted waves are all required for calculating the stress and strain in the specimen. They need to be recorded separately as shown in Figure 2.10.

In conventional SHPB tests, short loading pulses are used with long bars to avoid the overlap of the incident and reflected signals at the gauges where each is recorded [35]. This places a limit on the

maximum testing duration. If longer testing durations are required, the length of the bars must be increased to avoid the overlap of the signals. Along with the longer bars, longer and heavier strikers are also required to generate the incident wave. Practical limitations on the length and mass of the bars and strikers that can be used limit the testing duration.

The following examples compare the classic SHPB setup required for testing a 5 mm long specimen to 20% strain at a strain rate of 1000 s^{-1} and 10 s^{-1}. Steel 20 mm diameter HPB and striker with a wave speed of 5000 m/s are assumed for both scenarios. At a strain rate of 1000 s^{-1} it takes 0.2 ms to strain the specimen to 20%. To generate a 0.2 ms input pulse requires a striker 0.5 m long, this will weigh 1.23 kg. The striker velocity required to generate the strain rate of 1000 s^{-1} is 5 m/s. This results in 15.4 J of energy stored in the striker available to deform the specimen. An incident bar length of approximately 1.2 m will be required to avoid overlap of the signals recorded at the strain gauges. However, these lengths increase drastically as the strain rate is reduced. At a strain rate of 10 s^{-1} it takes 20 ms to strain the specimen to 20%. To generate a 20 ms input pulse requires a striker 100 m long. The striker velocity required to generate the strain rate of 1000 s^{-1} is only 0.05 m/s. Therefore, to store 15. 4 J of energy in the striker will require a striker mass of 12.3 tonnes. An incident bar length of around 240 m will be required to avoid overlap of the signals.

The above examples illustrate that the bar length and striker mass requirements quickly become unmanageable as the strain rate decreases with the classic SHPB setup. For this reason the classic SHPB setup is generally not used for testing below strain rates of 300 s^{-1} [10].

2.3 Extension of The Classic SHPB

Two significant limitations of the SHPB need to be overcome in order to extend the testing range into the IST. The first is that the testing duration needs to be significantly extended and the second is that an alternate loading technique needs to be developed to generate the required loading pulse to deform the specimen. In this section several techniques from the literature used to overcome these limitations are covered.

2.3.1 Wave Separation Techniques

Some researchers have resorted to implementing wave separation techniques to increase the duration of SHPB experiments. This technique requires the use of more than one strain or velocity measurement at different positions on the bar [35]. The different measurements are used to reconstruct the incident and reflected pulses once they overlap. The result of this is that the testing duration is no longer limited by the length of the bars. However, wave separation techniques tend to amplify noise on the measured signal that increases with increasing testing duration [9]. The effects of dispersion also increase with testing duration and must be accounted for when performing long duration SHPB tests [35]. Zhao and Gary report testing durations in the order of 100 times the length of a classic SHPB setup, although only results up to 32 times have been published [35].

Zhao and Gary [35] used a two gauge wave separation technique to extend the testing duration of the SHPB. The wave separation technique implemented corrects for dispersion and allows testing durations of up to 12 ms. Double gauged, 3 m long, 40 mm diameter nylon incident and transmitter bars are used for the polymeric foam tests. The loading pulse for the ISR test is generated using a hydraulic oil ram powered by a reservoir of compressed air. A schematic of the testing configuration is shown in Figure 2.11. A striker is used to generate the input pulse for the higher rate tests at a strain rate of 250 s^{-1}. Strains of up to 80% are achieved [35] and strain rates as low as of 30 s^{-1} are reported. However, no strain rate history is shown and no mention is made about how constant the strain rate is.

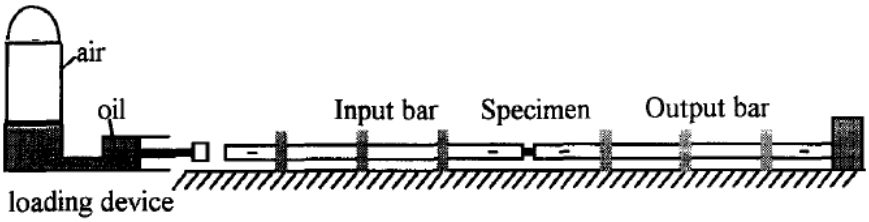

Figure 2.11: Hydraulic ram loaded SHPB layout used by Zhao and Gary [35]

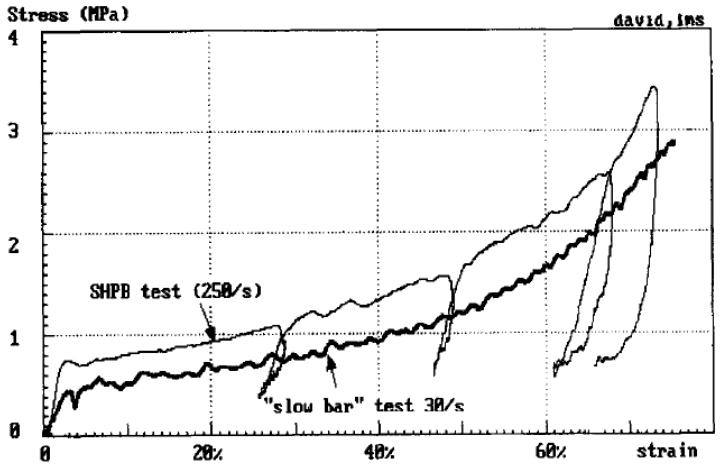

Figure 2.12: Ram loaded slow bar and SHPB results for polymeric foam presented by Zhao and Gary [35]

Shim and Mohr [15] characterised Polyurea at low, intermediate and high strain rates. A classic SHPB setup is used for the high strain rate tests while a SHPB setup with a wave separation technique is used for the intermediate rate tests. Nylon incident and output bars are used along with a wave separation technique that incorporated 3 strain gauge readings and a displacement sensor per bar, as shown in Figure 2.13. The incident and transmitter bars used are both 40 mm diameter and approximately 3 m and 2 m long respectively. A hydraulic ram is used to provide the loading pulse, average loading velocities vary between 0.5 and 5 m/s. The difference in force readings between the incident and transmitter bars, seen in Figure 2.14, was attributed to the poor quality of the displacement measurement used in the wave separation technique [15]. The inertia of the bars is not large enough to supply the reaction force on the specimen and hence the fixed end support are necessary. The fixed end support release the bars before their elastic buckling limit is reached [15]. The releasing of the fixed end support resulted in the unloading and reloading of the specimen, this can be seen at 20 ms and 60 ms in Figure 2.14(a) and Figure 2.14(b). The unloading is also visible in the stress strain plots shown in Figure 2.15(a). Shim and Mhor do show the strain rate histories for the tests performed, the results are shown in Figure 2.15(b). The unloading and reloading of the specimen greatly affects the strain rate, which falls to near zero each unloading cycle, as shown in Figure 2.15(b).

Although the wave separation techniques provide a useful method to extend the testing duration it is a challenge to achieve a uniform strain rate for long duration SHPB tests. The incident pulse is a function of the velocity of the loading device until the reflected wave reaches the loading device/incident bar interface. For the remainder of the experiment the incident wave is a function of the wave generated by the loading device and the reflected wave. The reflected wave continues to travel up and down the incident bar, adding and subtracting from the generated pulse as it changes from tensile to compressive wave with each reflection. This results in the strain rate varying with the period equal to the bar length

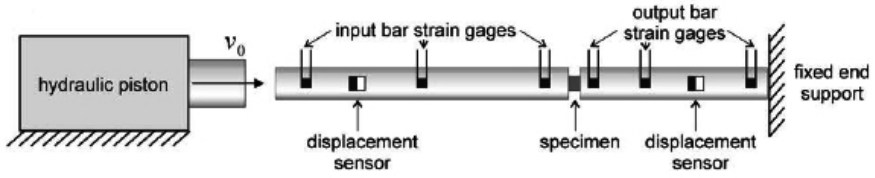

Figure 2.13: Nylon SHPB layout used by Shim and Mohr [15]

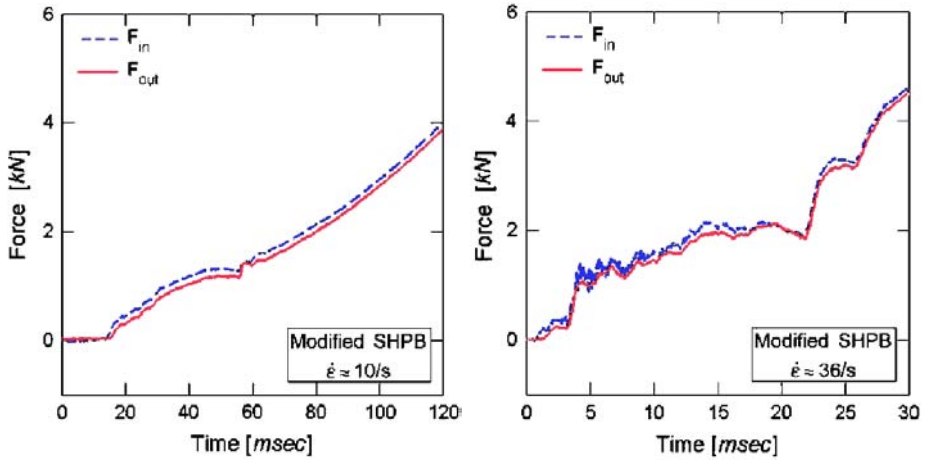

(a) Force time data for a test performed at $\dot{\epsilon} = 10\ s^{-1}$ [15]

(b) Force time data for a test performed at $\dot{\epsilon} = 36\ s^{-1}$ [15]

Figure 2.14: Raw data for the nylon SHPB presented by Shim and Mohr [15]

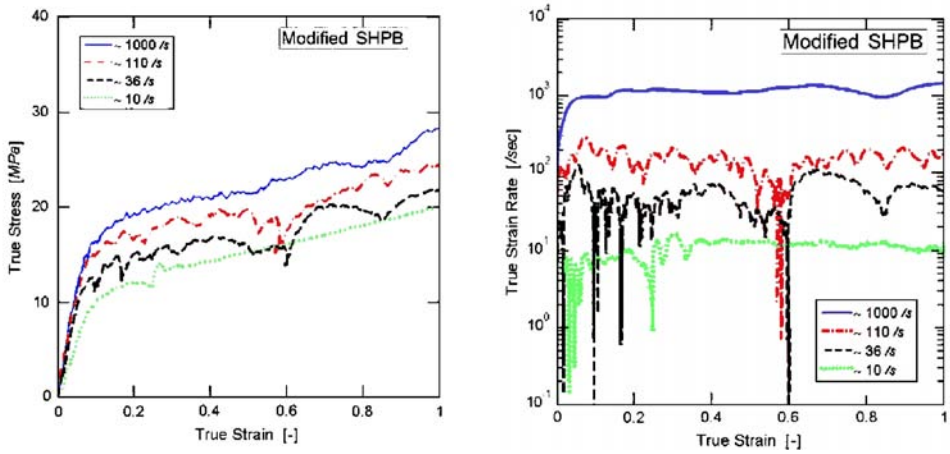

(a) True stress vs. strain data showing the effect of strain rate [15]

(b) Strain rate vs. strain data [15]

Figure 2.15: Test results for the nylon SHPB presented by Shim and Mohr [15]

divided by the wave speed. Shim and Mohr [15] reported near constant strain rates can be achieved by using bars shorter than 0.5 m or longer than 20 m. However, two 20 m bars are impractical as the total length will be in excess of 40 m long and the short bars will reduce the testing duration as the testing duration is linked to the number of reflections that can be separated using a wave separation technique.

2.3.2 Long Hopkinson Pressure Bar

Gilat and Matrka [10] used a 40 m long Hopkinson Pressure Bar (HPB) loaded using a hydraulic actuator for ISR testing. The experiment setup used is shown in Figure 2.16(a). The long HPB is set up down the length of a corridor as shown in Figure 2.16(c). One end of the specimen is placed in contact with the HPB while the other is directly loaded with the hydraulic actuator shown in Figure 2.16(d). Loading the specimen generates a compressive stress wave in the HPB. The transmitted stress wave in the HPB is measured using strain gauges mounted five diameters from the specimen and is used to calculate the force in the specimen [10]. Digital Image Correlation (DIC) is used to measure the strain in the specimen directly. To enable this the specimen, HPB and actuator are painted with a speckle pattern as shown in Figure 2.16(b).

As no wave separation technique is implemented, the duration of the test is limited to twice the time it takes the stress wave to propagate from the strain gauges to the free end of the HPB, approximately 16 ms.

The strain time, force time and stress strain curve presented for an PR-520 epoxy specimen are shown in Figure 2.17. The results shown in Figure 2.17(b) and 2.17(c) show the HPB provides a smooth force measurement free from oscillations[2]. However, once again, no strain rate history is reported.

The strain rate history shown in Figure 2.18(b) is calculated by digitizing and processing the data shown in Figures 2.17(a) and 2.17(b). A polynomial is fitted to the strain time data and differentiated to give the strain rate history. The calculated strain rate history shows the strain rate varies over the duration of the experiment. The strain rate increases from 80 s^{-1} at yield to 120 s^{-1} at around 20% strain before falling off to 50 s^{-1} towards the end of the experiment, the quoted strain rate for this experiment is 80 s^{-1} [10]. Note how the strain rate varies with the variation in flow stress in the specimen. As the stress increases until yield the strain rate drops off rapidly. As the flow stress drops off between yield and 20% strain, the strain rate increases again before dropping off over the remainder of the experiment.

[2]The author offers no explanation for the small drop in force seen at around 3200 µs

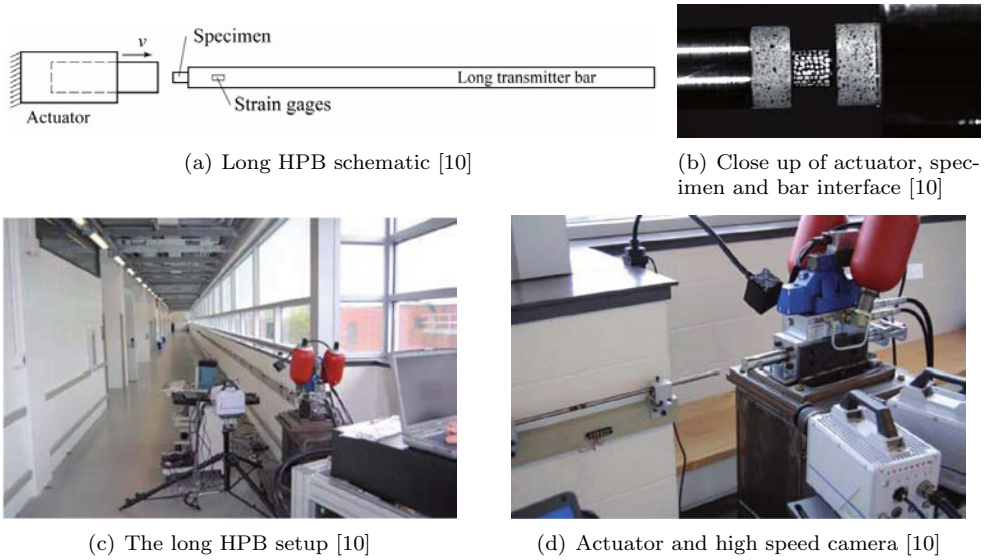

(a) Long HPB schematic [10]

(b) Close up of actuator, specimen and bar interface [10]

(c) The long HPB setup [10]

(d) Actuator and high speed camera [10]

Figure 2.16: Hydraulic piston loaded long HPB testing setup used by Gilat and Matrka [10]

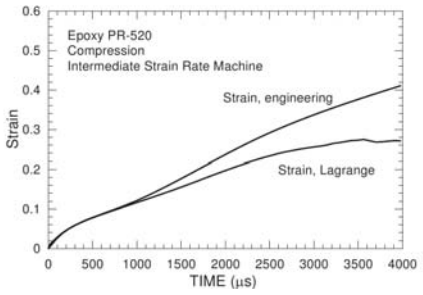

(a) Raw strain time data [10]

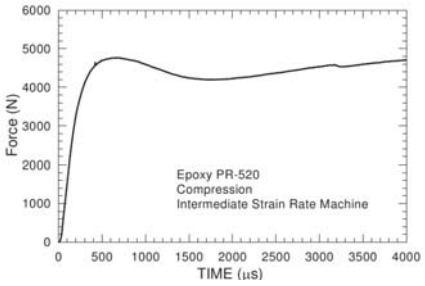

(b) Raw force time data [10]

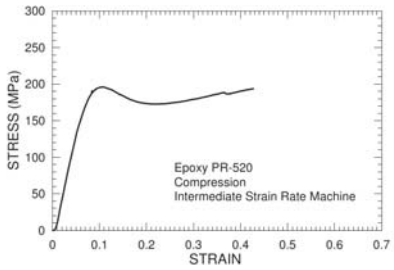

(c) Stress Strain Curve for Epoxy PR-520 [10]

Figure 2.17: Published results for long HPB

2.3.3 ESH Loading of HPBs

Othman et al. [9] used an ESH testing machine to load a HPB for intermediate rate testing as an alternative to a striker or hydraulic ram. The HPB and ESH testing machine are configured for tensile testing as shown in Figure 2.19(a). The test duration is extended by implementing a wave separation technique. This technique implemented uses strain measurements taken at three different locations along the bar and accounts for dispersion [9]. The specimen is held by grips on either end.

It is necessary to correct for the inertial effects of the mass of the specimen grips as their mass is significant. The acceleration of the grips is calculated from the strain gauge signals and used along with the mass of the grips to calculate the inertial component of the measured force. The inertial force is then subtracted from the measured force, in theory, leaving only the specimen force [9]. The inertial correction reduces the oscillations in the signal by 50% [9] but do not remove them completely, as shown in Figure 2.19(b) and Figure 2.20(a).

Once the inertial correction was implemented, the results from the HPB load-cell gave significantly better results than the piezo-electric load-cells. The test performed at strain rates of 6 s^{-1} has smaller magnitude oscillations compared to the test performed at strain rates of 120 s^{-1}. It is expected that this is due to the lower test velocities and therefore softer impact at the start of the experiment. The tests performed at strain rates of 6 s^{-1} show good correlation between the quasi static and ISR data as expected for aluminium, shown in Figure 2.20(b). However, even at these lower strain rates oscillations are still visible in the ISR data.

2.3.4 Evaluation of Modified HPB and SHPB Configurations

The quality of the force measurement achieved when using wave separation techniques varies depending on the implementation. The results presented by Zhao and Gary [35] provide reasonably smooth force measurement but those presented by Shim and Mohr [15] contain undesirable oscillations. In contrast, the force measurement achieved using the long HPB are good with no oscillations present on the signals. The duration of the loading pulse generated using the hydraulic rams or ESH testing machines is sufficient. However, none of the authors achieved uniform strain rates using these methods.

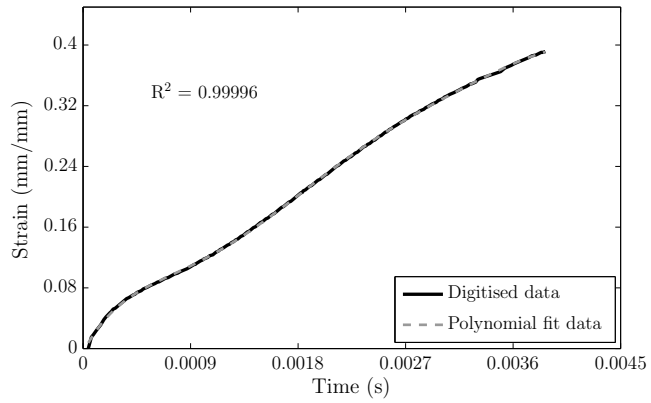

(a) Digitised strain time data

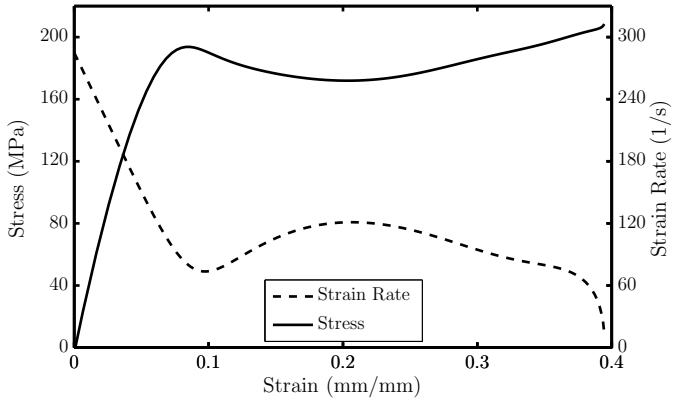

(b) Processed results

Figure 2.18: Processed results for long HPB

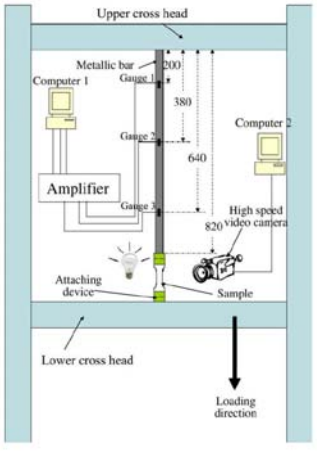

(a) Schematic [9]

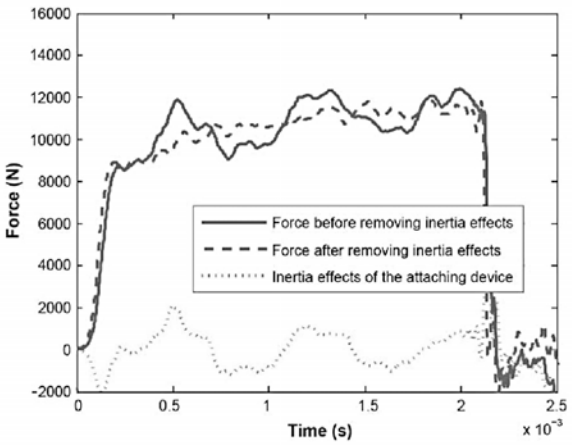

(b) Inertia correction results [9]

Figure 2.19: Tensile ESH machine with HPB load-cell presented by Othman et al. [9]

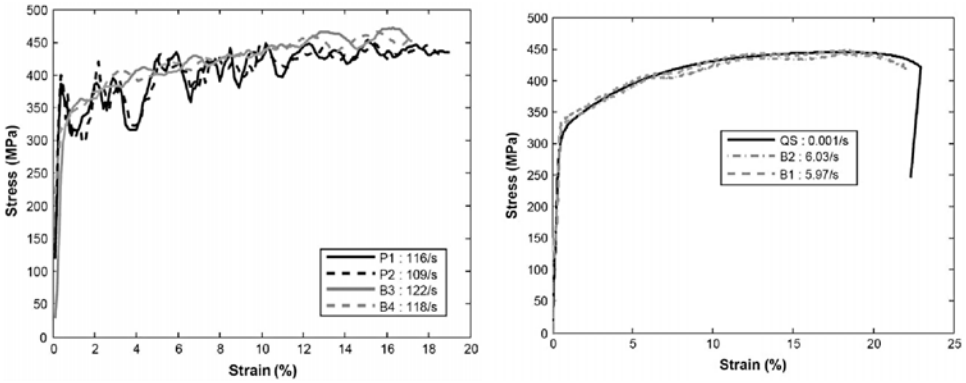

(a) Piezoelectric vs. HPB load-cell, $\dot{\epsilon} = 120\ s^{-1}$ (b) QS and ISR results

Figure 2.20: Testing results for aluminium 2017 presented by Othman et al. [9]

2.4 Extension of The ESH Testing Machine

The use of ESH testing machines for ISR testing is appealing as many test facilities already have these machines available. In this section, concepts used to extend the testing range of ESH testing machines into the ISR regime are reviewed. Wood et al. [32] and Boyce and Dilmore [8] developed tensile grips that allow the ESH testing machines to reach testing speed before the specimen is deformed. Custom-built load-cells are used to improve the force measurement.

2.4.1 Fast Jaw Grip

Wood et al. [32] describe the concept of the Fast Jaw Grip shown in Figure 2.21. One side of the specimen has an elongated tab, as shown in Figure 2.21(c). At the start of the experiment the tab moves through the jaws. Once the testing speed is reached, the fast grip jaw rapidly grips the elongated tag of the specimen thereby starting the experiment. The fast jaw grip extends the tensile testing range up to strain rates of 600 s^{-1}.

Force measurements are taken from the machine mounted load-cell as well as strain gauges mounted on the specimen. True strain and strain rate measurements are taken from the gauge mounted at the centre of the specimen and force measurements are taken from two gauges mounted on the thicker tabbed Section [32], as shown in Figure 2.21(c). The maximum strain measurement is limited to 10% for the specimen mounted strain gauge [32]. After this point, the machine mounted displacement measurement can be used[3]. The strain gauge data is compared with the machine mounted force and displacement sensor data to allow error estimates to be made [32]. The error in the machine mounted displacement measurement varies between 10% and 50% depending on the specimen gauge length [32]. The specimen mounted force measurement shows a significant reduction in the magnitude of the oscillations seen.

One additional specimen is manufactured per batch and tested to failure under quasi static conditions to calibrate the strain gauges. The calibration factors calculated from this test are then used for all the specimens in the batch [32]. This assumes consistent gauge application. Any variation in specimen geometry, gauge position or alignment of the gauge will introduce errors. From the Author's experience, up to a 5% variation can occur.

[3]Most strain gauge bridges are only linear to approximately 5% strain and require non linear correction thereafter. Unless high-elongation gauges are employed, the resistive grid of many strain gauges begins to fracture between 8-10% strain rendering the gauge useless, even if it is still bonded to the specimen.

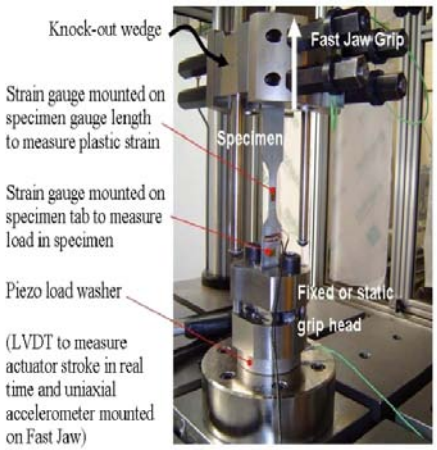

(a) Fast Jaw Grip atachments [32]

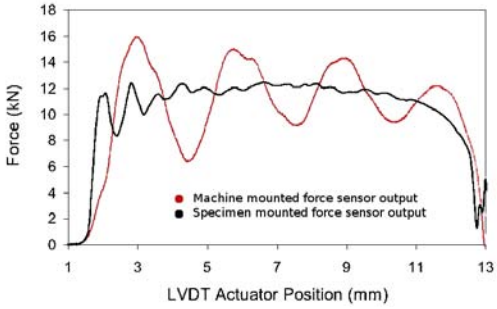

(b) Results [32]

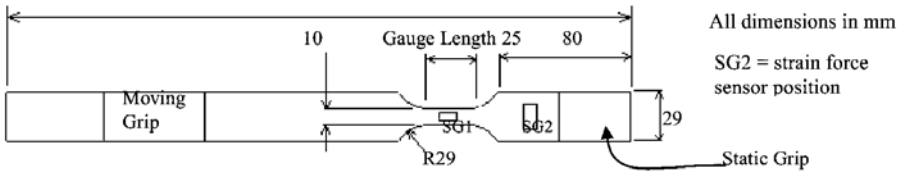

(c) Fast Jaw Grip specimen [32]

Figure 2.21: Fast Jaw Grip layout and results presented by Wood et al. [32]

The results presented in Figure 2.21(b) are for a test performed at a strain rate of 600 s^{-1}. No strain rate history is shown and no information given about how much the strain rate varies over the experiment. The strain rate quoted for the experiment is calculated by dividing the initial actuator velocity by the specimen gauge length. Results are not shown for tests performed at lower rates. Oscillations are visible in both the specimen and machine mounted force sensors.

2.4.2 Slack Adapter

Boyce and Dilmore [8] presented the "slack adapter" shown in Figure 2.22. It is similar in concept to the Fast Jaw Grip in that it accelerate up to testing speed before deformation of the specimen begins. A schematic diagram of the slack adapter is shown in Figure 2.22(a). A slot machined into the slack adaptor piston slides over a pin which is fixed to the slack adaptor sleeve. As the cross heads move apart the pin slides freely through the slack adaptor piston until it impacts the rubber damper loading the specimen.

The rubber damper inserted at the base of the slot is used to help suppress stress wave generation by softening the impact at the start of the experiment. The use of the rubber damper is analogous to the practice of pulse shaping used in SHPB experiments where a thin sacrificial element is placed on the impact surface of the incident bar. The deformation of rubber damper reduces oscillations on the input signal by increasing the rise time of the incident pulse. However, the strain rate in the specimen is decreased while the damper is deforming.

Two custom load-cells are constructed, each consisting of two diametrically opposed biaxial strain gauges mounted on a short elastic bar. The specimen screwed directly into the load-cells [8]. A load-cell is placed either side of the specimen to check for dynamic equilibrium during the test [8]. Typical results are shown in Figure 2.23(b). Strain is measured using a high elongation strain gauge fitted

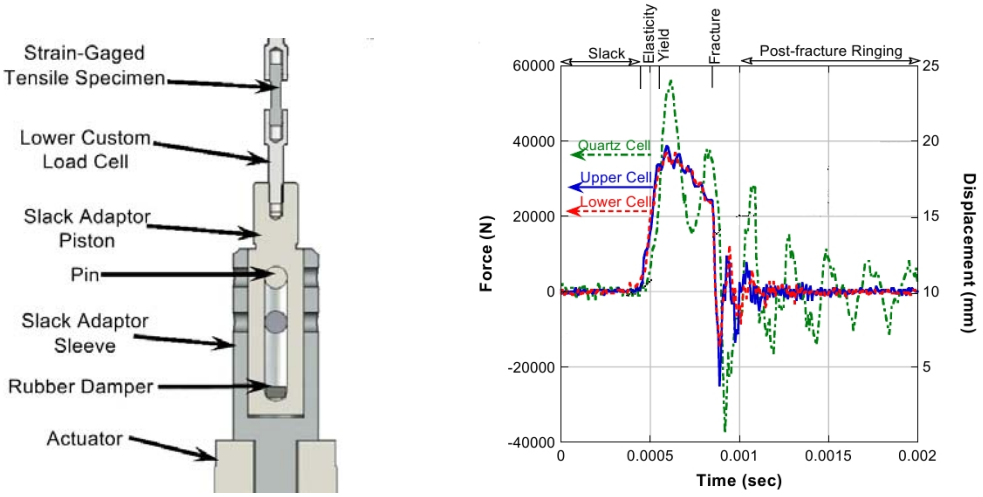

(a) Gripping mechanism [8]

(b) Custom and quartz load-cell raw data [8]

Figure 2.22: Slack adapter by Boyce and Dilmore [8]

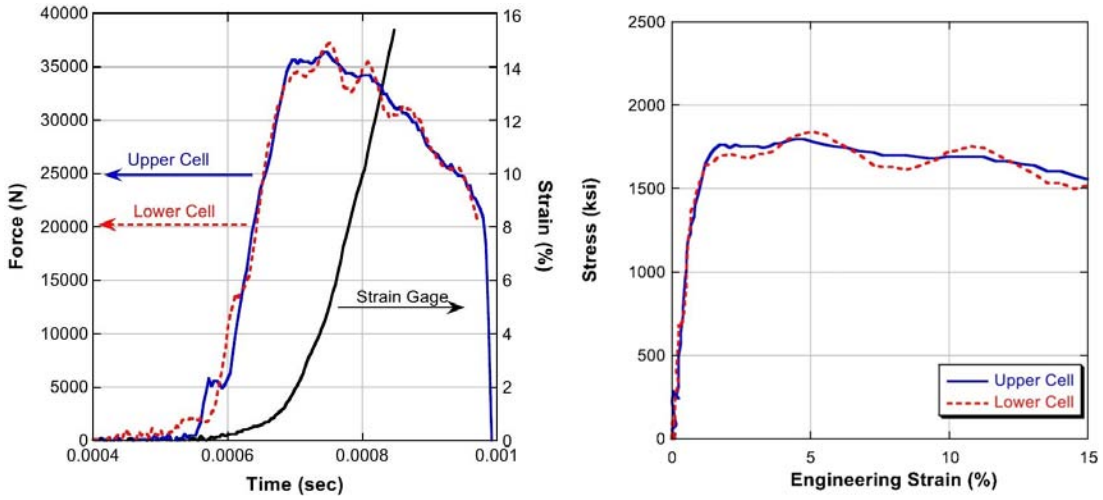

(a) Slack adapter raw data [8]

(b) Slack adapter stress equilibrium [8]

Figure 2.23: Slack adapter published results presented by Boyce and Dilmore [8]

to the centre of each test specimen [8]. This is expensive and time consuming for regular testing but necessary because accurate strain measurement is not available from the machine.

Raw data for a test performed at a cross head displacement of 7.1 m/s, a nominal strain rate of 560 s^{-1}, is shown in Figure 2.22(b). Tests are performed at strain rates ranging from 0.2^{-3} $s^{-1}$to 200 s^{-1}, but once again strain rate histories are not shown. The strain rate is reported as varying by a factor of two during the experiment while the rate near yield is reported as the rate for the test [8]. The strain rate history shown in Figure 2.24(b) is calculated from digitizing the strain time data, shown in Figure 2.24(a).

The strain rate varies from 0 to 650 s^{-1} during the experiment, although from yield to UTS the strain rate varies by a factor of approximately 2.5. The force measurements from the custom load-cells are significantly smoother than the force measurement from quartz load-cell. Larger oscillations are visible

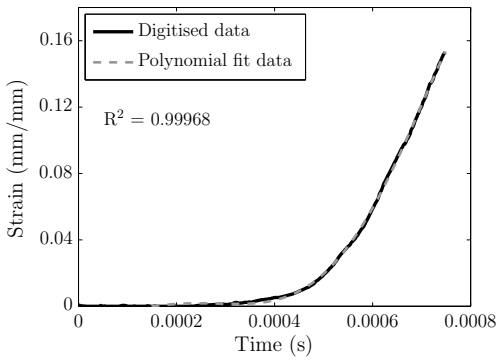

(a) Digitised strain time data

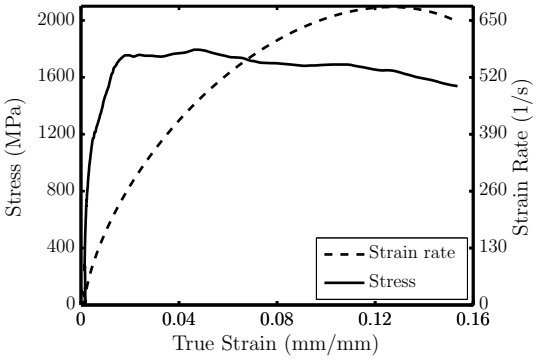

(b) Processed stress and strain rate results

Figure 2.24: Slack adapter processed results

in the load-cell closest to the slack adapter. This indicates that the oscillations are being dampened by the specimen, which is not ideal.

2.4.3 Evaluation of Modified ESH Testing Machines

Modifying ESH testing machines for ISR testing has its challenges. Using strain gauges mounted on the specimen to measure force shows improvements over the machine mounted force sensors [8, 32], but the gauging of each individual specimen is expensive and tedious for routine testing. The short and stiff custom load-cells used with the slack adapter show a significant improvement over the machine mounted quartz load-cell, although small oscillations in the signals are still visible, as shown in Figure 2.23(a) and Figure 2.22(b). It is expected that these oscillations are caused by the dynamic response of the load path and not the response of the load-cell itself. It is expected that the magnitude of the oscillations will decrease for tests performed at lower strain rates but this has not been reported. The use of a short, stiff load-cell in an IST will be discussed in Section 3.1.

The use of the rubber damper in the slack adapter effectively reduces stress wave oscillation caused by the initial impact. The negative effect of this is that the rubber damper compresses during the experiment resulting in a varying strain rate. The rubber damper also makes it necessary to strain gauge each specimen (adding considerable cost and time) to achieve accurate strain measurements.

2.5 Energy Storage Devices

In this section, the use of energy storage devices in ISR testing is reviewed. An energy storage device is a term used to describe loading techniques that store large amounts of energy, compared to the energy required to deform the specimen. In theory, if sufficient energy is stored in the loading device the loading rate of the specimen should be relatively constant as only a small percentage of the available energy is required to deform the specimen. Drop towers and flywheels are two examples of energy storage devices. Although some of the drop towers and flywheel devices presented below are used for testing at the lower end of the high strain rate regime rather than for ISR testing, the concepts and their implementation is relevant to this dissertation.

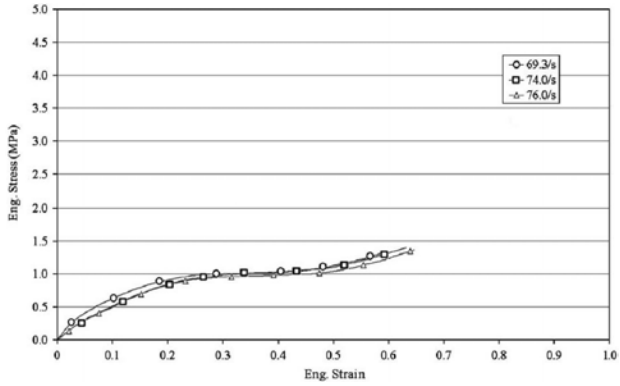

Figure 2.25: Drop test results presented by Oullet et al. for 110 kg/m^3 HDPE

2.5.1 Drop Testers

Ouellet et al. [12] and Mott et al. [34] used drop testers to perform ISR tests. In a conventional drop tester a free falling weight impacts the specimen directly, compressing it. Force measurement remains a problem with drop testers. Quartz load-cells are typically used for force measurement. As with servo-hydraulic machines this often results in oscillations on the measured signals obscuring the specimen response [9].

Ouellet et al. [12] used a controlled drop tower to test polymeric foams at rates from 10 s^{-1} to 100 s^{-1}. An accelerometer is attached to the falling weight and used to calculate stress while strain is calculated from the drop weight displacement [12], the results are shown in Figure 2.25. The strain rate varies as the specimen is compressed and the drop weight slows down despite the weak material tested. The strain rate quoted is the average rate for the test [12]. No strain rate history is shown, but the variation in strain rate is quoted as 30% [12].

The strain rate in typical drop testers is directly related to the drop mass speeds. The lower the impact speed of the drop mass, the larger the mass required to ensure enough energy is stored to deform the specimen. At the lower velocities required for ISR tests a very large drop mass is necessary. To solve this problem Mott et al. [34] modified a drop tester to impact two L-shaped lever arms, as shown in Figure 2.26(a). The effect of the lever arms is to decrease the loading rate of the specimen for a given impact velocity. This allows for higher drop mass speeds and therefore the use of lighter drop masses. Strain rates ranging from 14 to 588 s^{-1} are reported, however raw data is only shown for rates of 588 s^{-1}. The strain rate is calculated using high speed photography while load-cells mounted on the shuttles are used for force measurement.

Accelerometers mounted on the shuttles are used to correct for inertia effects of the system. A test is done with no specimen present, the force and acceleration data is used to calculate the effective mass of the setup. This mass, along with the accelerometer data, is then used to correct for the inertia effects. As the inertial force is large compared to the sample force, any error in the inertia correction will result in a large error in the corrected force measurement, as shown in Figure 2.26(b).

Shock absorbers are mounted in the loading path near the shuttle to damp out vibrations caused by the impact at the start of the experiment [34]. The combined effect of the dampers and the high inertia of the system resulted in slow acceleration up to testing speed, as shown in Figure 2.26(b). The strain rate for the reported test is quoted as 588 s^{-1} but no strain rate history is shown. The raw data from Figure 2.26(b) has been digitised and processed to give the results in Figure 2.27(b). Note the large variation in the strain rate over the experiment.

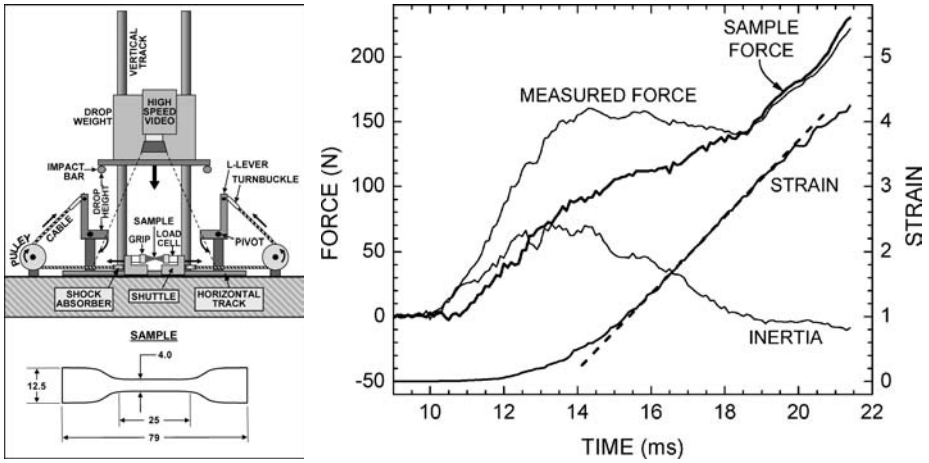

(a) Modified drop tester layout [34]

(b) Raw data $\dot{\epsilon} = 588$ s^{-1}. Notice the large inertial forces measured [34]

Figure 2.26: Modified drop tester presented by Mott et al. [34]

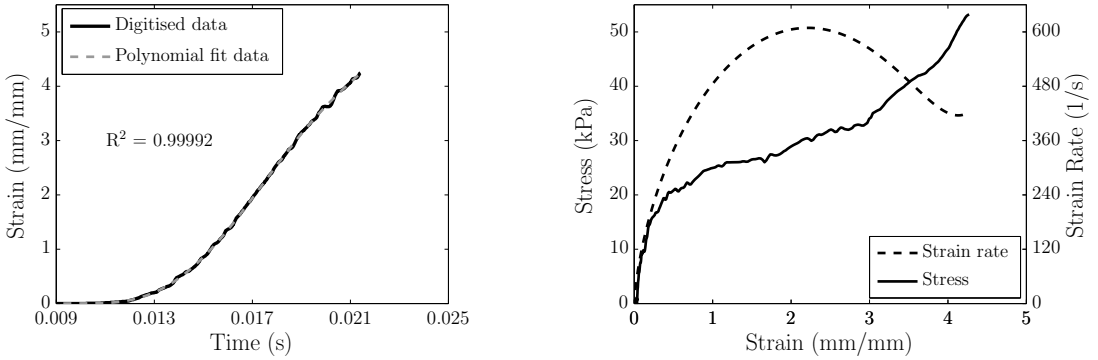

(a) Digitised and polynomial fit strain time data

(b) Modified drop tester results, quoted $\dot{\epsilon} = 588$

Figure 2.27: Modified drop tester results, quoted $\dot{\epsilon} = 588$

2.5.2 Fly Wheel Devices

Several authors have used flywheel devices for ISR testing [4, 36, 37]. A typical setup consists of a flywheel which is spun up to testing speed using an electric motor. Once the testing speed is reached, a trigger releases a hammer that impacts the specimen directly [37], or an attachment connected to the specimen [36, 38]. As the flywheel can store a large amount of energy there is a negligible change in velocity during the experiment as the energy absorbed by the deforming specimen is negligible compared to the energy stored in the rotating disk. Lambert et al. [38] reported a maximum variation of 1.5% over the experiment. However, force measurements in the fly-wheel devices remains problematic, with ringing occurring in the measured signals of many of the configurations investigated.

Manjoine and Nadai [4] used a rotating flywheel device to investigate the strain rate and temperature effects on soft annealed copper under compression. The fly-wheel is driven by a d.c. motor. Once the flywheel is up to speed the hammer is rotated into the striking position, impacting the specimen directly and deforming it at near constant velocity, to failure. Strain rates of 135 to 900 s^{-1} are achieved. At the higher strain rates, oscillations are visible on the signals making the results difficult to interpret.

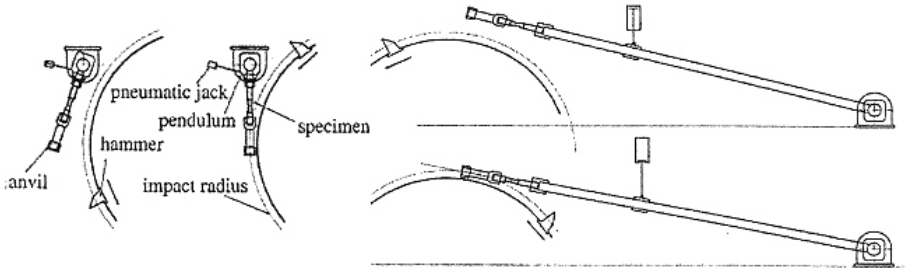

Figure 2.28: Force measurement techniques used by Lambert and Lassilia [38]

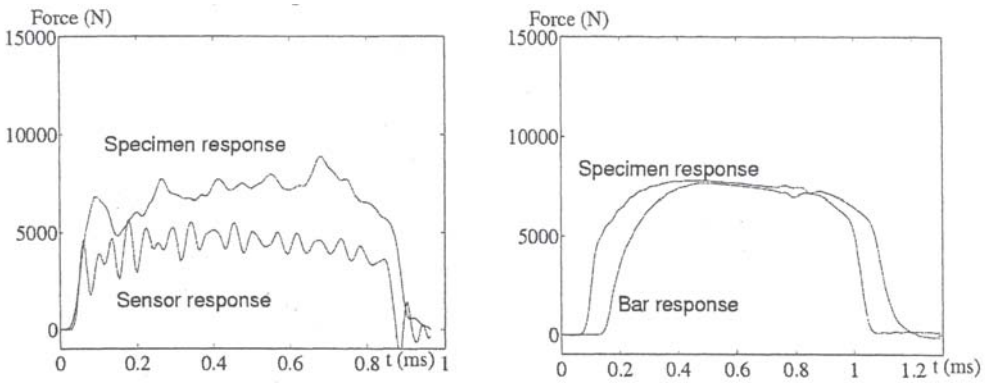

(a) Piezo-electric load-cell [38]

(b) HPB load-cell [38]

Figure 2.29: Fly wheel results presented by Lambert and Lassilia [38]

Lambert and Lassilia [38] used a fly-wheel device for ISR tests under tension. The setup used allows for impact velocities between 1-40 m/s. A piezo-electric force sensor as well as a HPB are used for force measurement, a schematic of the layout used is shown in Figure 2.28. No wave separation technique is used. The bar length limits the testing duration to 1.4 ms, giving a maximum strain of 14% at a strain rate of 100 s^{-1}. The results from the piezo-electric sensor and HPB are compared with the results from strain gauges mounted on the specimen. The signals from the piezo-electric sensor contained severe oscillations which obscured the specimen response, as shown in Figure 2.29(a). In comparison, the HPB signals are significantly smoother and better match the specimen response, as shown in Figure 2.29(b) [38]. Furthermore, the time to failure when using the HPB sensor is longer than the time to failure for the piezo-electric sensor. Lambert et al. proposed that the premature failure of the specimen tested with the piezo-electric sensor is due to the stress wave fluctuations in the specimen during testing [38]. This error cannot be accounted for by post-processing the signals. It is important to note the force sensor used can have a significant effect on the specimen response.

Xia and Wang [36] used a flywheel to load a tensile SHPB. The test duration is extended by implementing a wave separation technique. Once the flywheel reaches the required speed, a hammer on the flywheel impacts a deformable metal bar connected to the incident bar. The magnitude and duration of the input pulse is modified by changing the diameter and length of the deformable bar. The plastic deformation of the deformable bar acts as a mechanical damper absorbing any stress wave oscillations caused by the impact of the hammer generating a smooth input pulse. Strain rates as low as 70 s^{-1} are reported, but once again, no strain rate history is shown.

2.5.3 Evaluation of Energy Storage Devices

The large amount of energy stored in energy storage devices helps ensure a constant loading rate. However, at the low velocities required for ISR testing very large masses are required to store sufficient

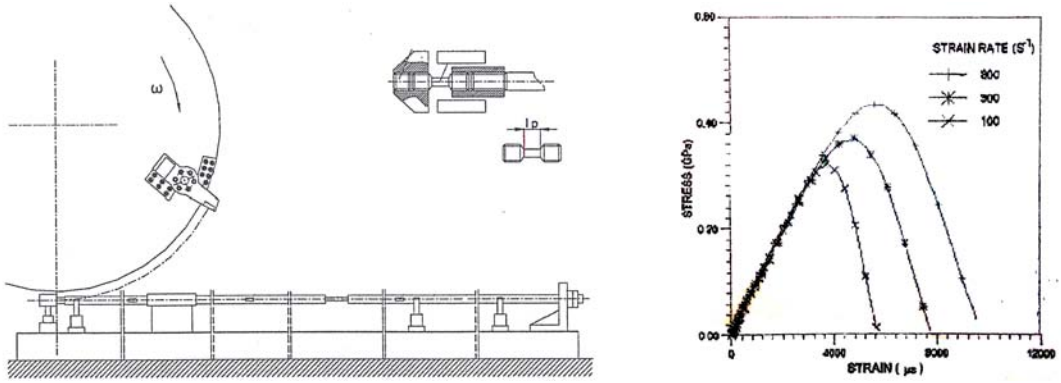

(a) Schematic [36] (b) Results [36]

Figure 2.30: Fly wheel loaded tensile SHPB presented by Xia and Wang [36]

energy to ensure constant loading rates. The practical limitations on the mass of the flywheels and drop weights limit the lower end of the strain rates achievable. However, the achievable strain rate can be reduced if a speed reduction mechanism is used to reduce the loading rate of the specimen. In theory the energy storage devices presented should provide very constant loading, but it is important to note that strain rate histories are not provided for the flywheel experiments and the calculated rate history is not very constant for the drop tester results presented by Mott et al. [34]. Energy storage devices provide an appealing solution for loading, but force measurement remains a challenge.

2.6 Custom-Built Machines

Due to the inherent limitations of the established QS and high strain rate testing methods a number of authors have developed custom-built machines specifically for testing at intermediate strain rates [1, 39, 40]. The two examples presented here are the Hydro-Pneumatic machine developed by Albertini and Montagnani and later modified by Tarigopula et al. [31] and the wedge bar intermediate strain rate tester developed by Cloete and Oxtoby [1]. As these testing methods are specifically developed for ISR testing their design helps avoid many of the problems inherent with the modified ESH and SHPB testing techniques discussed above.

2.6.1 Hydro-Pneumatic Machine

To overcome the large inertia, long load path and relatively low stiffness that plague ESH testing machines Albertini and Montagnani developed a hydro-pneumatic machine for ISR testing that uses light weight moving components, short stiff load-cells and a short load path [39]. A schematic of the hydro-pneumatic machine is shown in Figure 2.31. This machine resembles the pneumatic-pneumatic machine presented by Maiden and Green in 1966 [40]. The hydro-pneumatic machine developed by Albertini and Montagnani is capable of tensile testing in the range of 1 s^{-1} to 20 s^{-1} [39]. This machine was then modified by Tarigopula et al. [31] to extend the testing range up to strain rates of 150 s^{-1}. Figure 2.31 shows a schematic of the hydro-pneumatic machine.

The motion of the piston is controlled by the difference in pressure in the two chambers either side of the piston. The driving pressure is supplied by nitrogen at 180 bar in the first chamber. Water, initially also at 180 bar, fills the second chamber. The pressure difference is created up by opening the rapid firing valve allowing water to escape through an orifice. As the volume of water decreases, the piston moves to the left thereby loading the specimen. The piston velocity is controlled by the size of the orifice selected for the experiment. The orifice is sized so that chocked flow occurs as the

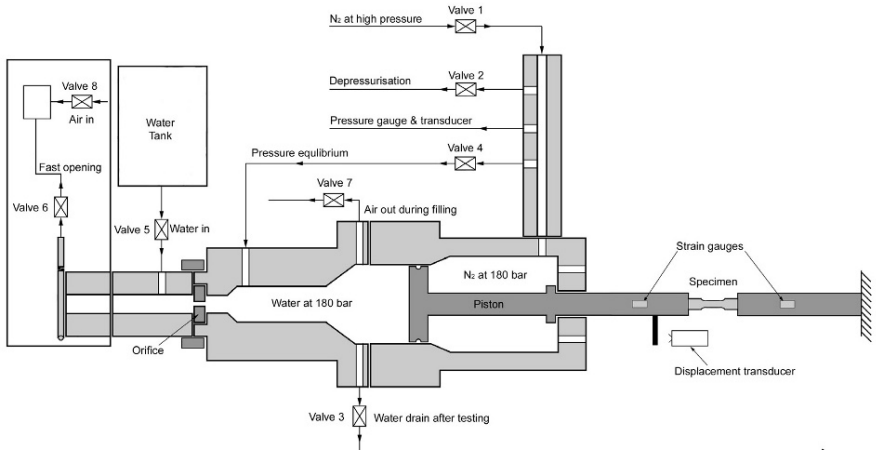

Figure 2.31: Hydro-pneumatic testing machine schematic [39]

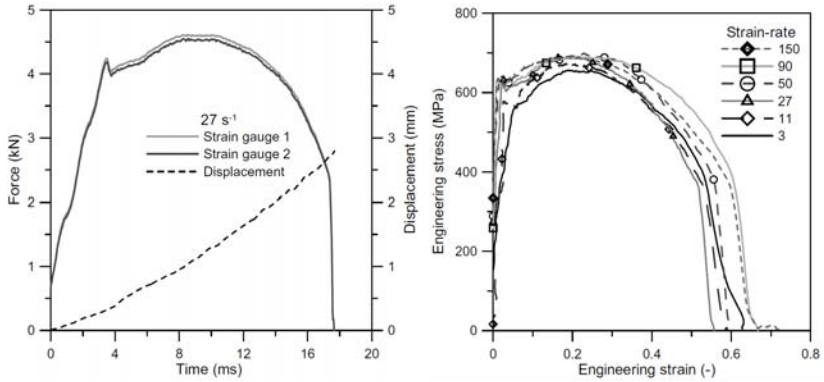

(a) Raw data [39]

(b) Results [39]

Figure 2.32: Hydro-pneumatic testing machine results

water passes through the orifice. This results is a near constant piston velocity and strain rate [41]. The only moving component is the piston. The mass of the piston is kept as low as possible to ensure it will accelerate up to testing speed quickly. Despite this a bit of lag is still present at the beginning of the experiment [31].

The specimen is mounted between two load-cells made from short elastic bars fitted with strain gauges. The raw data for a test performed at a strain rate of approximately 30 s^{-1} is shown in Figure 2.32(a). There is a close correlation between the force readings taken from the two load-cells either side of the specimen, indicating that the specimen is in equilibrium and not affected by the stress wave oscillation or inertial effects [31]. However, some oscillations are visible in the elastic portion of the experiment during specimen "ring-up". The specimen took longer than 20% of the test duration to yield. It is expected that the delay in yielding is caused by a combination of machine compliance and the slow acceleration of the piston over the initial portion of the experiment. There is no mechanism to allow the piston to accelerate up to testing speed before deformation of the specimen begins. Furthermore, the run-up portion of the experiment is not shown in Figure 2.32(a).

No strain rate histories are given for the test results shown in Figure 2.32(b). The raw data in Figure 2.32(a) has been digitised and processed to give the results shown in Figure 2.33. During the data processing it was noticed that the amount of oscillations in the strain rate data is highly dependent on the numerical methods chosen to convert the digitised displacement data to strain rate.

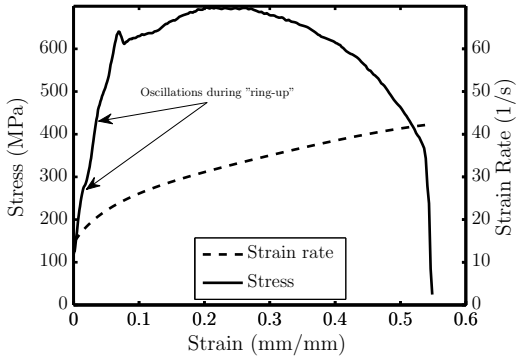

Figure 2.33: Hydro-pneumatic testing machine processed results

As the raw data is obtained from digitising an image it was decided to present the strain rate history that is probably overly smoothed but represents the global response well. It is expected that the strain rate calculated from the original data will contain low frequency oscillations. Machine compliance or the deformation of the specimen outside the gauge section is not taken into account as there is not enough information available to do so. Comparing Figure 2.32(b) and Figure 2.33 shows that the stress strain curve calculated from the raw data agrees well with the stress strain curve presented. This analysis shows that the strain rate varies by a factor of two during the plastic region of the test.

2.6.2 Wedge Bar Intermediate Strain Rate Tester

To address some of the limitations of the testing techniques discussed previously Cloete and Oxtoby [1] developed a prototype for a new technique for ISR testing with the end goal of performing interrupted compression tests on small quasi-brittle specimens. The wedge bar Intermediate Strain rate Tester (IST) consists of a striker, wedge bar, stopper bar and a load-frame assembly as show in Figure 2.34 and Figure 2.35. The striker fired from a gas gun impacts the wedge bar (1). The impact rapidly accelerates the wedge bar, which then moves to the right through the load-frame assembly. As the wedge bar slides through the load-frame assembly, the sliding anvil (3) and lower portion of the load-frame (4) are moved apart due to the wedge angle on the wedge bar. This compresses the specimen between the sliding anvil and the top portion of the load-frame. At the end of the experiment the wedge bar impacts the stopper bar, rapidly stopping the experiment. This concept incorporates a number of the design features successfully implemented by other authors:

- The load path length is minimised, resulting in a load-frame less than 50 mm long.
- A short custom-built strain gauge based load-cell is incorporated into the load-frame.
- A loading method is used that incorporates a velocity reduction between the moving mass and the loading surface. Significantly more energy is stored in the wedge bar than is required to deform the specimen.
- The mass of the moving parts is minimised, reducing inertial effects

As elastic impact principles are used to start and end the experiment, the testing speed is reached rapidly [1]. The momentum of the striker is transferred to the wedge bar within one stress wave reflection as the impedance of the striker and wedge bar are the same. The portion of the wedge bar in contact with the sliding anvil accelerates from stationary up to testing velocity in less than 1% of the test duration (approximately 133 μs) [1] and stops in the same time. Despite the rapid initiation of the experiment, the striker accelerates over a relatively long distance. This allows the use of 10 bar shop air to drive the gas gun.

The 1/300 angle of the wedge bar allows a wedge bar velocity of over 10 m/s while deforming the specimen at strain rates of around 10 $s^{-1}$when testing a 5 mm long specimen. Due to the high wedge

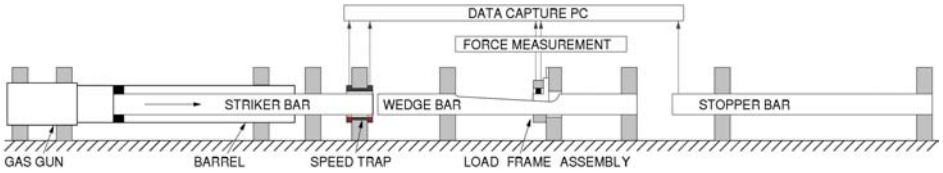

Figure 2.34: Wedge bar IST concept [1]

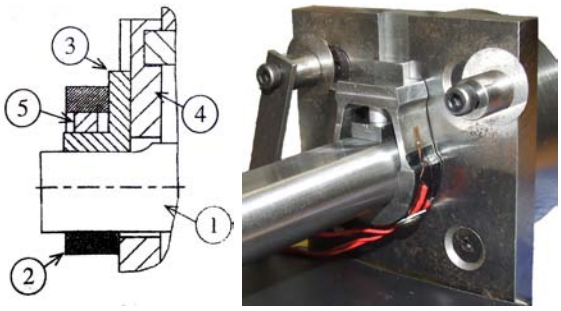

(a) Schematic [1] (b) Photo [1]

Figure 2.35: Wedge bar IST load-frame assembly [1]

bar velocities, the kinetic energy stored in the wedge bar is significantly higher compared to the energy required to deform the specimen and overcome the friction in the system. This is a similar principle to the flywheel devices discussed in Section 2.5.2. This results in a near uniform strain rate up to strains of 20% [1] as shown in Figure 2.38.

A small stiff custom-built load-frame with a natural frequency of 33 kHz is used. As a result, specimen equilibrium is rapidly reached. However, due to space constraints, it was only possible to place strain gauges on the outside of the load-frame. Therefore, it is not possible to correct for any bending in the load-frame arms [1]. As the mass of the loading platform is only 9.92 g, the inertial forces acting on the specimen are assumed insignificant [1].

Raw data shown from a typical experiment is shown in Figure 2.36. The two vertical lines seen at the start of the experiment are light trap readings used to calculate the initial velocity of the wedge bar. The vertical line at 20 ms is the trip gauge used to determine the end of the experiment. A large amount of high frequency noise is present in the raw signals. The raw data is smoothed using a smoothing span of 300 µs, which removes most of the high frequency noise. However, some low frequency noise is still visible on the smoothed signal [1], as shown in Figure 2.38.

The wedge bar displacement time history is calculated assuming a constant friction coefficient. As the initial velocity of the wedge bar, testing duration and the total wedge bar displacement are known, the equations of motion of the wedge bar could be integrated to calculate the average friction coefficient for the experiment [1]. Once the friction coefficient is known the displacement history is calculated. The specimen displacement is then inferred from the wedge bar displacement using the slope of the wedge bar [1]. This approach is verified with the use of a high speed camera. The results are presented in Figure 2.37. The high speed camera footage also shows the sliding anvil moves smoothly and remained in contact with the wedge bar over the duration of the experiment.

The test results for commercially pure aluminium are presented in Figure 2.38. The QS and ISR results match closely between 3% and 9% strain. However, significant oscillations are visible over the initial portion of the experiment and after a strain of 0.007 the flow stress drops below the QS results. As the QS data is obtained from tensile tests, it is expected that the flow stress will lie

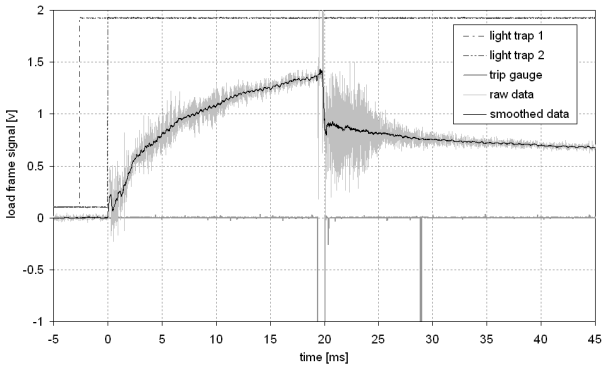

Figure 2.36: Wedge bar IST raw data for commercially pure aluminium [1]

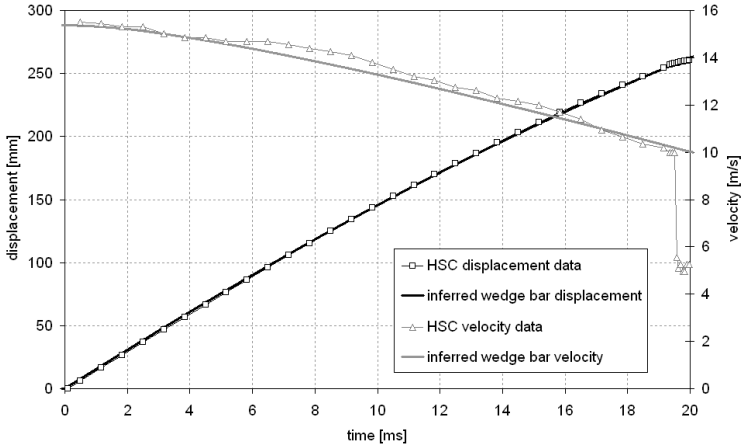

Figure 2.37: Wedge bar IST high speed camera data [1]

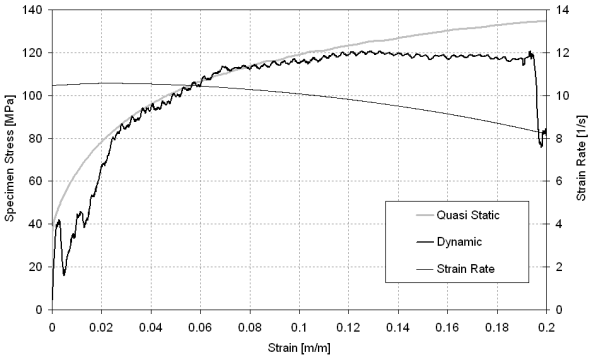

Figure 2.38: Wedge bar IST results for commercially pure aluminium [1]

below the ISR data, specifically over the later portion of the experiment where the friction effects are expected to become more pronounced. It is expected that the drop in flow stress over the latter part of the experiment is due to the non-linear response of the load-frame that is not properly captured during calibration. The strain rate varies by approximately 30% over the experiment which is an improvement over previously discussed techniques.

2.6.3 Evaluation of Custom-Built Machines

The short, stiff custom-built load-cells and lightweight moving components of the Hydro-Pneumatic machine resulted in good force equilibrium in the specimen and a smooth force history over the plastic portion of the experiment. However, there are still oscillations in the force signal, particularly in the elastic region. The strain rate history is an improvement compared to other ISR testers for which strain rate histories are available. However, the strain rate ramps up over the duration of the experiment as there is no mechanism to allow testing speed to be reached before deformation of the specimen begins.

In comparison, the wedge bar IST developed by Cloete and Oxtoby [1] uses impact principles to start and stop the experiment. Testing speed is reached within 1% of the testing duration. The wedge bar angle allows enough kinetic energy to be stored in the striker to ensure the strain rate is maintained over the duration of the experiment with a variation in strain rate of around 20%. The custom-built high frequency load-frame contains lots of high frequency noise and does not follow the specimen response as expected during yield, or over the later part of the experiment. However, this concept shows promise if the issues around force measurement can be solved. In addition, the wedge bar IST concept has the added advantage that it can be used for interrupted tests and possibly also for viscous unloading experiments on visco-elastic materials due to the ability to rapidly start and stop the experiment.

2.7 Specimen Friction Effects

During compression tests the friction between the specimen and loading surfaces can restrict the radial expansion of the specimen. This increases the compression force required to deform the specimen. On stress strain curves this is visible as artificial hardening of the specimen.

Hartley et al. [42] investigated the friction effects present during QS and SHPB experiments for copper, mild steel and aluminium specimen. Compression tests are performed on ring specimen. The change in the internal and external diameters of the specimen is used to calculate the friction factor for the material. QS and dynamic friction factors are presented for copper, mild steel and aluminium. The surface finish of the specimen and loading anvils are varied to investigate the effect this has on the friction factor. The results are presented in Table 2.1 and Table 2.2.

Note that for the dynamic tests the friction factors for copper are largest in all cases investigated. The friction factors for the dynamic tests are lower compared to the friction factors for the QS tests. This is expected as the longer testing durations of the QS tests allow more time for the lubrication to be squeezed out between the anvils and specimen resulting in higher friction effects. It is expected that the friction factors for the ISR tests will lie between the QS and SHPB results but closer to the QS results. However, this will need to be verified experimentally.

Based on these friction factors it is possible to estimate the error in the measured flow stress as follows

$$\frac{P_{ave}}{\sigma_y} = 1 + \frac{2}{3}\frac{m}{\sqrt{3}}\left(\frac{d}{h}\right) \text{ [42]} \tag{2.1}$$

Where P_{ave} is the average surface pressure on the deforming specimen, σ_y is the nominal flow stress of the material, m is the constant friction factor found in Table 2.1 and 2.2 and l and d are the length and diameter of the specimen respectively. The theoretical error due to friction, for friction factors ranging between 0.05 and 0.4, is shown in Figure 2.39.

Table 2.1: Friction factors (m) for QS tests presented by Hartley et al. [42]

		600-grit anvil			1200-grit anvil			0.25 µm diamond polished anvil		
	Specimen finish	600	1200	1 µm	600	1200	1 µm	600	1200	1 µm
Dry	Mild Steel	—	—	0.28	—	0.18	0.36	0.14	—	0.18
	Copper	—	0.20	—	0.20	0.18	—	—	0.14	—
	Aluminium	0.14	—	0.38	—	0.15	0.38	—	—	0.24
Greased	Mild Steel	0.14	0.07	—	0.16	0.16	0.22	0.10	0.10	0.12
	Copper	0.18	0.15	0.22	0.08	—	—	0.12	—	0.18
	Aluminium	0.24	0.14	0.18	0.20	0.18	0.08	—	—	—

Table 2.2: Friction factors (m) for SHPB tests presented by Hartley et al. [42]

	Series I—light greasing single strain increments	Series II—light greasing eight strain increment	Series III—dry four strain increments
Steel	0.08	0.10	0.20
Copper	0.13	0.14	0.28
Aluminium	0.08	0.12	0.26

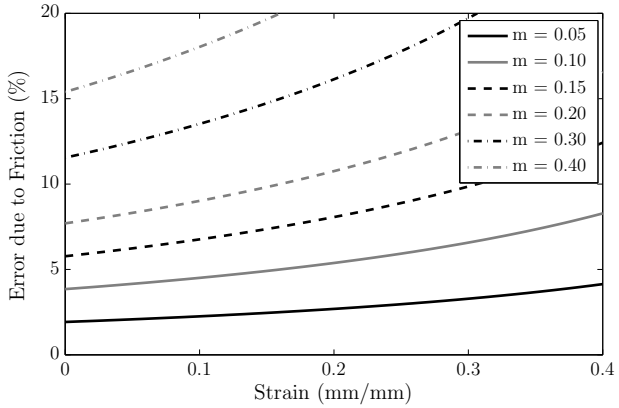

Figure 2.39: Error due to friction

2.8 Conclusions From Literature

Two key aspects of an intermediate strain rate testing machine are the quality of the force measurements and the uniformity of the strain rate history. Several concepts evaluated managed to achieve either a smooth force history or claimed a uniform strain rate. However, achieving both of these design goals is uncommon.

The force measurement achieved using the piezo-electric load-cells do not perform well in any of the cases where they are used [8, 9, 32, 38]. The impact at the start of the experiment excites resonance in the load-cell resulting in undesirable oscillations on the signals, obscuring the specimen response. Smooth force histories and good specimen equilibrium are achieved by authors who used custom-built short stiff load-cells [8, 31, 41] as well as the HPB [10, 33, 35, 36]. Using sacrificial strain gauges mounted on the specimen also gave improved force readings [32]. However, this approach is tedious and expensive for regular testing. Of the options reviewed for force measurement, the short stiff load-cells are the preferred option as they give smooth force measurement while still allowing for a compact design and do not place an upper limit on the testing duration.

The loading method used has a large effect on the variation of the strain rate over the experiment. The strain rate histories tended to ramp up slowly over the duration of the experiment for testing techniques using hydraulic rams and ESH testing machines for loading [9, 10, 15, 33, 35]. These methods do not store enough kinetic energy to ensure constant strain rates and respond too slowly to allow the use of a feedback control system to control the strain rate.

The loading method used which store significantly more energy than required to deform the specimen resulted in the smallest change in loading rates. Variations in loading rates as low as 5% are reported for flywheel devices, however, no strain rate history is reported for the specimen [36, 38]. Of the authors who reported strain rate histories, the wedge bar IST presented by Cloete and Oxtoby [1] had the least variation over the experiment.

Minimising the time to accelerate up to test speed and to stop the experiment ensures the majority of the experiment is performed at testing speed. Minimising the mass of the moving components in the load path will help enable the testing machine to accelerate up to testing speed quickly as well as to reduce the inertial forces present [1, 10]. A number of authors characterised the dynamic response of the testing machines and used this during post-processing to remove the inertial component of the measured force [9, 33, 34]. This improved the quality of the force measurements, but the results are still inferior to the testing methods that eliminated inertial forces by design.

The wedge bar IST presented by Cloete and Oxtoby [1] uses impact principles to start and stop the experiment in less than 1% of the testing duration. This enables the IST to capture yield stress at testing speed as well as testing brittle materials that fracture at small strains. Of the loading methods reviewed, the use of impact principles to start and stop the experiment is the preferred option as it allows yield stress to be captured at testing speed, the recovery of specimens and the testing of brittle materials that fracture at small strains.

The strain rate history is affected by the loading method used and the compliance of the testing machine. Even with constant loading rates the strain rate will vary if the compliance of the testing machine is low as the load-frame deflects with increasing specimen force. A high load path compliance is desired. The natural frequency of the load path must be as high as possible as this ensures the testing machine's response does not mask the specimens response with unwanted oscillations during testing.

Although the use of sacrificial elements or dampers can help reduce the impact at the start of the experiment, they also significantly reduce the compliance of the load path as they are being compressed. A number of the authors who use sacrificial elements or dampers require additional instrumentation to measure specimen displacement [8, 14, 33] as the machine mounted displacement sensors could not account for the compression of the sacrificial element or damper. If avoidable, sacrificial elements and dampers should not be used in the load path.

Chapter 3

Design

This chapter starts by describing the chosen concept followed by the design calculations for the wedge bar, load-frame and strain gauge load-cell. This is followed by the results of the Finite Element Analysis (FEA) which is used to fine tune the design. Last, the wedge bar displacement sensor design is presented.

3.1 Chosen Concept

The chosen concept for the Intermediate Strain rate Tester (IST) is based on the wedge bar IST presented by Cloete and Oxtoby [1]. The results presented by Cloete and Oxtoby demonstrate the concept has a lot of potential. However, there are a number of aspects of the design that can be improved upon. The new IST has been redesigned with the only common component being the back plate. The new configuration is shown in Figure 3.1. Modifications have been made to load-frame, wedge bar, loading methods and instrumentation used. The goals of these modifications are:

- To reduce the level of noise on the measured force signal
- To investigate the effect of using different loading methods
- To add displacement measurement to the wedge bar

To fulfil these goals it was decided to further investigate the high frequency load-frame implemented by Cloete and Oxtoby [1] and to develop a new Monolithic Load-Frame (MLF) to be used in conjunction with a custom-built high frequency strain gauge load-cell. A close-up of each load-frame is shown in Figure 3.1. In addition to the new load-frame, the following three loading methods are also investigated:

- Impact driven with specimen pre-load
- Impact driven without specimen pre-load
- Back pressure driven without specimen pre-load

The loading methods investigated are illustrated in Figure 3.2(a), Figure 3.2(b) and Figure 3.2(c). The impact driven tests work as described by Cloete and Oxtoby [1] for the wedge bar IST, covered in Section 2.6.2. Unless stated otherwise, the impact driven experiments are done using specimen pre-load. The specimen is pre-loaded by sliding the wedge bar, to the right through the load-frame, until all the slack has been taken up and the specimen is firmly in contact with the loading platform and load-cell.

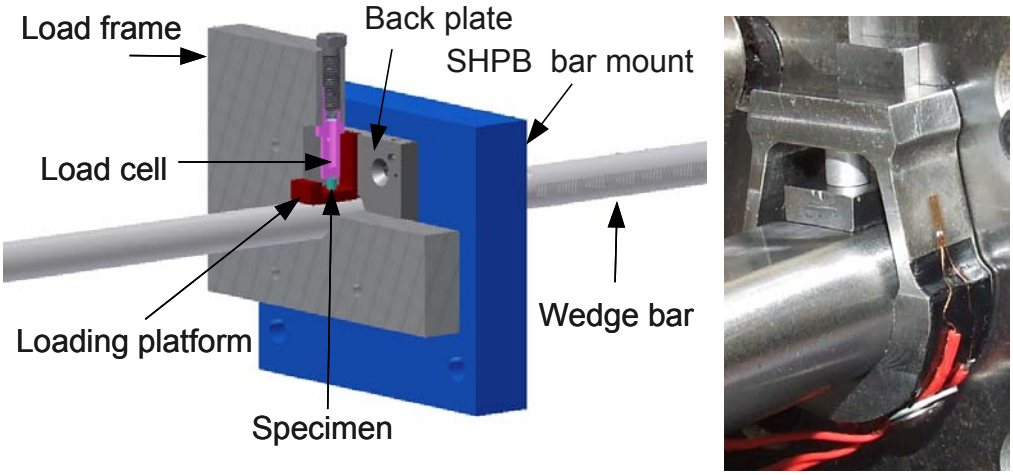

(a) Monolithic load-frame

(b) High frequency load-frame [1]

Figure 3.1: Load-frames

During the back pressure driven experiments a piston is attached to the back of the wedge bar which is then inserted into the gas gun barrel. This allows the pressure from the gas gun to act on the piston over the duration of the experiment. When using back pressure driven loading it is not possible to use specimen pre-load. A small gap is left between the specimen and load-cell to allow the wedge bar to accelerate up to testing speed before deformation of the specimen begins. As with the impact driven experiments, the back pressure driven experiments are stopped using the stopper bar after the pressure acting on the piston is vented. Impact driven experiments without pre-load are done to investigate the affect pre-load has on the performance of the IST and the measured specimen response. This is used to investigate if the back pressure loading will have effects on the specimen properties measured.

3.2 IST Design Calculations

In this section the design calculations used for preliminary sizing for the wedge bar, load-frame and load-cell are presented. Detailed modelling of the IST components is then done (using the FEA package ABAQUS v6.81) to investigate the stress wave propagation effects and to make revisions to the basic design as required. These results are presented in Section 3.3.

Several assumptions are made to simplify the basic design calculations. A material with a yield stress of 200 MPa with no strain hardening is used for the specimen and the maximum required strain is set to 20%. Constant friction is assumed for the contact between the wedge bar, loading platform and load-frame. The effects of stress wave propagation are also ignored. A 5 mm long, 5 mm diameter specimen is chosen as this allows the same specimen to be used for IST, SHPB and QS compression tests. The critical dimensions of the wedge bar, load-cell and load-frame are then calculated as described below.

3.2.1 Wedge Bar

The dimensions of the wedge bars are specified first as they affect all the other components. The key variables are the wedge bar length (L_{wb}), diameter (ϕ_{wb}), wedge length (L_w) and wedge angle (θ_{wb}), as shown in Figure 3.4. Several combinations of wedge bar length, diameter, wedge length and

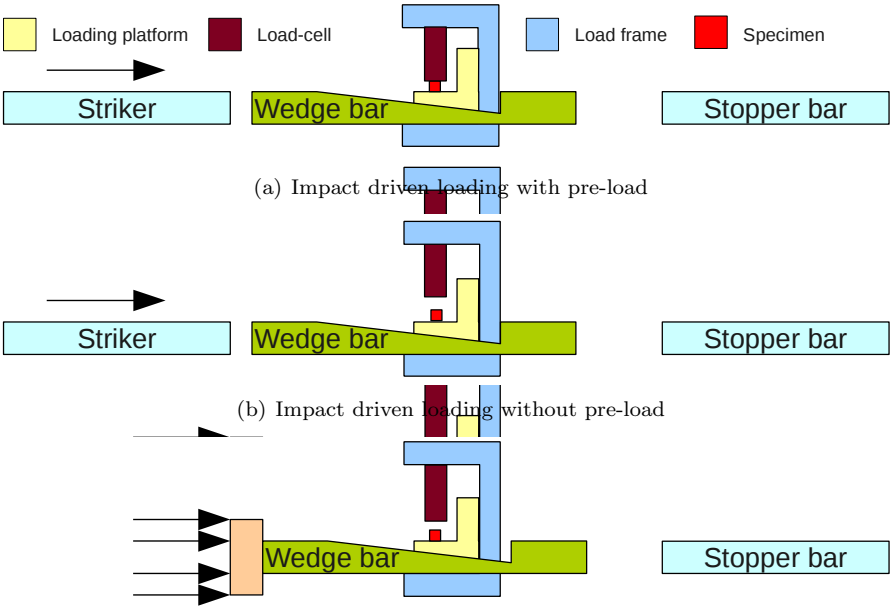

(a) Impact driven loading with pre-load

(b) Impact driven loading without pre-load

(c) Back pressure driven loading without pre-load

Figure 3.2: Loading methods investigated

Figure 3.3: ROS displacement sensor

wedge angle are investigated. For each wedge bar the theoretical strain rate history is calculated, as described in Appendix D. The calculations shown in Appendix D show that heavier strikers travelling at high velocities will produce more uniform wedge bar velocities and hence strain rates. For practical reasons the length of the bars is limited to 1.5 m and the diameter to 20 mm. The upper limit on the wedge bar velocity is 10 m/s to prevent yielding of the bars.

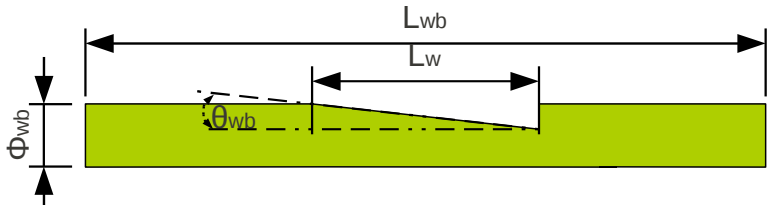

Figure 3.4: Wedge bar schematic

Two wedge bars were manufactured to extend the testing range of the IST. The total length and

diameter of the wedge bars are 1.5 m and 20 mm respectively. The wedge bar angles of 1/500 and 2/500 are chosen to cover the strain rate range between 4 and 10 s^{-1}. The length of the wedge on each bar is 500 mm. The striker bars, stopper bars and wedge bars are all manufactured out of centerless ground silver steel. The machining drawings are shown in Appendix G. The theoretical strain rate histories achievable for the selected wedge bar geometries are shown in Figure 3.5.

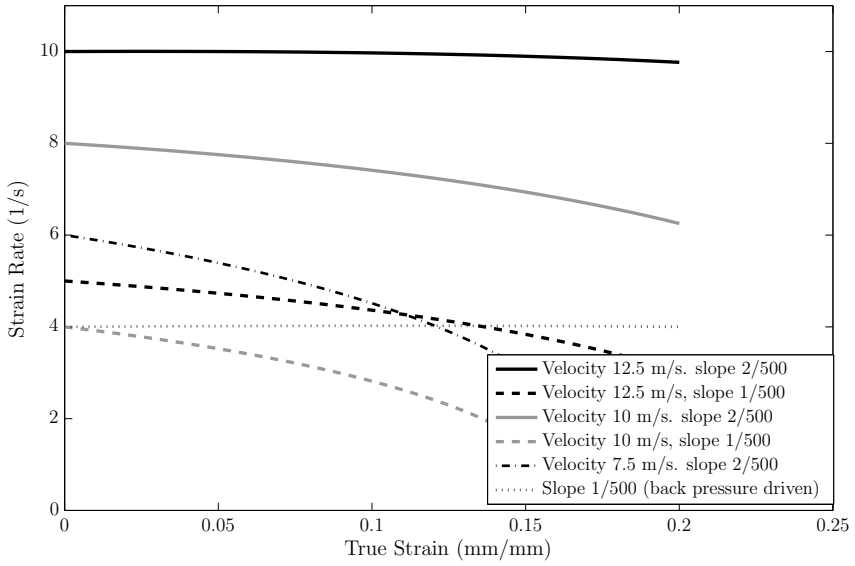

Figure 3.5: Theoretical strain rate histories achievable for the selected wedge bar geometry

The 2/500 wedge bar gives a near constant strain rate at 10 s^{-1}. This falls midway between the 0.1 to 10^3 s^{-1} range. For lower strain rates the strain rate history begins to drop off over the experiment, due the decreasing amounts of energy stored in the wedge bar at the lower velocities. The use of the 1/500 striker allows near constant strain rates down to 7 s^{-1}. For strain rates below 6 s^{-1} it becomes necessary to use the back pressure configuration as it is not possible to store enough energy in the wedge bar to ensure a uniform strain rate.

The 2/500 wedge bar allows the wedge bar to travel up to 250 mm before the start of the test and still achieve up to 20% strain in the specimen. This allows the wedge bar adequate time to reach testing speed before the beginning of the experiment when using the back pressure driven configuration.

3.2.2 Load-Frame

The IST developed by Cloete and Oxtoby [1] uses the lightweight and stiff high frequency load-frame shown in Figure 3.1. The design philosophy behind the high frequency load-frame is that it will rapidly reach equilibrium during testing due to its high natural frequency. However, as discussed in Section 2.6.2, the measured signal contained lots of high frequency noise and appears to give a non-linear response.

For these reasons it was decided to develop the Monolithic Load-Frame (MLF) used together with the high frequency load-cell. This combination allows for a compact design resulting in a short, stiff load path free from any hydraulic or pneumatic components. The design philosophy behind the MLF is to develop a load-frame that will dissipate the stress wave reflections away from the load-cell. To aid this, the load-frame is manufactured from grey cast iron due to its inherent damping properties as a result of the graphite flakes present in the material. The graphite flakes also give the cast iron a self-lubricating property, reducing the friction between the load-frame and wedge bar. It is anticipated

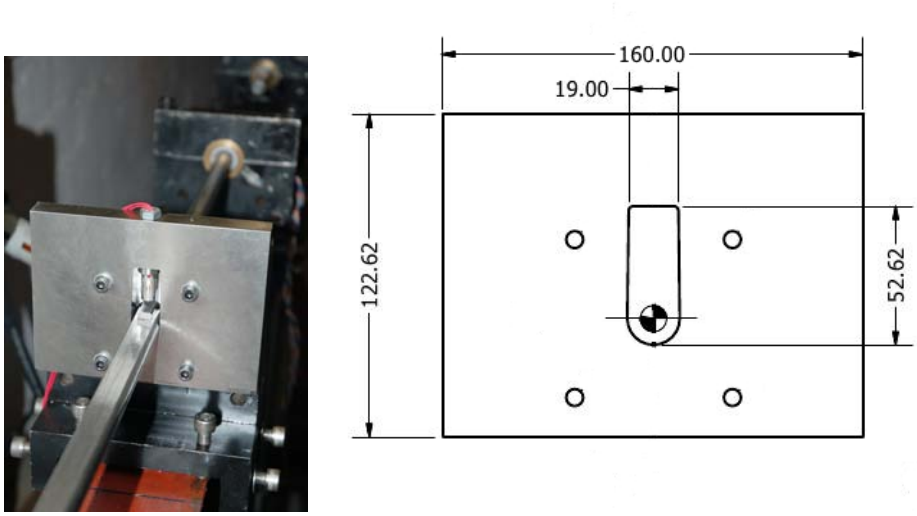

(a) MLF assembly (b) MLF dimensions

Figure 3.6: Monolithic Load-Frame

that the MLF and high frequency load-cell used in combination will give a measured signal free from both high and low frequency oscillations. The dimensions of the MLF are shown in Figure 3.6 and the machining drawings are shown in Appendix G. The design calculations are presented in detail in Appendix D. The dynamic response of the IST is investigated using the FEA package ABAQUS, the results are presented in Section 3.3.

3.2.3 Load-Cell

The load-cell is designed with a 10 kN force limit. This equates to an engineering stress of 500 MPa in the specimen. The load-cell dimensions are shown in Figure 3.7(c) and the machining drawings are shown in Appendix G. The wall thickness of the load-cell is chosen to ensure the strain in the load-cell is large enough to use foil strain gauges for force measurement. Strain gauge theory is used to calculate the output voltage of the load-cell over the design range. The maximum output voltage of the strain gauge amps is also calculated to ensure the measured signal fell within operating limits of the data capture card. The detailed calculations are given in Appendix D.

The noise on signals recorded with the data acquisition system used for the IST is in the order of $\pm$ 0.01 V. This is used to calculate the theoretical signal to noise ratio for the load-cell at an engineering stress in the specimen ranging from 25 to 500 MPa. The calculations are described in more detail in Appendix D. The results of the signal to noise ratio investigation are shown in Table 3.1. At a specimen stress of 25 MPa, the signal to noise ratio is approximately 8:1 and increases to 75:1 at a specimen stress of 500 MPa. The output voltage while measuring 500 MPa stress in the specimen will be approximately 3.5 V, which is within the operating limit of the data acquisition system.

3.3 FEA Investigation into Dynamic Response of IST

Due to the complex geometry of the IST, Finite Element Analysis (FEA) is used to investigate the dynamic response of the system. The results of this analysis are used to make modifications to the initial design. The goals of the FEA are to minimise noise on the measured signals and to ensure the

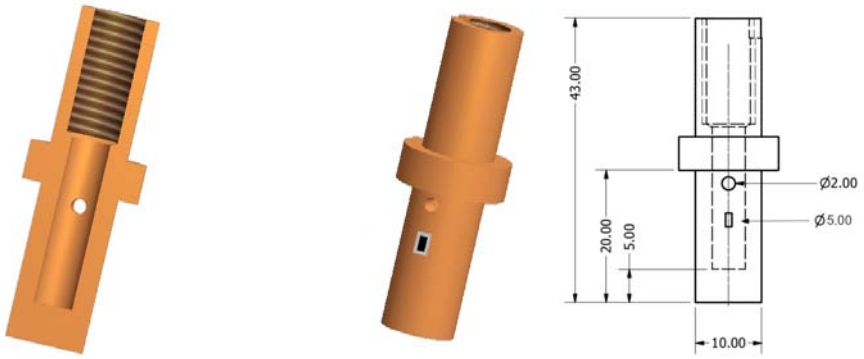

(a) Sectioned view (b) Gauge position shown in black (c) Dimensions

Figure 3.7: Load-cell

Table 3.1: Measured voltage and signal to noise ratio

Specimen Stress (MPa)	Theoretical Measured Voltage (V)	Signal to Noise Ratio
25	0.2	8.8
50	0.4	17.5
75	0.5	26.3
500	3.5	175.0

recorded stress strain curve from the virtual experiment match the material model of the specimen as closely as possible. A parametric study is also performed on several components to investigate the effect each has on the dynamic response of the system. The primary components investigated are the load-frame, loading platform and loading technique used. The components modelled using FEA are shown in Figure 3.8(a) and Figure 3.8(b). The geometry calculated from the initial calculations is used as a starting point for the FEA simulations.

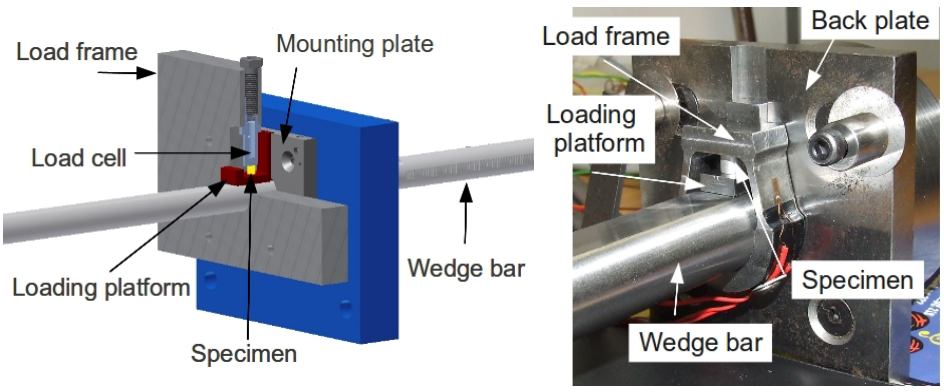

(a) Monolithic load-frame FEA components (b) High frequency load-frame FEA components [1]

Figure 3.8: Monolithic and high frequency load-frame components

The material model for the specimen used in the FEM simulations is Elastic Perfectly Plastic (EPP) with a yield stress of 200 MPa and an elastic modulus of 200 GPa. This material model is chosen as it gives a harsh transition between the elastic and plastic portion of the test. This will tend to excite any undesirable response from the IST load path that will otherwise not be clearly visible if a smooth

transition between elastic and plastic deformation is used. The EPP material model also simplifies comparisons between the virtual experiment results and the material model used for the specimen. Any strain hardening or softening can immediately be identified as an artefact of the IST's dynamic response.

The IST is modelled in half symmetry to reduce simulation time required. A 1 mm part seeding is used on the specimen and load-cell and a 2 mm part seeding is used on the load-frame and wedge bars. A mesh refinement study conducted using a 0.5 mm part seeding for the load-cell and 1 mm part seeding for the load-frame show no significant variations in the results, hence the results are considered to have converged.

As the IST is modelled in half symmetry all components have an x symmetry boundary condition applied to them. In addition to this a zero displacement and rotation (Encastre) boundary condition is set on the outer diameter of the bushes that the wedge bar runs through as well as the clamp on the mounting plate that the load-frame bolts to. Surface to surface contact is used for modelling the contact between components that interact. Contact pairs were defined for all the surfaces that interact. This includes the wedge bar and bushes, wedge bar and load-frame, wedge bar and loading platform, loading platform and load-frame, loading platform and specimen, specimen and load-cell and in the HFLF simulations between between the HFLF and backing plate. Contact between the wedge bar and bushes is set to be frictionless while a friction factor of 0.1 is assumed between all other sliding surfaces. The initial condition of all components is stationary except for the striker which is set to 10 m/s.

The wedge bar displacement and strain readings taken from the load-cell are recorded for each virtual experiment. This data is then processed as described in Section 4.5 to generate the stress strain curves.

3.3.1 High Frequency Load-Frame

The High Frequency Load-Frame (HFLF) used by Cloete and Oxtoby [1] is modelled first as this allows the FEA to be verified against experimental results previously presented. A comparison between the experimental and FEA virtual experiment results are shown in Figure 3.9(a) and Figure 3.9(b). The experimental results presented by Cloete and Oxtoby have been smoothed significantly. The raw data is shown in Figure 2.36. The FEA results show slightly more high frequency noise which is expected as no dampening is included in the FEA model. The experimental results clearly show the unloading and reloading of the specimen at the start of the experiment, noticeable to a lesser degree in the FEA results. The FEA results also show a partial unloading of the specimen half way through the elastic portion of the virtual experiment while the yield stress is recorded lower than expected[1]. Both the experimental and FEA results show a region, between A and B, where the IST results closely match the material behaviour. The region before A can be considered the time it takes the load-frame to "ring up". After point B, the experimental results fall below the QS test results and the FEA virtual experiment results fall marginally below the specimen material model.

3.3.2 Monolithic Load-Frame

The agreement in the trends seen in the experimental work and FEA of the HFLF provides confidence in the modelling technique used. Work on the MLF was then started. For the initial simulation the MLF is attached to the backing plate using two bolts. The bolts are modelled as a surfaces, equal to the area of a bolt, on the load-frame and backing plate tied together. The results show that the MLF moves relative to the backing plate during the experiment. This presents as two unloading cycles visible in the elastic portion of the experiment. The virtual experiment results are shown

[1]The material model used for the specimen has a yield stress of 200 MPa

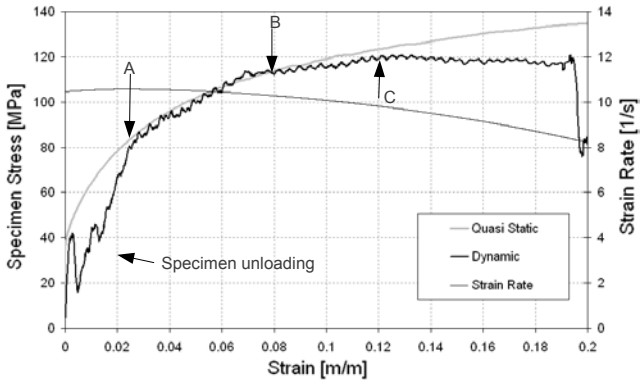

(a) HFLF experimental results [1]

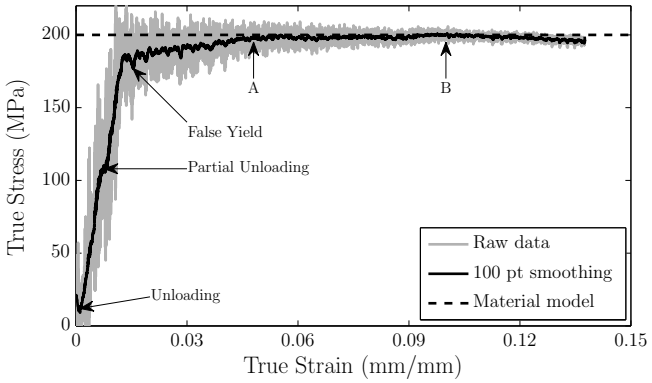

(b) HFLF FEA results

Figure 3.9: Experimental and FEA results for HFLF

in Figure 3.10(a). Also note the false yield stress captured and the large amount of low frequency oscillations visible in the smoothed data.

The next simulation used four bolts to attach the MLF to the backing plate. A comparison of the results is shown in Figure 3.10(a) and Figure 3.10(b). The use of four bolts reduces the movement of MLF which has the following effects. First, one of the unloading cycles in the elastic region is removed and the magnitude of the other is reduced. Second, the error between the false yield and the material model used for the specimen is reduced. Last, the low frequency noise levels are significantly reduced on the raw signals. From point A to B in Figure 3.10(b) the results closely match the material model and from point B to C the IST results lie directly on top of the material model. This highlights the importance of securely mounting the load-frame.

3.3.3 HFLF vs. MLF

The noise levels in the FEA are similar for the MLF and HFLF, as shown in Figure 3.9(b) and Figure 3.10(b). However, the FEA does not include the dampening effects of the cast iron load-frame. The MLF follows the material model better than the HFLF, although the results still deviate slightly from the material model over the initial portion of the experiment. After approximately 3% strain the MLF follows the material model closely.

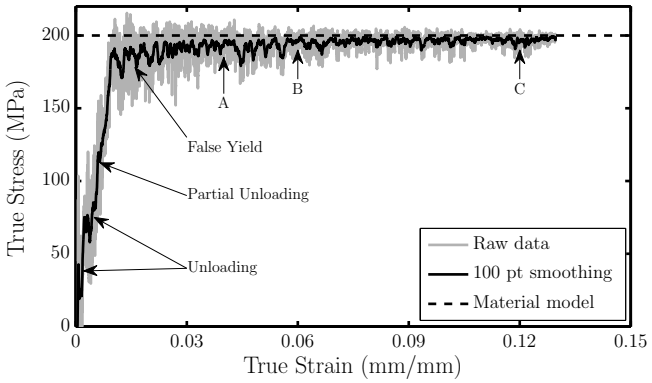

(a) MLF FEA results (2 bolts)

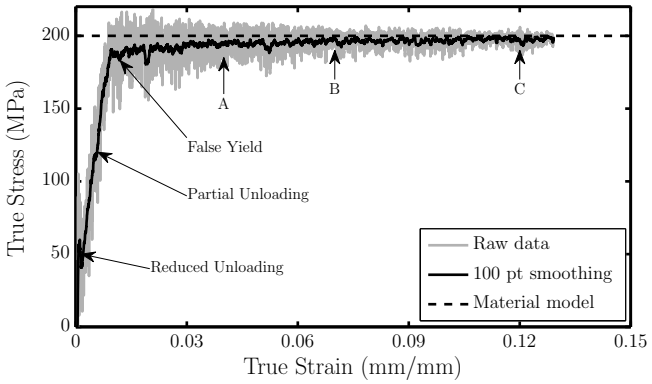

(b) MLF FEA results (4 bolts)

Figure 3.10: FEA results comparing the 2 bolt and 4 bolt attachment method for the MLF

3.3.4 Impact vs. Back Pressure Driven Loading

The back pressure driven loading is investigated as an alternative loading method to extend the lower limit of the IST. During the back pressure driven loading the pressure from the gas gun acts over a piston attached to the wedge bar over the duration of the experiment. The extra driving force helps to overcome the friction effects and therefore lowers the minimum achievable strain rate. The results are shown in Figure 3.11(b). The back pressure loading has the following additional advantages. First, the back pressure driven eliminated the partial unloading during the elastic portion of the experiment as shown by comparing Figure 3.11(a) and Figure 3.11(b). Second, the noise on the signal is significantly reduced for the back pressure driven loading. The experimental results for the back pressure driven loading are shown in Section A.3.7.

3.3.5 Load Path Compliance

During testing the wedge bar displacement is measured. The specimen displacement is then inferred using the wedge bar angle. To give accurate results using this method the deflection of the load path of the IST must be taken into account. The FEA virtual experiment results were initially processed without accounting for the displacement of the load path. The elastic modulus measured from the

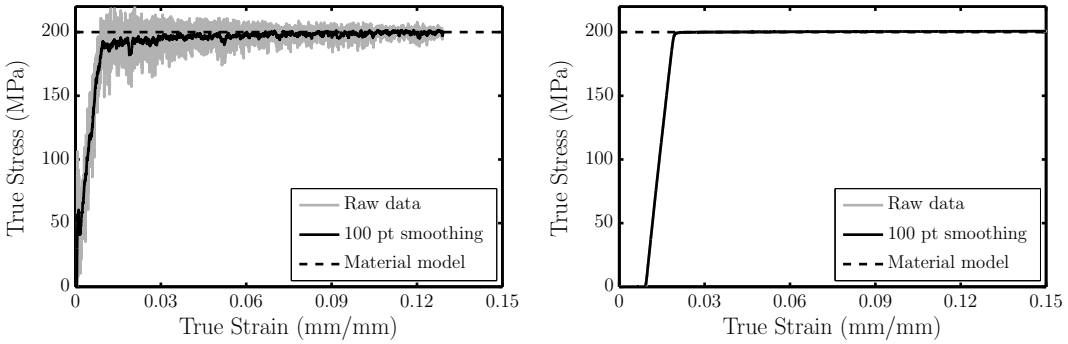

(a) Impact loading, rate = 5 s^{-1}

(b) Back pressure loading, rate = 6 s^{-1}

Figure 3.11: Comparison between impact loading and back pressure driven experiments

virtual experiments fell between 25.83 to 25.88 GPa. This value is nearly 8 times lower than the 200 GPa modulus used in the material model of the specimen due to the compliance of the IST.

The specimen and IST load path can be considered as two springs acting in series, as shown in Figure 3.12. During the experiment both the specimen and load-frame deflect. The Elastic modulus measured off the stress strain curves is a function of the specimen modulus and the compliance of the load-frame. As the specimen modulus is specified in the FEA model, the equivalent modulus can be measured off the stress strain curve generated from the virtual experiment results. The compliance of the IST is then calculated as follows.

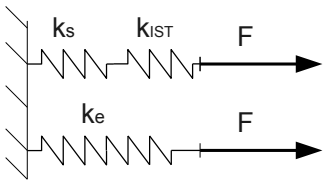

Figure 3.12: Springs in series

The equivalent stiffness of springs in series is given by the expression

$$\frac{1}{k_e} = \frac{1}{k_1} + \frac{1}{k_2} \cdots + \frac{1}{k_n} \tag{3.1}$$

where k, is the spring stiffness and subscript e refers to the equivalent properties. When considering only the load path and specimen acting in series this simplifies to

$$\frac{1}{k_e} = \frac{1}{k_s} + \frac{1}{k_{IST}} \tag{3.2}$$

where subscripts s and IST refer to the specimen and IST properties.

The stiffness of uniform shaped objects are calculated as follows

$$k = \frac{AE}{L} \tag{3.3}$$

where A, E and L are area, elastic modulus and length. The equivalent stiffness of the IST and specimen in series is calculated from the modulus measured off the stress strain curve as follows

$$k_e = \frac{A_s E_m}{L_s} \tag{3.4}$$

where the subscript m denotes a measured property. The stiffness of the specimen is calculated as follows

$$k_s = \frac{A_s E_s}{L_s} \tag{3.5}$$

The equivalent stiffness of the load path is calculated by substituting Equation 3.5 and 3.4 into Equation 3.2 and rearranging, giving

$$k_{IST} = \left(\frac{l_s}{A_s E_m} - \frac{l_s}{A_s E_s} \right)^{-1} \tag{3.6}$$

Substituting $A_s = 19.63 \times 10^{-6} m^2$, $E_m = 25.8$ GPa, $L_s = 0.005\ m$ and $E_s = 200$ GPa gives $k_{IST} = 116$ MN/m = 116 kN/mm. This agrees very well with the experimentally determined stiffness of the load path which is presented in Section 6.3. However, this is nearly half the analytical value calculated in Appendix D.3. This will be discussed more in Section 6.3.

Once the stiffness of the IST load-frame is known, it is possible to approximate the error involved in the displacement measurements if the load path compliance is rigid. Two material models are used for this analysis. The material model used is a bilinear material with a 70 GPa elastic modulus, 200 Mpa yield stress and the flow stress increases linearly to 400 MPa at 20 % strain. The results are presented in Table 3.2.

Table 3.2: Specimen displacement vs. inferred displacement (model 2)

Strain (%)	Measured displacement (mm)	Actual specimen displacement (mm)	Actual/Measured (%)	Actual/Measured plastic displacement (%)
Yield	0.04	0.005	13%	
5%	0.29	0.25	86%	97%
10%	0.55	0.5	91%	97%
15%	0.81	0.75	93%	97%
20%	1.07	1	94%	97%

The results shown in Table 3.2 show that ignoring the IST compliance results in a small error in the plastic strain measurements. However, including the compliance of the IST will significantly increase the accuracy of the strain measurements over the initial portion of the experiment, for this reason it will be included.

3.3.6 Balanced vs. Unbalanced Loading Platforms

All virtual experiment results presented previously use the 1/500 wedge bar and the loading platform shown in Figure 3.13(a) with L1 = 20 mm, W = 15 mm and mass = 23.5 g. Once these simulations were complete, simulations were run using the 2/500 wedge bar. When the 2/500 wedge bar is used with continuous back pressure loading, partial unloading of the specimen is clearly visible just after the yield point, as shown in Figure 3.14(b).

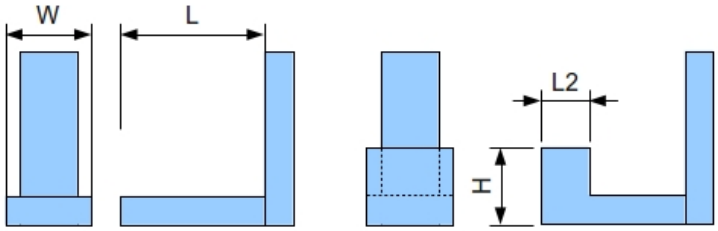

(a) Original loading platform (b) Balanced loading platform

Figure 3.13: Different loading platforms investigated

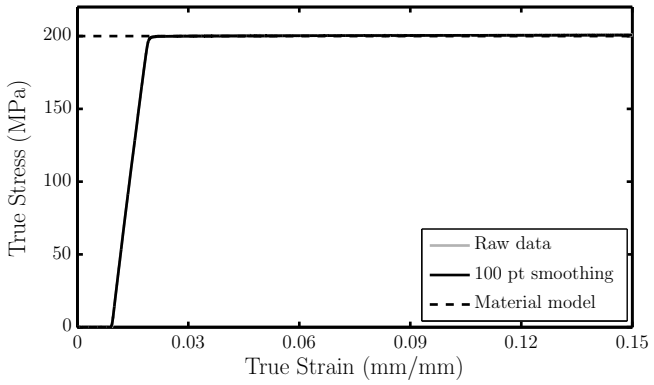

(a) 1/500 wedge bar

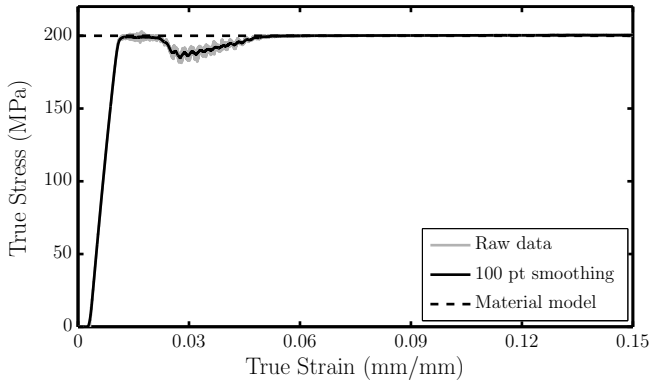

(b) 2/500 wedge bar

Figure 3.14: Effects of changing the wedge bar angle, back pressure loading

It was initially thought that this unloading could be avoided if the loading platform had enough inertia to resist rebounding. The width of the loading platform (W) was increased to 18 mm and the length (L) increased to 41 mm and then 64 mm. This increased the mass of the loading platform from 23.6 g to 40.5 g and 56.5 g respectively. The results are shown in Figure 3.15(a) and Figure 3.15(b). The increased mass reduces the magnitude of the unloading cycle but significantly increases the duration.

The increased length of the loading platform resulted in the Center of Gravity (CG) moving further

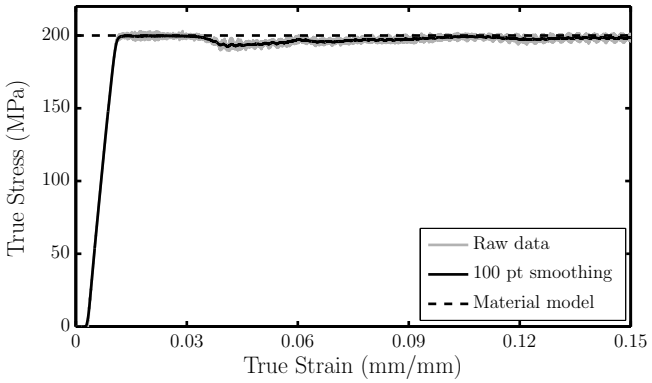

(a) CG 5.4 mm in front of the specimen (m=40.48 g)

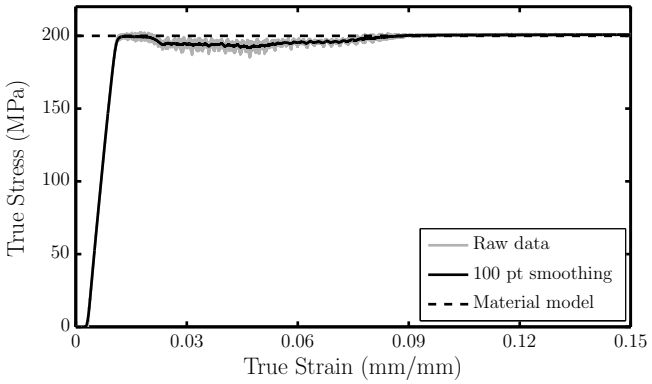

(b) CG 16.4 mm in front of the specimen (m=56.6 g)

Figure 3.15: Effect of increasing loading platform mass

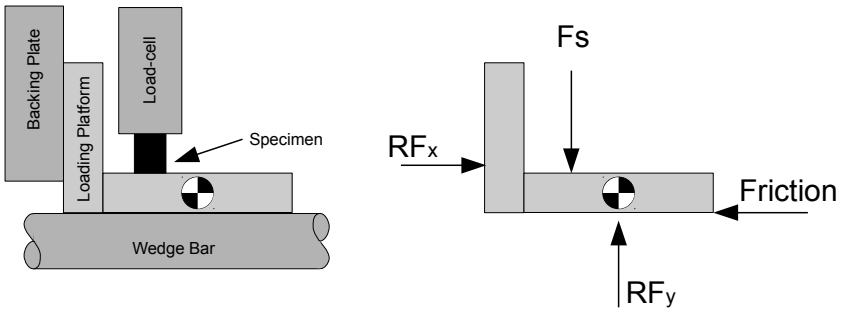

Figure 3.16: Loading platform CG

away from the specimen, see Figure 3.16. It is thought that this might play a role in the increased duration in the unloading cycle seen with the increase in platform mass.

The next simulation is run for the loading platform shown in Figure 3.13(b) with L = 20, L2 = 10 and H = 10. This gives a loading platform mass of 40.5 g, the same as the loading platform used in Figure 3.15(a) but with the CG of the loading platform 1 mm closer to the specimen. This removes the unloading seen after yield as is shown in Figures 3.17(a). The next simulation is run with the

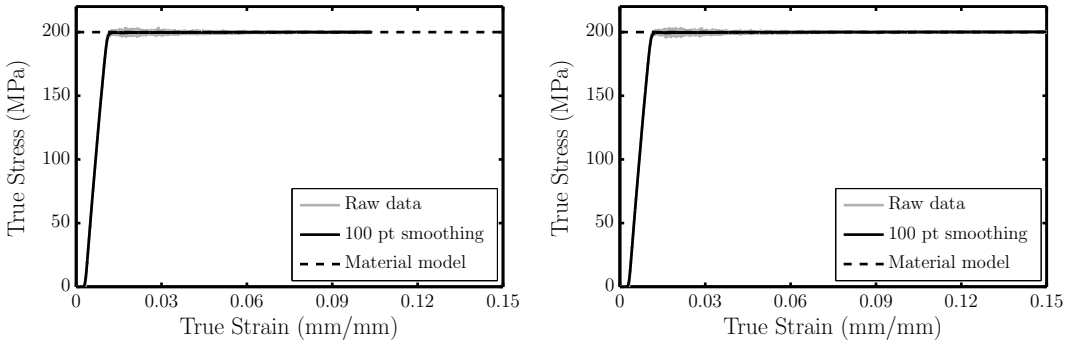

(a) CG 4.4 mm in front of the specimen (m=40.95 g) (b) CG inline with specimen (m=31.1 g)

Figure 3.17: Balanced loading platform results

loading platform geometry that placed the CG directly under the specimen, L = 20, L2 = 6.5 and H = 10. This allows the weight to be reduced to 31 g and still eliminate the unloading after yielding. The results are shown in Figure 3.17(b).

3.3.7 Conclusions of Numerical Work

The numerical work informed the following two design decisions. First, the MLF used in conjunction with the high frequency load-cell produces better results than the HFLF previously implemented. For this reason the experimental work will be focused solely around the MLF. Second, the numerical work also shows that the balanced loading platform reduces the amount of unloading seen during the elastic portion and early part of the plastic portion of the experiment. In order to investigate this experimentally both the balanced and unbalanced loading platforms will be manufactured. Experimental results comparing the balanced and unbalanced loading platforms are shown in Section 5.4 and discussed further in Section 6.7.

3.4 Displacement Sensor Design

There are two options available to calculate the specimen displacement. The specimen displacement can either be measured directly or inferred from the wedge bar displacement. Cloete and Oxtoby [1] inferred the specimen displacement from the wedge bar displacement. The wedge bar displacement was calculated using the constant friction assumption as discussed in Section 2.6.2. However, during back pressure driven experiments the constant friction approach cannot be used to calculate the wedge bar displacement as the exact pressure and hence the driving force acting on the wedge bar is not known. For back pressure driven experiments a new method of measuring specimen displacement is required.

The total displacement measured using direct displacement measurement is in the region of 1 mm, while for indirect displacement measurement the wedge bar moves 250 mm to give 1 mm specimen displacement[2]. Therefore, lower resolution is required when indirect measurement is used. The indirect displacement measurement will not work if the loading platform does not remain in contact with the wedge bar during the experiment. However, the finite element simulations, high speed camera footage and the continuous force signal show that the loading platform remains in contact with the wedge

[2]When using the 2/500 wedge bar

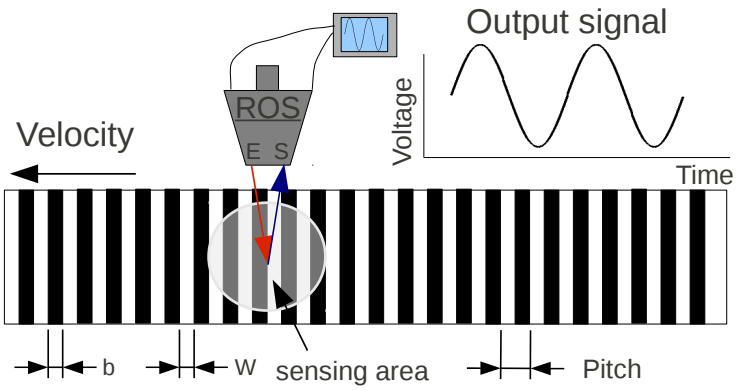

Figure 3.18: ROS displacement sensor schematic

bar for the duration of the experiment, as shown in Sections 3.3 and Appendix B. This provides confidence that the indirect displacement measurement will provide accurate results.

A contact displacement sensor is not desirable for the direct displacement measurement of the loading platform as the rapid acceleration of the loading platform at the start of the experiment could excite resonance in the sensor. Developing a non-contact displacement sensor for direct strain measurement is beyond the scope of this dissertation and off the shelf solutions are prohibitively expensive. For this reason it was decided to proceed with a Reflective Object Sensor (ROS) to measure the wedge bar displacement. A conceptual diagram of the ROS displacement sensor is shown in Figure 3.18.

The advantages of the ROS are the low cost and that the concept lends itself well to measure large displacements. The stroke of the measurement is limited only by the length of the strip of graduated lines. Several applications exist at BISRU that should benefit from the development of this technology and at the time of writing it has already been implemented in two other projects [43, 44].

3.4.1 Sensor Capabilities Investigation

Two reflective object sensors manufactured by Fairchild are investigated, the QRB 1113 and the QRB 1134. Both made use of an infra-red emitting diode and a photo transistor mounted side by side on a converging optical axis [45, 46]. The sensing area approximated a 5 mm diameter circle [45, 46]. The QRB 1134 is a high sensitivity model that also has integrated leads. The main purpose of the investigation is to select a suitable sensor and determine the shortest usable pitch. Selecting the pitch is a trade-off between sensor response and resolution. The full sensor response will be measured for a pitch that is larger than the sensing area of the ROS, as shown in Figure 3.19(a), but the resolution will be coarse . A pitch that is smaller than the sensing area of the sensor, as shown in Figure 3.19(a), will increase the resolution but reduce the amplitude of the response. The noise on the signal may obscure the sensor response when fine pitches are used.

The rise time and fall time of the Fairchild sensors is 8 µs [45, 46]. This places a lower limit on the width of each graduation line as each line must take longer that 8 µs to pass by the sensor. For a velocity of 10 m/s this sets the lower limit at 0.16 mm, which is significantly finer than the required resolution.

Although the response time of the sensor is quick enough to measure graduated lines with a pitch as short as ± 0.16 mm, the sensing area is a 5 mm diameter circle. As a result, such a small pitch may not be measurable. An analysis is done in MATLAB to investigate the affect pitch has on the sensor response. For this analysis it is assumed that the reflective and non-reflective surfaces are

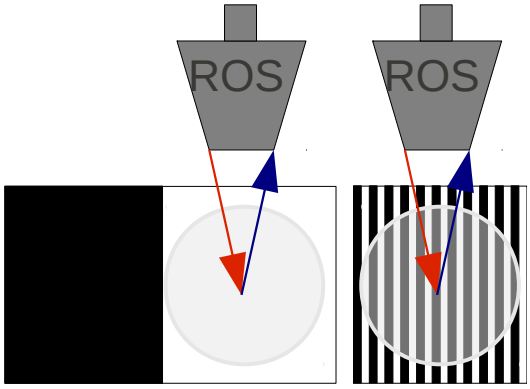

(a) Spacing too coarse (b) Spacing too fine

Figure 3.19: Graduated line pitch scenarios

perfectly reflective and non-reflective respectively. For a given pitch the maximum and the minimum area ratio between the reflective and non-reflective surfaces are calculated. The difference between the maximum and minimum area ratio is the approximated sensor response[3]. As the reflective surfaces are not perfectly reflective and non-reflective, the actual sensor response is expected to be less than predicted. The code used is given in Appendix F.

The results for the sensor response vs. graduated line pitch is shown in Figure 3.20. Note that for certain pitches the sensor response is zero. For these pitches the ratio between the pitch length and sensing area is such that as one reflective line enters the sensing area a reflective line leaves the sensing area and no change in the reflectivity of the surface occurs. Also note that the sensor response is very sensitive to the size of the sensing area. For these reasons it was decided that experiments should be done before deciding on the final pitch to use.

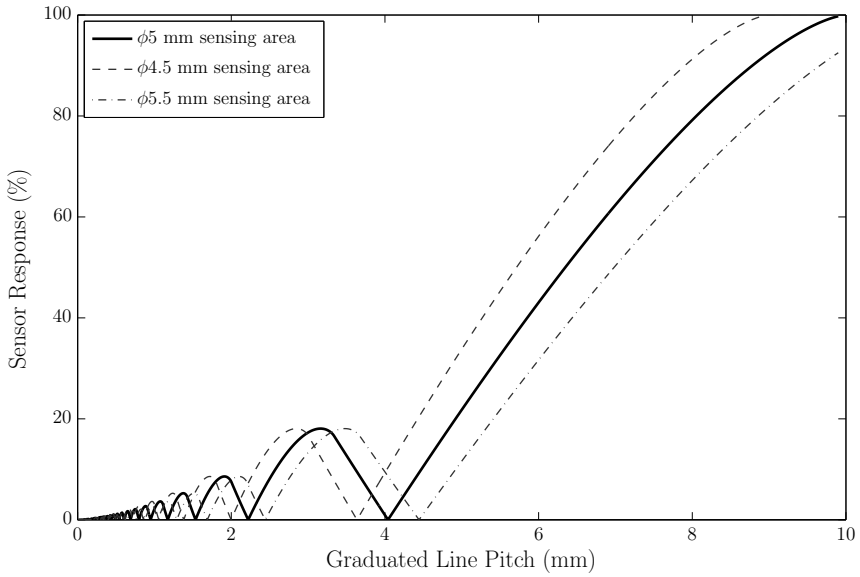

Figure 3.20: Sensor response vs. pitch

[3]For example a pitch that results in a maximum and minimum area ration of 70% and 30% gives a sensor response of 40%

3.4.2 Experimental Set-Up

The initial calculations of the sensor response highlighted two problem areas that needed further investigation. First, the response of the sensor is very dependent on the sensing area of the ROS, especially for short pitches. Second, the noise on the measured signal also needs to be determined as a small variation in the output voltage from the sensor is acceptable if it is noise free, but if the noise is significant the measured signal will be obscured. The goal of the experimental program is not to characterise the sensor fully but to select a graduate line pitch that will provide usable results.

A schematic of the experimental layout is shown in Figure 3.21. The reflective object sensors are mounted side by side and data is recorded from both sensors for each test done. This allows for easy comparison of the two sensors. High density foam is used to stop the projectiles at the end of the experiment.

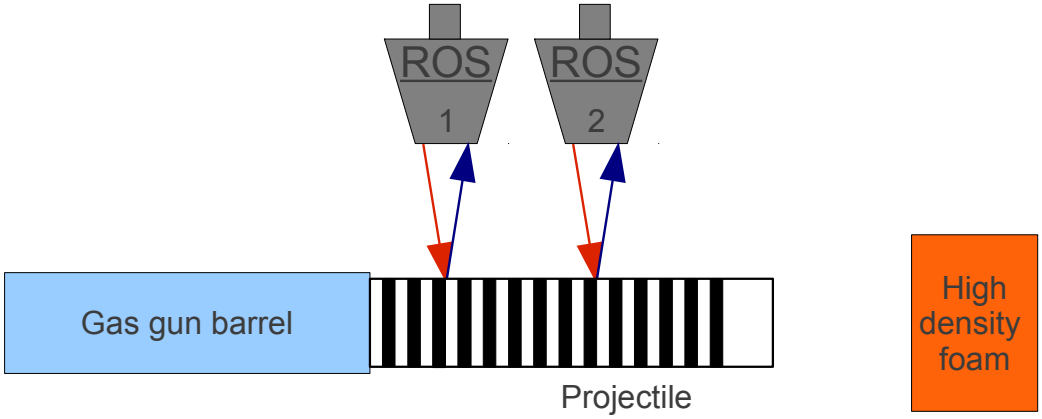

Figure 3.21: Graduated line pitch investigation, experimental layout

Two sets of projectiles with a pitch of 1 mm, 2 mm, 3 mm and 4 mm were manufactured. One set is 50% reflective, 50% non-reflective while the other is 25% reflective and 75% non-reflective. The projectiles used are shown in Figure 3.22. During testing the projectiles are fired from a gas gun at velocities ranging from 10 to 30 m/s. Typical results for a 2 mm pitch projectile are shown in Figure 3.23. The noise seen at the beginning of the raw signal is the front of the projectile moving past the ROS. This behaviour is not visible in the wedge bar tests. The time each peak occurred at is determined using the built in MATLAB function “findpeaks”. As the time and distance between peaks is known the velocity can be calculated. The results are shown in Figure 3.23(b).

Figure 3.22: Projectiles used

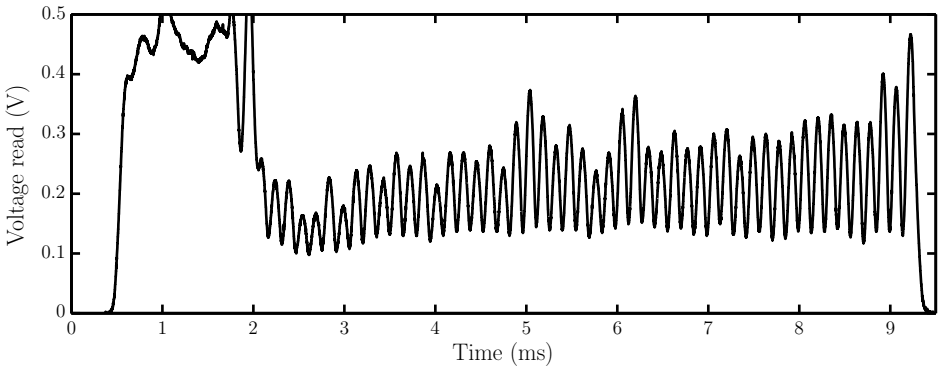

(a) Raw data

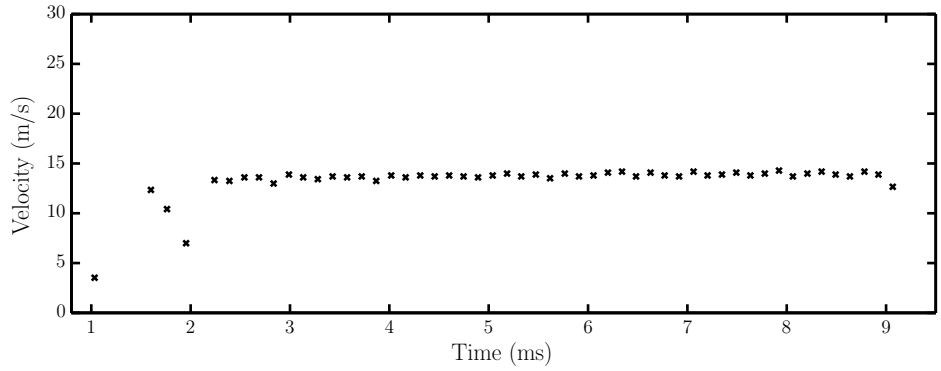

(b) Velocity time data

Figure 3.23: Typical result of a constant velocity test using a 2 mm pitch projectile

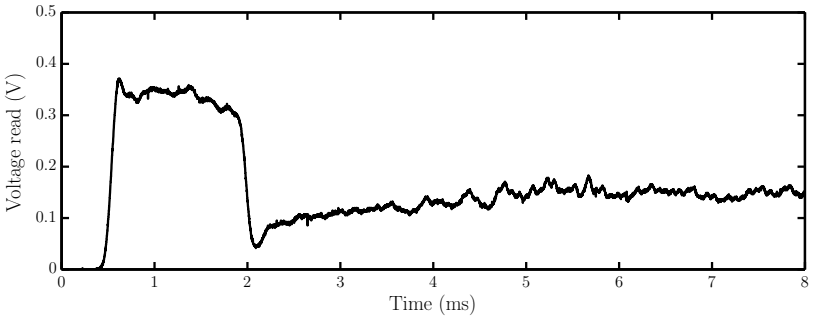

(a) 1 mm pitch raw data

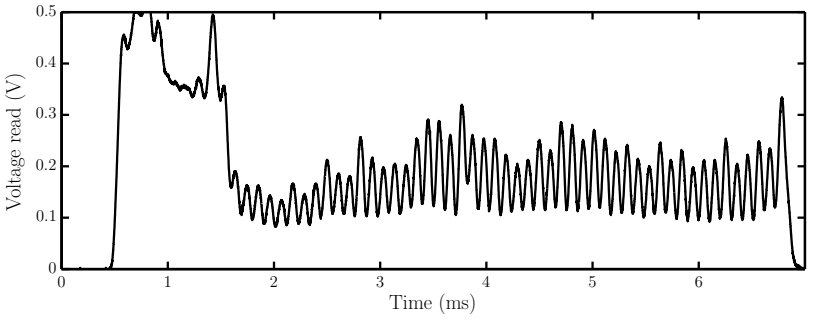

(b) 2 mm pitch raw data

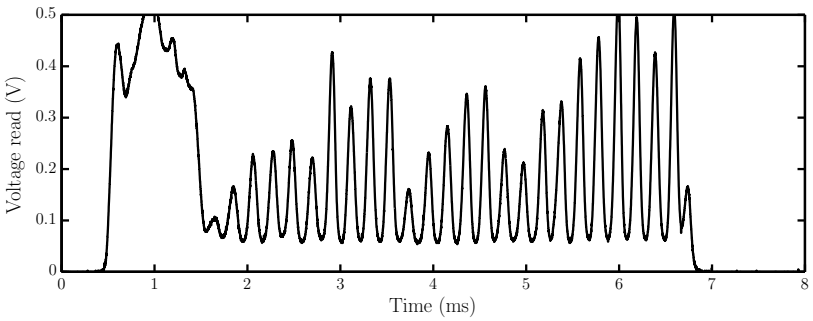

(c) 4 mm pitch raw data

Figure 3.24: Raw data for 1 mm, 2 mm and 4 mm pitch projectiles

3.4.3 Pitch Comparison Results

The experimental results comparing the sensor response for the 1 mm, 2 mm and 4 mm pitch projectiles are presented in this section. Typical results for the raw signals are shown in Figure 3.24. From these results it is clear that the results for the 1 mm pitch are not usable as the noise from the signal completely obscures the sensor response, as shown in Figure 3.24(a). However, the 2 mm and 4 mm pitch projectiles both give clearly distinguishable peaks, as shown Figure 3.24(b) and Figure 3.24(c). The velocity histories calculated from the 2 mm and 4 mm pitch projectiles are shown in Figure 3.25. As expected the velocity calculation worked well for both the 2 mm and 4 mm pitches. Although the sensor response for the 4 mm pitch is better than for the 2 mm pitch it provides half the resolution. The 2 mm pitch is selected as the response is sufficient and it provides better resolution than the 4 mm pitch.

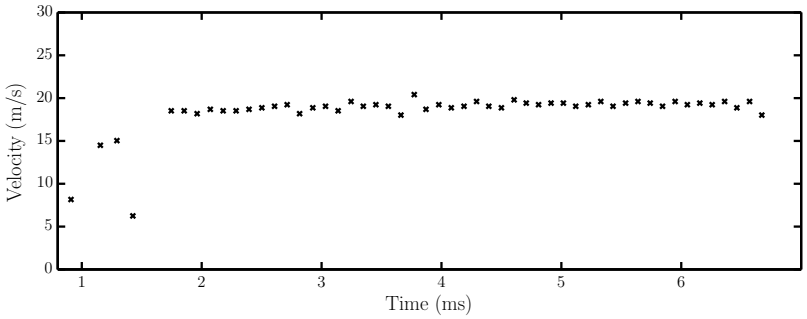

(a) 2 mm pitch velocity

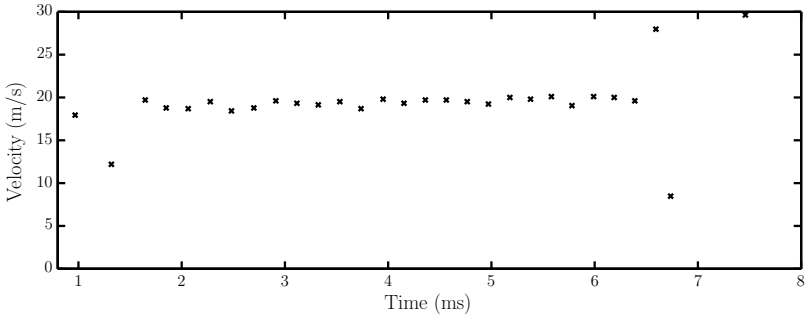

(b) 4 mm pitch velocity

Figure 3.25: Velocity comparison of the 2 mm and 4 mm pitch projectiles

3.4.4 Sensor Comparison Results

The results for the raw signals and velocity obtained from the QRB 1114 and QRB 1134 are shown in Figures 3.26(a) to 3.26(c). The displacement time data from each sensor describes an identical curve, as shown in Figure 3.26(b). This provides confidence that both sensors are accurately recording the position of the peaks in the signal. There is a significant difference in amplitude between the two signals. For the test shown, the QRB1134 sensor gave the largest response, but in other tests done the results are reversed. Although the amplitude of the signals varies between sensors, the position of their peaks is nearly identical. As both sensors provided similar results the QRB1114 is selected as it included integral leads, simplifying the manufacturing process.

3.4.5 Deceleration Tests

For the majority of the tests the projectile is only stopped after it has passed by the ROS giving a constant measured velocity. For several of the tests the foam is positioned to slow down the projectile as it moves past the ROS to investigate the ability of the sensor to measure deceleration. A typical result is shown in Figure 3.27. The sensors captured the velocity of the projectile as it decelerated from 20 m/s to just above stationary before the projectile passed the ROS. The response of the sensor to capture changing velocities is satisfactory.

3.4.6 Determining Direction of Motion

It is possible to determine if the direction of motion changes during the experiment if two sensors are used. This is done by comparing the order of the peaks from two sensors mounted side by side. A typical example of the raw data from an IST experiment is shown in Figure 3.28. In this example the peaks of sensor 1 always occur before the peaks of sensor 2. This order will only change during the experiment if the direction of motion of the wedge bar changes. This check is used to determine if the wedge bar has rebounded at the end of the experiment.

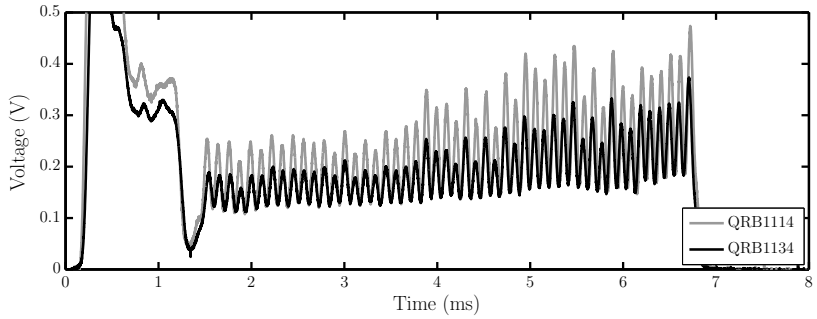

(a) Raw signals

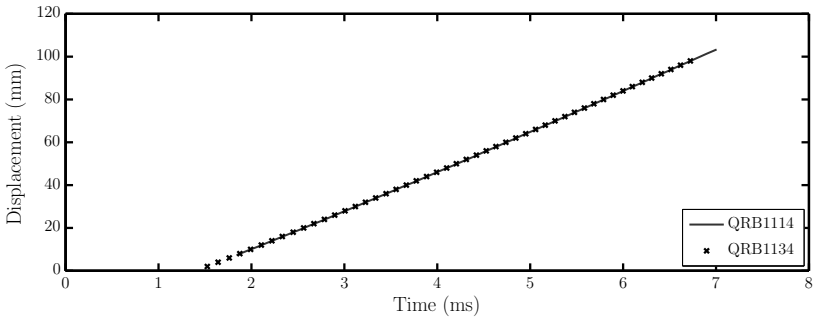

(b) Displacement

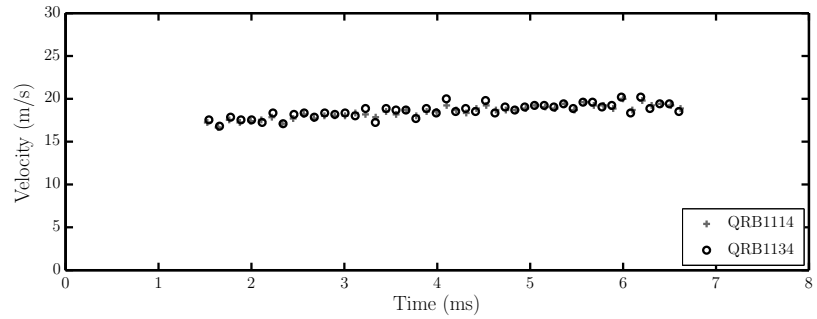

(c) Velocity

Figure 3.26: QRB1114 and QRB1134 ROS comparison at constant velocity

3.4.7 Data Processing Methods Investigated

Once the sensor and graduated line pitch were chosen, the data processing method used to convert the raw data to displacement and velocity time was investigated. There are two decisions that need to be made regarding the data processing. First, should the peaks and troughs be used during data processing? Second, should one or two sensors be used?

When considering the troughs as well as the peaks it is assumed that the troughs occur half way between the peaks. This allows the calculation of the displacement in increments equal to half the pitch. Although this doubles the resolution it also amplifies the noise, as is shown in Figure 3.29. The advantage of doubling the resolution is offset by the need for additional smoothing of the signal. Therefore, it is concluded that the assumption that the troughs appear half way between the peaks is incorrect.

The results of including the second sensor is also shown in Figure 3.29. There is a significant increase in the noise in the calculated velocity when using a second sensor. It was initially thought that

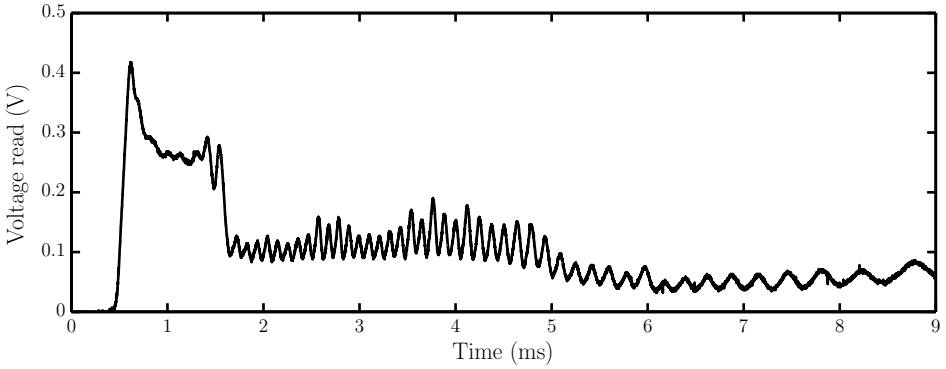

(a) Raw data

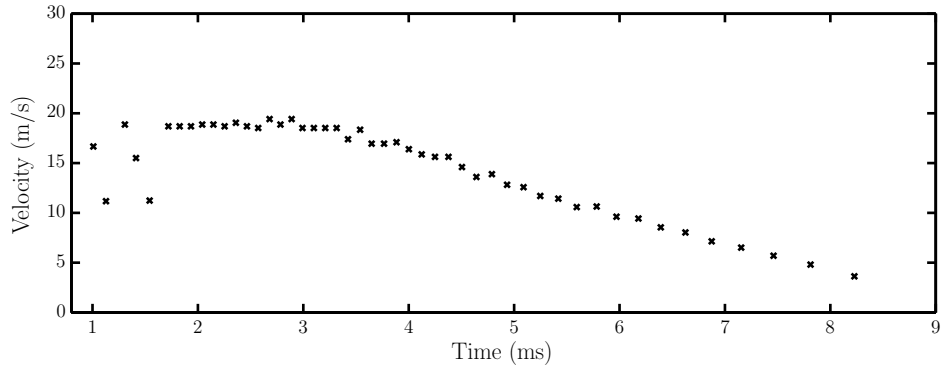

(b) Velocity time data

Figure 3.27: Typical result for a deceleration test using a 2 mm pitch projectile

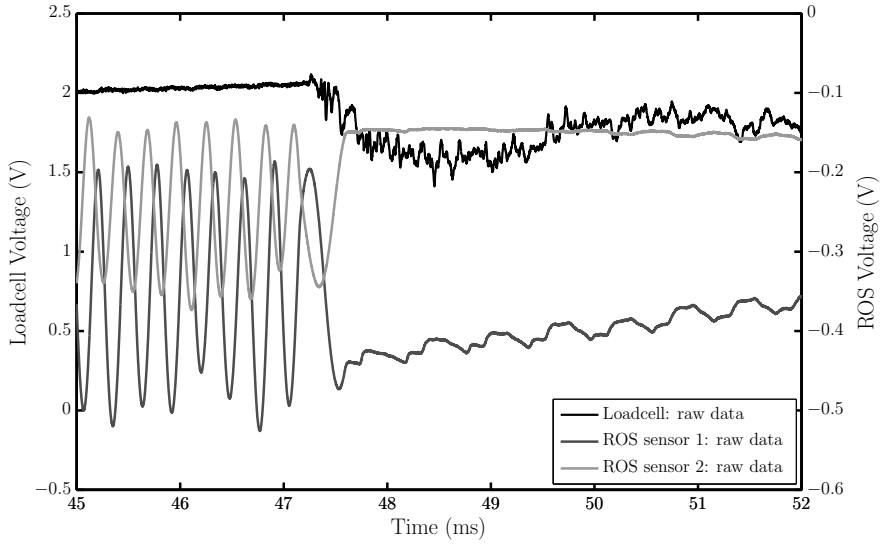

Figure 3.28: ROS signals, annealed aluminium specimen 2

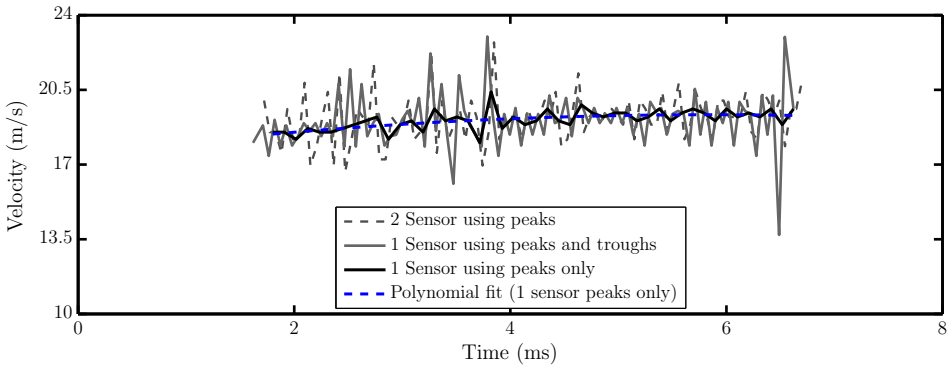

Figure 3.29: Effect of processing method on noise on the velocity signal

using an incorrect offset distance between the sensors resulted in the increased noise on the signal. The approximate offset between the two sensors calculated, based on the dimensions given in the data sheet, gives a value of 5.33 mm. The offset distance is varied between 5.2 mm and 5.5 mm to determine the effect the offset distance has on the noise level. Results for 3 different offset distances are shown in Figure 3.30. An offset distance of 5.34 mm results in the minimum noise on the velocity history. However, even when this offset distance is used, the addition of the second sensor still results in a significant increase in noise on the velocity history.

For the initial results presented, the velocity is calculated by differentiating the displacement time history. To reduce the noise levels a polynomial is fitted to the displacement time data and then differentiated to give the velocity. This greatly reduces the noise on the velocity time data. The results are shown in Figure 3.31. The velocity time histories obtained from the different processing methods match closely. Therefore, there is no advantage to using the troughs or the second sensor when calculating the wedge bar displacement and velocity. However, retaining the second sensors makes it possible to detect if the direction of motion of the wedge bar has changed.

It was decided to use only one sensor using the peaks only when calculating the displacement and velocity. This gives a resolution of 2 mm on the wedge bar displacement measurement. This equates to a resolution of 0.008 mm on the specimen displacement measurement when the 2/500 wedge bar is used, which is within 0.8% of the total specimen displacement. Using the 1/500 wedge bar will double this resolution. A second sensor is used only to allow the direction of motion to be determined.

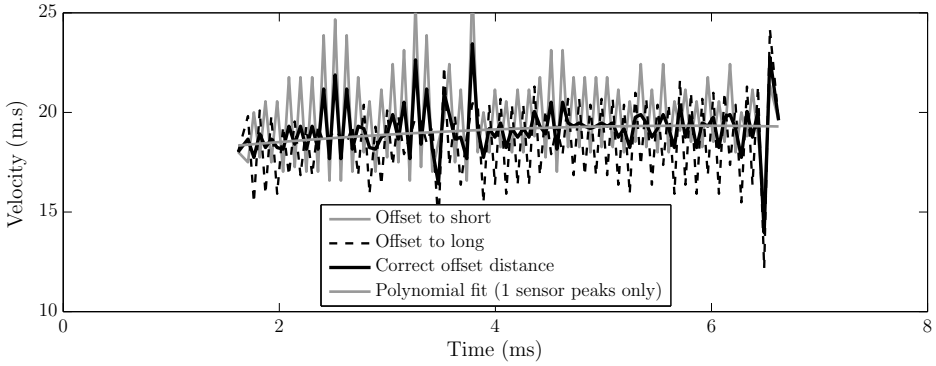

Figure 3.30: Effect of sensor offset distance on noise in the velocity signal

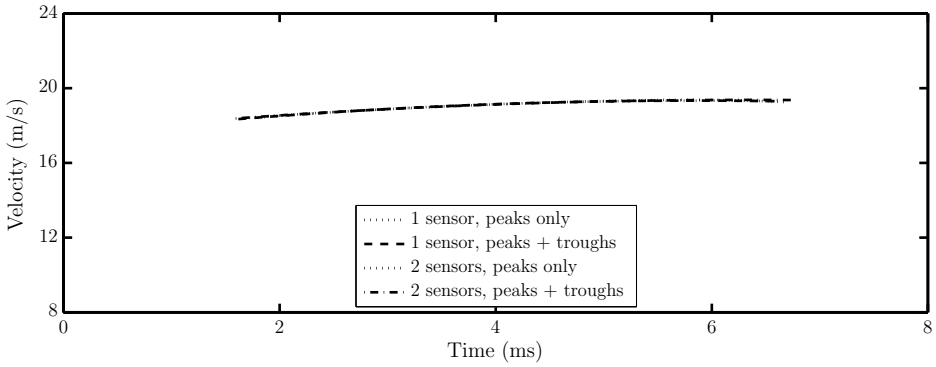

Figure 3.31: Curve fit data comparison for the different processing methods

Chapter 4

Experimental Method

This chapter starts by describing the testing program which covers the benchmarking tests, interrupted tests and the load-frame comparison tests. This is followed by the specimen preparation procedures used. Finally, the experimental setup and data processing of the QS, SHPB and ISR tests are presented.

4.1 Testing Program

The testing program is drawn up to benchmark the performance of the IST as well as to investigate the effect of certain parameters on the IST's response. The testing program is split up into the following sections:

- Benchmarking tests - The benchmarking tests include the QS, SHPB and ISR tests for aluminium, copper, mild steel, PMMA and nylon. These results are compared with data found in the literature and are used to benchmark the performance of the IST.
- Loading method comparison - Impact driven and back pressure driven tests are done to investigate the effect the loading method has on the IST's performance. These results are compared to the FEA results presented in Section 3.3.4 which show that the back pressure experiments contain significantly less noise and unwanted oscillations.
- Loading platform comparison - The balanced and unbalanced loading platforms are compared to verify the FEA results presented in Section 3.3.6 which shows superior results given by the balanced loading platform.
- Interrupted tests - The interrupted tests are used to give an indication of the friction effects present in the IST.
- High speed camera work - The high speed camera is used to check the IST for any unusual behaviour and unwanted movement during an experiment

4.2 Specimen Preparation

The test specimen geometry is chosen to allow the use of the same specimen for quasi static, intermediate and high strain rate testing. The specimen geometry chosen is a 5 mm diameter, 5 mm long cylinder. The specimen are machined to 5 mm diameter and 5.5 mm length. Each specimen is then polished down to 5 mm length using a polishing wheel with 1000 grit silicon carbide paper. This allows the final length of the specimen and the surface finish to be adjusted as necessary. A polishing

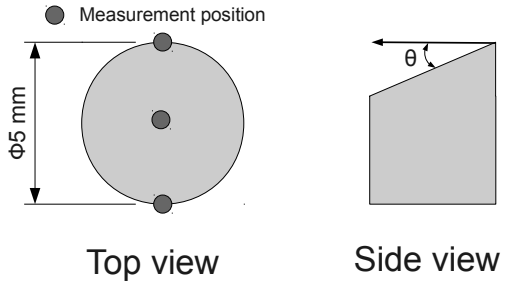

Figure 4.1: Compression test specimen

jig is used to hold the specimen during polishing to ensure the specimen faces remain perpendicular to the sides. Three length measurements are taken on each specimen using a micrometer, one in the centre and two diametrically opposite from one another, as shown in Figure 4.1. The variation in specimen length across the specimen surface is typically less than 20 μm. This gives a maximum angular deviation of $\theta = 0.2 \times 10^{-3}$ degrees. Three diameter measurements are taken along the length of the specimen. No significant variation is present and therefore the average is used.

4.3 Quasi Static Testing

The quasi static tests are done on a Zwick 1484 universal materials testing machine fitted with compression testing anvils. The specimen described in Section 4.2 are used. Compression tests are done at a cross head speed of 0.33 mm/min giving a nominal strain rate of 10^{-3} s^{-1}.

4.3.1 Experimental Set-Up

At the start of each experiment a thin layer of grease is applied to the specimen surfaces to minimise friction. The specimen is then carefully placed in the centre of the anvils. The depth gauge of a vernier calliper is used to measure the distance from the outside of the anvil to the specimen and ensure it is centrally placed. The specimen preload is set to 100 N. Once this is reached, the experiment starts. The experiment is stopped after a cross head displacement of 1.5 mm.

4.3.2 Data Processing

The outputs recorded from the Zwick for each experiment are the force and cross head displacement. The cross head displacement measured, x_m, comprises of the displacement of the specimen, x_s and the displacement of the testing machine, x_z, often called the machine compliance. To accurately determine the specimen displacement the machine compliance must be removed from the measured displacement.

The stiffness of the Zwick fitted with the compression testing anvils fitted has been measured by Govender et al. [47] to be 80 kN/mm. The displacement of the load path of the Zwick materials tester is calculated as follows

$$x_z = \frac{F}{k_z} \tag{4.1}$$

where F is the measured specimen force, k_z is the machine compliance and x_z is the machine compliance component of the measured displacement. The corrected specimen displacement is then calculated by subtracting the machine compliance from the measured specimen displacement as follows

$$x_s = x_m - x_z \tag{4.2}$$

The force and corrected displacement data is converted to engineering stress and engineering strain as follows

$$\sigma_e = \frac{F}{A_s} \tag{4.3}$$

$$\epsilon_e = \frac{\delta L_s}{L_s} \tag{4.4}$$

The engineering stress and strain is then converted to true stress and true strain using Equations 4.5 and 4.6.

$$\sigma_t = \sigma_e(1 + \epsilon_e) \tag{4.5}$$

$$\epsilon_t = \ln(1 + \epsilon_e) \tag{4.6}$$

4.4 SHPB Testing

The high strain rate testing is done using a classic SHPB. The nominal strain rate for the SHPB test is 1000 s^{-1}. The SHPB setup comprises of a gas gun used to fire a 11 mm diameter 350 mm long striker, a 12.7 mm diameter 1.2 m long incident bar, a 12.7 mm diameter 0.7 m long transmitter bar, bar mounts and a data acquisition system. The bars and striker are manufactured from precipitation hardened stainless steel. Strain gauge pairs are mounted diametrically opposed centrally on the incident bar and 100 mm from the specimen end of the transmitter bar. The wave speed of the bars is approximately 5000 m/s giving a maximum usable testing duration around 215 µss and a maximum strain of 22% at a strain rate of 1000 s^{-1}@. An ADLINK PCI-9812 data capture card is used to record the output signals from the strain gauge amplifiers. The maximum sampling rate is 20 Mhz, but the selected sampling rate is 10 MHz.

4.4.1 Experimental Set-Up

The first step in the set-up process is to align the bars on the SHPB bed. The HPBs are aligned by hand. The bars are considered to be aligned when the bars move through the bushes with minimal friction, the bar ends meet flush and remain flush as the bars are moved together. Machinists blue is used to check for uniform contact between the bar ends. This helps check bar alignment and indicates if high spots are present on either of the bars.

The setup procedure for each test is as follows. First, the striker is loaded into the gas gun barrel. Spanjaard RB2 grease is then applied to the faces of the specimen before being placed between the incident and transmitter bars. The grease serves two purposes: it lubricates the specimen during the experiment and helps hold the specimen in place between the HPBs before the experiment starts. The gas gun is then charged to the pressure required to give the desired striker velocity. Finally, the data capture system is armed and the experiment is triggered.

4.4.2 Calibration

The Hopkinson pressure bars are calibrated before each series of tests done. The first step in the calibration process is to measure the elastic wave speed in the bars. This was done using a tap test. Once the distance from the strain gauge to the end of the bars has been measured the bar is placed in the SHPB supports with both ends free to move. One end of the bar is tapped with the hemispherical end of a ball peen hammer to generate an input pulse with a gradual rise and fall time which results in negligible dispersion. The return trip time the pulse takes to travel from the strain gauge to the free end of the bar and back is measured. As the distance is known the wave speed in the bar can then be calculated. This is repeated for both the input and output bars.

The two established methods available for calibrating a HPB are the momentum calibration and stress calibration methods. Both the momentum and maximum stress calibration factors are calculated for each calibration test. As a check, the calibration coefficients obtained from these two methods are compared to the theoretical output calculated from strain gauge theory. A variation of 5% or less is expected between these methods.

During the calibration tests the striker is fired at the HPB. The velocity of the striker is recorded using a light trap just before the striker impacts HPB, while the voltage outputs from the strain gauge amps are recorded using a data capture card as in a routine experiment. This information is used along with the physical properties of the bars to calculate the calibration coefficients.

The first step in the calibration process is to measure the physical properties of the bars. The length, diameter, mass and density of the bars are recorded as well as the position of the strain gauges. The speed of sound in the bars is then measured. Once the density and speed of sound in the bars are known, the elastic modulus is calculated. The properties of the bars used are shown in Table 4.1.

Table 4.1: Incident and transmitter bar properties

	units	Input bar	Transmitter bar
Speed of sound	m/s	5013	5011
Density	kg/m^3	7766	7780
Elastic modulus	GPa	195	196

4.4.3 Theoretical Strain Gauge Output

The theoretical strain gauge output is calculated first based on the geometric and material properties of the HPB and strain gauge theory. The theoretical bridge voltage output (V_{WB}) for a strain gauge connected to a Wheatstone Bridge is calculated as follows

$$V_{WB} = \frac{K_{gf} V_{BV} N \epsilon}{4} \quad [48] \tag{4.7}$$

where K_{gf} is the strain gauge factor supplied by the manufacturer, V_{BV} is the bridge voltage, N is the number of active arms in the Wheatstone bridge and ϵ is the strain in the strain gauge.

Making the substitutions

$$V_{out} = \frac{V_{out}}{Gain} \quad \text{and} \quad E = \frac{\sigma}{\epsilon} \tag{4.8}$$

and rearranging, gives

$$\sigma = \left(\frac{4E}{Gain K_{gf} N V_{BV}} \right) V_{out} \quad [48] \tag{4.9}$$

where V_{out} and $Gain$ are the output voltage of the amplifiers and the amp gain and E and σ are the elastic modulus and stress of the parent material. This can be simplified further to

$$\sigma = KV_{out} \quad \text{where} \quad K = \left(\frac{4E}{GainK_{gf}NV_{BV}}\right) \tag{4.10}$$

Making the substitutions E = 195GPa, $Gain$ = 1000, K_{gf} = 2.21, N = 2 and V_{BV} = 4.02 gives a theoretical calibration factor of K = 43.9 MPa/V.

4.4.4 Momentum Balance Calibration

It is possible to determine the impulse transferred to the HPB by applying a momentum balance to the striker before and after it impacts the HPB. When the striker and HPB are manufactured from the same material the rebound velocity (V_r) of the striker is calculated as follows

$$V_r = \frac{v_0\left(\frac{A_s}{A_b} - 1\right)}{1 + \frac{A_s}{A_b}} \quad [48] \tag{4.11}$$

where V_0 is the initial velocity of the striker and A_s and A_b are the areas of the striker and HPB respectively. Once the rebound velocity is known, the impulse transferred to the HPB is calculated as follows

$$I = m_{striker}(V_0 - V_r) \tag{4.12}$$

where $m_{striker}$ is the mass of the striker. In integral form the impulse is calculated as follows

$$I = \int_{t_1}^{t_2} F\,dt \tag{4.13}$$

The following substitutions are then made for force and stress

$$F = \sigma A_b \quad \text{and} \quad \sigma = KV$$
$$I = A_b K \int_0^t V(t)\,\delta t \tag{4.14}$$

and then rearranged to solve for the momentum balance calibration factor K

$$K = \frac{I}{A_b \int_0^t V(t)\,\delta t} \tag{4.15}$$

4.4.5 Maximum Stress Calibration

The maximum stress calibration factor is calculated by comparing the plateau stress from the input pulse recorded from the strain gauge amps to the theoretical maximum stress in the HPB. As with the momentum calibration factor, a light trap is used to calculate the speed of the striker before impacting the bars. When the striker and HPB are manufactured from the same material the stress in the HPB is calculated as follows

$$\sigma_2 = \frac{A_1}{A_1 + A_2}\rho c V_0 \quad [48]$$

where A is the area of the bars, ρ is the density and c is the speed of sound in the material. Subscript 1 refers to the striker and subscript 2 refers to the HPB. The calibration factor K is calculated as follows

$$K = \frac{\sigma_2}{V_{max}} \quad [48] \tag{4.16}$$

4.4.6 Calibration Test Results

Eight calibration tests were done for the incident and transmitter bars. The results are shown in Table 4.2 and compared to the theoretical calibration factor of 43.9 MPa/V. As expected, there is only a 2% variation between the momentum, maximum stress and theoretical calibration values. The standard deviation on the momentum calibration factor is lower compared to the deviation on the maximum stress calibration factor and is therefore selected.

Table 4.2: Calibration coefficients

	Stress calibration factor		Impulse calibration factor	
—Test No.	Input bar (MPA/V)	Output bar (MPA/V)	Input bar (MPA/V)	Output bar (MPA/V)
1	43.40	43.84	43.86	43.93
2	43.22	43.50	43.29	43.83
3	42.63	42.89	43.35	43.63
4	42.35	42.96	43.17	43.40
5	42.07	43.72	43.08	43.85
6	44.05	44.48	44.33	44.85
7	42.58	43.04	42.86	43.22
8	42.65	43.05	42.73	43.53
Average	42.87	43.44	43.33	43.78
Deviation	0.52	0.45	0.38	0.33

4.4.7 Data Processing

Before the details of the data processing are described, a short overview of the data processing procedure is given. The starting point is the raw signals recorded during an experiment. A typical example is shown in Figure 4.2(a). The following steps are followed

- The signals are shifted from the position recorded at the strain gauges to the specimen bar interface. The recorded signals are converted from voltage time to stress time using the calibration factors calculated above.
- The stress time history is converted to velocity time history
- The velocity time history is integrated to give the displacement history of the faces of the bars and therefore the change in specimen length. The change in specimen length is used to calculate the strain in the specimen and specimen area.
- The stress in the specimen is calculated from the stress in the bars using the area ratio between the bars and the specimen.

A schematic of the SHPB and specimen interface, showing the variables used in these derivations is shown in Figure 4.3. The first step in the data processing procedure is to shift the incident, reflected and transmitted waves from the position recorded at the strain gauge stations to the specimen bar interface. The waves are shifted using 1-D shifting without any correction for dispersion. The Incident pulse is shifted forwards by $t_i = x_i/c_i$ where x_i and c_i are the strain gauge to specimen distance and speed of sound of the incident bar. The reflected pulse is shifted back by t_i. The transmitted pulse is shifted back by $t_t = x_t/c_t$ where x_t and c_t are the strain gauge to specimen distance and speed of sound of the transmitter bar. The shifted signals are shown in Figure 4.2(b).

Once the signals have been shifted to the bar/specimen interface the voltage time signal is converted to stress time using the calibration factors. The velocity of the bar faces is then calculated. The velocity in the bar is related to the stress in the bar as follows

$$\sigma = \rho c V \text{ [48]} \tag{4.17}$$

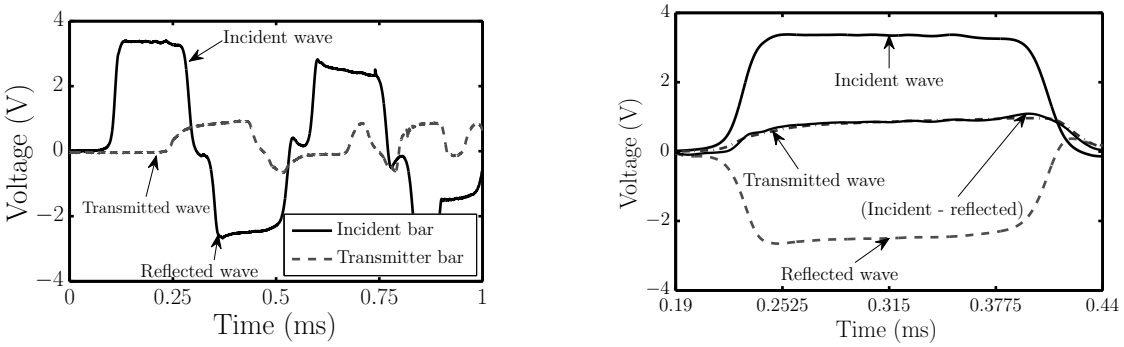

(a) Raw signals

(b) Shifted signals

Figure 4.2: Raw data and shifted data for a typical SHPB test

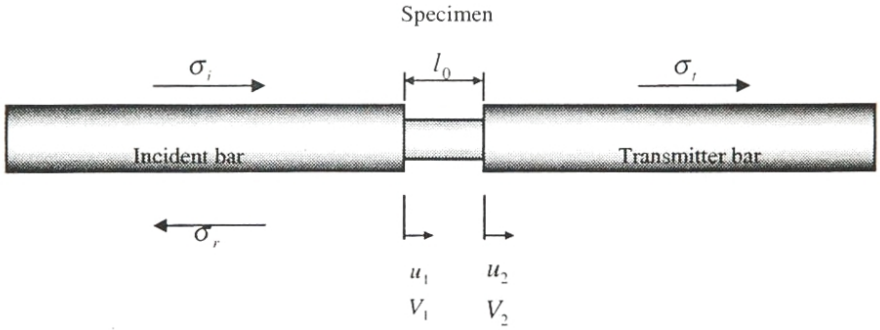

Figure 4.3: Incident and transmitter bars [48]

Rearranging gives the velocity in the bars as follows

$$V_1 = \frac{\sigma_1}{\rho_i c_i} \quad \text{and} \quad V_2 = \frac{\sigma_2}{\rho_t c_t} \tag{4.18}$$

where V_1 and V_2 are the velocities of the face of the incident and transmitter bars in contact with the specimen, $\sigma_1 = \sigma_i + \sigma_r$ and $\sigma_2 = \sigma_t$ and ρ_i and ρ_t are the density of the incident and transmitter bars respectively. The displacement of the bars is then calculated by integrating the velocity time history as follows

$$u_1(t) = \int_0^t V_1(t)\delta t \tag{4.19}$$

$$u_2(t) = \int_0^t V_2(t)\delta t \tag{4.20}$$

Once the displacement of the bar ends are known, the change in length of the specimen and the strain in the specimen is calculated as follows

$$\begin{aligned} \Delta L(t) &= u_1(t) - u_2(t) \\ L_s &= L_o - \Delta L(t) \\ \epsilon(t) &= Ln\left(\frac{L_s}{L_0}\right) \end{aligned} \tag{4.21}$$

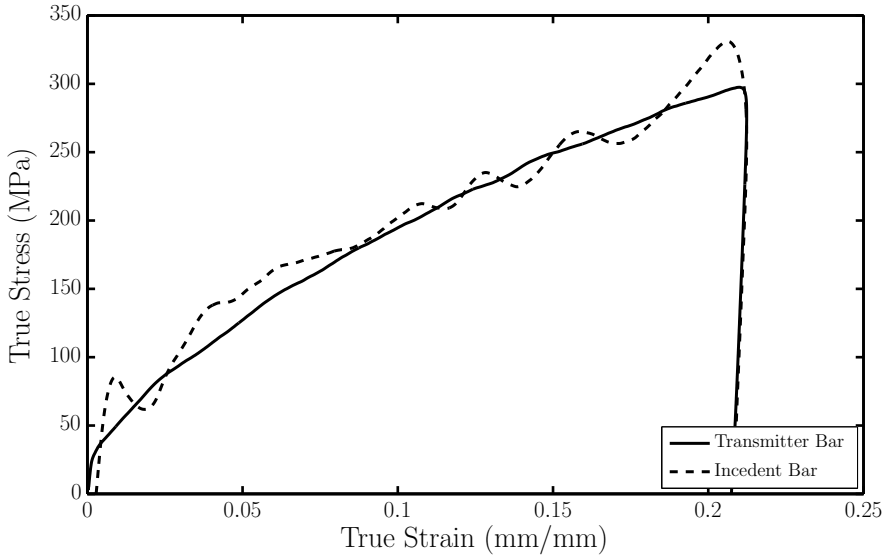

Figure 4.4: Comparison of incident bar and transmitter bar stress

The strain rate is calculated from the velocity of the bars and the instantaneous length of the specimen as follows

$$\dot{\epsilon}(t) = \frac{V_1 - V_2}{L_s} \tag{4.22}$$

The stress on the transmitter bar side of the specimen is calculated as follows

$$\sigma_{st} = \sigma_t \times \frac{A_t}{A_s} \tag{4.23}$$

where A_t is the area of the transmitter bar and A_s is the instantaneous area of the specimen calculated using the instantaneous length and a constant volume assumption.

Stress on the incident bar face of the specimen is calculated as follows

$$\sigma_{si} = (\sigma_i + \sigma_r) \times \frac{A_i}{A_s} \tag{4.24}$$

Comparing the stress on either face of the specimen allows equilibrium to be checked as shown in Figure 4.4.

4.5 ISR Testing

In this section the experimental set-up and data processing methods used for the IST are discussed. The intermediate strain rate testing is done on the IST. A schematic of the layout is shown in Figure 3.2.

4.5.1 Experimental Set-Up

During set-up the striker, wedge bar and stopper bar are mounted on an I-beam using the standard SHPB supports used at BISRU. A laser alignment system is used for the initial alignment of the bars while the final alignment is done by manual inspection. The bars are considered to be aligned when they move through the bushes with minimal friction and the bar ends meet flush and remain flush as the bars are moved together.

As discussed previously, two different loading methods are used, impact driven loading and back pressure driven loading. The experimental method followed is very similar for the different loading methods, only the impact driven loading will be discussed in detail.

Prior to each test, the position of the stopper bar and energy absorber is reset. A lubricant is then applied to the wedge bar before each experiment to help reduce friction between the wedge bar, load-frame and loading platform. Two types of lubricants are investigated, 15W40 motor oil and Spanjaard RB2 grease.

Spanjaard RB2 grease is applied to both ends of the specimen before it is placed on the loading platform. Once the specimen is in place on the loading platform, the wedge bar is slid through the load-frame until the wedge bar, loading platform, specimen and load-cell are all firmly in contact. This "preload" helps reduce noise during the experiment, which is discussed further in Section 5.5. Shims are placed between the loading platform and the specimen to minimise the amount of wedge bar displacement necessary to achieve the preload and to compensate for variations in specimen length.

Once the wedge bar is placed in position the striker is then moved into the firing position in the gas gun barrel. The distance the striker is inserted into the barrel, as well as the gas gun pressure, is selected depending on the striker velocity required. The striker velocity can be accurately controlled and yields repeatable results. After the striker is loaded into the barrel, the gas gun pressure is set, the data capture system armed and the experiment triggered.

After the experiment the wedge bar is moved backwards, releasing the specimen. However, after some tests the friction in the system made it difficult to move the wedge bar and remove the specimen. A mechanism which allows the specimen to be removed without the need to move the wedge bar will simplify this process.

4.5.2 Data Processing

A brief overview of the data processing steps followed is given first before each is discussed in detail below. For each test performed voltage time histories are recorded for the strain gauge load-cell and the wedge bar displacement sensor, shown in Figure 4.5(a). The first step in the data processing is to convert the recorded voltage time signals from the load-cell and ROS into force time and wedge bar displacement time data. The results of this are shown in Figure 4.5(b). The specimen displacement is then calculated from the wedge bar displacement using the wedge bar angle and correcting for the compliance of the IST. Once the force and the displacement history of the specimen are known, the stress strain and strain rate history is calculated.

The voltage time signal is converted to a force time history as follows

$$F = K_f V_{read} \quad \text{where} \quad K_f = 2791 \ N/V \tag{4.25}$$

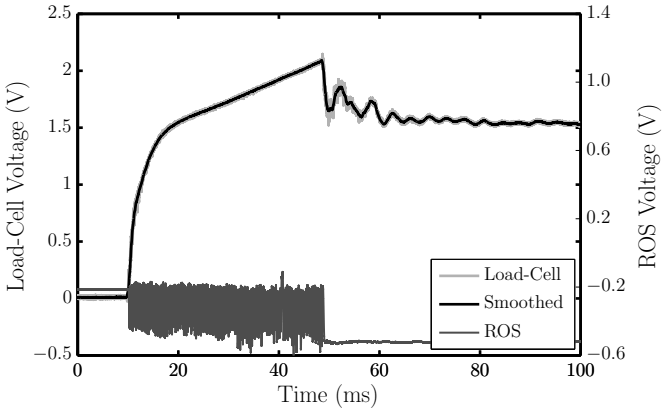

(a) Raw data for a typical IST test

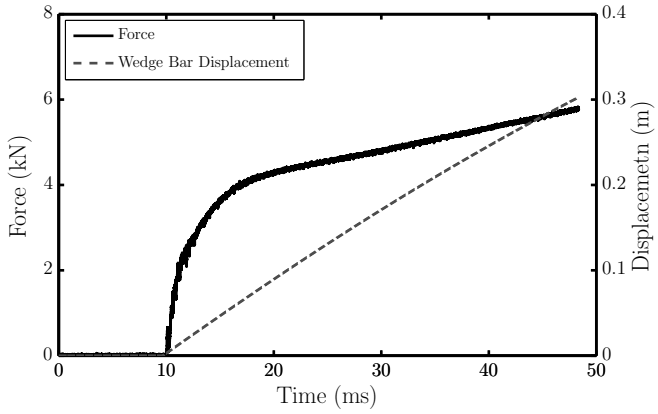

(b) Force and Displacement data

Figure 4.5: IST Data

The calculation of K_f is shown in Appendix D.2.2. The wedge bar displacement is calculated as described in Section 3.4.7. The specimen length is then calculated from the wedge bar displacement as follows

$$\begin{aligned} L_s &= L_i - (d_{LP} - d_L) \\ d_{LP} &= WBD * Tan(\theta) \\ d_L &= \frac{F}{K_{IST}} \\ L_s &= L_i - \left(WBD * Tan(\theta) - \frac{F}{K_{IST}} \right) \end{aligned} \tag{4.26}$$

where L_s is the length of the specimen, L_i is the initial length of the specimen, d_{LP} is the displacement of the loading platform, d_L is the displacement due to load path compliance, WBD is the wedge bar displacement, θ is the wedge bar angle, F is the force measured by the load-cell and K_{IST} is the stiffness of the IST, measured as discussed in Sections 3.3.5 and 6.3. The loading platform displacement, load path compliance and specimen displacement are shown in Figure 4.6(a). Note how linear the displacement time data looks. The effect of load path velocity is discussed later.

As with the QS tests the engineering stress and strain in the specimen is calculated using Equations 4.3 and 4.4. The true stress and strain are then calculated using Equations 4.5 and 4.6. Once this is complete the strain rate is calculated as follows

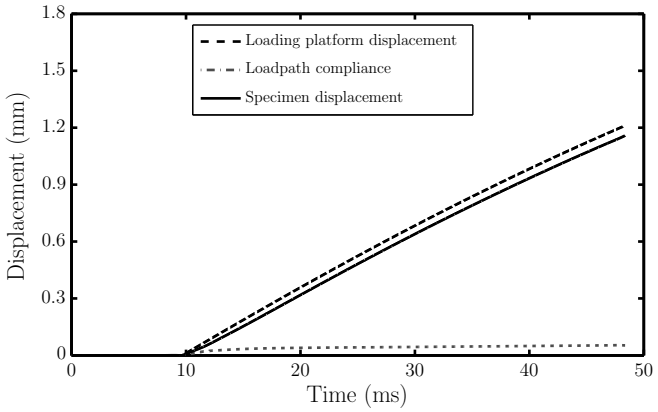

(a) Specimen displacement

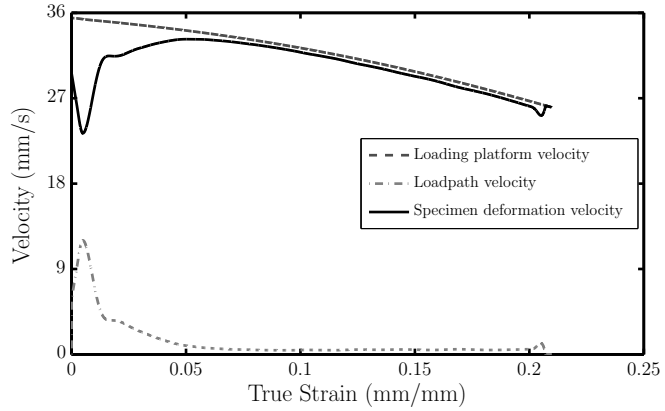

(b) Velocity

Figure 4.6: Displacement and velocity

$$\dot{\epsilon}(t) = \frac{\delta\epsilon}{\delta t} = \frac{V(t)}{L_s(t)} \tag{4.27}$$

where V is the deformation velocity of the specimen. The deformation velocity of the specimen is calculated by differentiating equation 4.26. As shown in Figure 4.6(a), the displacement of the load path is small compared to the total specimen displacement. However, the load path velocity is significant over the elastic portion of the experiment as shown in Figure 4.6(b), and needs to be taken into account when calculating strain rate.

The results for the strain rate history calculated assuming the load path is rigid, accounting for the load path deflection and accounting for both the load path deflection and velocity are shown in Figure 4.7(a). The final processed results for an aluminium specimen are shown in Figure 4.7(b). Note how the specimen displacement time history "implies" a very linear strain rate over the duration of the experiment[1], but when the strain rate is calculated the variations in strain rate become much more noticeable. As the variations in strain rate typically occurs over a short duration, compared to the total duration of the experiment, they are not noticeable on the strain time or specimen displacement time plots. This is important to remember when comparing strain rate histories to strain time histories presented in the literature.

[1]The strain time history looks equally as linear

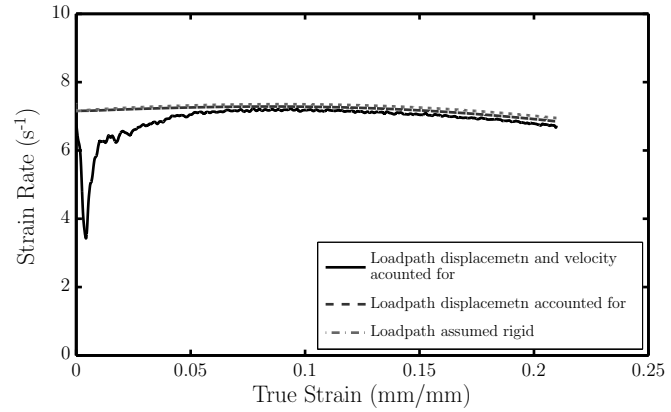

(a) Strain rate

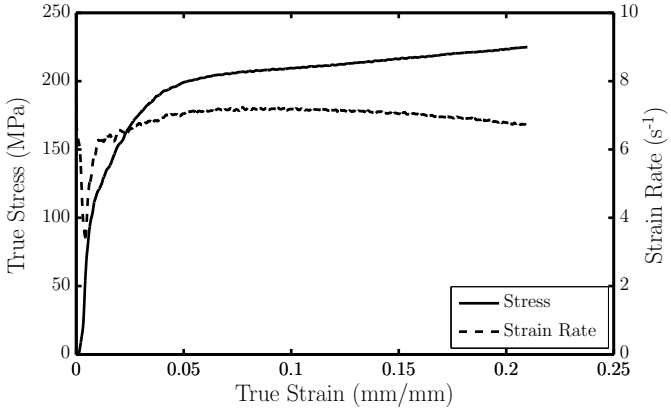

(b) Final results

Figure 4.7: Stress and strain rate verses strain

Chapter 5

Test Results

In this section the testing results are presented. The benchmarking tests used to demonstrate the performance of the IST are presented first, followed by typical strain rate histories of the different materials tested. The tests done to investigate the effects of specimen friction, the different loading platforms, the effects of specimen preload on specimen response and certain characteristics of the IST are then presented. Finally, the high speed camera footage is covered.

5.1 Benchmarking Tests

Comparing the IST results with those obtained from the established testing methods is useful in benchmarking the performance of the IST. For rate insensitive or mildly rate sensitive material like aluminium we expect very little variation between the QS, IST and SHPB results. For highly rate sensitive materials like steel and polymers we expect a significant increase in material properties with increased flow rate. However, for all the materials tested we expect the IST results to fall somewhere between the QS and SHPB results.

5.1.1 Aluminium

The first set of tests is done on aluminium specimens remaining from the testing work done by Cloete and Oxtoby [1]. This enables an easy comparison of the performance of the two ISTs. The results for the aluminium specimen are shown in Figure 5.1. The QS, IST and SHPB results all show a smooth transition between the elastic and plastic portions of the test with no distinct yield point visible. The QS, IST and SHPB data match closely over the initial portion of the experiment. Thereafter the flow stress of the IST and SHPB tests increase above the QS test. Over the final portion of the experiment the flow stress of the IST results further increases up to and above that of the SHPB tests.

It is expected that specimen friction is responsible for the artificial hardening seen in the IST results over the later portion of the experiment. Hartley et al. [42] reported friction factors of up to 0.2 for aluminium for QS testing. At 22% strain this results in approximately a 12% increase in the flow stress measured. The friction effects do not appear to be greater than is expected based on the friction factors reported in the literature for aluminium. The friction effects are discussed further in Section 6.8. The flow stress is given in Table 5.1 at 6%, 12% and 22% strain. The aluminium is mildly rate sensitive with an increase of 10% between the QS ($\dot{\epsilon}$ =0.001 s^{-1}) and SHPB ($\dot{\epsilon}$ =1800 s^{-1}) tests at 22% strain. A comparison between the results of the two intermediate strain rate testers is

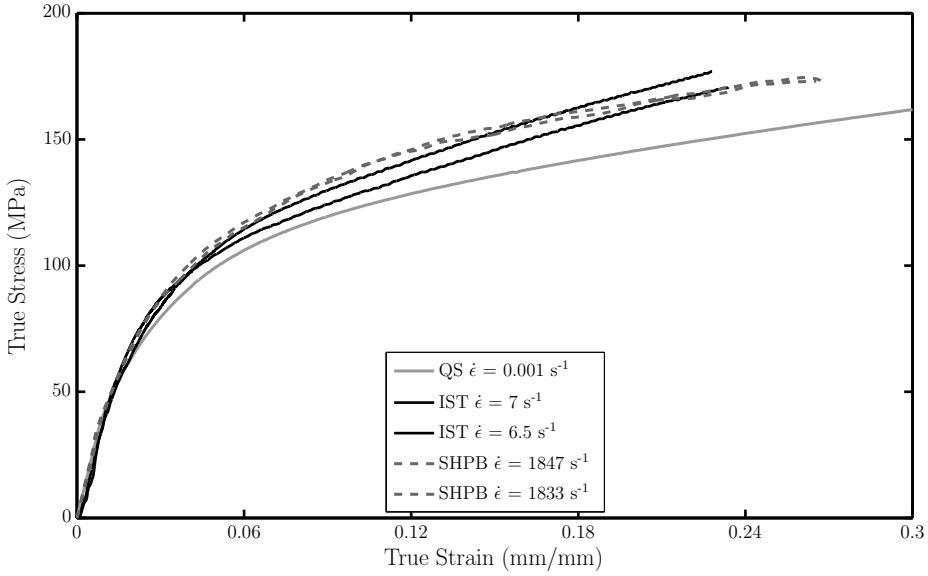

Figure 5.1: Cloete and Oxtoby's aluminium specimen

Table 5.1: Cloete and Oxtoby's aluminium specimen testing results

Test	Flow stress (6% strain) (MPa)	Flow stress (12% strain) (MPa)	Flow stress (22% strain) (MPa)
QS compression	108	130	147
IST	115	143	167-175
SHPB	115	143	167

presented is Section 6.2. In Section 6.1 the results are compared with results found in the literature and discussed in more detail.

The annealed aluminium results for the QS, SHPB and IST tests are shown in Figure 5.2. The results for all the testing methods gave an unusual "double yield" behaviour with two distinct changes in the flow stress gradient. The first occurring at 120 MPa and the second at approximately 190 MPa. As this material behaviour is visible in the QS, SHPB and IST tests, it is unlikely that it is caused by a problem in the testing method. A detailed investigation of this behaviour is beyond the scope of this Dissertation. As with the aluminium results presented in Section 5.1.1, the QS, IST and SHPB compression test data match closely over the initial portion of the experiment, the flow stress of the IST and SHPB tests then increase above that of the QS compression tests. After 10% strain, friction effects become visible as artificial hardening. Over the final portion of the experiment the flow stress of the IST test increases above that of the SHPB test. The flow stress is given in Table 5.2 at 5%, 10% and 20% strain. The aluminium is mildly rate sensitive with an increase of 10% between the QS ($\dot{\epsilon}$ =0.001 s^{-1}) and SHPB ($\dot{\epsilon}$ =1000 s^{-1}) tests at 20% strain. In Section 6.1 the results are compared with results found in the literature and discussed in more detail.

5.1.2 Annealed Copper

The annealed copper results for the QS, IST and SHPB tests are shown in Figure 5.3. There is no distinct yield point with a smooth transition between the elastic and plastic portions of the experiment. Copper is known to be mildly rate sensitive with a small difference expected between the QS and SHPB results. The IST results are expected to fall between them. However, from the start of the experiment

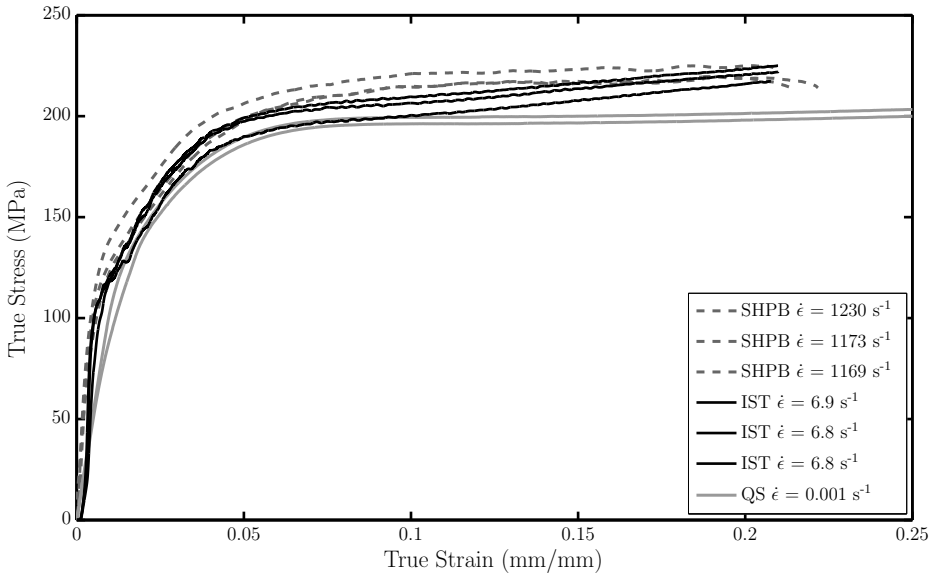

Figure 5.2: Annealed aluminium

Table 5.2: Annealed aluminium testing results

Test	Flow stress (5% strain) (MPa)	Flow stress (10% strain) (MPa)	Flow stress (20% strain) (MPa)
QS compression	190	198	198-201
IST	197	209	216-223
SHPB	199	213	218-225

the IST results give a significantly greater flow stress compared to the SHPB result. The friction factors published by Hartley et al. [42] are greater for copper than for aluminium. The artificial hardening due to friction seen is expected to be greater for copper than in the aluminium specimen, but the difference is not expected to be this big. This is discussed in more detail in Section 5.3 where these results are compared to the interrupted test results. The flow stress is given in Table 5.3 at 5% and 20% strain. The copper specimens are mildly rate sensitive with a 15% increase in flow stress between the QS ($\dot{\epsilon}$ =0.001 s^{-1}) and SHPB ($\dot{\epsilon}$ =1200 s^{-1}) tests at 20% strain. In Section 6.1 the results are compared with results found in the literature and discussed in more detail.

Table 5.3: Copper testing results

Test	Flow stress (5% strain) (MPa)	Flow stress (20% strain) (MPa)
QS compression	116	245-252
IST	150	352-355
SHPB	122	287-290

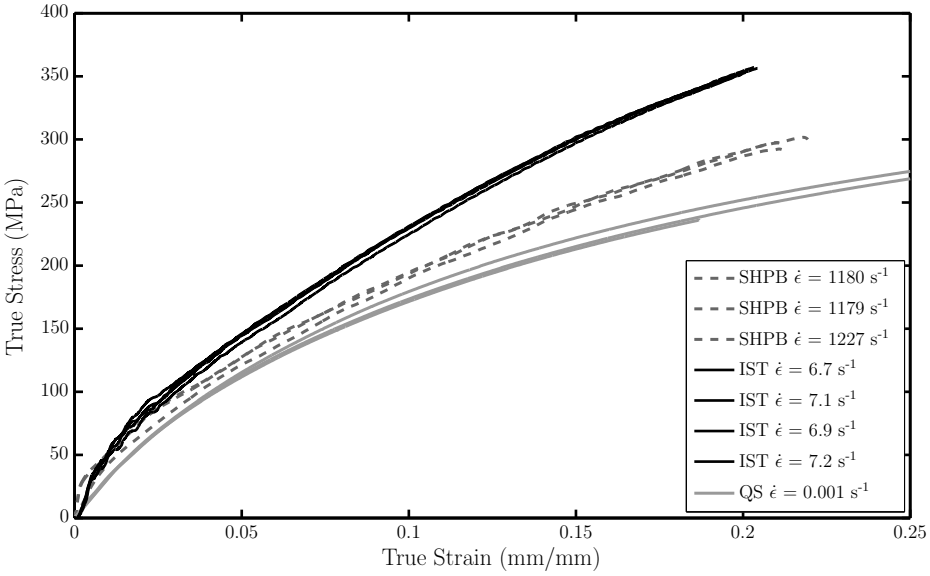

Figure 5.3: Annealed copper

5.1.3 Annealed Steel

The annealed steel results for the QS, SHPB and IST tests are shown in Figure 5.4. The yield point for steel is clearly visible on all the tests performed. A significant increase in yield and flow stress is visible with increasing strain rate. The artificial hardening seen falls between that seen for the aluminium and copper tests. The artificial hardening seen due to friction begins to dominate the specimen response from after yield, and by 5% strain the flow stress has increased above that of the SHPB tests. The flow stress is given in Table 5.4 at yield and 5% strain. The mild steel specimen are highly rate sensitive with an 80% increase in yield stress seen between the QS ($\dot{\epsilon}$ =0.001 s^{-1}) and SHPB ($\dot{\epsilon}$ =±700 s^{-1}) tests. In Section 6.1 the results are compared with results found in the literature and discussed in more detail.

Table 5.4: Steel testing results

Test	Lower yield (MPa)	Upper yield (MPa)	Flow stress (5% strain) (MPa)
QS compression	255		373-378
IST	355	400	460-475
SHPB	465	500	460

5.1.4 Nylon

The nylon results for the QS, SHPB and IST tests are shown in Figure 5.5. There is a smooth transition between the elastic and plastic portion of the experiment with no clear yield point visible. Friction effects on the IST tests are not noticeable with no artificial hardening evident. The results presented in Section 6.1.4 show the UCS measured agrees well with the results presented in the literature. After 5% strain the IST tests stays roughly 25 MPa above the QS test for the remainder of the experiment. The flow stress is given in Table 5.5 at 5% and 20% strain. The Nylon specimens are highly rate sensitive with a 52% increase in flow stress between the QS ($\dot{\epsilon}$ =0.001 s^{-1}) and SHPB ($\dot{\epsilon}$ =1650 s^{-1}) tests at 20% strain. In Section 6.1 the results are compared with results found in the literature and discussed in more detail.

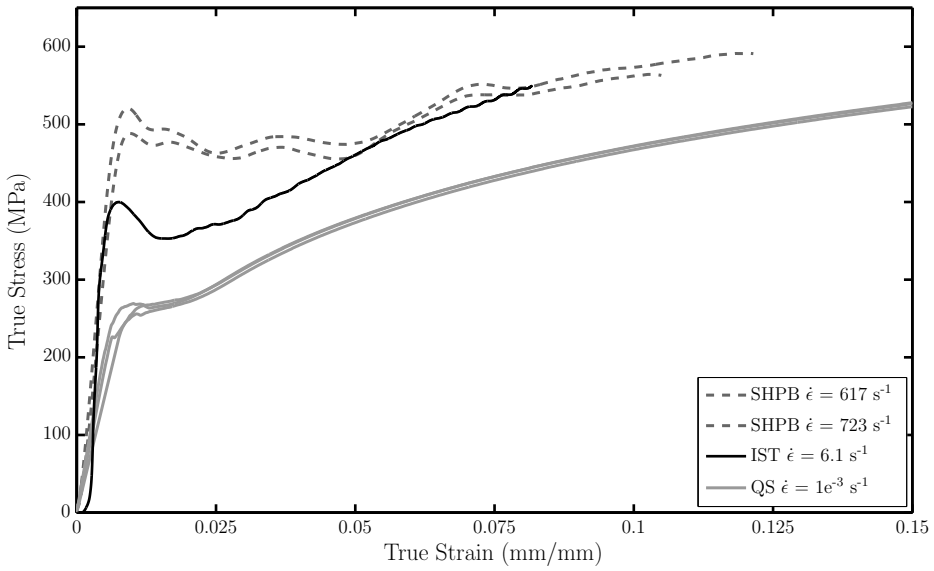

Figure 5.4: Annealed steel

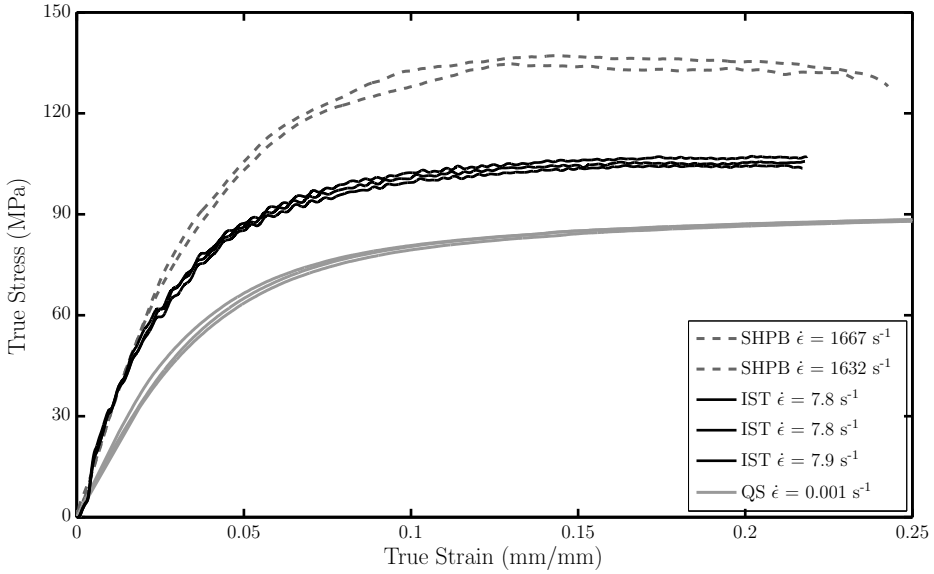

Figure 5.5: Nylon

Table 5.5: Nylon testing results

Test	Flow stress (5% strain) (MPa)	Flow stress (20% strain) (MPa)
QS compression	65	86-87
IST	88	104-107
SHPB	104	132-135

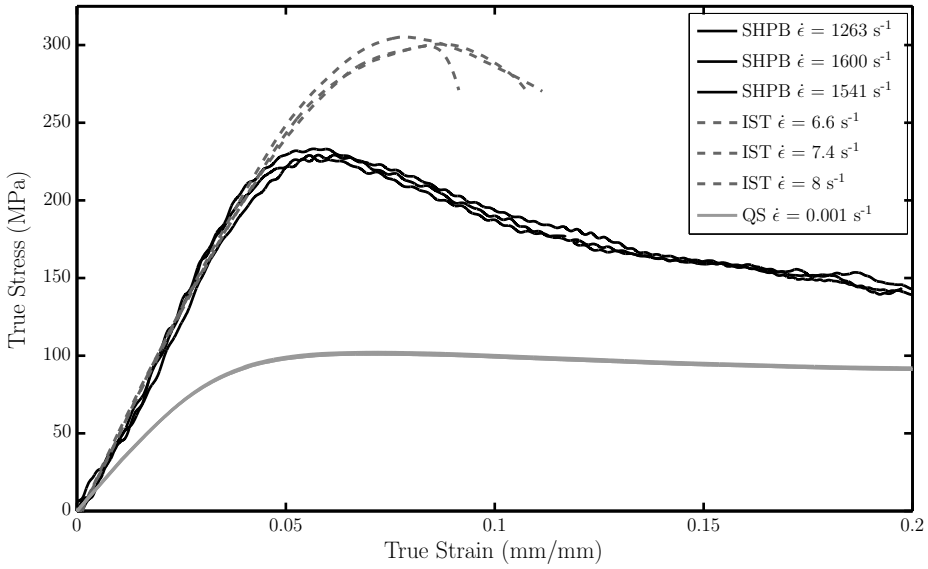

Figure 5.6: PMMA

5.1.5 PMMA

The results for the QS, SHPB and IST tests for PMMA are shown in Figure 5.6. There is a smooth transition between the elastic and plastic portion of the tests. As with the nylon tests, the friction effects are not noticeable. The results presented in Section 6.1.5 show the UCS measured agrees well with the results presented in the literature. The flow stress is given in Table 5.6 at 5% strain and UCS. The PMMA specimen gave the greatest rate sensitivity with an increase of 300% between QS ($\dot{\epsilon}$ =0.001 s^{-1}) and SHPB ($\dot{\epsilon}$ =0.001 s^{-1}) tests. In Section 6.1 the results are compared with results found in the literature and discussed in more detail.

Table 5.6: PMMA testing results

Test	Flow stress (5% strain) (MPa)	UCS (MPa)
QS compression	98	100-102
IST	221-229	229-233
SHPB	239-248	300-305

5.2 Strain Rate History

Typical results of strain rate histories of aluminium, copper, steel, nylon and PMMA are shown in Figure 5.7 and Figure 5.8, while the values of the average strain rate, initial strain rate, minimum and maximum strain rates as well as the ratio of strain rate at yield ($\dot{\epsilon}_y$) to average strain rate ($\dot{\epsilon}_{ave}$) are shown in Table 5.7. A full set of results is given in Table A.2 in Appendix A.3.

Figure 5.7 and Figure 5.8 shows that the strain rate history varies over the duration of the experiment dropping off during the elastic region before rising again and remaining reasonably constant over the plastic portion of the experiment. As shown in Section 4.5.2, the initial dip in strain rate is

proportional to the yield stress of the material. This can also be seen by comparing the ratio of the strain rate at yield to the average strain rate for successive interrupted copper tests in Table 5.7. The yield stress for PMMA, nylon and Cloete and Oxtoby's aluminium specimen is captured at above 80% of the average strain rate for the experiment.

Table 5.7: Strain rate history results

Test	Stain rate				
	Average	Initial	Min	Max	$\frac{\dot{\epsilon}_y}{\dot{\epsilon}_{ave}}$
Cloete and Oxtoby's Al Specimen	7	7.5	5.7	7.5	0.82
PMMA	7.3	9	6	9	0.82
Al	6.9	7.4	3.4	7.4	0.5
Nylon	7.8	7.5	6.4	8.5	0.81
Cu	6.9	7.6	5.6	7.6	0.82
Steel	5.9	7.6	0.6	7.6	0.1
Interrupted Cu test 1 of 5	6.6	8.3	5.8	8.3	0.87
Interrupted Cu test 2 of 5	6.7	8.5	3.1	8.5	0.46
Interrupted Cu test 3 of 5	6.7	7.9	1.7	8	0.25
Interrupted Cu test 4 of 5	6.9	8.1	0.1	8.3	0.012
Interrupted Cu test 5 of 5	7.2	9.3	0.1	9.3	0.01

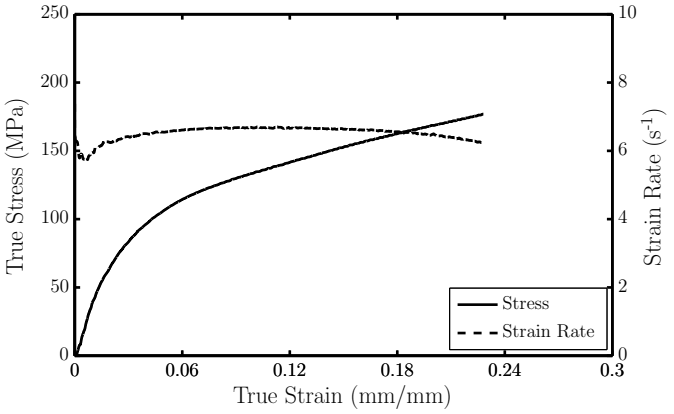

(a) Cloete and Oxtoby's aluminium

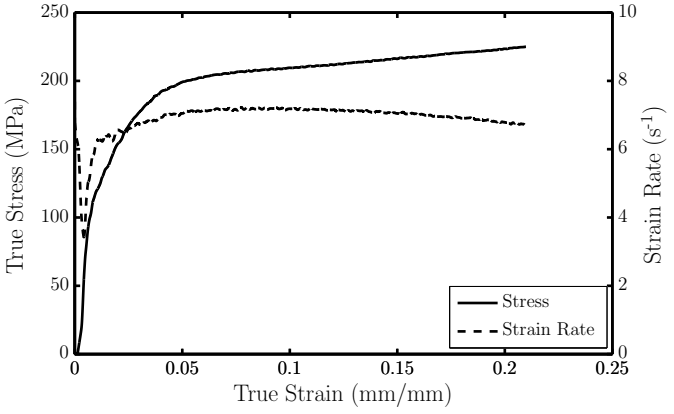

(b) Aluminium

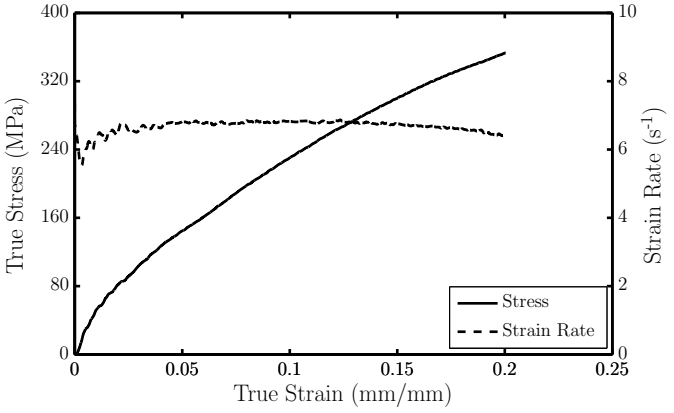

(c) Copper

Figure 5.7: Typical strain rate histories for aluminium, and copper

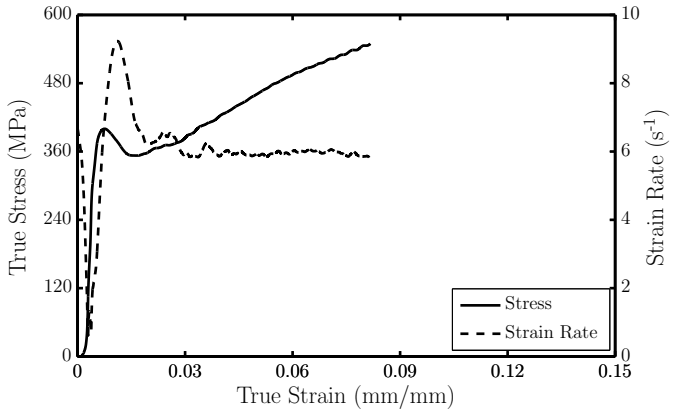

(a) Steel

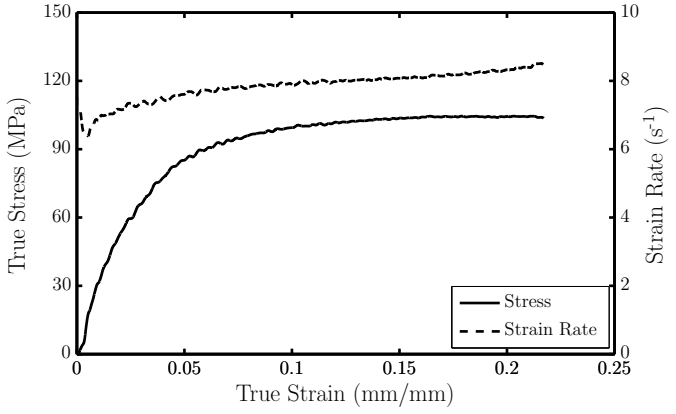

(b) Nylon

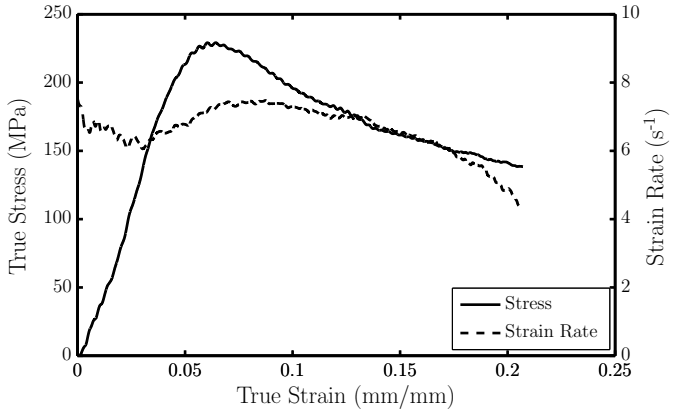

(c) PMMA

Figure 5.8: Typical strain rate histories for steel, nylon and PMMA

5.3 Interrupted Tests

One of the advantages of the IST is that it uses impact principles to start and stop the experiment. The advantage of starting the experiment with impact principles is that yield stress can be captured at testing speed. The advantage of stopping the experiment rapidly using impact principles is that the specimen can be recovered. This makes it possible to do interrupted tests. During the interrupted tests, 5 tests are performed to strain the specimen to between 20% and 25% strain. After each test the specimen is measured and lubricated. Therefore, the specimen is lubricated 5 times while while straining the specimen to the equivalent of one "standard" test. This reduces the specimen friction present and is useful for investigating the friction present in a standard test. The results from the interrupted tests are compared to the QS compression tests, SHPB tests and a continuous IST test. The results for the individual tests are shown in Appendix A, Section A.3.1 and Section A.3.3.

5.3.1 Copper Tests

The results for the first set of interrupted copper tests are shown in Figure 5.9. The first incremental test in the series performed as expected, following the IST results closely. Subsequent tests show a drop in flow stress between the interrupted tests and the standard IST test. The reduction in flow stress increases with increasing strain. Although the interrupted tests reduce the specimen friction the results still lies above the SHPB results. This indicates significant friction is still present. It is expected that the jump in stress in the third test is caused by inadequate lubrication of the specimen resulting in increased specimen friction effects during the test.

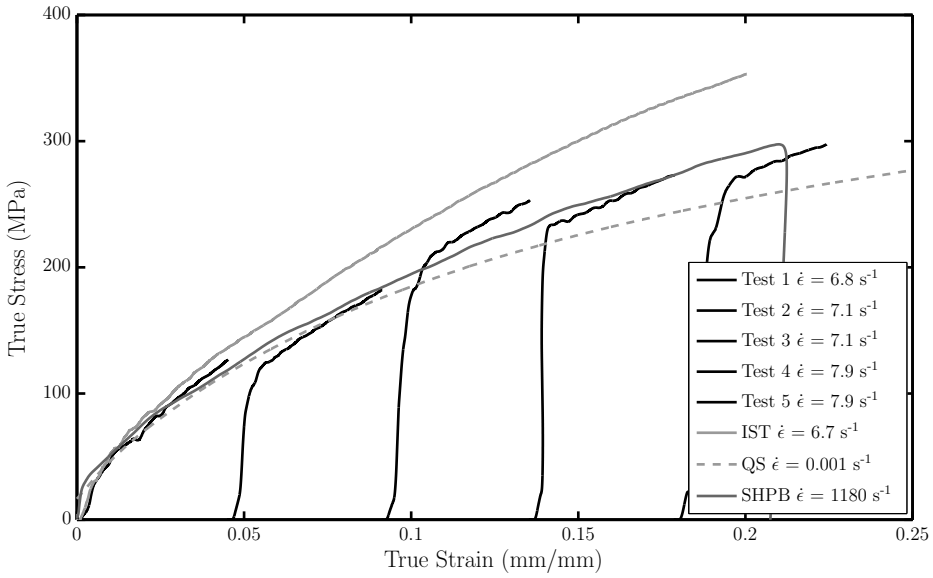

Figure 5.9: Interrupted copper, grease lubrication test

Initially the wedge bar was lubricated using Spanjaard RB2 grease. As the grease took a long time to apply to the wedge bar it was decided to investigate using 15W40 motor oil to lubricate the wedge bar. This cuts down the time taken to lubricate the bar allowing lubrication to be applied before each test. The results for the second set of interrupted tests using 15W40 motor oil to lubricate the wedge bar are shown in Figure 5.10.

The flow stress measured during the interrupted tests dropped significantly compared to the individual tests. These results indicate that the friction effects dominate the specimen response for the copper specimens at large strains. However, these results also show the interrupted tests provide an effective, although time consuming way to lower the specimen friction effects present.

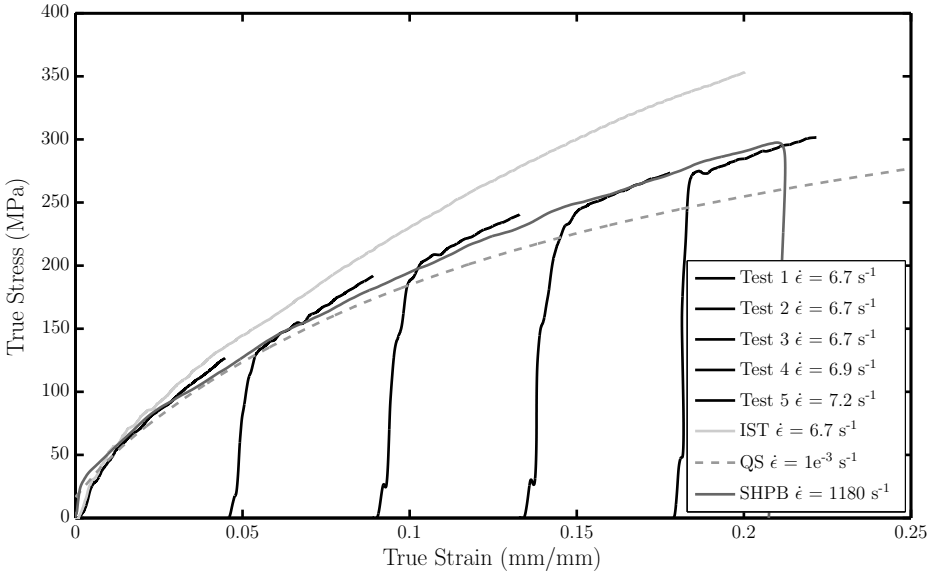

Figure 5.10: Interrupted copper, 15W-40 motor oil lubrication test

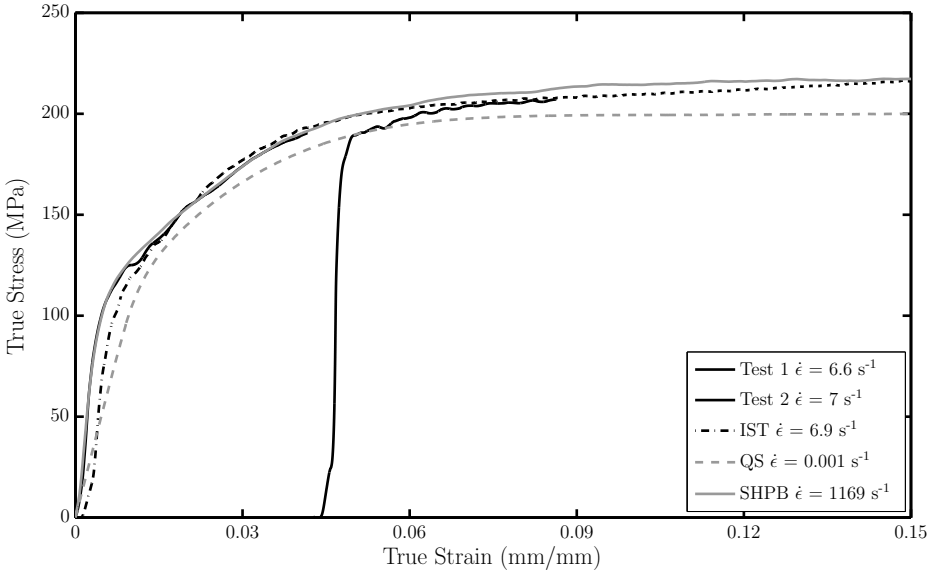

Figure 5.11: Interrupted aluminium, 15W-40 Motor oil lubrication

5.3.2 Aluminium Tests

The results for the interrupted aluminium tests are shown in Figure 5.11. The interrupted tests closely match the IST results indicating friction is not significant over the initial 10% of the experiment for aluminium.

5.4 Loading Platform Comparison

The FEA results presented in Section 3.3.6 show the loading platform used has a significant effect on the specimen response. The FEA simulations show that partial specimen unloading occurs in the plastic portion of the experiment when the unbalanced loading platform is used but not when the balanced loading platform is used. The tests presented in this section are performed to investigate if this behaviour is visible in the experimental results.

A comparison between the balanced and unbalanced loading platform is shown in Figure 5.12. The global response for the balanced and unbalanced loading platforms is nearly identical, as shown in Figure 5.12(a). Four of the six results match closely, one of the unbalanced loading platform results falls higher than the average and one of the balanced loading platform results falls below the average. However, a close up of the elastic region shows balanced loading platform significantly reduces the magnitude and duration of the partial unloading that occurs at the start of the tests, see Figure 5.12(b).

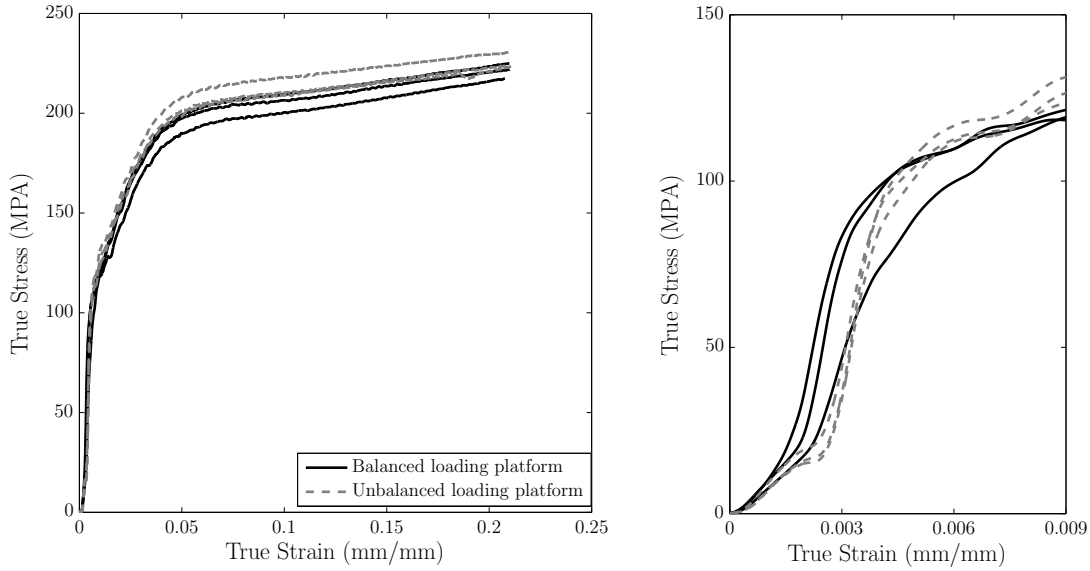

(a) Global response

(b) Elastic response

Figure 5.12: Loading platform comparison

5.5 Effects of Specimen Pre-Load

As discussed previously, tests can be performed with or without specimen preload applied. When no preload is required a small gap can be left between the specimen and the load-cell allowing the wedge bar to accelerate up to testing speed before the start of the experiment. This gap is necessary for the back pressure driven experiments, but is optional for the impact driven experiments. The comparison between the two is done to determine the preferred loading method for impact driven tests and to investigate the effect the lack of preload will have on the back pressure driven tests.

The effect that preload has on the global response of the specimen is shown in Figure 5.13(a). The specimen tested without preload all show a lower elastic modulus and flow stress than the specimens tested with preload. The lower modulus is expected. Additional play in the system is taken up over the initial portion of the experiment as the wedge bar seats against the loading platform. The flow

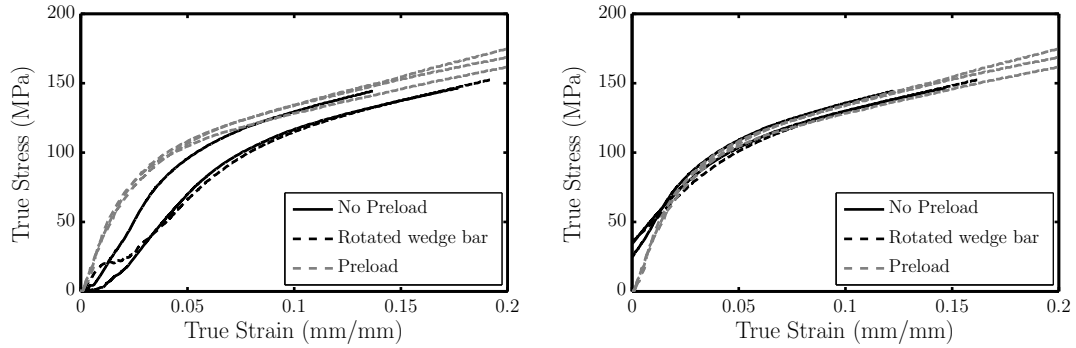

(a) Global response (b) Shifted Results

Figure 5.13: Effect of preload on the global response

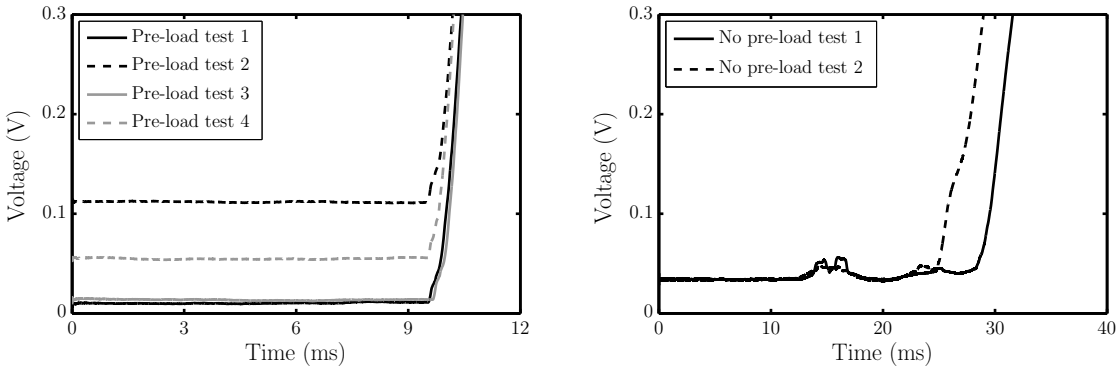

(a) Specimen with preload (b) Specimen without preload

Figure 5.14: The effect of preload on the start of the experiment

stress matches closely over the remainder of the experiment once the tests without preload are shifted to correct for the lower modulus over the initial portion of the experiment, see Figure 5.13(b).

The results showing the raw signals for the initial portion of the tests performed with and without specimen preload are shown in Figure 5.14(a) and Figure 5.14(b). The results for the tests performed without specimen preload contained oscillations on the force signals before the start of the experiment. The wedge bar is free to rotate before it makes contact with the loading platform. It is expected that the wedge bar was slightly rotationally misaligned relative to the loading platform and that the oscillations are caused by the wedge bar seating itself against the loading platform. To test this theory, the wedge bar was intentionally rotated for the next test. The results shown in Figure 5.15 show that the magnitude of the oscillations increase for the test with the rotated wedge bar. This result is viewed as confirmation that the rotational misalignment of the wedge bar is responsible for the oscillations seen on the force signals before the start of the experiment.

5.6 Back Pressure Driven Experiments

The results for an aluminium specimen tested using the back pressure driven loading is shown in Figure 5.16. From the start of the experiment at $\epsilon = 0.04$ to the end of the experiment the strain rate remains reasonably constant between 3 to 3.6 s^{-1}. This is a significant reduction in the strain rate compared to the impact driven experiments. It is expected that the slight rise in stress seen between $\epsilon = 0.02$ to 0.04 is caused by the wedge bar seating itself against the loading platform, as discussed in more detail in Section 5.5.

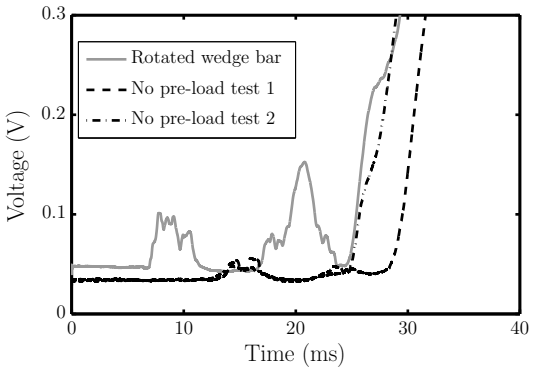

Figure 5.15: The effect of wedge bar alignment during a soft start experiment

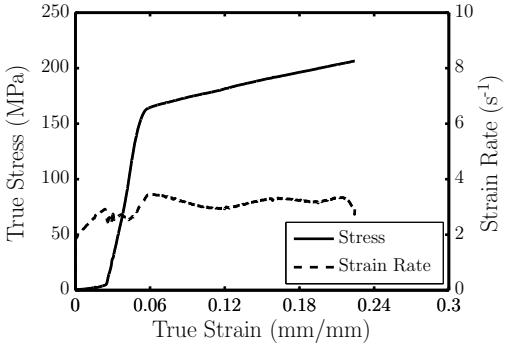

Figure 5.16: Back pressure driven experiment, aluminium specimen

5.7 High Speed Camera Footage

The high speed camera footage is used to check for any unexpected behaviour during an experiment. The unbalanced loading platforms and copper specimen are used for the high speed camera test. The results of the test are shown in Figures 5.17, 5.18 and 5.19, a full set of the frames extracted from the high speed camera footage is shown in Appendix B. The movement of the IST can be seen by comparing the vertical grid line to the position of the load-frame. The labels a to o in Figure 5.17 indicate the times of frames a to o in Figures 5.18 and Figure 5.19. The high speed footage again shows that the loading platform remains in contact with the wedge bar over the duration of the experiment. The wedge bar is in motion from t = 8.4 to 45 ms. During this period the flow stress of the specimen, and hence the friction force acting between the wedge bar and load-frame, increases. As the friction force acting on the load-frame increases, the load-frame deflects further backwards as shown in frames a to g in Figure 5.17. The wedge bar strikes the stopper bar at 45 ms. After this point the wedge bar is stationary relative to the load-frame, but the two oscillate backwards and forwards together.

The movement seen in the high speed camera footage, frames h to o in Figure 5.19, corresponds to the movement seen on the ROS signal in points h to o in Figure 5.17. This movement is taking place in the SHPB mounting bracket used to attach the backing plate and load-frame to the I-beam. The SHPB mounts are not designed to resist high axial forces. This movement could explain the reduction in specimen stress seen after the termination of the experiment to be discussed in Section 6.10.

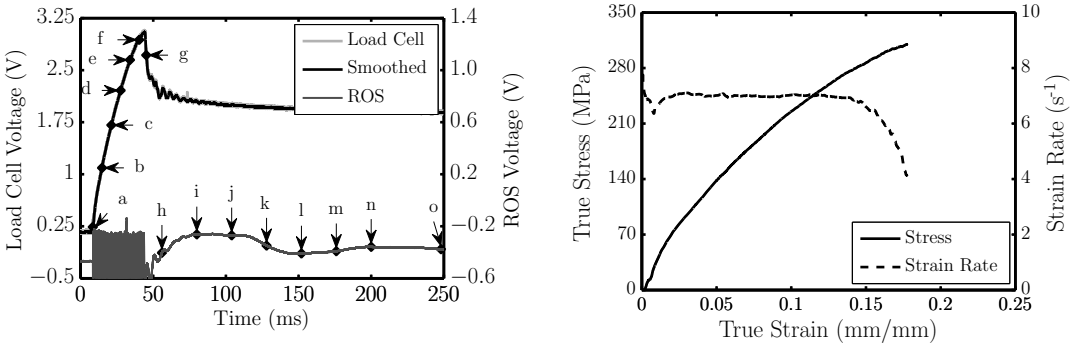

(a) Raw data (b) Stress and strain rate vs. strain

Figure 5.17: High speed camera test, copper specimen

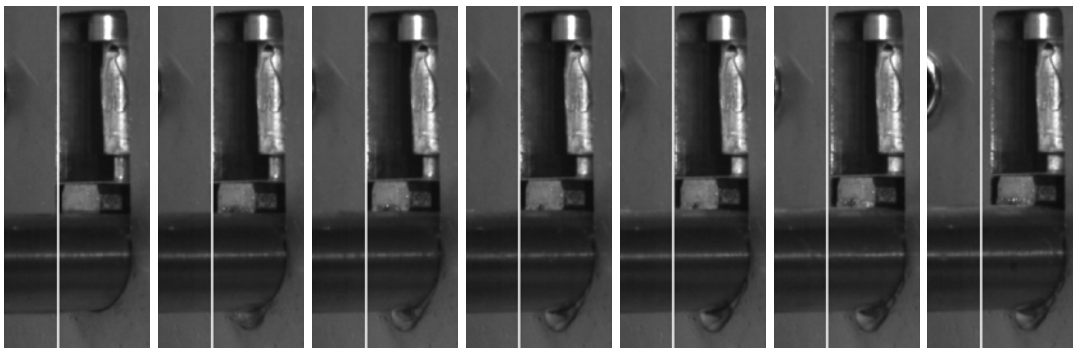

(a) t=8.4ms (b) t=14.8ms (c) t=21.2ms (d) t=27.6ms (e) t=34ms (f) t=40.4ms (g) t=45.2ms

Figure 5.18: High speed camera results during experiment

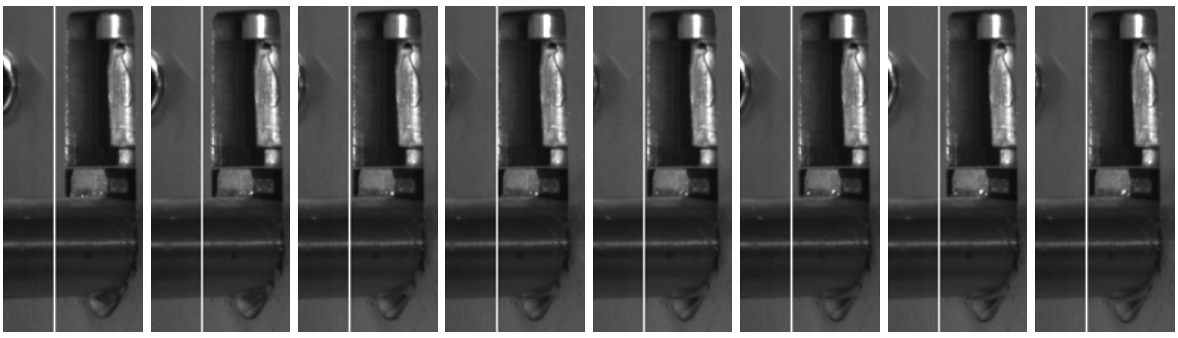

(h) t=56ms (i) t=80ms (j) t=104ms (k) t=128ms (l) t=152ms (m) t=176ms (n) t=200ms (o) t=248ms

Figure 5.19: High speed camera results after termination

Chapter 6

Discussion of Results

The results from Section 5 are discussed in more detail in this chapter. First, the benchmark test results are compared with the data found in the literature to benchmark the performance of the IST. A comparison between the IST results presented by Cloete and Oxtoby and the new IST is then presented to show the effects the modifications have made. Following this the additional analysis of the IST results is presented.

6.1 Comparison of Results

The QS, ISR and SHPB test results are compared to published data in the literature to benchmark the performance of the IST. Intermediate strain rate data is scarce for all the materials tested. However, the most data was found for mild steel. These results are presented first, followed by the other metals and finally the polymers.

6.1.1 Mild Steel

A comparison of the mild steel test results with the results found in literature is shown in Figure 6.1. The QS and ISR test data agrees well with the results from literature, while the SHPB results lie slightly lower than average, but still within the range of the data in the literature.

6.1.2 Aluminium

As expected, the results found in literature for different aluminium alloys with different temper vary significantly, as is shown in Section 2.1.2. Due to the limited amount of intermediate strain rate data available in the literature it is not possible to find data for the same alloy and temper. The test results are therefore compared to results which presented with comparable QS properties. The results presented by Smerd et al [21] for aluminium AA5754 at T79 temper as well as the results presented by Cloete and Oxtoby [1] are used for comparison and shown in Figure 6.2.

The rate sensitivity of the annealed aluminium specimen compares well with the results presented by Smerd et al. [21]. The QS and SHPB data match closely with the IST data falling between the QS and SHPB data as expected. The results of the tests performed on the aluminium specimens remaining from Cloete and Oxtobys testing agree well with the results presented by Cloete and Oxtoby [1]. The results for Cloete and Oxtoby's specimens follow a similar trend to the annealed aluminium specimen despite being significantly softer. The rate sensitivity for the aluminium specimen tested is very mild.

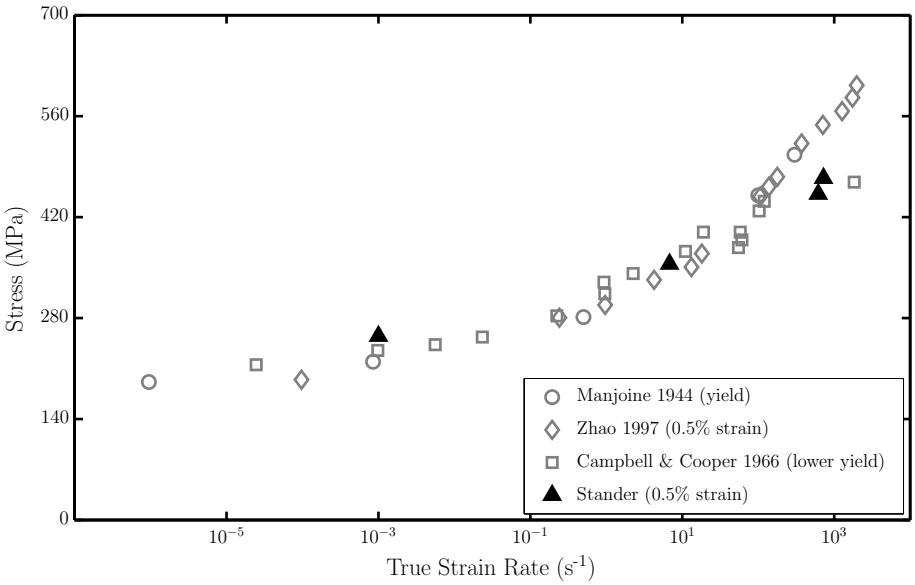

Figure 6.1: Rate effects for mild steel

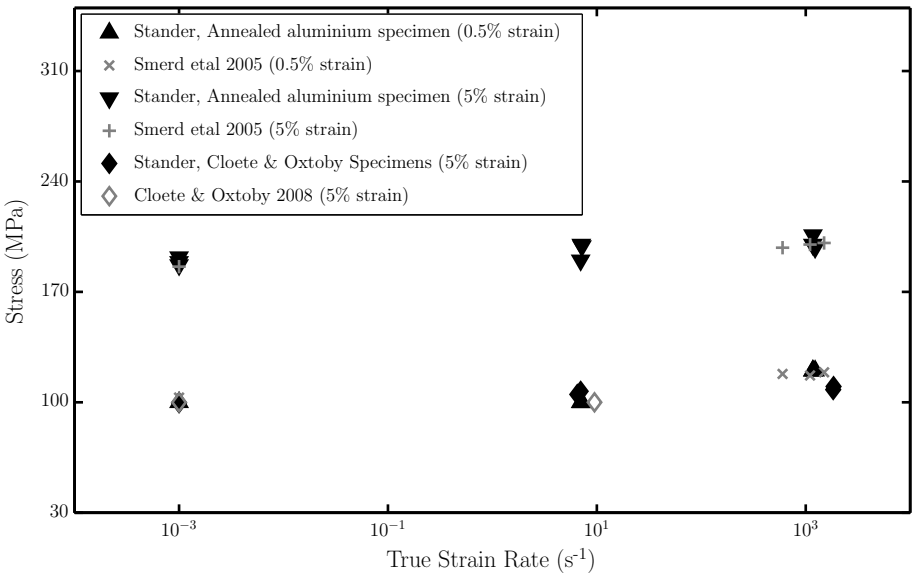

Figure 6.2: Rate effects for aluminium

6.1.3 Copper

A comparison of the copper test results with the results found in the literature is shown in Figure 6.3. The trends seen for the QS and SHPB tests data matches the results presented by Liang and Khan [23] well at both 5% and 20% strain. However, the IST results for the copper specimen display larger than expected friction effects to the extent that the flow stress of the ISR tests is greater than for the SHPB tests. The measured stress is approximately 15% higher than expected at 5% strain and 20% higher than expected and 20% strain (assuming a rate sensitivity similar to that reported by Liang and Khan [23]). Referring back to Figure 2.39 this equates to a friction factor of between m = 0.35 and m = 0.4 which is approximately twice the values found in literature for lubricated copper [42]. Possible explanations for this are discussed in more detail in Section 6.8.

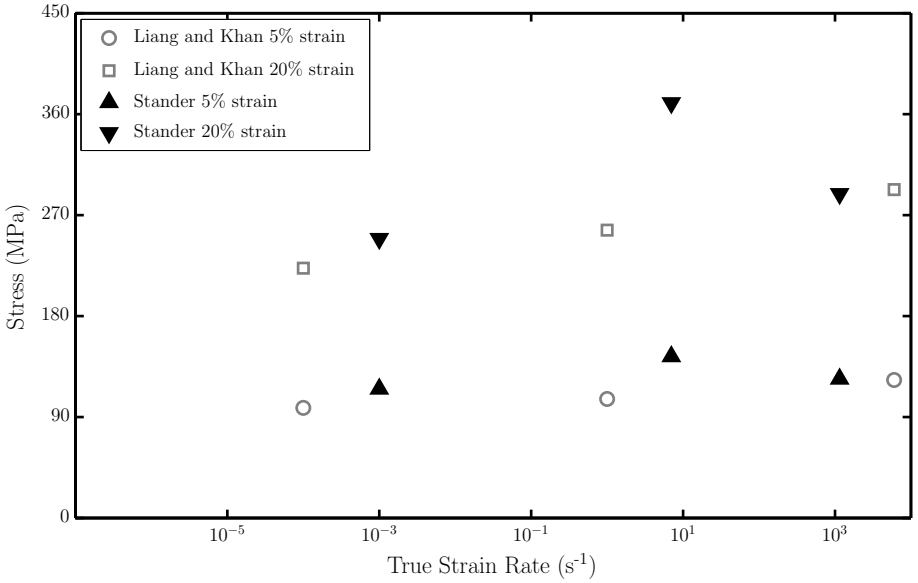

Figure 6.3: Rate effects for copper

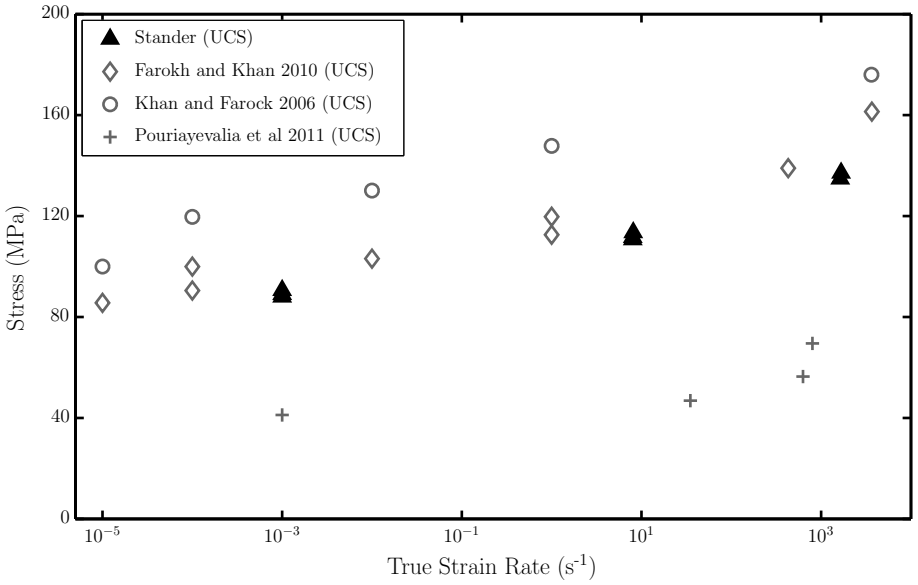

Figure 6.4: Rate effects for nylon

6.1.4 Nylon

A comparison of the nylon test results with the results found in the literature is shown in Figure 6.4. The IST results for UCS agree well with the results presented by Farrokh and Khan [28], while the results presented by Khan and Farrokh [29], lie slightly higher. However, the rate hardening seen is consistent between these three data sets. The results presented by Pouriayevali [30] for nylon 6 lie significantly lower, but exhibit similar rate hardening effects.

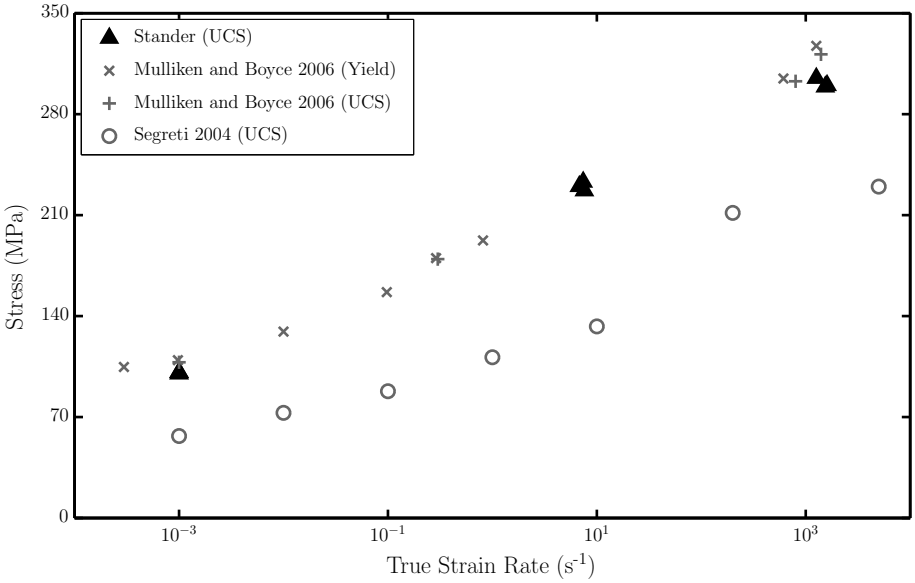

Figure 6.5: Rate effects for PMMA

6.1.5 PMMA

A comparison of the PMMA test results with the results found in the literature is shown in Figure 6.5. The test results match very closely with the results presented by Mulliken and Boyce [27]. The UCS increases linearly with the log of the strain rate. The results presented by Segreti et al.[26] fell significantly lower than the results presented by Mulliken and Boyce [27] but shows similar rate hardening effects.

6.1.6 Conclusions

The intermediate strain rate data presented match the results found in the literature well for all materials tested except the copper specimen, which presented with unusually high friction effects. The good correlation between the IST results and the results found in literature provide confidence in the IST results.

6.2 Old vs. New IST

The initial tests are done using specimen remaining from the work presented by Cloete and Oxtoby [1]. Comparing these results with the ones presented by Cloete and Oxtoby [1] is helpful to demonstrate the impact the design modifications have on the performance of the IST. Comparing the raw signals shown in Figures 4.5(a) and 2.36 shows the raw data from the new load-frame contains significantly less high and low frequency noise. The processed stress strain curves for the new load-frame shows a significant improvement in both the amount of high frequency noise and low frequency oscillations on the measured signal. The IST data matches the QS and SHPB data well over the initial portion of the experiment. However, friction effects begin to dominate the specimen response as the strain increases over the latter portion of the experiment.

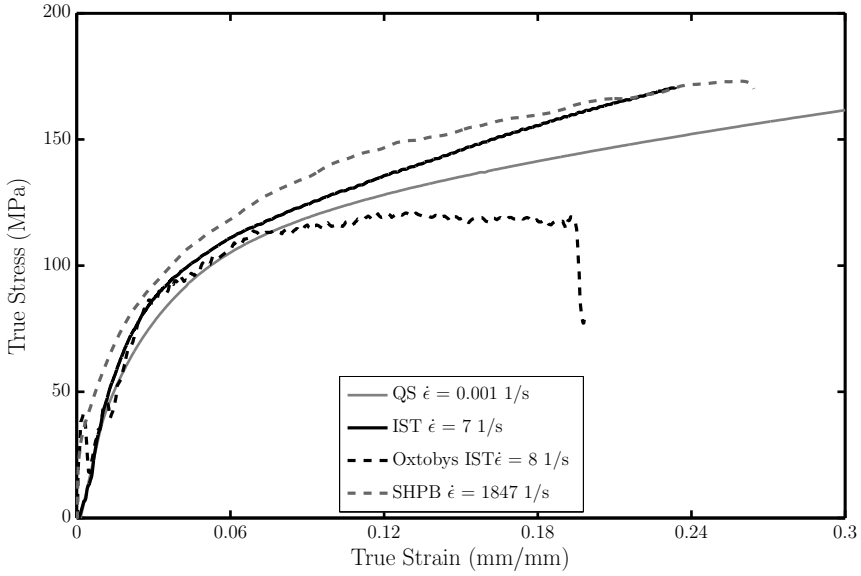

Figure 6.6: Comparison of results from the old and new IST

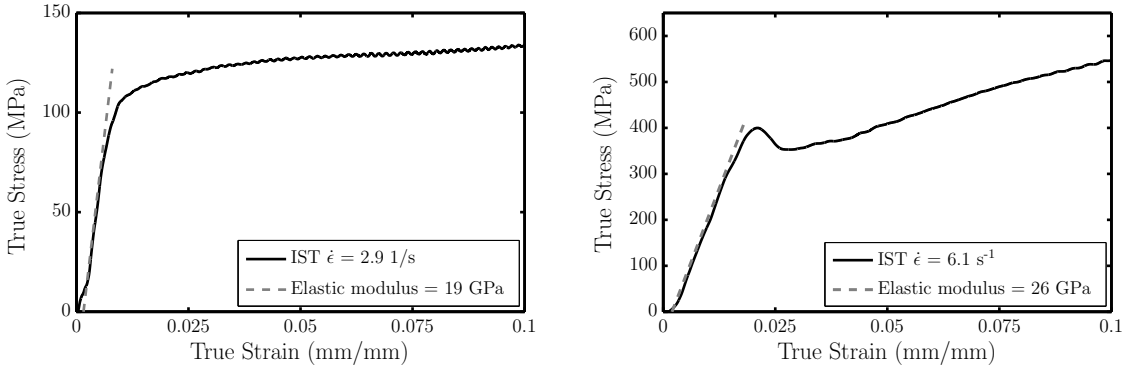

(a) Aluminium (b) Steel

6.3 Load Path Compliance

In Section 3.3.5 the stiffness of the load path is calculated to be 116 kN/mm based on the FEA results. In this section the same method is used to calculate the stiffness of the load path using the experimental results. On many of the tests it is difficult to determine the elastic modulus as the specimen are annealed and do not have a clearly defined elastic region. The results used in this analysis display a clearly defined elastic modulus, as shown in Figure 6.7(a) and Figure 6.7(b). The aluminium specimen was strained to 15% strain, before being re-measured and checked to ensure the sides remained parallel, while the steel specimen display a clearly defined elastic region.

The stiffness of the load path is calculated from the experimental results following the same procedure as described in Section 3.3.5 using Equation 3.6. The apparent modulus measured off the experimental results for the aluminium and steel specimen are 19 GPa and 26 GPa respectively. The material modulus used in this analysis for the test specimens is taken from the literature, 70 GPa for the aluminium and 200 GPA for the Steel. For the aluminium specimen the stiffness of the load-path is calculated as follows

$$
\begin{aligned}
k_{IST} &= \left(\frac{l_s}{A_s E_m} - \frac{l_s}{A_s E_s} \right)^{-1} \\
k_{IST} &= \left(\frac{0.0047}{\frac{\pi * 0.005^2}{4} \times 19 \times 10^9} - \frac{0.0047}{\frac{\pi * 0.005^2}{4} 70 \times 10^9} \right)^{-1} \\
k_{IST} &= 109 \times 10^6 \ N/m = 109 \ kN/mm
\end{aligned}
\tag{6.1}
$$

For the steel specimen the stiffness of the load-path is calculated as follows

$$
\begin{aligned}
k_{IST} &= \left(\frac{l_s}{A_s E_m} - \frac{l_s}{A_s E_s} \right)^{-1} \\
k_{IST} &= \left(\frac{0.0053}{\frac{\pi * 0.005^2}{4} \times 26 \times 10^9} - \frac{0.0053}{\frac{\pi * 0.005^2}{4} 200 \times 10^9} \right)^{-1} \\
k_{IST} &= 108 \times 10^6 \ N/m = 108 \ kN/mm
\end{aligned}
\tag{6.2}
$$

These results compare well the FEA value of 116 kN/mm. The slightly lower stiffness calculated from the experimental results is due to the FEA simulations not including the shims used to position the specimen or the grease used for lubrication on the wedge bar and the specimen. The value of 108 kN/m is used for correcting the calculated specimen displacement.

The analytical value calculated for the load path compliance is 194 kN/mm, see Appendix D.3. This is nearly twice the value obtained using the FEA and experimental results. It is expected that the most likely source of this difference is that flexing occurs in the shoulder that transfers force between the load-cell and load-frame. However, more investigation is needed to confirm this.

6.4 Strain Rate History

The results shown in Table 5.7 and Table A.2 show the yield stress is repeatedly captured at up to 80% of the average strain rate of the test for the aluminium, nylon and copper specimens. This ratio drops off for materials with higher yield stress. This is not as good as initially hoped but could still be an improvement on the results found in the literature. As many of the authors do not provide strain rate histories, and those that do don't provide much detail as to how they are calculated, it is difficult to validate this.

As shown in Section 4.5.2 and Section 5.2, the initial dip in strain rate is proportional to the force measured at yield point and the compliance of the IST. Therefore, all else remaining constant, the compliance will need to be doubled to result in a 50% reduction in the dip in strain rate seen over the elastic portion of the experiment.

Alternatively, lowering the force measured at yield by reducing the cross sectional area of the specimens will also limit the deflection of the load path and reduce the drop in strain rate seen over the elastic region. Reducing the specimen diameter from 5 mm to 4 mm will result in a 36% reduction in the force measured at yield. As the relationship between force and deflection of the load path is assumed linear, this should result in a 36% reduction in the drop in strain rate seen over the elastic region. Developing a tensile configuration of the IST will allow very slender specimen to be used. This should further reduce the drop in strain rate seen over the elastic region.

For most of the tests performed, the strain rate history is reasonably constant over the plastic portion of the experiment. For these tests, as the specimen is compressed and gets shorter, the velocity of the wedge bar decreases due to the friction forces acting on the wedge bar. When these two factors balance each other out the result is a near constant strain rate over the plastic portion of the experiment. However, for most of the interrupted tests and the nylon tests the strain rate increased gradually over the experiment. This can be avoided in future tests by developing a mechanism to add friction to the wedge bar in a controlled manner to ensure it slows down sufficiently to compensate for the shortening of the specimen.

6.5 Effects of Specimen Pre-Load

The results presented in Section 5.5 show that tests performed without specimen pre-load results in lower modulus measurement as well as increased low frequency oscillations on the measured signal over the initial portion of the experiment. The oscillations are attributed to the wedge bar being rotationally misaligned relative to the loading platform. If tests without specimen pre-load are required, for example when back pressure driven loading is used, a method of restraining wedge bar rotation should be developed to ensure the wedge bar remains aligned to the loading platform as it is accelerated up to testing speed.

6.6 Back Pressure Driven Experiments

In its current configuration, the back pressure loading allows the strain rate to be dropped from a strain rate of 7 s^{-1} to 3 s^{-1} while maintaining a reasonably constant strain rate. At these rates there will be a significant drop off in strain rate over the duration of the experiment when using impact driven loading. As well as lowering the minimum achievable strain rate, the back pressure driven loading could also be useful when testing at higher strain rates when testing high strength materials such as steel. The driving force supplied by the back pressure loading will help overcome the friction forces and limit the change in loading velocity over the experiment.

The back pressure configuration consists of a nylon piston attached to the back of the wedge bar which is inserted into the gas gun barrel. This worked well to show the potential of the system, as shown in Section 5.6. However, air leaked around the piston reducing the driving force available. As a result, trial and error is needed to set the run up distance and the gas gun pressure required for the experiments. Further development work will be required before the back pressure driven loading is suitable for routine testing, which is outside the scope of this project.

6.7 Finite Element Analysis

The FEA was done to investigate the dynamic response of the IST and use these results to fine tune the design. The first design change implemented, due to the FEA results, was to increase the number of bolts attaching the load-frame to backing plate from two to four. The FEA results show that unloading occurs during the elastic portion of the test when the load-frame is attached to the backing plate using two bolts. The unloading reduces when four bolts are used to attach the load-frame to the mounting plate, as shown in Figure 3.10. This analysis also shows that movement in the load-frame can result in unloading in the specimen at the start of the experiment, and increasing the rigidity of the load-frame can reduce the unloading seen.

The unloading in the elastic portion of the experiment is seen in the experimental results for the annealed aluminium, annealed steel and interrupted copper tests but to a lower degree than predicted by the FEA for the impact driven tests. The HPB mount's rigidity varies depending on the torque

applied to the bolts used to attach the mounts to the I-beam. This explains why the unloading during the elastic region is seen in some of the experiments and not in others.

The FEA correctly shows that the balanced loading platform reduces the duration and magnitude of the specimen unloading during the elastic portion of the experiment, as shown in Figure 5.12. The experimental results show that during the elastic region the IST deviated less from the material response than predicted by the FEA.

6.8 Friction in the IST

Artificial hardening of the specimen due to friction between the specimen and loading surfaces is significant for the metals tested. For the copper and steel tests the specimen friction dominates the specimen response from shortly after the yield point. The friction factor required to explain the increase in flow stress seen in the copper specimen is significantly higher than those presented in the literature. Friction effects are noticeable for the aluminium tests but to a lesser extent. Approximate friction factors for the aluminium tests are within the range of results presented in the literature.

The high friction present when testing metals limits the maximum usable strain measurement of the IST. However, the large strain behaviour of metals can still be investigated by performing interrupted tests. The friction effects appear to be negligible for the polymers tested, as the UCS agrees well with the results found in the literature.

It is expected that the higher friction seen in the IST compared to the SHPB is due to the longer testing duration. The ISR tests are in the order of 100 times longer than the SHPB tests. This allows more time for the lubrication to be forced out from between the specimen and loading surfaces. As the lubrication escapes, the friction effects increase. The interrupted copper tests show that the friction effects decrease due to the specimen being re-lubricated after each test.

Despite the limitations caused by specimen friction effects, IST is well-suited for testing polymers, capturing yield stress and small strain measurement in metals and testing quasi-brittle materials where friction is expected to be insignificant. Alternatively, the development of a tensile configuration will alleviate the problems with friction completely.

6.9 Impulse Unloading of the IST

After the termination of the experiment, oscillations are visible on many of the load-cell signals and some of the ROS signals. An example is shown in Figure 6.7 and the full set of results is presented in Appendix A.3. During the experiment the frictional force the wedge bar exerts on the load-frame increases gradually as the flow stress of the specimen increases. This results in the IST gradually deflecting backwards over the duration of the experiment, as shown in the high speed camera footage in Section 5.7. This friction force is in the range of 2 kN for a specimen stress of 500 MPa.

However, when the wedge bar impacts the stopper bar it comes to a stop in approximately 0.4 ms. Once the wedge bar is stationary, the frictional force acting on the IST (which caused the initial deflection) reduces to zero. This rapid or impulse unloading of the IST causes the IST to oscillate backwards and forwards slightly after the experiment. This movement is not visible with the naked eye but is visible on the high speed camera footage and also presents as oscillations in the ROS and load-cell signal after the experiment has been stopped. This is shown in Figure 6.7[1]. Note that the oscillations in the signals from the ROS and load-cell seem to coincide. Increasing the stiffness of the load-frame mounts will limit the movement of the load-frame during the experiment and reduce the oscillations seen after the termination of the experiment.

[1] The original results can be seen in Figure A.20

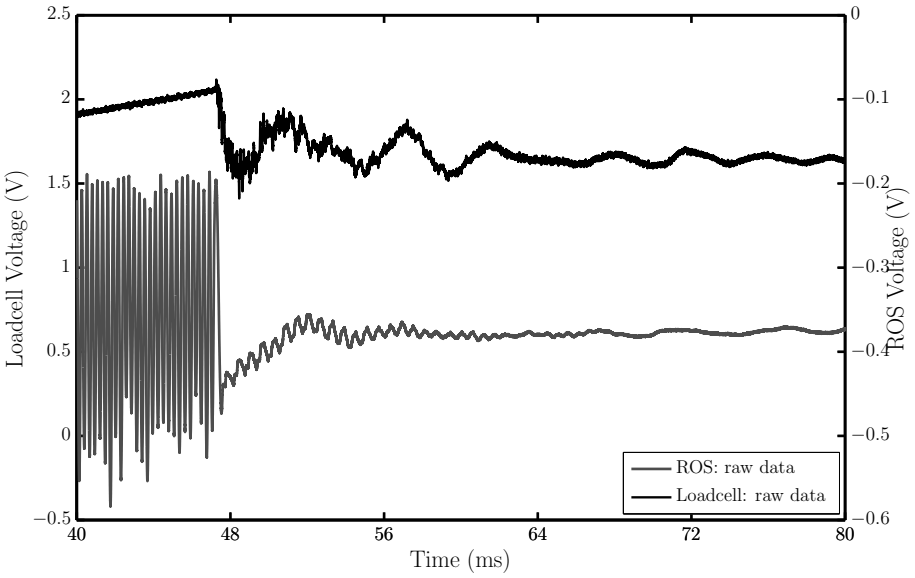

Figure 6.7: Impulse unloading at the end of the experiment. Note the correlation between the oscillations in the load-cell signals and ROS signals

Table 6.1: Post experiment specimen unloading

Material	Unloading $\left(\frac{\sigma_u}{\sigma_e}\right)$
Annealed Aluminium	68.9
Annealed Copper	71.9
Annealed Steel	68.7

6.10 Post Experiment Unloading

The raw data for the ISR tests presented in Appendix A.3 shows that the force measured in the load-cell drops off after the experiment. A typical example for a test of a copper specimen is shown in Figure 6.8(a). The degree of unloading seen varies for the different materials tested. The ratio of the unloaded stress(σ_u) to stress at the end of the experiment(σ_e) for aluminium, copper and mild steel is shown in Table 6.1.

It was initially thought that this drop in stress could be the result of the wedge bar rebounding slightly at the end of the experiment. To determine if the wedge bar had rebounded, the direction of motion of the wedge bar is checked by using the second ROS as discussed in Section 3.4.6. This analysis shows that the wedge bar does not rebound at the end of the experiment, as is also confirmed by the high speed camera footage shown in Section 5.7.

The second cause of unloading investigated relates to the friction component of the measured force. Once the wedge bar is stationary and the specimen is no longer being compressed and expanding radially, the friction component of the measured stress should disappear. The unloaded stress measured in the specimen after the wedge bar is stopped is shown in Figure 6.8. The stress at the end of the experiment is 1.4 times greater than the unloaded stress. The unloaded stress falls nicely between the QS and SHPB test results. However, using equation 2.1, the friction factor (m) required to give $\frac{P_{ave}}{\sigma_y} = 1.4$ is 1. This is more than three times greater than the friction factor of m = 0.28 reported by Hartley et al. [42] for dry copper. For this reason it is expected that the "release" of the friction effects can only be partially responsible for the specimen unloading seen.

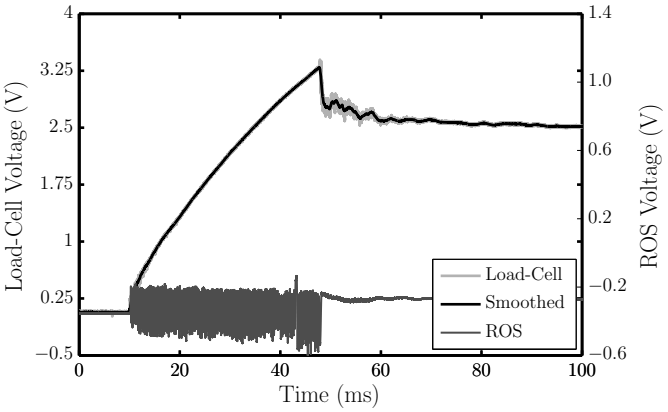

(a) Raw data

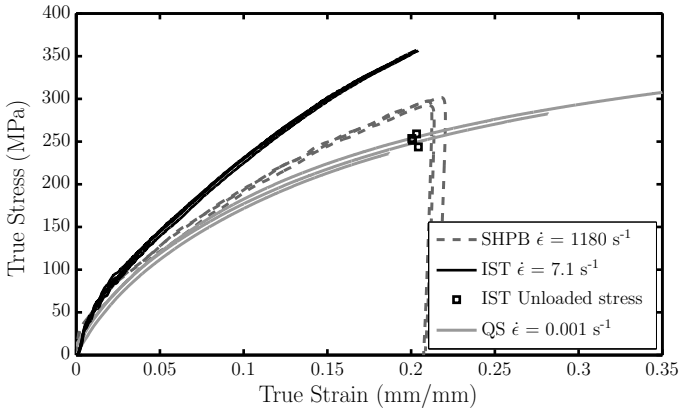

(b) Stress and strain rate vs. strain

Figure 6.8: Annealed copper

The final cause of the unloading investigated is linked to the load-frame deflection during the experiment. It is expected that as the load-frame deflects backwards during the experiment the wedge bar rotates slightly, relative to the load-frame, as shown in Figure 6.9. As the rotation takes place, the distance between the load-cell and wedge bar is shortened. Once the experiment is stopped the wedge bar returns to being perpendicular to the load-frame, allowing the specimen to relax slightly. As the specimen unloads along the elastic modulus, a displacement of only 3 µm will result in the 30% unloading seen in the copper specimen[2]. A rotation of only 0.02 degrees between the load-frame and wedge bar will result in this deflection.

It is expected that the specimen unloading seen in the IST results is a combination of the friction effects being dissipated after the experiment and the wedge bar rotating slightly, relative to the load-frame. However, it is not possible to quantify the contribution of each. As with the impulse unloading of the specimen described in Section 6.9, this analysis highlights the problems caused by the SHPB mountings used for the IST. As the deflections due to the rotation of the load-frame are in the order of microns, this has nearly no impact on the strain measurements. The total displacement of the specimen is in the order of 1 mm, 3 µm is only 0.3% of the total displacement.

[2]This is calculated substituting an elastic modulus of 128 GPa, specimen unloading of $\sigma = 100$ MPa and a final specimen length L = 4 mm into $E = \frac{\sigma}{\epsilon}$ and rearranging for $\delta l = \frac{\sigma L}{E}$

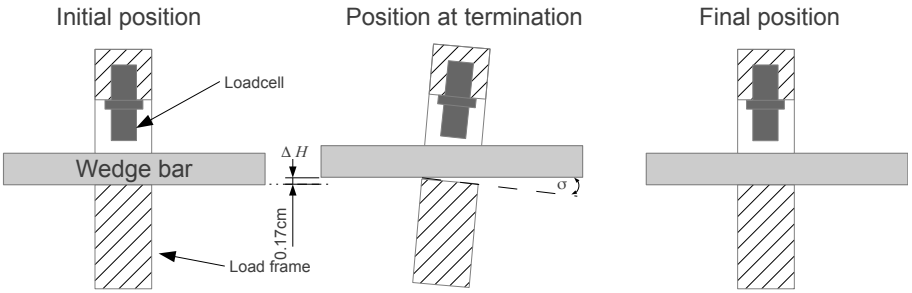

Figure 6.9: Load-frame deflection

6.11 ROS Displacement Measurements

The distance between the wedge bar and stopper bar is accurately set for each test performed. For standard tests of approximately 20% strain, the offset distance is set to 300 mm by placing a 300 mm steel ruler between the wedge bar and stopper bar. For the interrupted tests the offset distance is set using vernier callipers. The displacement measured from the ROS is then compared to the set displacement giving an indication of the accuracy of the displacement measurement.

The full set of results comparing the calculated to actual wedge bar displacement for each test performed is given in Table A.1. On average, the calculated wedge bar displacement is 1.2 mm less than the distance between the wedge bar and the stopper bar which is only 0.6% of the total displacement measured. This is within the resolution of the ROS. One test over-predicted the wedge bar displacement by 5 mm and 2 tests under-predicted by 3 mm. All other tests are within the resolution of the ROS.

A comparison between the final specimen length measured and the specimen length calculated from the wedge bar displacement is shown in Table 6.2 for the metal specimen. A negative value for the error indicates the specimen is shorter than predicted based on the wedge bar displacement.

For most of the tests the final measured length of the specimen is between 10% and 15% shorter than calculated, based on the wedge bar displacement. It is interesting to note that the error is significantly less for the interrupted tests. It is not expected that this is a load-frame compliance problem. If it was a compliance problem, the error in the small displacement measurements would be greater than for the large displacement measurements. It is expected that this deformation takes place after the experiment as the wedge bar and IST oscillate back and forth due to the impulse unloading of the IST. This is consistent with the smaller error seen in the interrupted tests. The friction between the wedge bar and load-frame is greatly reduced due to the smaller strain measurements and the re-lubrication of the wedge bar for each experiment. This reduces the magnitude of the impulse unloading at the end of the experiment. This will result in less back and forth movement after the experiment, resulting in less chance to further deform the specimen.

Table 6.2: Calculated vs. measured final specimen length

Test	Measured Length (mm)	Calculated Length (mm)	Error (mm)	Error (%)
Annealed Aluminium 1	3.62	3.78	-0.16	-12.33
Annealed Aluminium 2	3.63	3.8	-0.17	-12.49
Annealed Aluminium 3	3.63	3.79	-0.16	-11.97
Annealed Aluminium 4	3.69	3.87	-0.18	-13.09
Copper 1	3.74	3.93	-0.19	-14.18
Copper 2	3.64	3.85	-0.21	-15.61
Copper 3	3.69	3.89	-0.2	-14.7
Copper 4	3.64	3.82	-0.18	-13.37
Annealed Steel	4.8	4.84	-0.04	-7.06
Interrupted Copper 1 (1 of 5)	4.75	4.76	-0.01	-4.59
Interrupted Copper 1 (2 of 5)	4.49	4.51	-0.02	-6.68
Interrupted Copper 1 (3 of 5)	4.27	4.26	0.001	.36
Interrupted Copper 1 (4 of 5)	4.04	4.06	-0.01	-5.62
Interrupted Copper 1 (5 of 5)	3.83	3.83	-0.002	-.79
Interrupted Copper 2 (1 of 5)	4.82	4.82	-0.002	-.77
Interrupted Copper 2 (2 of 5)	4.56	4.56	-0.003	-1.26
Interrupted Copper 2 (3 of 5)	4.33	4.32	0.01	3.37
Interrupted Copper 2 (4 of 5)	4.12	4.11	0.01	2.88
Interrupted Copper 2 (5 of 5)	3.89	3.91	-0.02	-10.58

Chapter 7

Conclusions

The modifications made to the IST are successful. The new load-frame and load-cell results in a significant improvement in the quality of the measured signals. The wedge bar displacement sensor performed as expected, repeatedly performing within the design resolution of 2 mm. In addition, the strain rate histories obtained are reasonably constant with yield stress captured at above 80% of average strain rate for the majority of the materials tested.

In its current configuration the IST is suitable for testing specimen with lower friction factors, such as the polymers tested. These materials can be tested to large strain without specimen friction obscuring the specimen response. In addition, the ability of the IST to accelerate rapidly up to testing speed makes it suitable for testing quasi brittle materials which fracture at small strain, such as bone. Although friction effects dominate the specimen response of metals at large strains, the IST can be used for yield stress and small strain measurement. The maximum achievable strain for metals can be increased by using interrupted tests as the added lubrication helps reduce specimen friction effects.

A remaining flaw in the IST design is that the SHPB supports used to mount the IST to the I-beam can not carry the required axial load and this allows the load-frame to deflect backwards during testing. When the experiment is terminated, this leads to the impulse unloading of the IST which results in the load-frame oscillating back and forth after the experiment. This movement has been linked to the specimen unloading seen after the experiment and the discrepancy seen between the final measured specimen length and the calculated specimen length. However, this movement does not seem to affect the specimen displacement measurement during the experiment. These problems will be easily resolved by increasing the rigidity of the mounts used.

Chapter 8

Recommendations

- The SHPB mounts used to attach the load-frame to the testing bed should either be reinforced or redesigned to limit the deflection of the load-frame during testing.
- The development of a mechanism to pre-load the specimen at the beginning of the experiment and unload it afterwards, without moving the wedge bar, will make setting up and removing specimen after a test easier, specifically when testing metals.
- Reducing the specimen diameter from 5 mm to 4 mm will reduce the drop in strain rate seen in the elastic region by approximately 30%. In addition to this, developing a tensile IST will allow very slender specimen to be tested significantly reducing the drop in strain rate over the elastic region. A tensile configuration will also avoid the problem of high specimen friction faced with the metals tested.
- If the back pressure loading or testing without pre-load is required, some method of restraining the rotational movement of the wedge bar should be developed.
- If back pressure driven loading is required for routine testing, further work will need to be done on the pneumatic driving mechanism used to drive the wedge bar.

References

[1] Cloete, T. and Oxtoby, S. A new technique for compression tests at intermediate strain rates: Prototype results. In *DYMAT-International Conference on the Mechanical and Physical Behaviour of Materials under Dynamic Loading*, volume 1, pages 249–255. EDP Sciences, 2009.

[2] *Annual book of ASTM standards (03.01).* ASTM International, 2007.

[3] Sturges, J. L. and Cole, B. N. The flying wedge: A method for high-strain-rate tensile testing. part 1. reasons for its development and general description. *International Journal of Impact Engineering*, 25(3):251 – 264, 2001.

[4] Manjoine, M. J. and Nadai, A. High-speed tension tests at elevated temperatures. *ASTM*, 40:822–837, 1940.

[5] Gray, G. T. Classic split-hopkinson pressure bar technique. *ASM Volume 8 - Mechanical testing*, 8:1–36, 1999.

[6] Lindholm, U. S. Some experiments with the split hopkinson pressure bar*. *Journal of the Mechanics and Physics of Solids*, 12(5):317–335, 1964.

[7] Song, B., Chen, W. W., and Lu, W. Y. Mechanical characterization at intermediate strain rates for rate effects on an epoxy syntactic foam. *International Journal of Mechanical Sciences*, 49(12):1336–1343, 2007.

[8] Boyce, B. and Dilmore, M. The dynamic tensile behavior of tough, ultrahigh-strength steels at strain-rates from 0.0002 s-1 to 200 s-1. *International Journal of Impact Engineering*, 36(2):263–271, 2009.

[9] Othman, R., Guegan, P., Challita, G., Pasco, F., and LeBreton, D. A modified servo-hydraulic machine for testing at intermediate strain rates. *International Journal of Impact Engineering*, 36(3):460–467, 2009.

[10] Gilat, A. and Matrka, T. A. A new compression intermediate strain rate testing apparatus. *EPJ Web of Conferences*, 6:39002, 2010.

[11] Zhao, H. A constitutive model for metals over a large range of strain rates identification for mild-steel and aluminium sheets. *Materials Science and Engineering: A*, 230(1):95–99, 1997.

[12] Ouellet, S., Cronin, D., and Worswick, M. Compressive response of polymeric foams under quasi-static, medium and high strain rate conditions. *Polymer Testing*, 25(6):731–743, 2006.

[13] Ramo, J., Kuokkala, V. T., and Vuoristo, T. Influence of strain rate and adiabatic heating on the deformation behaviour of cold heading steels. *Journal of Materials Processing Technology*, 209(11):5186–5194, 2009.

[14] Groves, S. E., Sanchez, R. J., Lyon, R. E., and Brown, A. E. High strain rate effects for composite materials. *ASTM SPECIAL TECHNICAL PUBLICATION*, 1206:162–162, 1993.

[15] Shim, J. and Mohr, D. Using split hopkinson pressure bars to perform large strain compression tests on polyurea at low, intermediate and high strain rates. *International Journal of Impact Engineering*, 36(9):1116–1127, 2009.

[16] WESTHUIZEN, A. V. D. *The strain rate dependent properties and modelling of bovine cortical bone in compression.* Phd dissertation, University of Cape Town, 2008.

[17] Zhao, H. and Gary, G. The testing and behaviour modelling of sheet metals at strain rates from 10-4 to 104 s-1. *Materials Science and Engineering: A*, 207(1):46–50, 1996.

[18] Campbell, J. and Ferguson, W. The temperature and strain-rate dependence of the shear strength of mild steel. *Philosophical Magazine*, 21(169):63–82, 1970.

[19] Manjoine, M. J. Influence of rate of strain and temperature on yield stresses of mild steel. *Journal of applied mechanics*, 2:A 211–218, 1944.

[20] Dowling, A. and Harding, J. Tensile properties of mild steel under high strain rates. In *Proceedings of the 1st HERF Conf*, 1967.

[21] Smerd, R., Winkler, S., Salisbury, C., Worswick, M., Lloyd, D., and Finn, M. High strain rate tensile testing of automotive aluminum alloy sheet. *International Journal of Impact Engineering*, 32(1-4):541–560, 2005. Fifth International Symposium on Impact Engineering.

[22] Oosterkamp, L. D., Ivankovic, A., and Venizelos, G. High strain rate properties of selected aluminium alloys. *Materials Science and Engineering: A*, 278(1):225–235, 2000.

[23] Liang, R. and Khan, A. S. A critical review of experimental results and constitutive models for bcc and fcc metals over a wide range of strain rates and temperatures. *International Journal of Plasticity*, 15(9):963–980, 1999.

[24] Follansbee, P. High-strain-rate deformation of FCC metals and alloys. *Metallurgical applications of shock-wave and high-strain-rate phenomena*, pages 451–479, 1986.

[25] Tanner, A. B., McGinty, R. D., and McDowell, D. L. Modelling temperature and strain rate history effects in ofhc cu. *International Journal of Plasticity*, 15(6):575–603, 1999.

[26] Segreti, M., Rusinek, A., and Klepaczko, J. R. Experimental study on puncture of pmma at low and high velocities, effect on the failure mode. *Polymer Testing*, 23(6):703–718, 2004.

[27] Mulliken, A. D. and Boyce, M. C. Mechanics of the rate-dependent elastic-plastic deformation of glassy polymers from low to high strain rates. *International Journal of Solids and Structures*, 43(5):1331–1356, 2006.

[28] Farrokh, B. and Khan, A. A strain rate dependent yield criterion for isotropic polymers: Low to high rates of loading. *European Journal of Mechanics - A/Solids*, 29(2):274–282, 2010.

[29] Khan, A. S. and Farrokh, B. Thermo-mechanical response of nylon 101 under uniaxial and multi-axial loadings: Part i, experimental results over wide ranges of temperatures and strain rates. *International Journal of Plasticity*, 22(8):1506–1529, 2006. Special issue in honour of Dr. Kirk Valanis - Valanis Issue.

[30] Pouriayevali, H., Guo, Y. B., and Shim, V. P. W. A visco-hyperelastic constitutive description of elastomer behaviour at high strain rates. *Procedia Engineering*, 10(0):2274–2279, 2011. 11th International Conference on the Mechanical Behavior of Materials (ICM11).

[31] Tarigopula, V., Albertini, C., Langseth, M., Hopperstad, O. S., and Clausen, A. A hydro-pneumatic machine for intermediate strain-rates: Set-up, tests and numerical simulations. In *DYMAT 2009-9th International Conference on the Mechanical and Physical Behaviour of Materials under Dynamic Loading*, volume 1, pages 381–387, 2009.

[32] Wood, P. K. C., Schley, C. A., McGregor, I., Dutton, T., Bloomfield, M., and Bardenheier, R. Characterising performance of automotive materials at high strain rate for improved crash design. In *Journal de Physique IV (Proceedings)*, volume 134, pages 1167–1174, 2006.

[33] LeBlanc, M. M. and Lassila, D. H. A hybrid technique for compression testing at intermediate strain rates. *Experimental Techniques*, 20(5):21–24, 1996.

[34] Mott, P. H., Twigg, J. N., Roland, D. F., Schrader, H. S., Pathak, A. J., and Roland, C. M. High-speed tensile test instrument. *Review of scientific instruments*, 78(4):045105–045105, 2007.

[35] Zhao, H. and Gary, G. A new method for the separation of waves. application to the SHPB technique for an unlimited duration of measurement. *Journal of the Mechanics and Physics of Solids*, 45(7):1185–1202, 1997.

[36] Xia, Y. and Wang, Y. Dynamic testing of materials with the rotating disk indirect bar-bar tensile impact apparatus. *ASTM Journal of Testing and Evaluation*, 35(1):31–35, 2007.

[37] Clark, D. and Duwez, P. Discussion of the forces acting in tension impact tests of materials. *J. Appl. Mech*, 15(9):243–247, 1948.

[38] Lambert, M., Froustey, C., Charles, J. L., and Lataillade, J. L. High strain rate testing of aluminium alloy & high speed photography. *Journal de Physique IV*, 110:543–549, September 2003.

[39] Albertini, C. *Dynamic material properties of several steels for fast breeder reactor safety analysis: Final report*. EUR. Comm. of the European Communities, 1978.

[40] Maiden, C. J. and Green, S. J. Compressive strain-rate tests on six selected materials at strain rates from 10-3 to 104 in/in/sec. *Journal of applied mechanics*, 33:496, 1966.

[41] Albertini, C. Strain rate sensitivity of some steel and aluminium alloys of large industrial applications. In *Transient loading and response of structures*, pages 1–40, 1998.

[42] Hartley, R. S., Cloete, T. J., and Nurick, G. N. An experimental assessment of friction effects in the split hopkinson pressure bar using the ring compression test. *International Journal of Impact Engineering*, 34(10):1705–1728, 2007.

[43] Govender, R. A., Langdon, G. S., Nurick, G. N., and Cloete, T. J. Impact delamination testing of fibre reinforced polymers using hopkinson pressure bars. *Engineering Fracture Mechanics*, 101(0):80–90, 2013.

[44] Merrett, R. P., Langdon, G. S., and Theobald, M. D. The blast and impact loading of aluminium foam. *Materials & Design*, 44(0):311–319, 2013.

[45] Fairchild Semiconductor Corporation. *Fairchild QRB1114 phototransistor reflective object sensor data sheet*, ds300350 3/5/02 2002 edition, Available: http://datasheet.octopart.com/QRB1114-Fairchild-datasheet-41819.pdf.

[46] Fairchild Semiconductor Corporation. *Fairchild QRB1134 phototransistor reflective object sensor data sheet*, ds300351 7/2/01 2001 edition, Available: http://datasheet.octopart.com/QRB1134-Fairchild-datasheet-64775.pdf.

[47] Govender, R. A., Louca, L. A., Pullen, A., Fallah, A. S., and Nurick, G. N. Determining the through-thickness properties of thick glass fiber reinforced polymers at high strain rates. *Journal of Composite Materials*, 46:1219–1228, 2012.

[48] Bonorchis, D. and Nurick, G. The analysis and simulation of welded stiffener plates subjected to localised blast loading. *International Journal of Impact Engineering*, 37(3):260–273, 2010.

[49] Holman, J. P. *Experimental Methods for Engineers*. Mc Graw Hill, 2001.

Appendix A

Results

A.1 Quasi Static Results

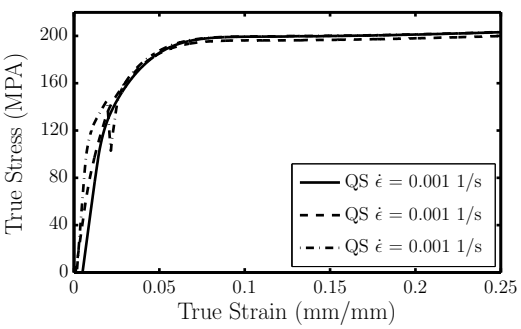

(a) Aluminium

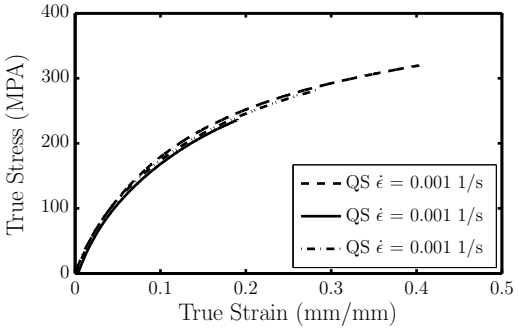

(b) Copper

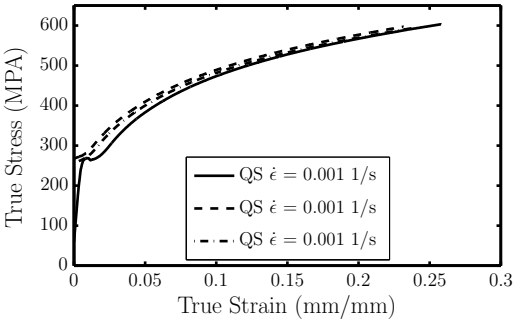

(c) Steel

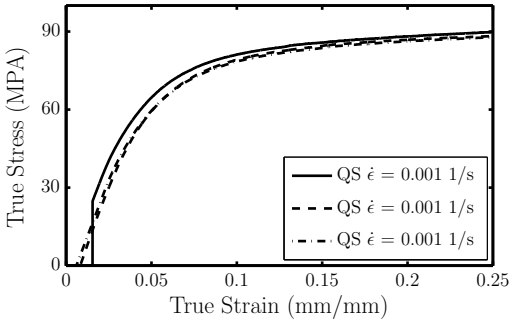

(d) Nylon

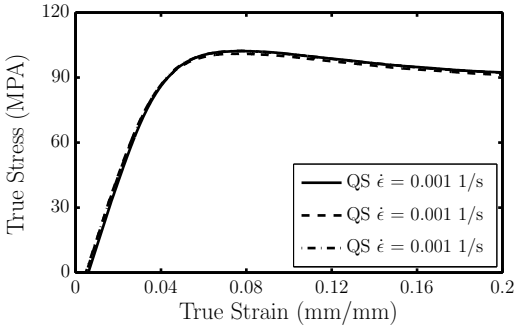

(e) PMMA

Figure A.1: Quasi static test results

A.2 SHPB Results

A.2.1 Aluminium

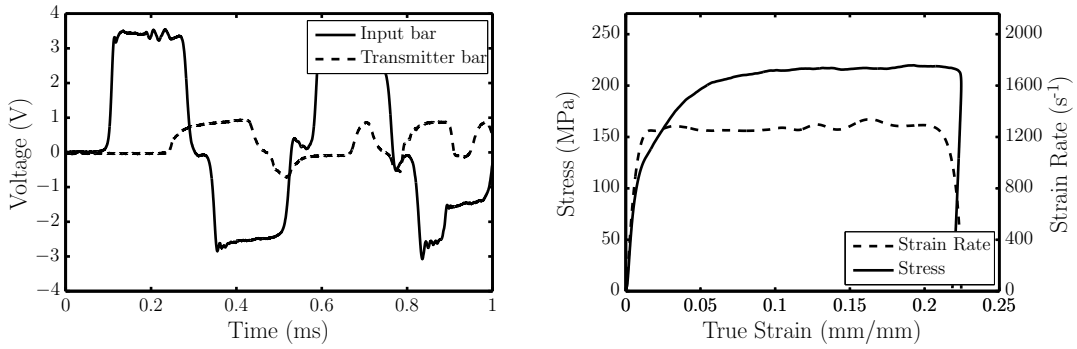

(a) Raw data (b) Stress and strain rate vs. strain

Figure A.2: Annealed aluminium - Test 1

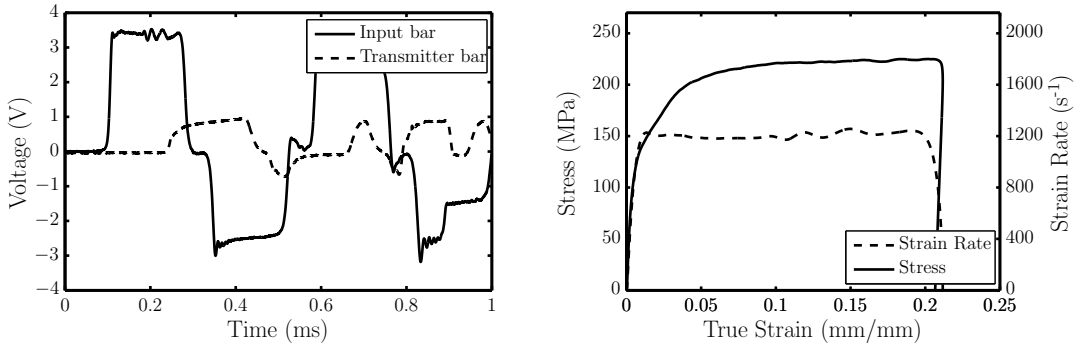

(a) Raw data (b) Stress and strain rate vs. strain

Figure A.3: Annealed aluminium - Test 2

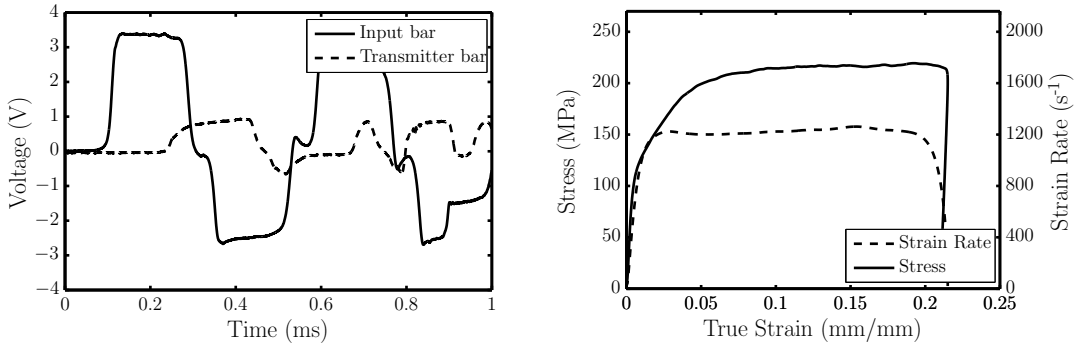

(a) Raw data (b) Stress and strain rate vs. strain

Figure A.4: Annealed aluminium - Test 3

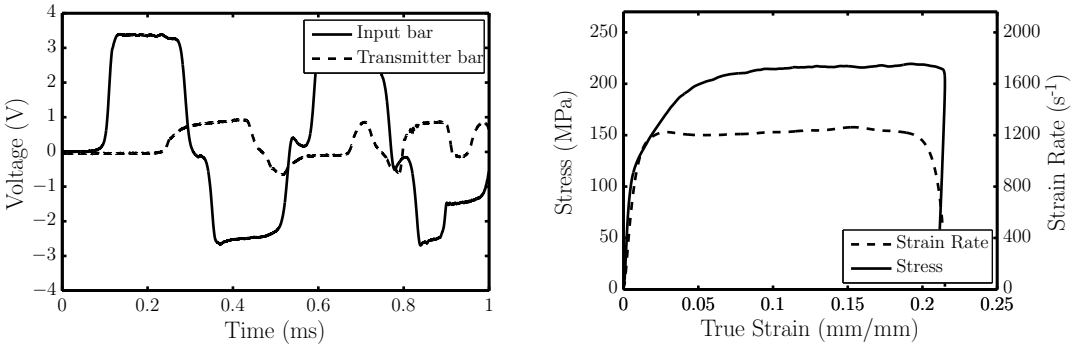

(a) Raw data (b) Stress and strain rate vs. strain

Figure A.5: Annealed aluminium - Test 4

A.2.2 Copper

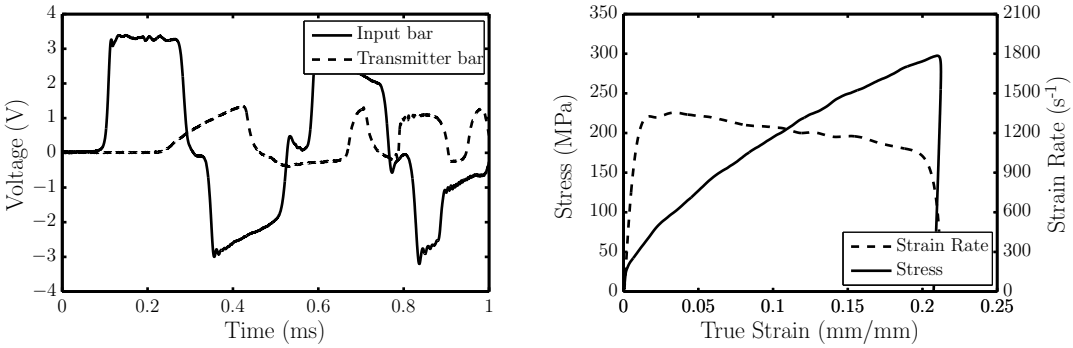

(a) Raw data (b) Stress and strain rate vs. strain

Figure A.6: Annealed copper - Test 1

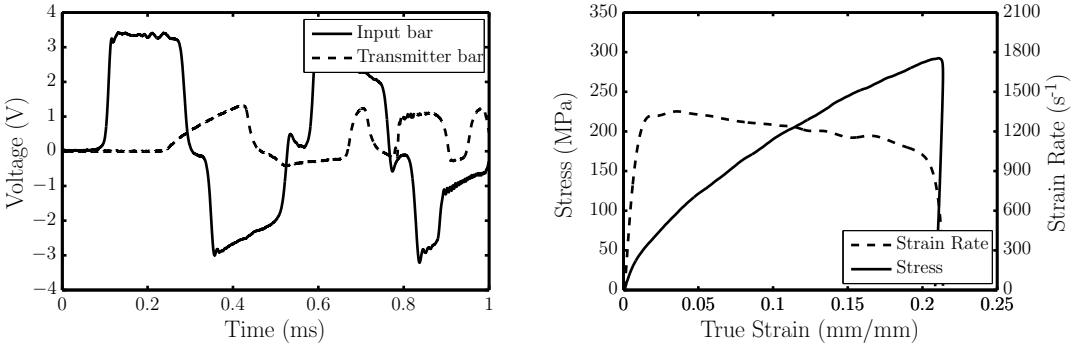

(a) Raw data (b) Stress and strain rate vs. strain

Figure A.7: Annealed copper - Test 2

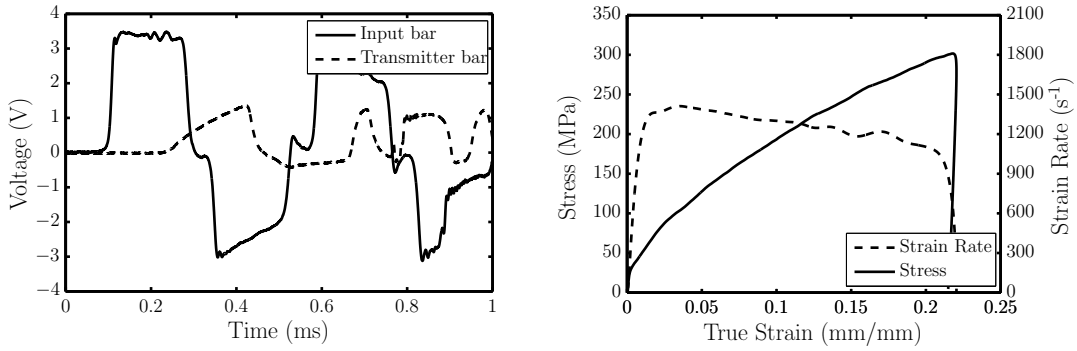

(a) Raw data (b) Stress and strain rate vs. strain

Figure A.8: Annealed copper - Test 3

A.2.3 Steel

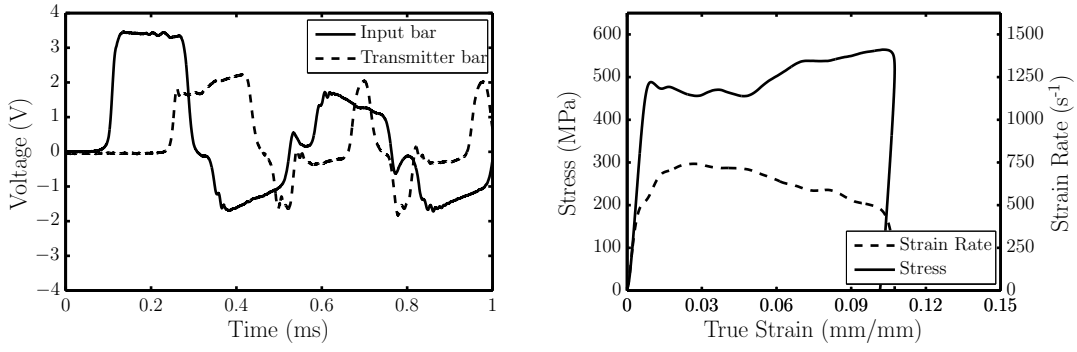

(a) Raw data (b) Stress and strain rate vs. strain

Figure A.9: Annealed steel - Test 1

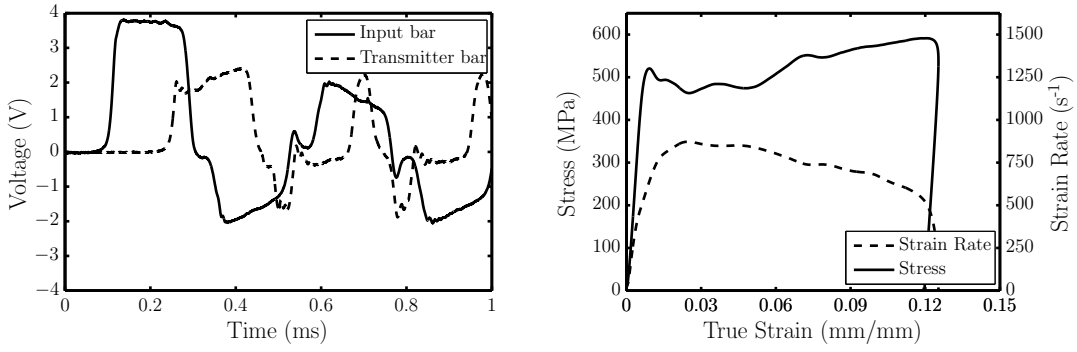

(a) Raw data (b) Stress and strain rate vs. strain

Figure A.10: Annealed steel - Test 2

A.2.4 PMMA

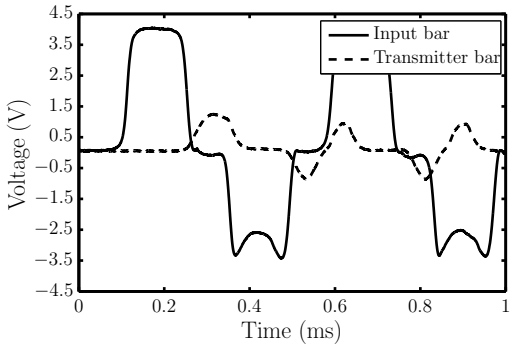

(a) Raw data

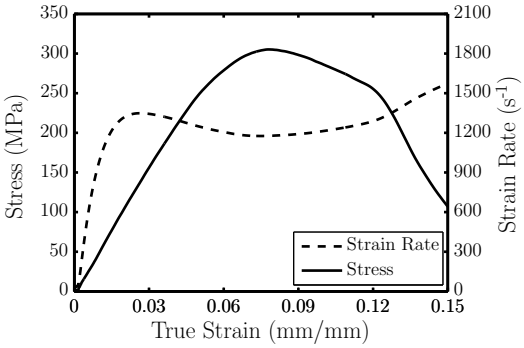

(b) Stress and strain rate vs. strain

Figure A.11: PMMA - Test 1

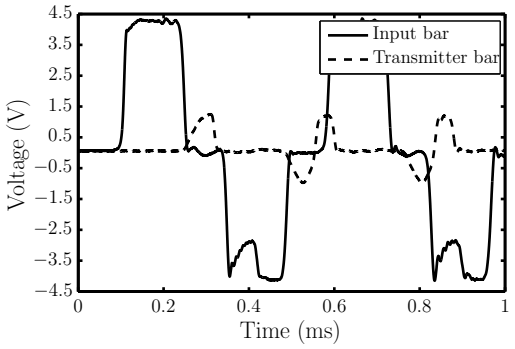

(a) Raw data

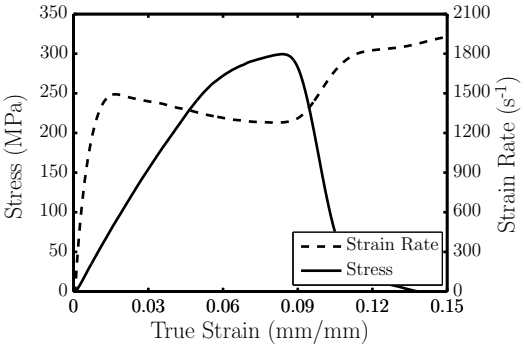

(b) Stress and strain rate vs. strain

Figure A.12: PMMA - Test 2

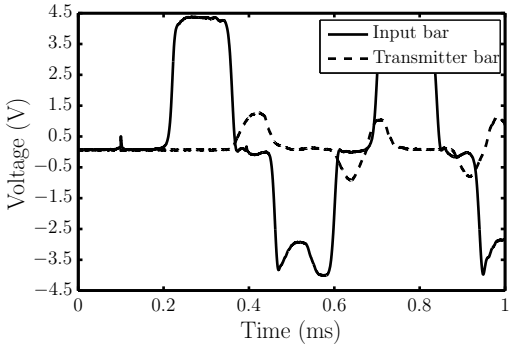

(a) Raw data

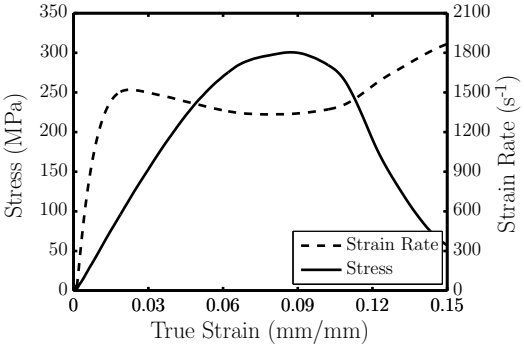

(b) Stress and strain rate vs. strain

Figure A.13: PMMA - Test 3

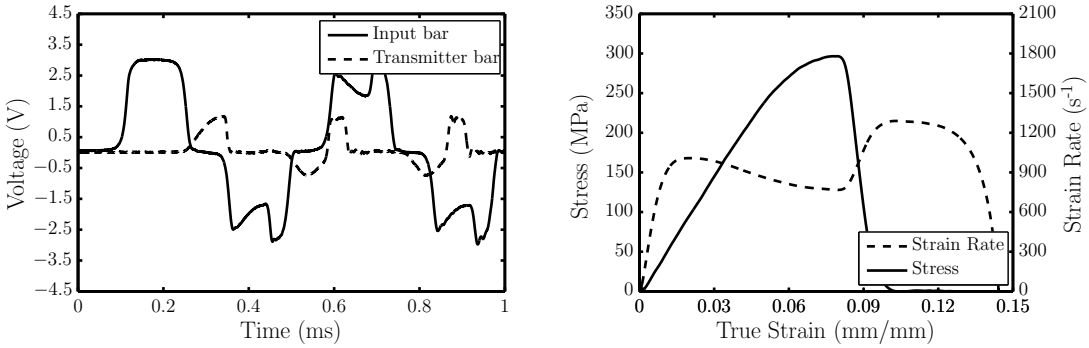

(a) Raw data (b) Stress and strain rate vs. strain

Figure A.14: PMMA - Test 4

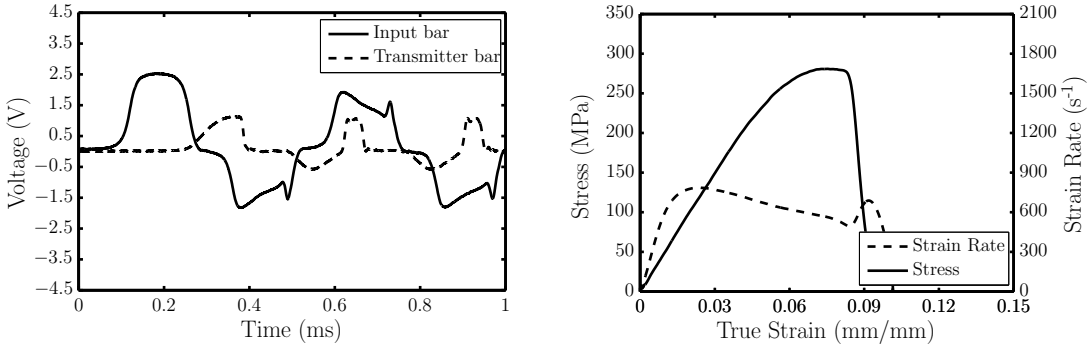

(a) Raw data (b) Stress and strain rate vs. strain

Figure A.15: PMMA - Test 5

A.2.5 Nylon

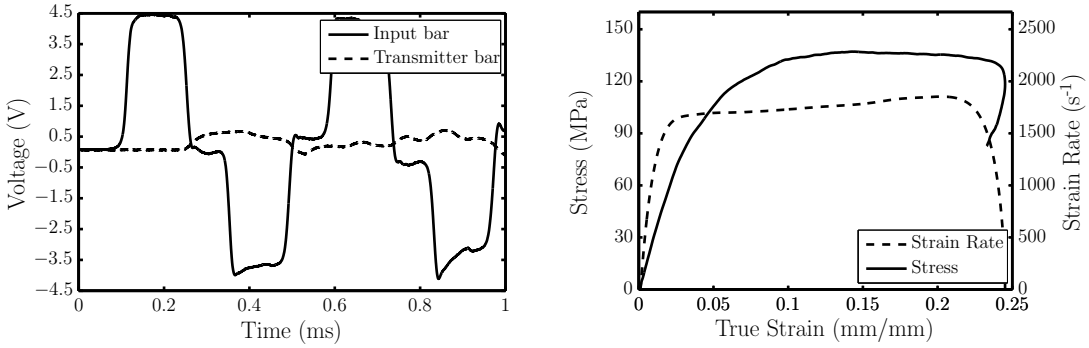

(a) Raw data (b) Stress and strain rate vs. strain

Figure A.16: Nylon - Test 1

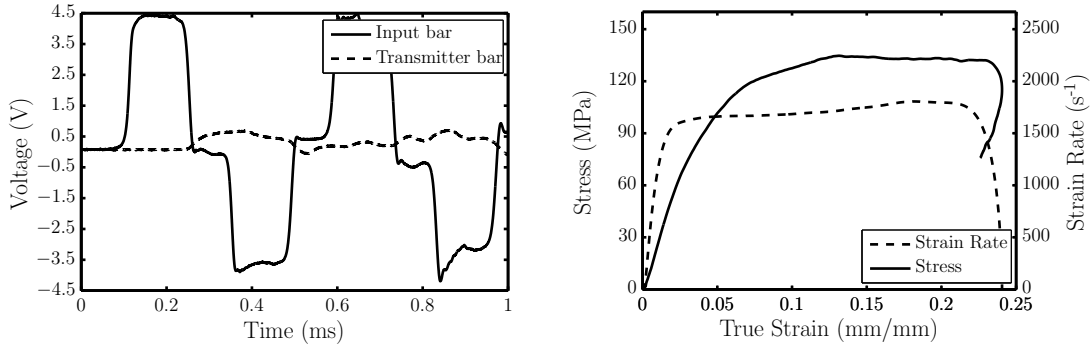

(a) Raw data (b) Stress and strain rate vs. strain

Figure A.17: Nylon - Test 2

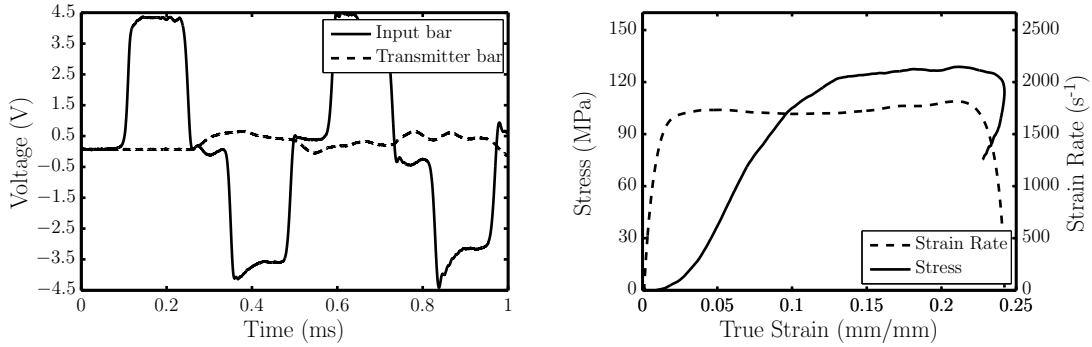

(a) Raw data (b) Stress and strain rate vs. strain

Figure A.18: Nylon - Test 3

A.3 IST Results

A.3.1 Aluminium

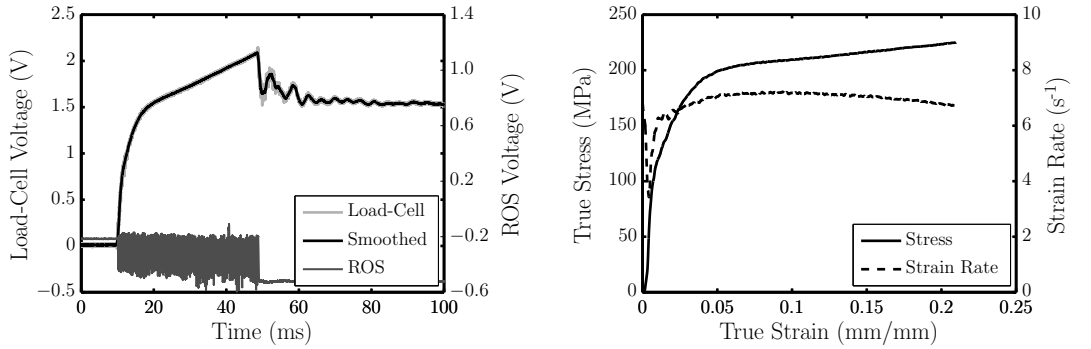

(a) Raw data (b) Stress and strain rate vs. strain

Figure A.19: Annealed aluminium - Test 1

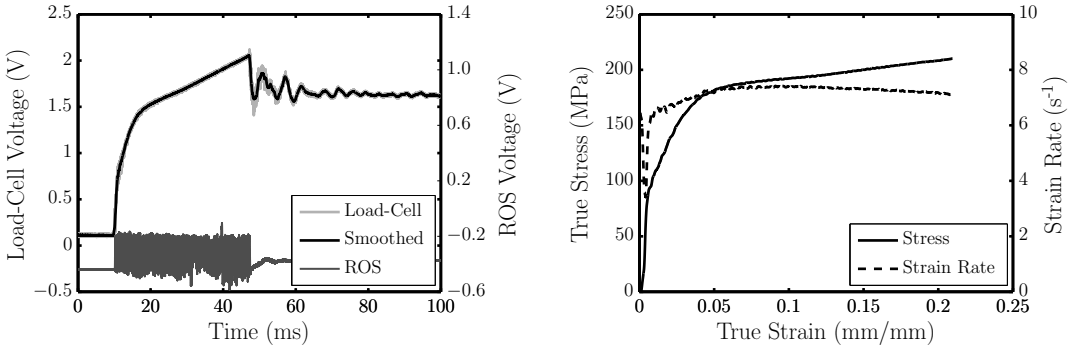

(a) Raw data (b) Stress and strain rate vs. strain

Figure A.20: Annealed aluminium - Test 2

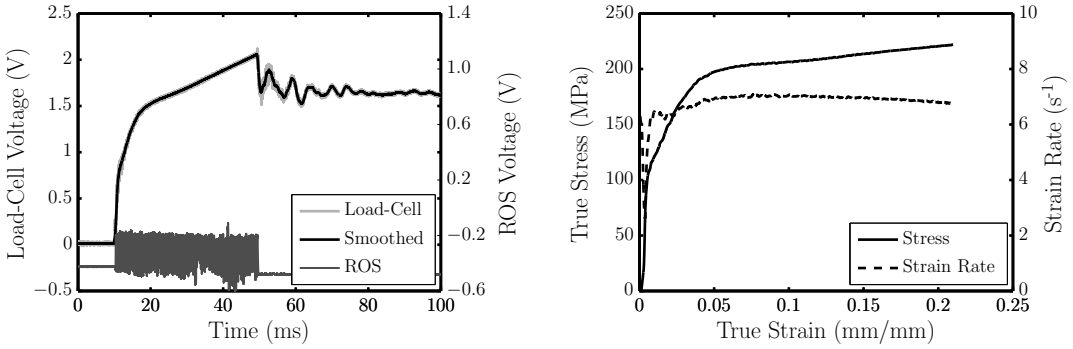

(a) Raw data (b) Stress and strain rate vs. strain

Figure A.21: Annealed aluminium - Test 3

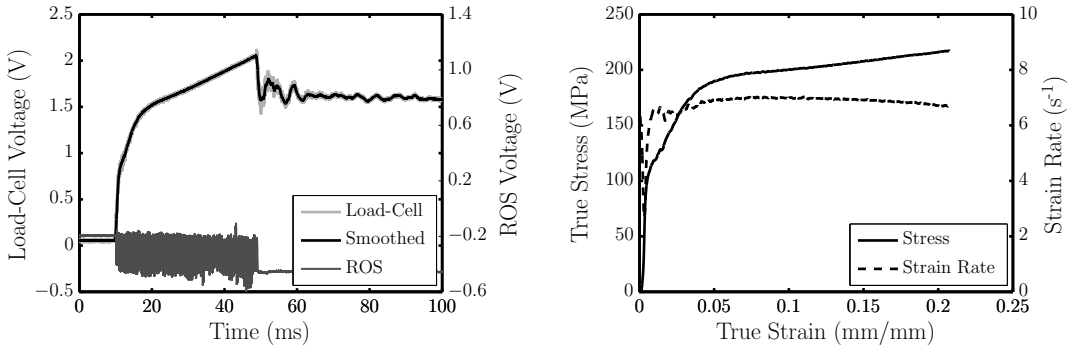

(a) Raw data (b) Stress and strain rate vs. strain

Figure A.22: Annealed aluminium - Test 4

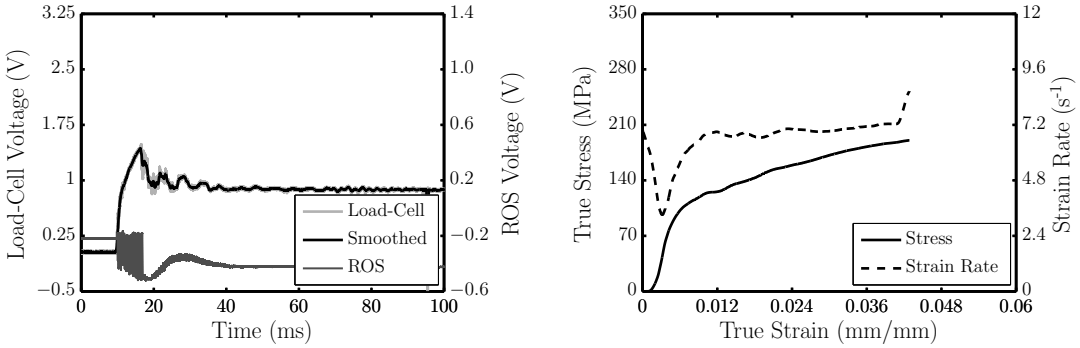

(a) Raw data (b) Stress and strain rate vs. strain

Figure A.23: Interrupted annealed aluminium - Series 1, Test 1 of 2

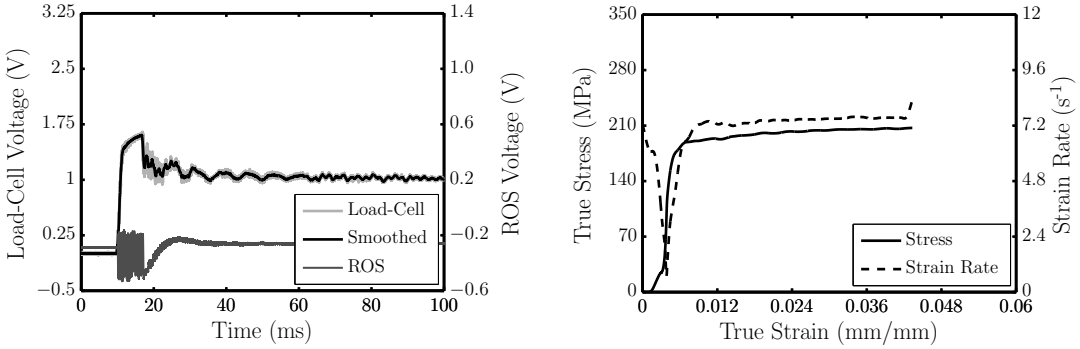

(a) Raw data (b) Stress and strain rate vs. strain

Figure A.24: Interrupted annealed aluminium - Series 1, Test 2 of 2

A.3.2 Annealed Steel

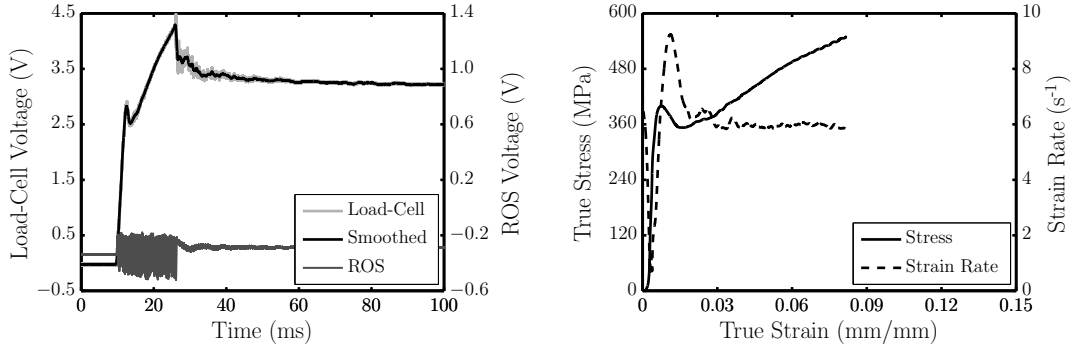

(a) Raw data (b) Stress and strain rate vs. strain

Figure A.25: Annealed steel - Test 1

A.3.3 Copper

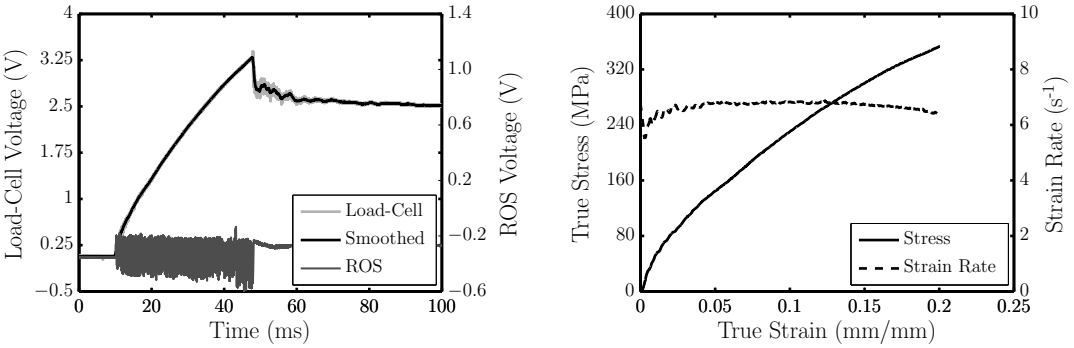

(a) Raw data (b) Stress and strain rate vs. strain

Figure A.26: Annealed copper - Test 1

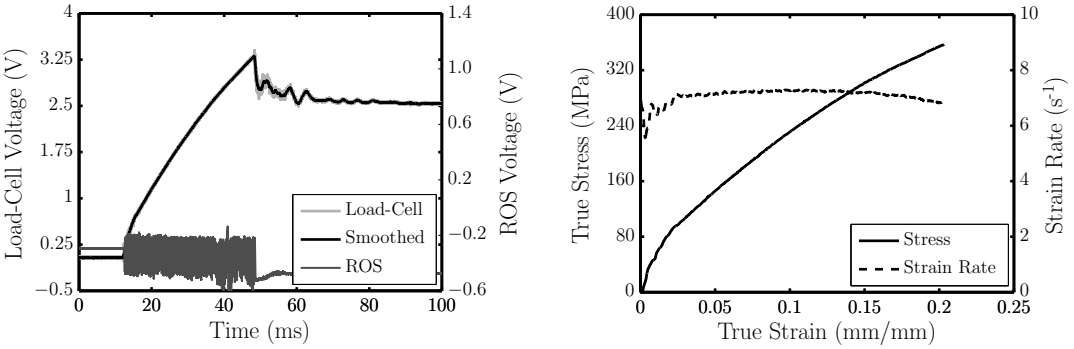

(a) Raw data (b) Stress and strain rate vs. strain

Figure A.27: Annealed copper - Test 2

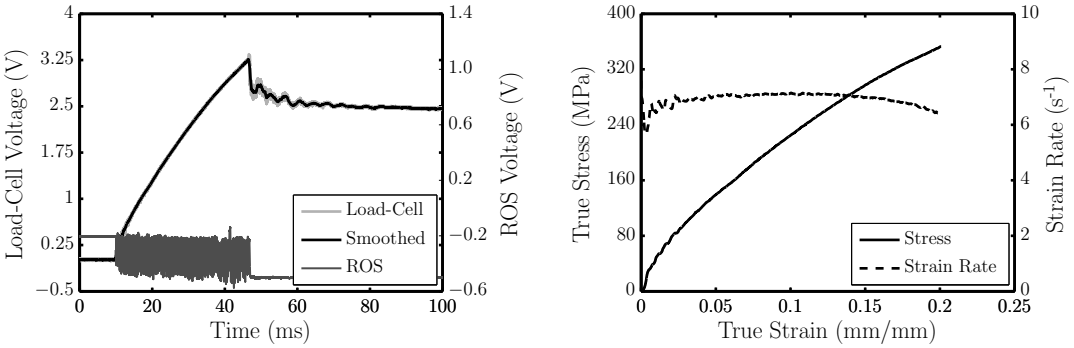

(a) Raw data (b) Stress and strain rate vs. strain

Figure A.28: Annealed copper - Test 3

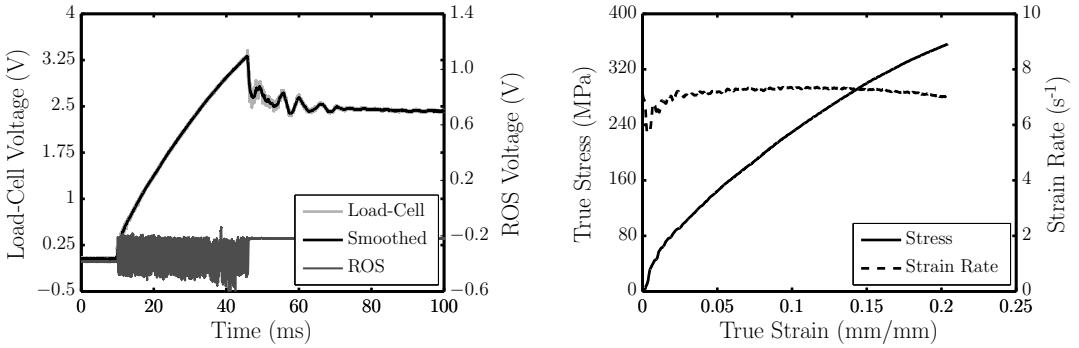

(a) Raw data (b) Stress and strain rate vs. strain

Figure A.29: Annealed copper - Test 4

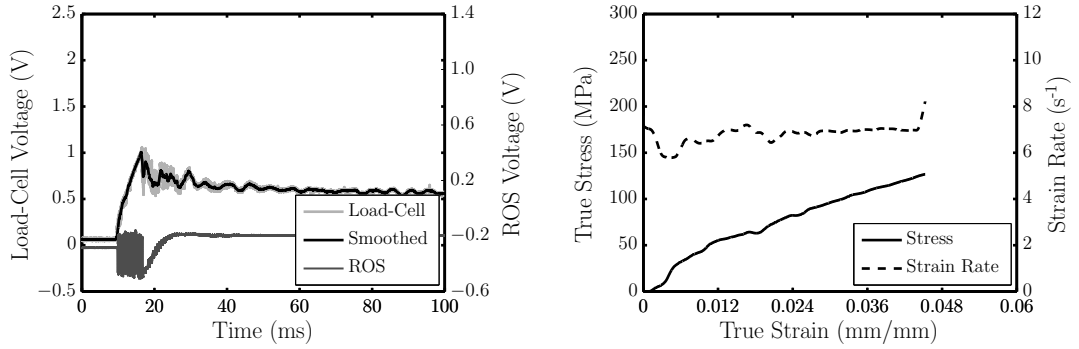

(a) Raw data (b) Stress and strain rate vs. strain

Figure A.30: Interrupted copper - Series 2, Test 1 of 5

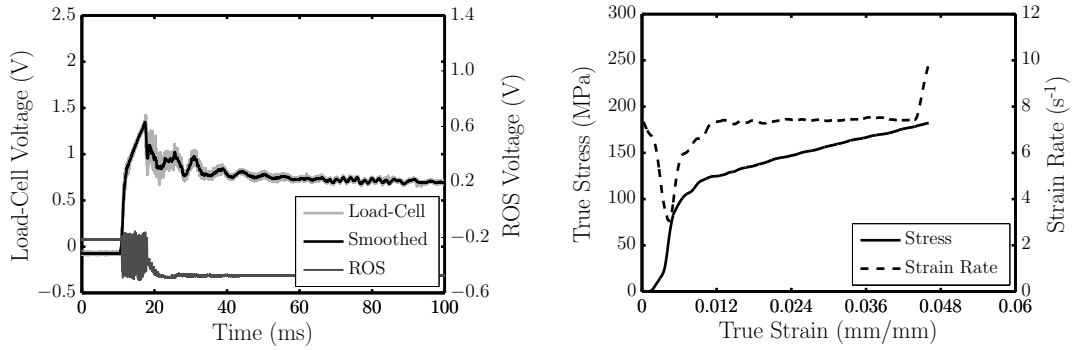

(a) Raw data (b) Stress and strain rate vs. strain

Figure A.31: Interrupted copper - Series 2, Test 2 of 5

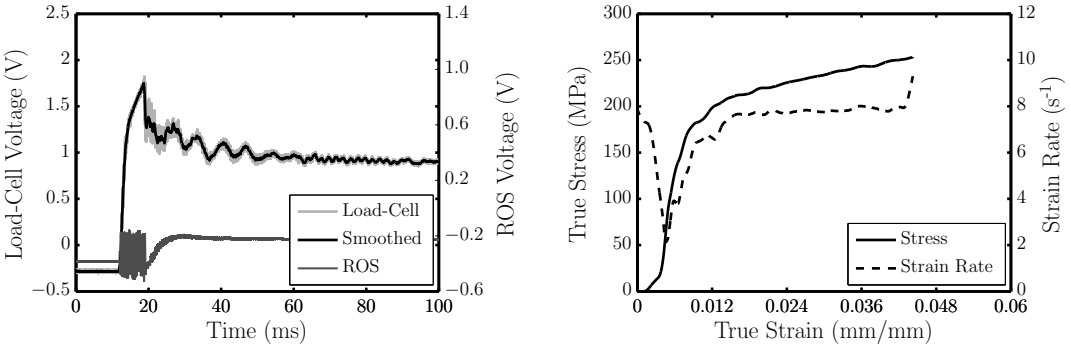

(a) Raw data (b) Stress and strain rate vs. strain

Figure A.32: Interrupted copper - Series 2, Test 3 of 5

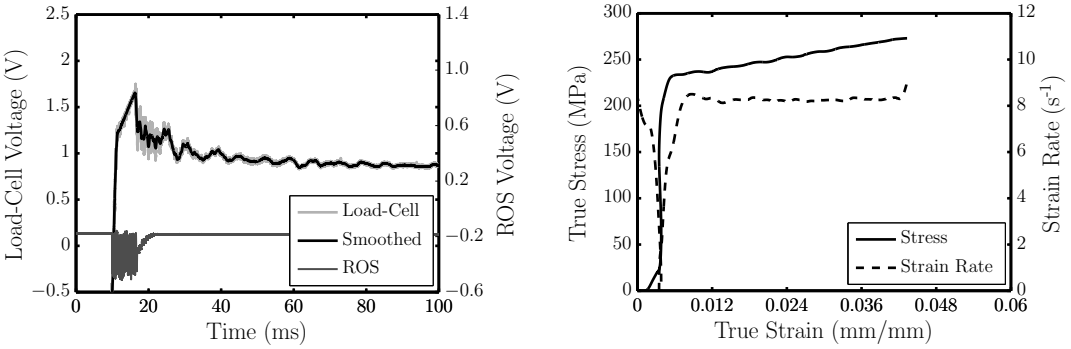

(a) Raw data (b) Stress and strain rate vs. strain

Figure A.33: Interrupted copper - Series 2, Test 4 of 5

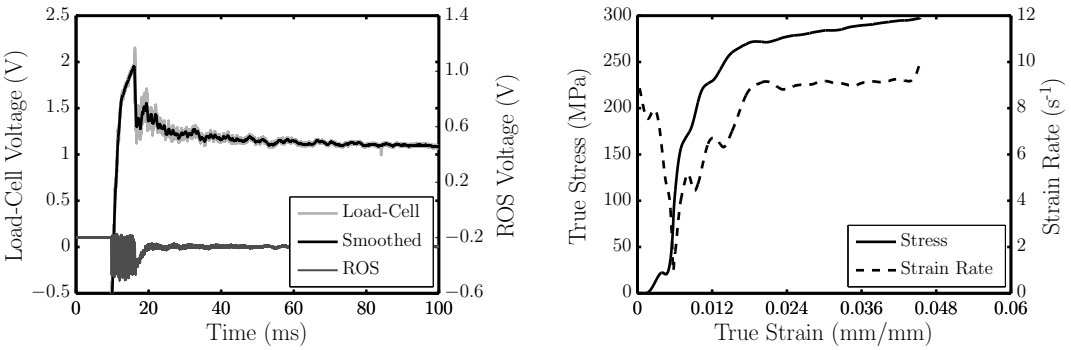

(a) Raw data (b) Stress and strain rate vs. strain

Figure A.34: Interrupted copper - Series 2, Test 5 of 5

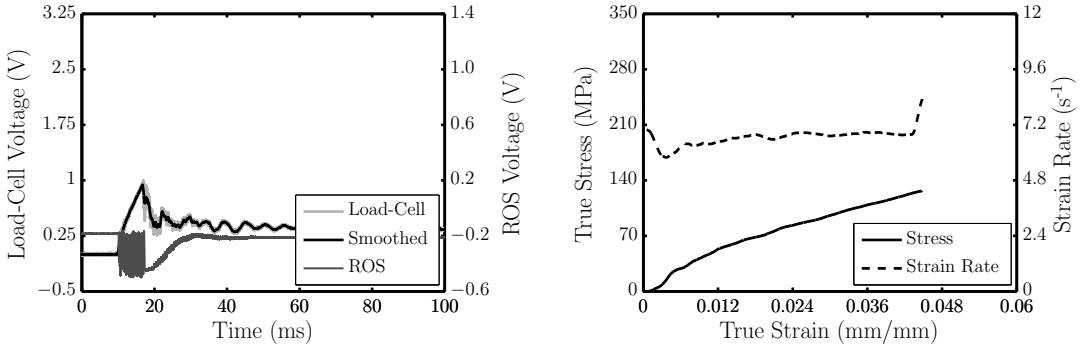

(a) Raw data (b) Stress and strain rate vs. strain

Figure A.35: Interrupted copper - Series 4, Test 1 of 5

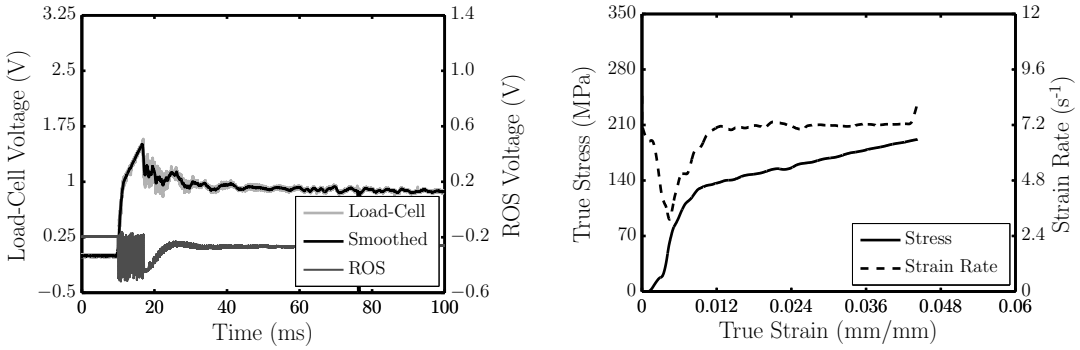

(a) Raw data (b) Stress and strain rate vs. strain

Figure A.36: Interrupted copper - Series 4, Test 2 of 5

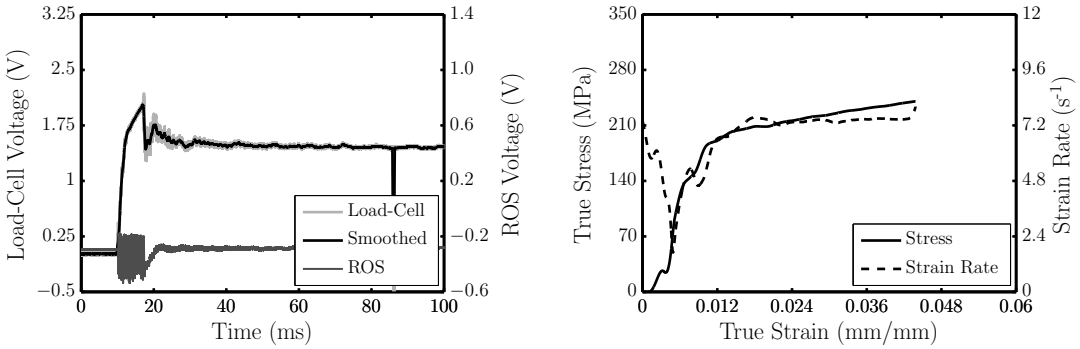

(a) Raw data (b) Stress and strain rate vs. strain

Figure A.37: Interrupted copper - Series 4, Test 3 of 5

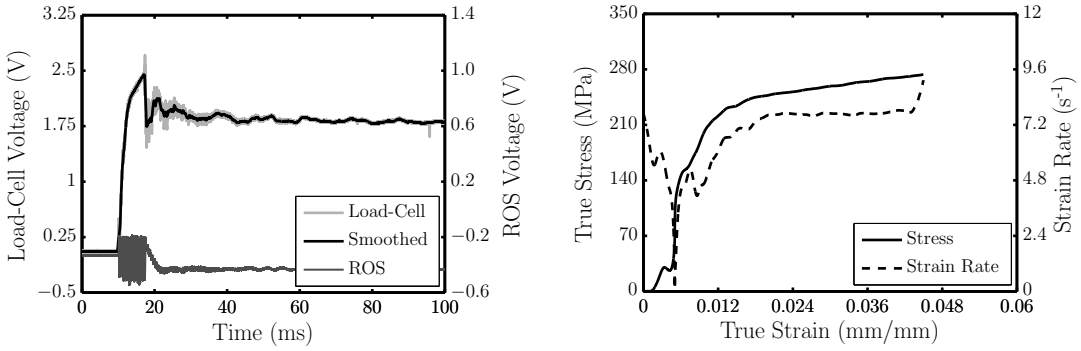

(a) Raw data (b) Stress and strain rate vs. strain

Figure A.38: Interrupted copper - Series 4, Test 4 of 5

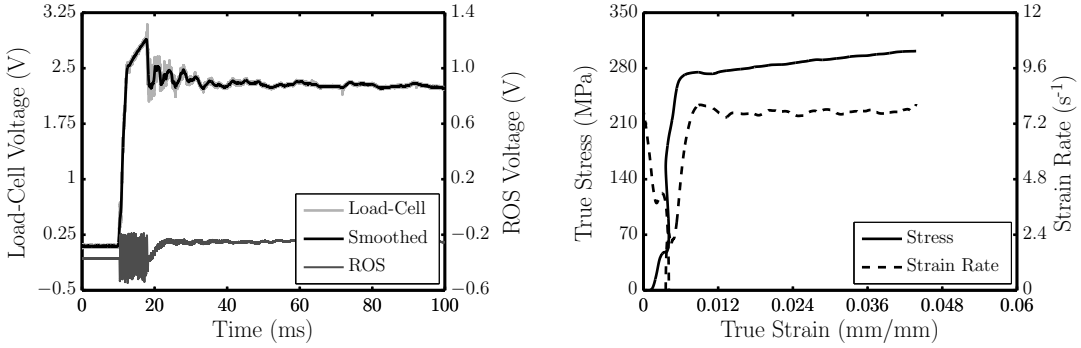

(a) Raw data (b) Stress and strain rate vs. strain

Figure A.39: Interrupted copper - Series 4, Test 5 of 5

A.3.4 Nylon

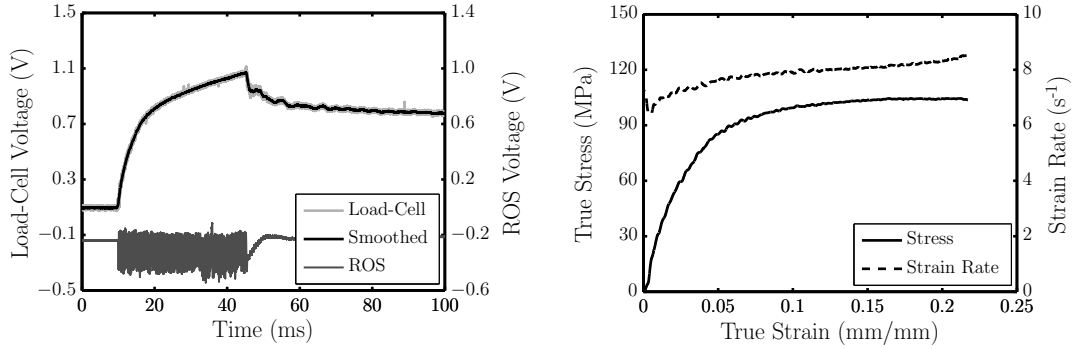

(a) Raw data (b) Stress and strain rate vs. strain

Figure A.40: Nylon - Test 1

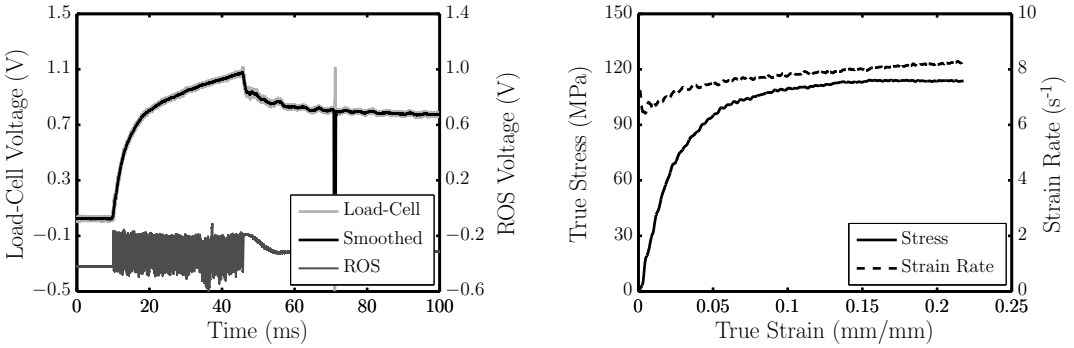

(a) Raw data (b) Stress and strain rate vs. strain

Figure A.41: Nylon - Test 2

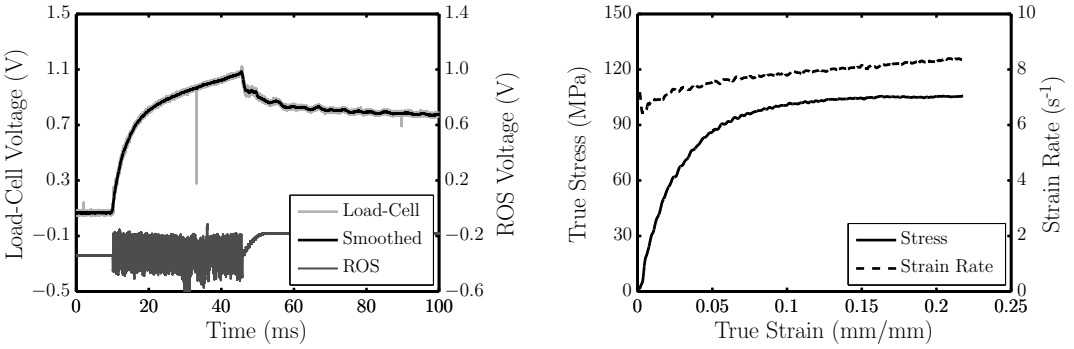

(a) Raw data (b) Stress and strain rate vs. strain

Figure A.42: Nylon - Test 3

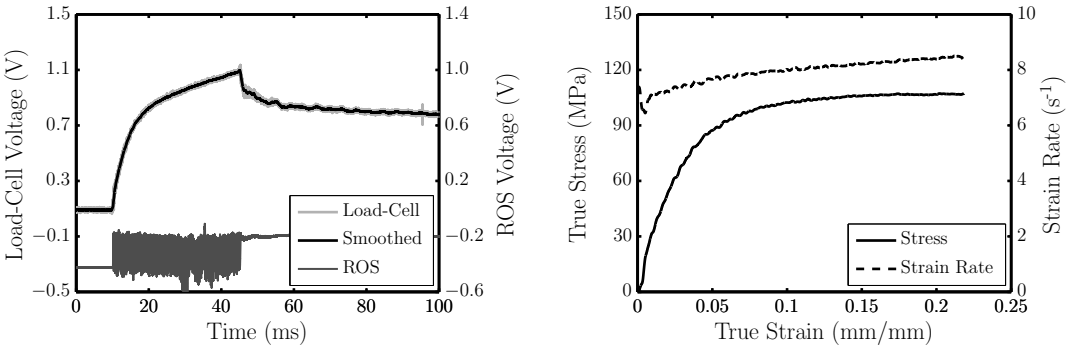

(a) Raw data (b) Stress and strain rate vs. strain

Figure A.43: Nylon - Test 4

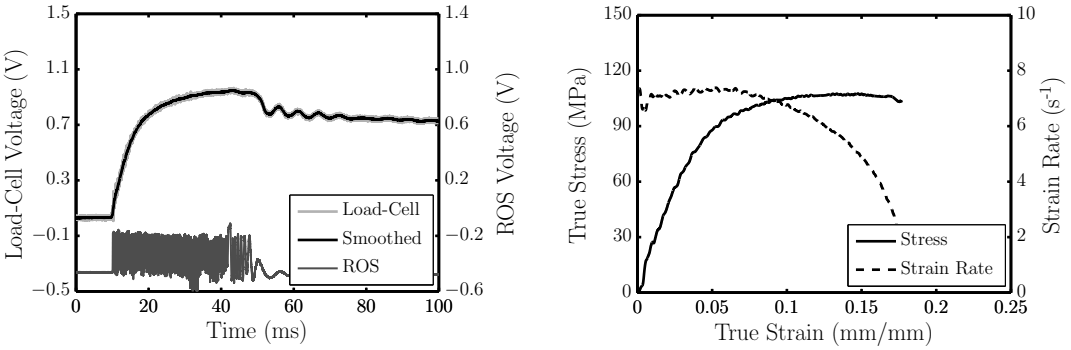

(a) Raw data (b) Stress and strain rate vs. strain

Figure A.44: Nylon - Test 5

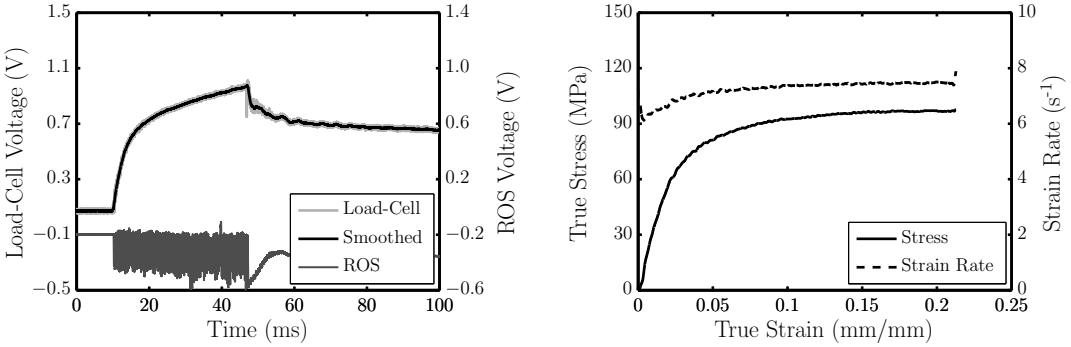

(a) Raw data (b) Stress and strain rate vs. strain

Figure A.45: Nylon - Test 6

A.3.5 PMMA

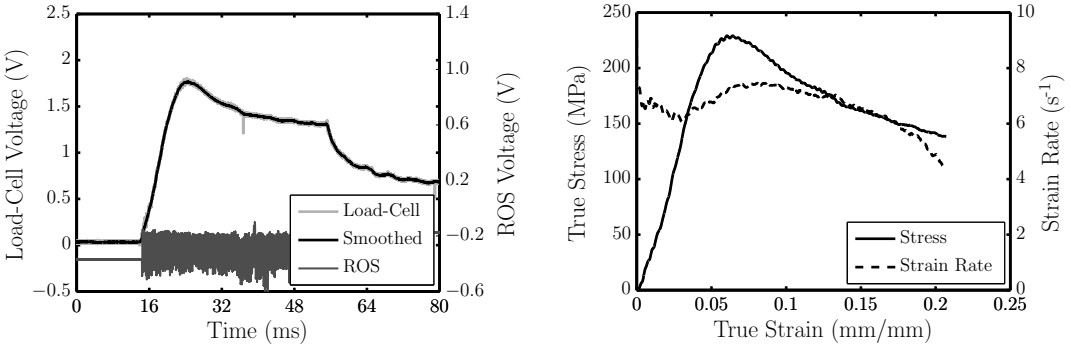

(a) Raw data (b) Stress and strain rate vs. strain

Figure A.46: PMMA - Test 1

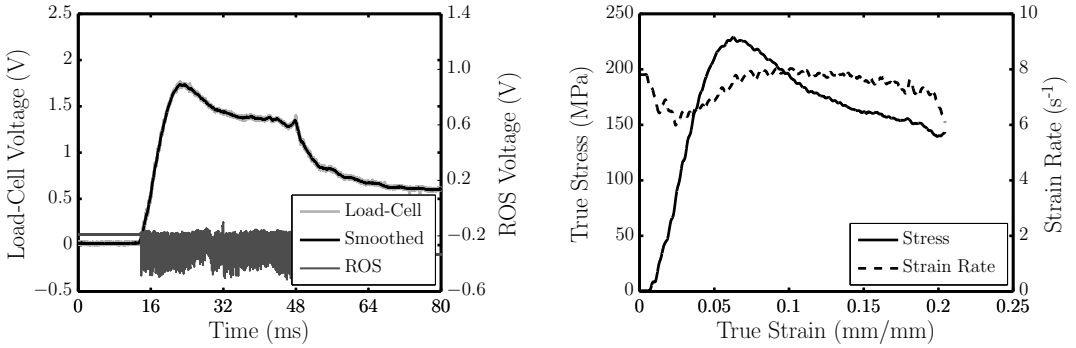

(a) Raw data (b) Stress and strain rate vs. strain

Figure A.47: PMMA - Test 2

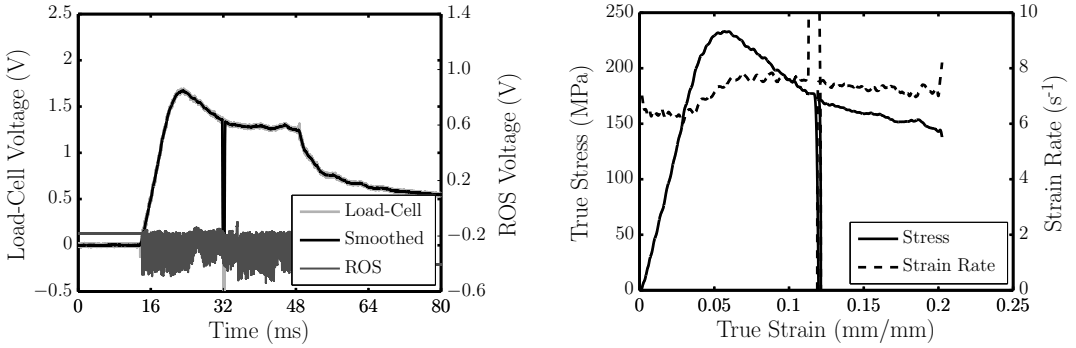

(a) Raw data (b) Stress and strain rate vs. strain

Figure A.48: PMMA - Test 3

A.3.6 Unbalanced Load-Frame Tests

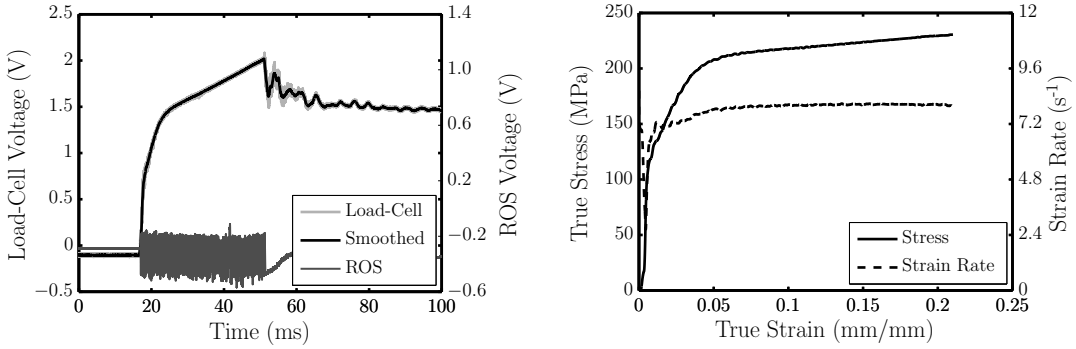

(a) Raw data (b) Stress and strain rate vs. strain

Figure A.49: Unbalanced load-frame: aluminium specimen - Test 1

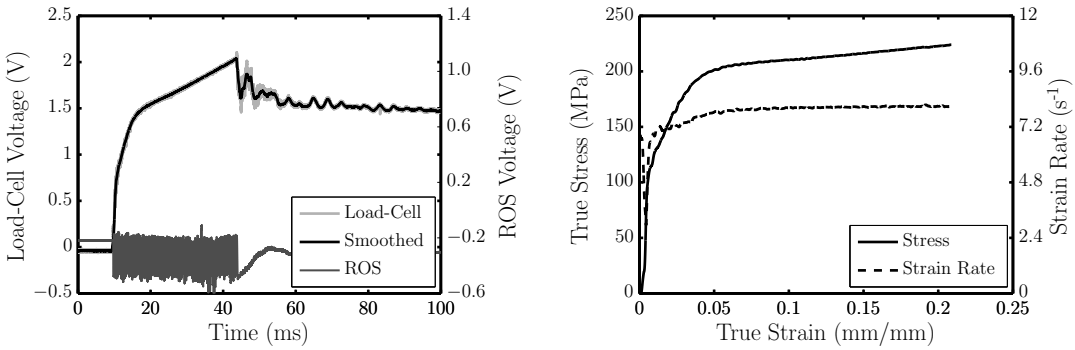

(a) Raw data (b) Stress and strain rate vs. strain

Figure A.50: Unbalanced load-frame: aluminium specimen - Test 2

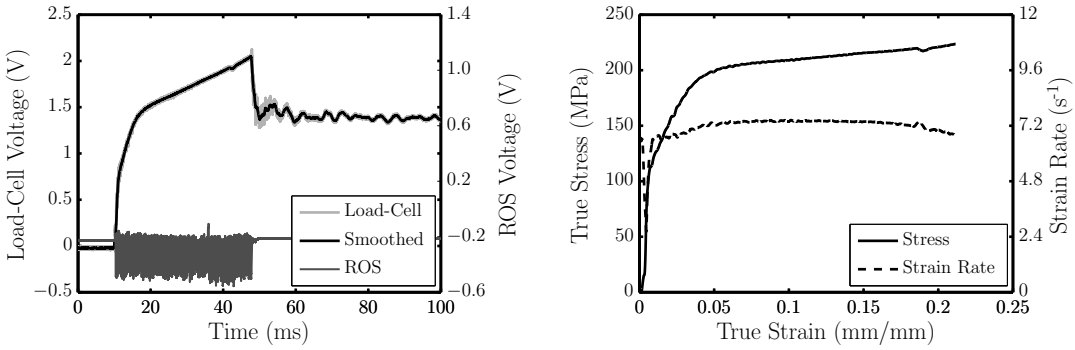

(a) Raw data (b) Stress and strain rate vs. strain

Figure A.51: Unbalanced load-frame: aluminium specimen - Test 3

A.3.7 Cloete and Oxtoby's Aluminium Specimen

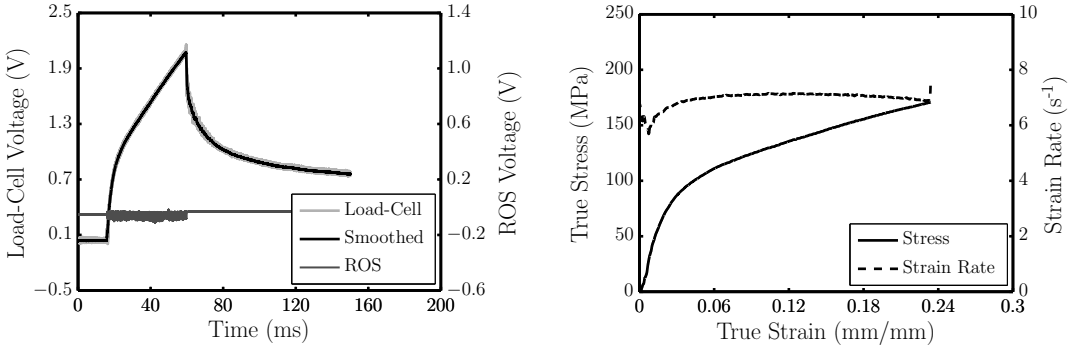

(a) Raw data (b) Stress and strain rate vs. strain

Figure A.52: Cloete & Oxtoby's aluminium specimen - Test 1, impact start

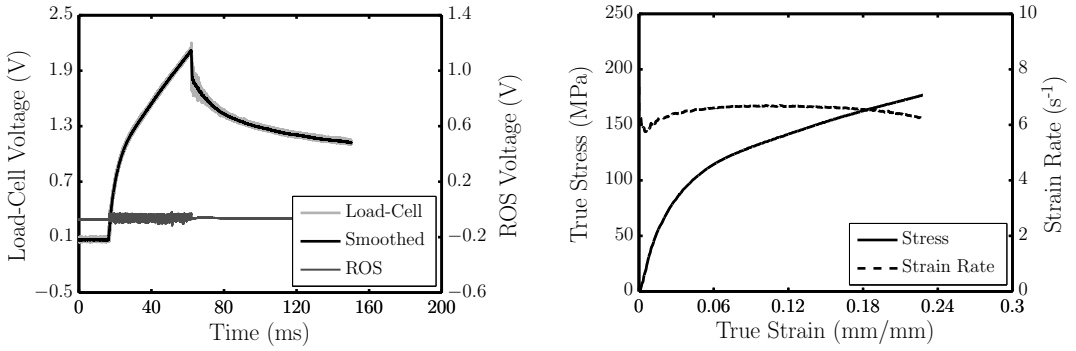

(a) Raw data (b) Stress and strain rate vs. strain

Figure A.53: Cloete & Oxtoby's aluminium specimen - Test 2, impact start

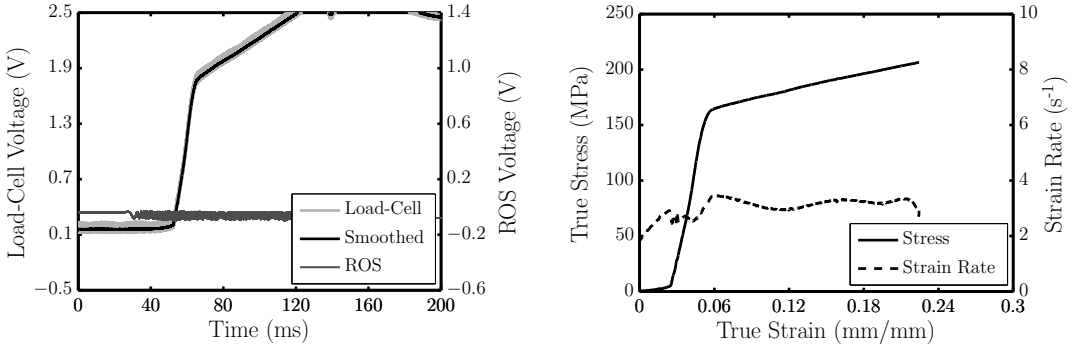

(a) Raw data (b) Stress and strain rate vs. strain

Figure A.54: Cloete & Oxtoby's aluminium specimen - Test 13, back pressure driven

A.3.8 High Speed Camera Test

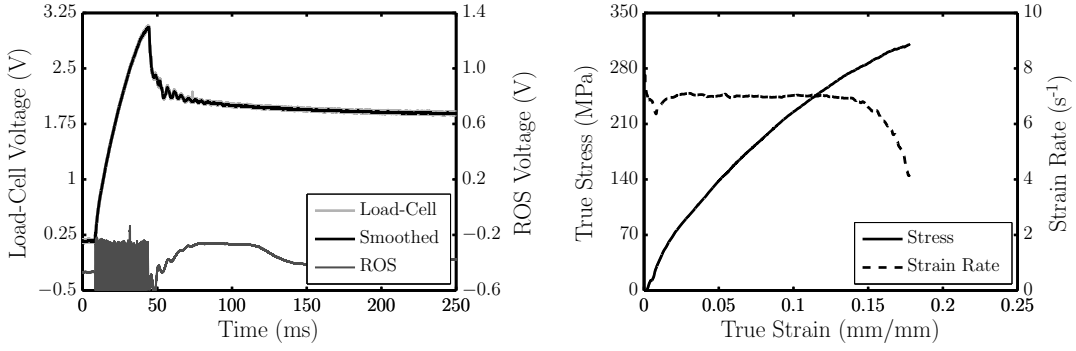

(a) Raw data (b) Stress and strain rate vs. strain

Figure A.55: High speed camera - Test 1, copper specimen

A.4 ROS Displacement Measurement

Table A.1 provides the results comparing the total wedge bar displacement obtained from the ROS to the actual distance set between the wedge bar and stopper bars.

Table A.1: Calculated vs. measured wedge bar displacement

Test	ROS displacement (m)	Actual displacement (m)	Ratio (%)
PMMA 1	0.298	0.300	99.2
PMMA 2	0.300	0.300	100.0
PMMA 3	0.305	0.300	101.5
Al 1	0.299	0.300	99.6
Al 2	0.297	0.300	99.0
Al 3	0.298	0.300	99.3
Al 4	0.298	0.300	99.3
Nylon 2	0.299	0.300	99.7
Nylon 3	0.300	0.300	99.9
Nylon 4	0.298	0.300	99.3
Nylon 5	0.300	0.300	100.1
Nylon 6	0.236	N/A	
Nylon 7	0.301	0.300	100.4
Cu 1	0.298	0.300	99.3
Cu 2	0.299	0.300	99.6
Cu 3	0.297	0.300	98.9
Cu 4	0.298	0.300	99.3
Steel 1	0.136	0.138	98.6
Unbalanced Al 1	0.298	0.300	99.3
Unbalanced Al 2	0.298	0.300	99.3
Unbalanced Al 3	0.300	0.300	100.1
Interrupted Al 1, 1 of 5	0.060	0.060	100.1
Interrupted Al 1, 2 of 5	0.060	0.060	100.0
Interrupted Al 1, 3 of 5	0.060	0.060	100.8
Interrupted Al 1, 4 of 5	0.036	0.060	
Interrupted Al 1, 5 of 5	0.058	0.060	96.7
Interrupted Cu 2, 1 of 5	0.060	0.060	100.0
Interrupted Cu 2, 2 of 5	0.060	0.060	100.2
Interrupted Cu 2, 3 of 5	0.060	0.060	100.1
Interrupted Cu 2, 4 of 5	0.058	0.060	96.7
Interrupted Cu 2, 5 of 5	0.060	0.060	100.1
Interrupted Cu 3, 1 of 5	0.061	0.060	101.1
Interrupted Cu 3, 2 of 5	0.058	0.060	96.7
Interrupted Cu 3, 3 of 5	0.060	0.060	100.0
Interrupted Cu 3, 4 of 5	0.060	0.060	100.6
Interrupted Cu 3, 5 of 5	0.058	0.060	96.9
Interrupted Cu 4, 1 of 5	0.060	0.060	100.0
Interrupted Cu 4, 2 of 5	0.060	0.060	100.0
Interrupted Cu 4, 3 of 5	0.060	0.060	100.1
Interrupted Cu 4, 4 of 5	0.060	0.060	100.2
Interrupted Cu 4, 5 of 5	0.058	0.060	96.8
Average			99.4
Std Deviation			1.2

A.5 Strain Rate History

Table A.2 provides the results for the strain rate history. The average, initial, minimum and maximum strain rate is given, as well as the ratio of the strain rate at yield to the average strain rate.

Table A.2: Strain rate history

Test	Strain rate (s^{-1})				
	Average	Initial	Min	Max	$\frac{\dot{\epsilon}_y}{\dot{\epsilon}_{ave}}$
PMMA 1	6.5	9	4.3	9	0.66
PMMA 2	7.3	9	6	9	0.82
PMMA 3	7.2	8.1	0	8.1	0
Al 1	6.9	7.4	3.4	7.4	0.5
Al 2	7.1	7.6	3.4	7.6	0.48
Al 3	6.8	7.5	2.6	7.5	0.38
Al 4	6.8	7.5	2.7	7.5	0.4
Nylon 2	7.8	7.5	6.4	8.5	0.81
Nylon 3	7.7	7.8	6.4	8.3	0.83
Nylon 4	7.8	7.7	6.4	8.4	0.82
Nylon 5	7.9	7.9	6.4	8.5	0.81
Nylon 6	6.3	7.6	1.4	7.6	0.22
Nylon 7	7.2	7.2	6.1	7.5	0.84
Cu 1	6.7	7.4	5.5	7.4	0.83
Cu 2	7.1	7.6	5.6	7.6	0.79
Cu 3	6.9	7.6	5.6	7.6	0.82
Cu 4	7.2	7.7	5.7	7.7	0.8
Steel 1	5.9	7.6	0.6	7.6	0.1
Unbalanced Al 1	7.8	8.6	2.6	8.6	0.34
Unbalanced Al 2	7.8	8.2	3	8.2	0.38
Unbalanced Al 3	7.2	8.1	2.6	8.1	0.37
Interrupted Al 1 (1 of 2)	6.6	7.4	3.3	7.6	0.5
Interrupted Al 1 (2 of 2)	7	8.6	0.7	8.6	0.1
Interrupted Cu 2 (1 of 5)	6.8	7.9	5.8	7.9	0.85
Interrupted Cu 2 (2 of 5)	7	8	3.1	8	0.43
Interrupted Cu 2 (3 of 5)	7.1	8.3	2.1	8.5	0.3
Interrupted Cu 2 (4 of 5)	7.9	9.9	0	9.9	0
Interrupted Cu 2 (5 of 5)	7.9	9.8	0.9	9.8	0.12
Interrupted Cu 4 (1 of 5)	6.6	8.3	5.8	8.3	0.87
Interrupted Cu 4 (2 of 5)	6.7	8.5	3.1	8.5	0.46
Interrupted Cu 4 (3 of 5)	6.7	7.9	1.7	8	0.25
Interrupted Cu 4 (4 of 5)	6.9	8.1	0.1	8.3	0.01
Interrupted Cu 4 (5 of 5)	7.2	9.3	0	9.3	0

Appendix B

High Speed Camera Results

B.1 Unbalanced Load-Frame

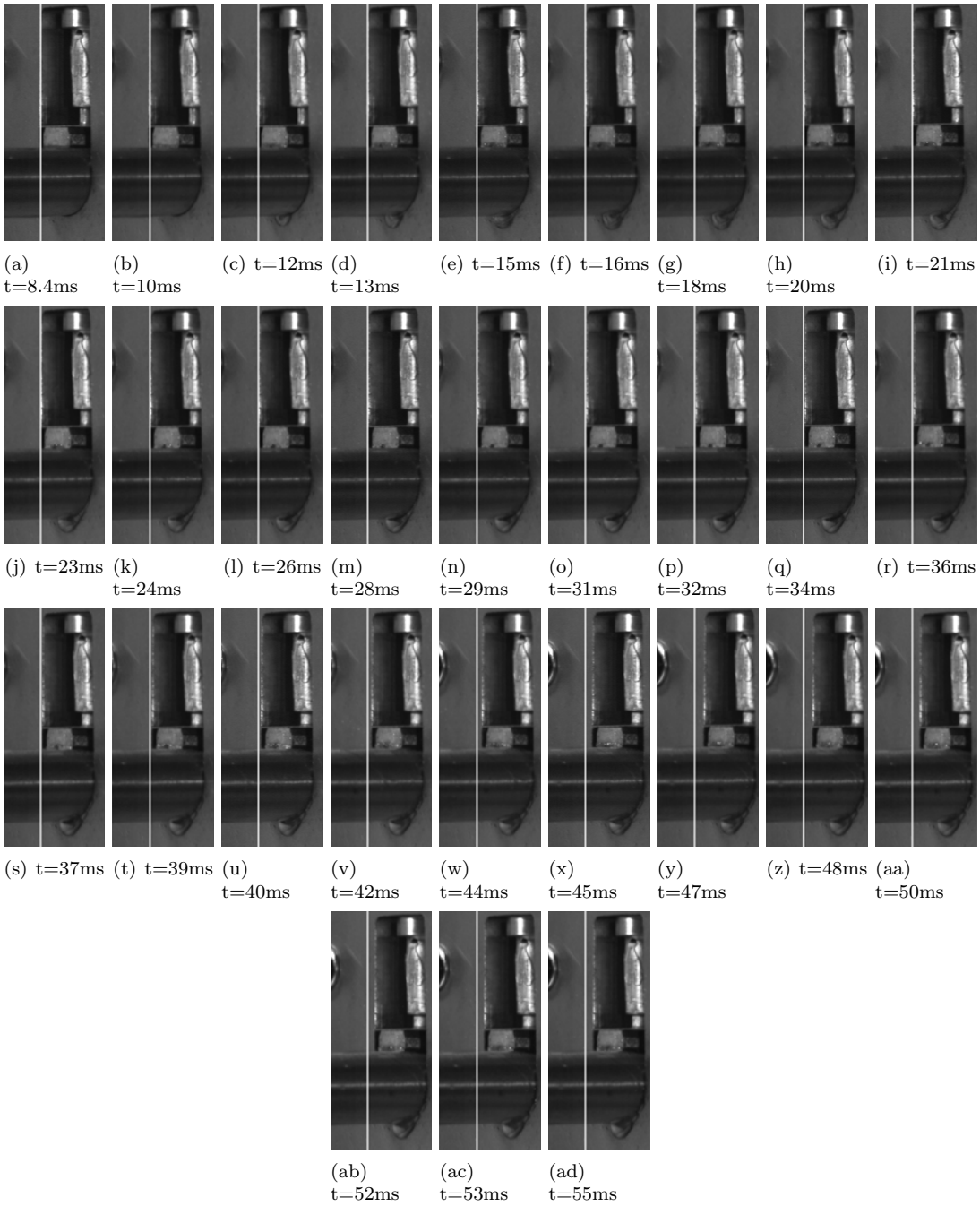

Figure B.1: Response during the experiment

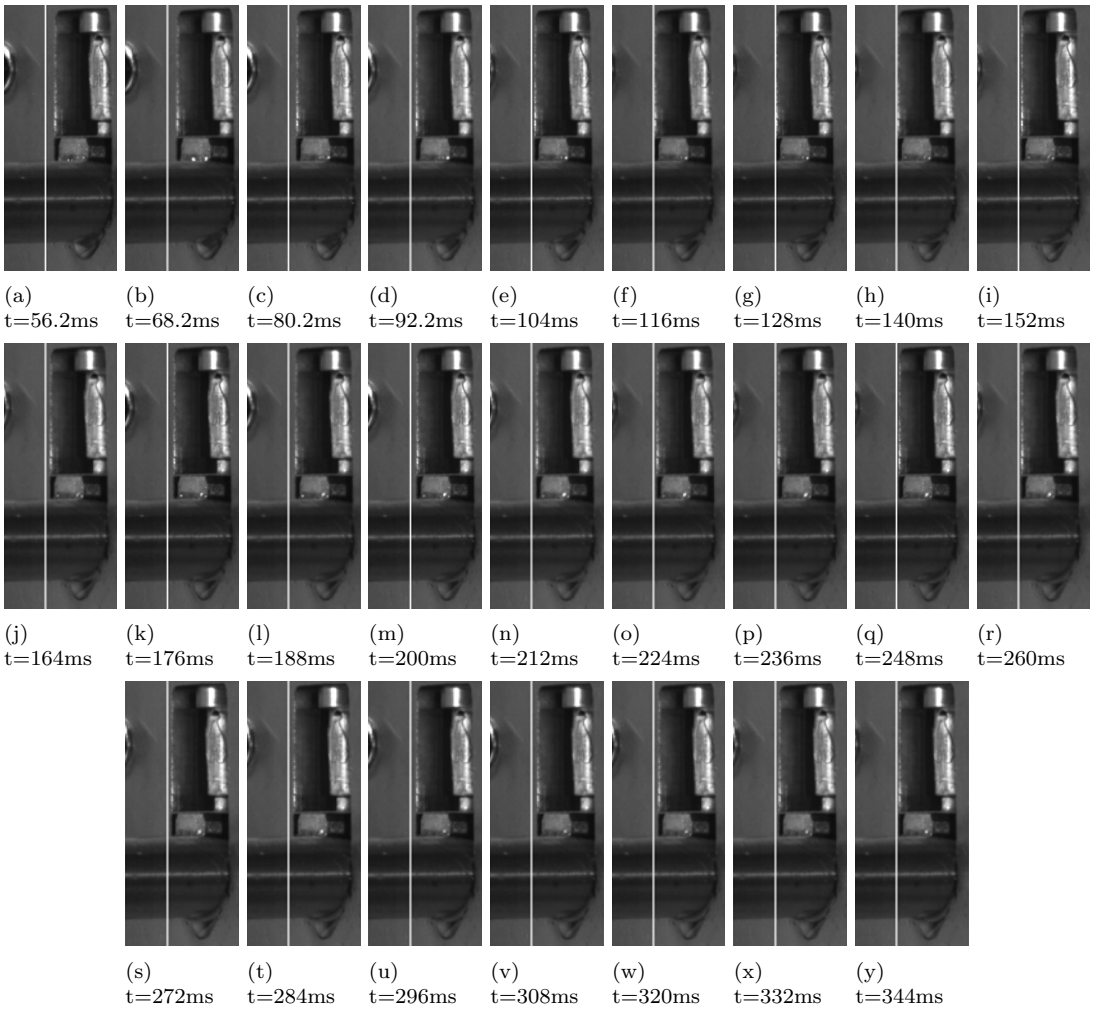

Figure B.2: The response after the experiment

B.2 Balanced Load-Frame

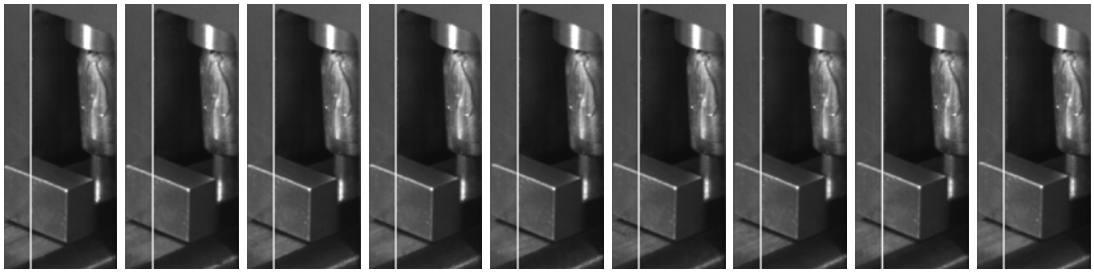

(a) t=0ms (b) t=1.6ms (c) t=3.2ms (d) t=4.8ms (e) t=6.4ms (f) t=8ms (g) t=9.6ms (h) t=11ms (i) t=13ms

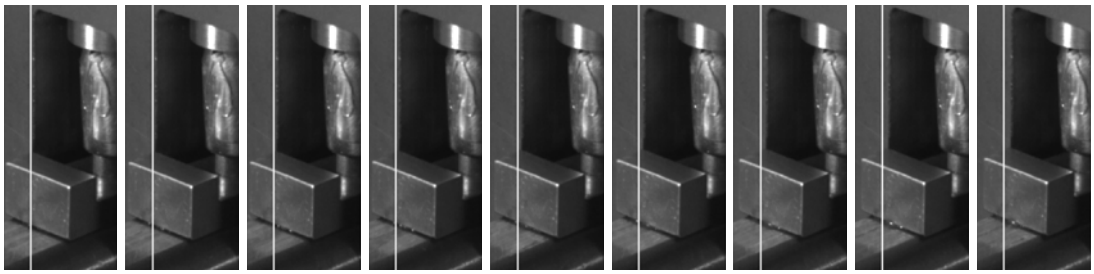

(j) t=14ms (k) t=16ms (l) t=18ms (m) t=19ms (n) t=21ms (o) t=22ms (p) t=24ms (q) t=26ms (r) t=27ms

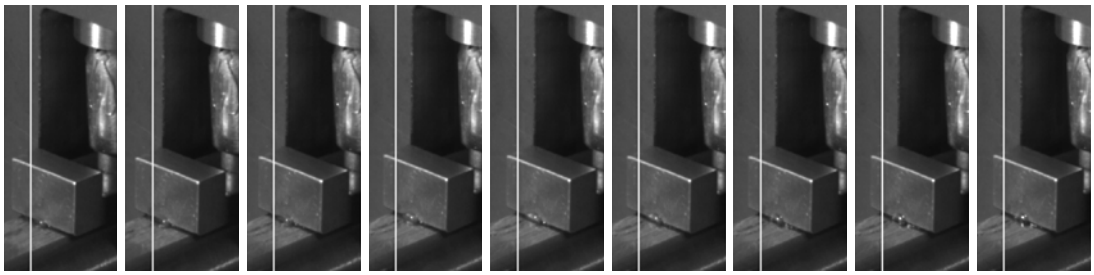

(s) t=29ms (t) t=30ms (u) t=32ms (v) t=34ms (w) t=35ms (x) t=37ms (y) t=38ms (z) t=40ms (aa) t=42ms

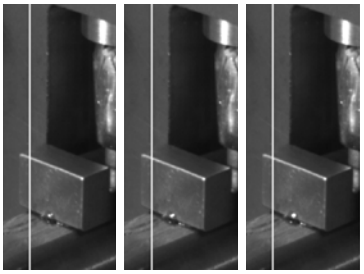

(ab) t=43ms (ac) t=45ms (ad) t=46ms

Figure B.3: The response during the experiment

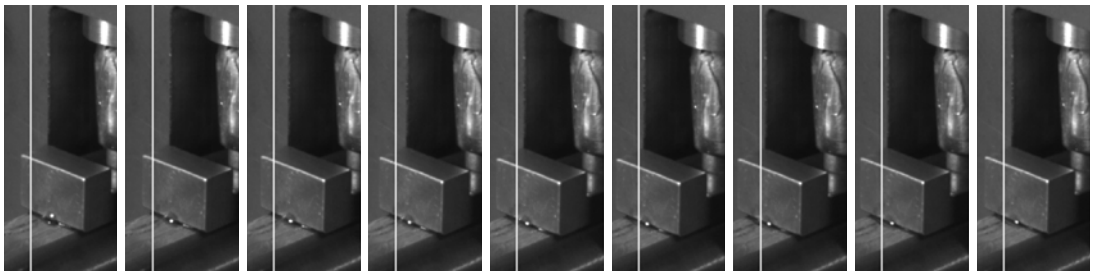

(a) t=47.7ms (b) t=59.7ms (c) t=71.7ms (d) t=83.7ms (e) t=95.7ms (f) t=108ms (g) t=120ms (h) t=132ms (i) t=144ms

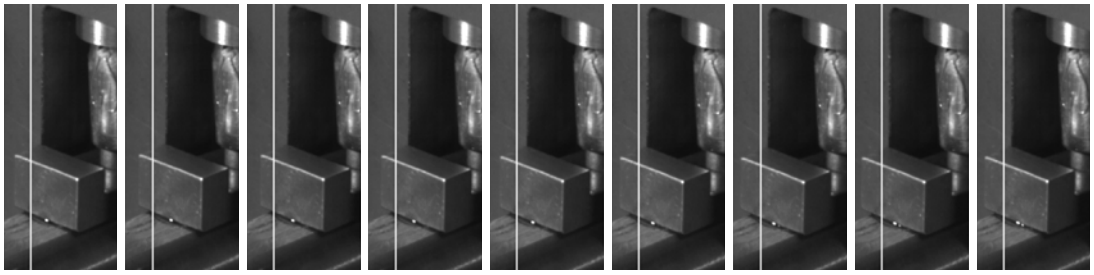

(j) t=156ms (k) t=168ms (l) t=180ms (m) t=192ms (n) t=204ms (o) t=216ms (p) t=228ms (q) t=240ms (r) t=252ms

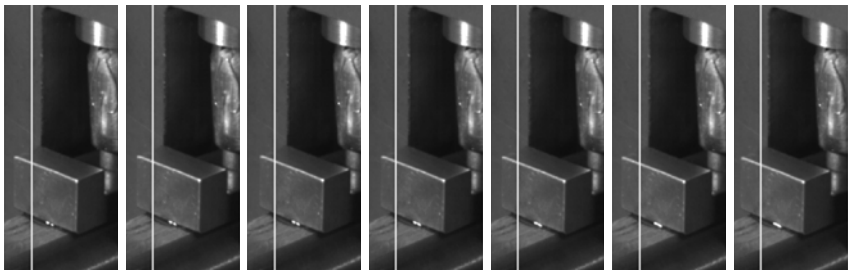

(s) t=264ms (t) t=276ms (u) t=288ms (v) t=300ms (w) t=312ms (x) t=324ms (y) t=336ms

Figure B.4: The response after the experiment

Appendix C

Strain Rate

The strain rate ($\dot{\epsilon}$) is the deformation rate of the specimen and is defined as follows

$$\dot{\epsilon} = \frac{V_1 - V_2}{L} \tag{C.1}$$

where V_1 and V_2 are the velocities of the boundary conditions either side of the specimen and L is the length of the specimen, see Figure C.1. It is desirable to have a constant strain rate over the experiment. The strain rate typically varies during the experiment, some average or otherwise determined value is normally quoted as the rate for the test.

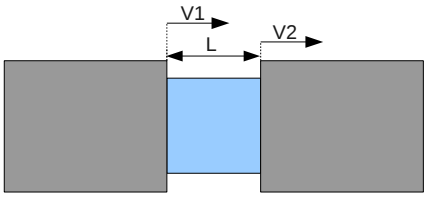

Figure C.1: Strain rate schematic

Appendix D

Calculations

In this appendix the design calculations discussed in Section 3.2 are presented in more detail. These calculations cover with the sizing the wedge bar, load-cell design and compliance calculations for the components of the IST.

D.1 Wedge Bars

The calculations presented here are used to calculate the strain rate history achievable for different wedge bars. The results are used to select the basic wedge bar length, diameter, slope and stroke. A free body diagram showing the forces acting on the wedge bar is shown in Figure D.1.

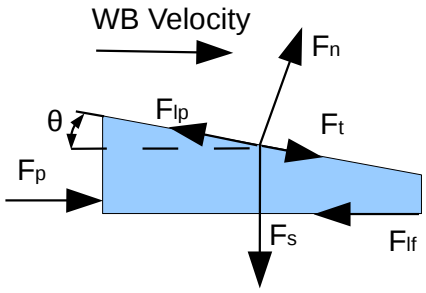

Figure D.1: Wedge bar free body diagram (F_p only present in the back pressure experiments)

where F_s is the specimen force, F_n is the normal reaction force, F_t is the tangential force, F_{LP} is the frictional force acting on the wedge bar from the loading platform, F_{lf} is the frictional force acting on the wedge bar from the load-frame and θ is the wedge bar slope. In the calculations presented below M, L, ϕ and ρ refer to mass, length, diameter and density respectively. Subscript wb and s refers to the wedge bar and specimen properties.

D.1.1 Impact Driven Experiments

The calculations for the impact driven experiments are presented first. An overview of the steps followed are:

- Calculate the energy stored in the wedge bar at the start of the experiment

- Calculate the forces retarding the wedge bar motion
- Calculate the velocity history of the wedge bar
- Calculate the strain rate history of the specimen

The wedge bar slope is selected first. Once selected, the corresponding wedge bar velocity required for a given strain rate is calculated as follows

$$V_{\mathrm{wb}} = \frac{\dot{\epsilon} L_s}{\tan(\theta_{\mathrm{wb}})} \tag{D.1}$$

The the mass of the wedge bar as follows

$$M_{\mathrm{wb}} = L_{\mathrm{wb}} \tfrac{1}{4} \pi (\phi_{\mathrm{wb}})^2 \rho_{\mathrm{wb}} \tag{D.2}$$

Once the wedge bar mass and velocity are known the energy stored in the wedge bar is calculated as follows

$$Ek_{\mathrm{wb}} = \frac{1}{2} M_{\mathrm{wb}} (V_{\mathrm{wb}})^2 \tag{D.3}$$

The stroke required to strain the specimen to a given strain is calculated as follows

$$Stroke = \frac{\epsilon L_s}{\tan(\theta)} \tag{D.4}$$

Frictional force acting on the wedge bar is calculated

$$\begin{aligned} F_s &= \sigma_s \frac{\pi \phi_s^2}{4} \\ F_n &= F_s \times cos(\theta) = \frac{\sigma_s \pi \phi_s^2 cos(\theta)}{4} \\ F_{lp} &= \mu F_n = \frac{\mu \sigma_s \pi \phi_s^2 \cos(\theta)}{4} \\ F_{lf} &= \mu F_s \end{aligned} \tag{D.5}$$

The forces retarding the motion of the bar are calculated as follows

$$F = F_s \sin\theta + F_{lp} \cos\theta + F_{lf} \tag{D.6}$$

As θ is small, $cos(\theta) \approx 1$ and $sin(\theta) \approx 0$. The above simplifies to

$$F = F_{lp} + F_{lf} = 2 \times \mu F_s \tag{D.7}$$

The total energy required to overcome friction in the experiment is calculated as follows

$$E = F \times d \tag{D.8}$$

The energy required to deform the specimen is insignificant compared to the friction acting on the wedge bar and can safely be ignored. Using conservation of energy the velocity of the wedge bar is calculated.

$$\begin{aligned} Ek_2 &= Ek_1 - F \times d \\ d &= \frac{\epsilon L_s}{tan(\theta)} \\ \frac{1}{2} M_{\mathrm{wb}} V_{2\mathrm{wb}}^2 &= \frac{1}{2} M_{\mathrm{wb}} V_{1\mathrm{wb}}^2 - F \times \frac{\epsilon L_s}{tan(\theta)} \\ V_{2\mathrm{wb}} &= \sqrt{V_{1\mathrm{wb}}^2 - \frac{2F\epsilon L_s}{M_{\mathrm{wb}} tan(\theta)}} \end{aligned} \tag{D.9}$$

Once the wedge bar velocity has been calculated the instantaneous strain rate in the specimen is calculated as follows

$$\dot{\epsilon} = \frac{V_2}{L_s \epsilon} \tag{D.10}$$

D.1.2 Back Pressure Driven Experiments

The process followed for the back pressure driven experiments is the same as for the impact driven experiments except that the back pressure provides an additional driving force during the experiments. The energy provided by the back pressure is calculated as follows

$$E_p = F_p \times d \tag{D.11}$$

The energy balance including the driving force provided by the back pressure is calculated as follows

$$\begin{aligned} Ek_2 &= Ek_1 - F \times d + F_p \times d \\ d &= \frac{\epsilon L_s}{tan(\theta)} \\ \frac{1}{2} M_{\mathrm{wb}} V_{2\mathrm{wb}}^2 &= \frac{1}{2} M_{\mathrm{wb}} V_{1\mathrm{wb}}^2 + (F_p - F) \times \frac{\epsilon L_s}{tan(\theta)} \end{aligned} \tag{D.12}$$

Rearranging for V_2 gives

$$V_{2\mathrm{wb}} = \sqrt{V_{1\mathrm{wb}}^2 + \frac{2\left(F_p - F\right)\epsilon L_s}{M_{\mathrm{wb}} tan(\theta)}} \tag{D.13}$$

Strain rate is calculated the same as is for the impact driven tests.

$$\dot{\epsilon} = \frac{V_2}{L_s \epsilon} \tag{D.14}$$

D.1.3 Rate Histories

The above formula are programmed into Open Office Calc to investigate the strain rate history assuming an elastic perfectly plastic specimen with a 200 GPa modulus and 200 MPa flow stress with no strain hardening. The results for the two wedge bars selected are shown in Figure D.2 for the impact and back pressure driven loading.

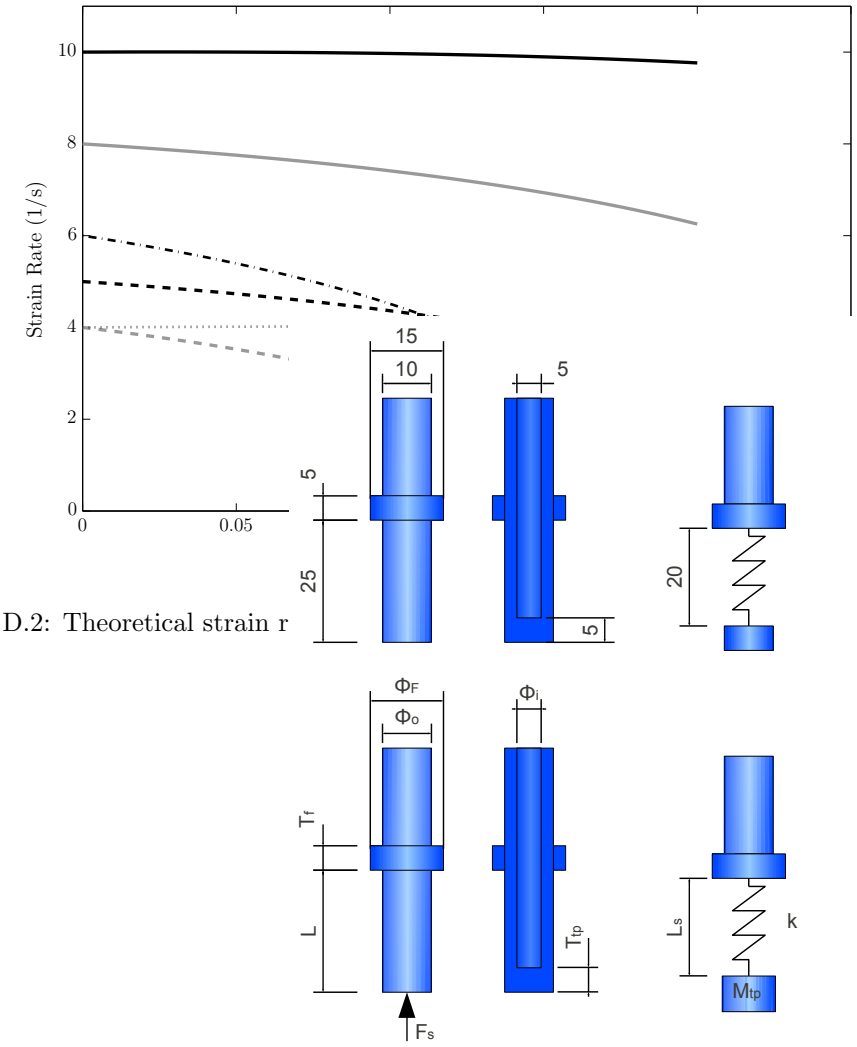

(a)

Figure D.2: Theoretical strain r ...etry

Figure D.3: Load-cell schematic

D.2 Load-Cell

This section details the calculations relating to the load-cell. The initial calculations of the load-cell focus on calculating the stress in the load-cell for a given specimen load, the signal to noise ratio and the natural frequency of the load-cell. The dimensions used in these calculations are shown in Figure D.5.

D.2.1 Stress Calculations

In the following calculations F, A σ, ϕ and E_{mod} are the force, area, stress, diameter and elastic modulus respectively. Subscripts s, o and i refer to the spring properties, outer and inner load-cell diameter. The stress in the load-cell walls is calculated as follows

$$\sigma = \frac{F_s}{A_s} = \frac{4F_s}{\pi\left(\phi_o - \phi_i\right)^2} \tag{D.15}$$

The strain in the load-cell walls is calculated as follows.

$$\epsilon = \frac{\sigma}{E_{mod}} = \frac{1}{E_{mod}} \times \frac{4F_s}{\pi \left(\phi_o - \phi_i\right)^2} \tag{D.16}$$

D.2.2 Theoretical Strain Gauge Output

The theoretical load-cell output is calculated based on strain gauge theory in a similar method to the HPB calibration presented in Section 4.4.3. The stress in the load-cell is calculated using equation 4.10 repeated here for convenience.

$$\sigma = KV_{out} \quad \text{where} \quad K = \left(\frac{4E}{GainK_{gf}NV_{BV}}\right) \quad [49] \tag{D.17}$$

To convert from stress in the load-cell to measured force we multiply by the area of the load-cell,(A_{lc}).

$$F = KV_{out}A_{lc} = K_f V_{out} \text{ where } K_f = \left(\frac{4E}{GainK_{gf}NV_{BV}}\right) A_{lc} \tag{D.18}$$

Making the substitutions E = 200 GPa, $Gain$ = 1000, K_{gf} = 2.12, N = 4, V_{BV} = 2.01 and A_{lc} = 58.9×10$^-$6 m^3 gives a theoretical calibration factor of K_f = 2791 N/V.

D.2.3 Signal to Noise Ratio

Once the output voltage is calculated the signal to noise ratio of the load-cell can be approximated. The signal to noise ratio is used to give an indication of the minimum stress that can be reliably measured with the load-cell. The noise on the measured signals of the SHPB experiments performed at BISRU is typically ± 0.01 V. The results of output voltage and signal to noise ratio vs. specimen stress are shown in Table D.1.

Table D.1: Theoretical signal to noise ratio

Specimen Stress (MPa)	Measured Voltage (V)	Signal to noise ratio
25	0.17	8.8
50	0.35	17.5
75	0.525	26.3
100	0.70	35.0
200	1.40	70.0
300	2.10	105.0
400	2.80	140.0
500	3.50	175.0

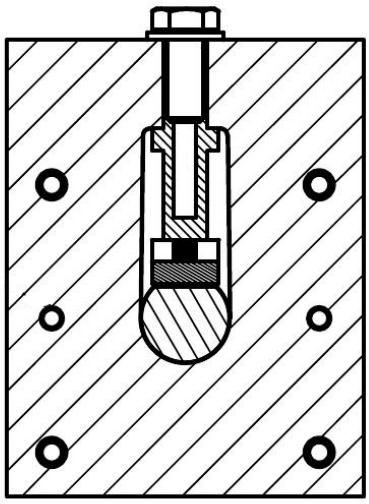

Figure D.4: IST Assembly cross section

D.3 IST Compliance

The overall compliance of the IST has been calculated in Sections 3.3.5 and 6.3 using the FEA and experimental results. The analytical calculations presented in this section are done to determine the contribution each individual component to the overall compliance of the IST. The assumptions made are expected to give a conservative value for the compliance of the IST. The cross sectional view of the load path of the IST is shown in Figure D.4. The load path consists of the load-frame, load-cell, loading platform and wedge bar. The machining drawings for the components analysed are shown in Appendix G. As all the components in the IST load path are steel the elastic modulus of 200 GPa is used in all calculations. Each component is broken down into sections whose compliance is then solved for as follows

$$k = \frac{AE}{L} \tag{D.19}$$

The total compliance, of each component and later the IST is calculated using the equivalent spring method

$$\frac{1}{k_e} = \frac{1}{k_1} + \frac{1}{k_2} \cdots + \frac{1}{k_n} \tag{D.20}$$

The load-cell dimensions are shown in Figure D.5. The compliance is calculated for the spring section, base and top platform and shown in Table D.2. The full area is taken for the spring and base sections, but the top platform compliance is calculated based only on the area in contact with the specimen.

The loading platform dimensions are given in Figure D.6. The IST is designed so that the loading platform operates under compression only. The high speed camera footage shown in Section 5.7 and the analysis done in Section 6.9 and Section 6.10 covers ways the IST deflects during testing and does not indicate that the loading platform experiences any bending. Bending compliance of the loading platform is therefore ignored. The specimen compresses directly against the loading platform and hence the compliance of the loading platform is approximated as that of a 5 mm diameter cylinder. The nominal thickness of the loading platform is used for the length.

Table D.2: Components compliance

Component	Area mm^2	Length mm	Stiffness kN/mm
Base	$\frac{\pi(15^2-5^2)}{4} = 157$	5	6283
Spring	$\frac{\pi(10^2-5^2)}{4} = 59$	15	785
Top Platform	$\frac{\pi(5^2)}{4} = 20$	5	785
Total			370

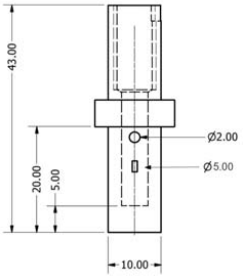

Figure D.5: Load-cell

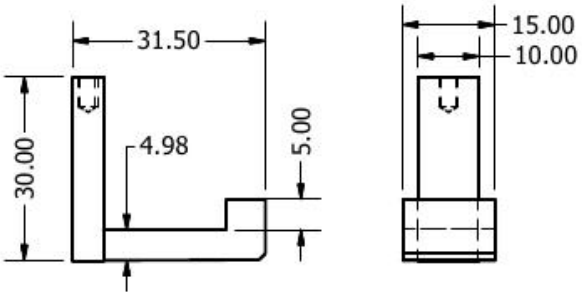

Figure D.6: Loading platform

$$
\begin{aligned}
K_{Lp} &= \frac{AE}{l} = \frac{\pi\phi^2 E}{4l} \\
&= \frac{\pi(0.005^2)200e^9}{4 \times 0.005} \\
&= 785 \times 10^6 \ N/m \qquad \text{(D.21)} \\
&= 785 \ kN/mm \qquad \text{(D.22)}
\end{aligned}
$$

The compliance of the wedge bar is approximated as a 20x20 mm square block 5 mm thick.

$$
\begin{aligned}
K_{Wb} &= \frac{AE}{l} \\
&= \frac{0.02 \times 0.005 \times 200e^9}{0.02} \\
&= 1000 \times 10^6 \ N/m \qquad \text{(D.23)} \\
&= 1000 \ kN/mm \qquad \text{(D.24)}
\end{aligned}
$$

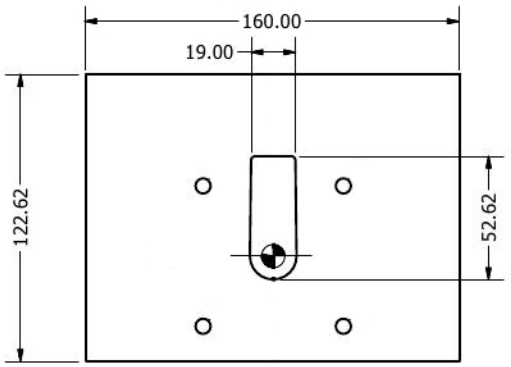

Figure D.7: Load-frame

It is expected that the deformation seen in the load-frame will be localised and not carried across the entire width of the load-frame. The assumption that 20 mm on either side of the wedge bar will carry the force is made.

$$\begin{aligned} K_{Lf} &= \frac{AE}{l} \\ &= \frac{2 \times 0.02 \times 0.02 \times 200e^9}{0.055} \\ &= 2909 \times 10^6 \ N/m \qquad \text{(D.25)} \\ &= 2909 \ kN/mm \qquad \text{(D.26)} \end{aligned}$$

D.3.1 IST

The analytical solution to the IST compliance is calculated using equation D.20 once the compliance of each individual component has been calculated. The compliance of each individual component and the combines compliance of the IST are shown in Table D.3.

Table D.3: Components compliance summary

Component	Area mm^2	Length mm	Stiffness kN/mm
Load-cell	59	20	369
Loading platform	20	5	785
Wedge bar	100	20	1000
Load-frame	800	55	2909
IST	-	-	194

Due to the assumptions made the calculated compliance is expected to be a conservative. However the calculated compliance of the IST is nearly twice that of the FEA and experimental results. It is expected that this due to localised deformation at the contact points between the wedge bar and load-frame and between the load-cell and load-frame.

Of all the components in the load path, the load-cell has the lowest compliance. However, even doubling the compliance of the load-cell will only increase the compliance of the IST by 35%. If larger increases in compliance are required the compliance of all the components in the load path will need to be increased.

Appendix E

FEA Input Deck

E.1 Typical FEA Input Deck

```
*Heading
 Loadframe(2mm) Loadcell(1mm) Specimen(0.5mm)
** Job name: CoarseMesh Model name: LoadframeLoadcellSpecimenCoarse
** Generated by: Abaqus/CAE Version 6.8-3
*Preprint, echo=NO, model=NO, history=NO, contact=NO
**
** PARTS
**
*Part, name=Loadcell
*Node
      1, 0.00499999989, 0.0135379564,           0.
      2, 0.00249999994, 0.0135379564,           0.
      3, 0.00249999994,  0.011537957,           0.
      4, 0.00499999989,  0.011537957,           0.
      5,           0., 0.0135379564, 0.00249999994
.
.
.
*Surface, type=ELEMENT, name=LoadcellShaft
_LoadcellShaft_S2, S2
_LoadcellShaft_S1, S1
** Section: Loadcell
*Solid Section, elset="Loadcell all", material="Steel Elastic"

*End Part
**
*Part, name="Momolythic Load Frame"
*Node
      1, 0.00624930998, -0.0098825302,           0.
      2, 0.0262499992, -0.0098825302,           0.
      3, 0.0262499992, -0.0350000001,           0.
```

```
      4, -0.00374999992, -0.0350000001,           0.
      5, -0.00374999992, -0.0199999996,           0.
.
.
.
*Surface, type=ELEMENT, name=LoadframeHole
_LoadframeHole_S2, S2
_LoadframeHole_S3, S3
_LoadframeHole_S4, S4
** Section: Loadframe
*Solid Section, elset=_PickedSet75, material=Loadframe

*End Part
**
*Part, name=Specimen
*Node
      1, 0.00249999994, 0.00124999997,           0.
      2,           0., 0.00124999997,          0.
      3,           0., 0.00374999992,          0.
      4,           0., 0.00124999997, 0.00499999989
      5, 0.00249999994, 0.00124999997, 0.00499999989
.
.
.
*Surface, type=ELEMENT, name="Specimen Loadcell"
"_Specimen Loadcell_S2", S2
** Section: Specimen
*Solid Section, elset="Specimen all", material=SpecimenMaterial

*End Part
**
**
** ASSEMBLY
**
*Assembly, name=Assembly
**
*Instance, name=Loadcell-1, part=Loadcell
-0.00375000000017455, 0.00758204324997961,         0.01
*End Instance
**
*Instance, name=Specimen-1, part=Specimen
-0.00375000000017455, 0.00761999999999999,      0.00875
-0.00375000000017455, 0.00761999999999999,      0.00875, 0.996250012687878, 0.00762000000000079,
*End Instance
**
*Instance, name="Momolythic Load Frame-1", part="Momolythic Load Frame"
*End Instance
**
*Nset, nset=_PickedSet57, internal, instance="Momolythic Load Frame-1"
    1,    5,    6,    8,   11,   15,   16,   20,   22,   61,   62,   63,   64,   65,   66,   67
   68,   79,   80,   81,   82,  126,  127,  128,  129,  140,  141,  142,  143,  144,  145,  146
  147,  179,  180,  181,  182,  183,  184,  185,  186,  197,  198,  199,  200,  244,  245,  246
  247,  258,  259,  260,  261,  262,  263,  264,  265,  315,  316,  317,  318,  319,  320,  321
```

```
.
.
.
** MATERIALS
**
*Material, name=Loadframe
*Density
7800.,
*Elastic
 2e+11, 0.3
*Material, name=SpecimenMaterial
*Density
7800.,
*Elastic
 2e+11, 0.3
*Plastic
 2.1e+08,0.
 2.1e+08,1.
*Material, name="Steel Elastic"
*Density
7800.,
*Elastic
 2e+11, 0.3
**
** INTERACTION PROPERTIES
**
*Surface Interaction, name="Contact with friction"
*Friction
 0.1,
*Surface Behavior, pressure-overclosure=HARD
*Surface Interaction, name=ContactNoFriction
*Surface Behavior, pressure-overclosure=HARD
**
** BOUNDARY CONDITIONS
**
** Name: Bar Type: Symmetry/Antisymmetry/Encastre
*Boundary
_PickedSet57, ENCASTRE
** ----------------------------------------------------------------
**
** STEP: Displacement
**
*Step, name=Displacement
Deform the specimen
*Dynamic, Explicit
, 0.025
*Bulk Viscosity
0.06, 1.2
**
** BOUNDARY CONDITIONS
**
** Name: Displacement Type: Velocity/Angular velocity
*Boundary, type=VELOCITY
```

```
Specimen-1."Specimen force", 2, 2, 0.05
**
** INTERACTIONS
**
** Interaction: Loadcell specimen
*Contact Pair, interaction=ContactNoFriction, mechanical constraint=PENALTY, cpset="Loadcell specime
Loadcell-1."Loadcell Specimen", Specimen-1."Specimen Loadcell"
** Interaction: LoadframeLoadcell
*Contact Pair, interaction=ContactNoFriction, mechanical constraint=PENALTY, cpset=LoadframeLoadcell
Loadcell-1."Loadcell Loadframe", "Momolythic Load Frame-1".LoadframeLoadcell
** Interaction: LoadframeLoadcellShaft
*Contact Pair, interaction=ContactNoFriction, mechanical constraint=PENALTY, cpset=LoadframeLoadcell
"Momolythic Load Frame-1".LoadframeHole, Loadcell-1.LoadcellShaft
**
** OUTPUT REQUESTS
**
*Restart, write, number interval=1, time marks=NO
**
** FIELD OUTPUT: F-Output-1
**
*Output, field, variable=PRESELECT
**
** HISTORY OUTPUT: Strain guage
**
*Output, history, time interval=1e-06
*Node Output, nset=Loadcell-1."Strain guage 1"
COOR2,
*Element Output, elset=Loadcell-1."Strain guage 1"
E22, S22
*End Step
```

Appendix F

Theoretical ROS Response

```
% Sensing area approximation

clc
clear
close all

PlottingParamaters



start  = 0.1
stop = 10
step = 0.01 ;
% pitch =2
Ratio = zeros((stop-start)/step, 6) ;
for l = 1:3
sensing = [4.5,5,5.5]
    SDia = sensing(l) ;

for k = 1:(stop-start)/step
    %  P_Number = SDia/pitch  % number of lines in half the sensing area.
pitch = k*step

 P_Number = (SDia/2 - pitch/4)/(pitch/2 ) +1

steps = ceil(P_Number)

area = zeros(1,length(pitch)) ;

% LWidth = pitch/2; % the width of each graduation

d = zeros(1,steps);           % the strart of every black line
SArea = zeros(1,steps+1);         % the area of every black segment
```

```
for i = 1:(steps)
   d(i+1) = pitch/4 + (i-1) * pitch/2 ;
   if d(i+1) >SDia/2
       d(i+1) = SDia/2 ;
   end
   SArea(i) =  (1/8)*(SDia^2)*(2*acos((2*d(i))/SDia) - sin(2*acos((2*d(i))/SDia))) ; % The area of e
end

d
SArea

 BlackArea = zeros(1,ceil(steps/2)) ;
for j = 1:ceil(steps/2)
    BlackArea(j) = SArea(2*j-1) - SArea(2*j);
end
BlackArea

BA = sum(BlackArea)/SArea(1)

ratio = abs(sum(BlackArea)/SArea(1) -(1 - sum(BlackArea)/SArea(1) ))*100

Ratio(k,l*2 -1 ) = pitch ;
Ratio(k,l*2 ) = ratio;
end

end
```

Appendix G

Drawings

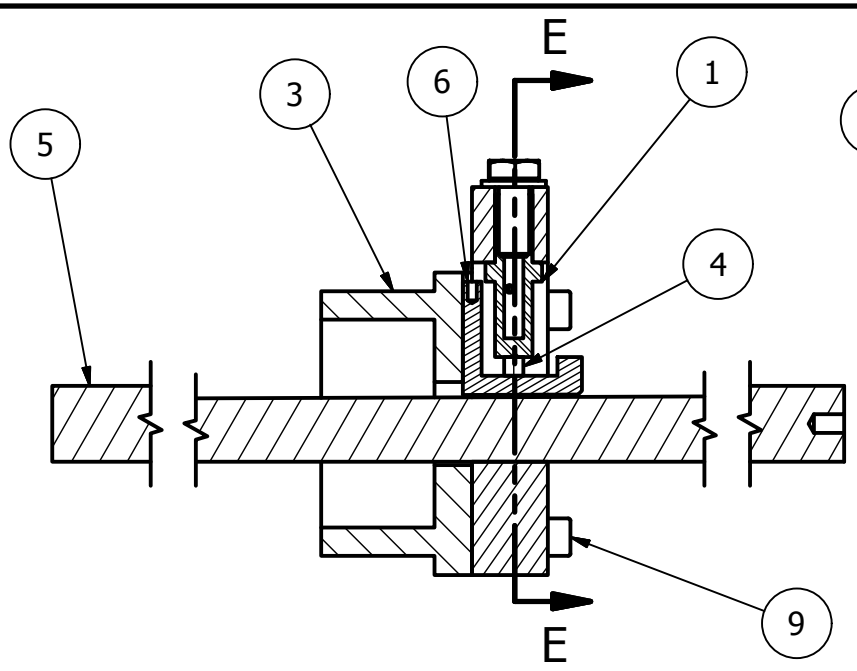

SECTION C-C

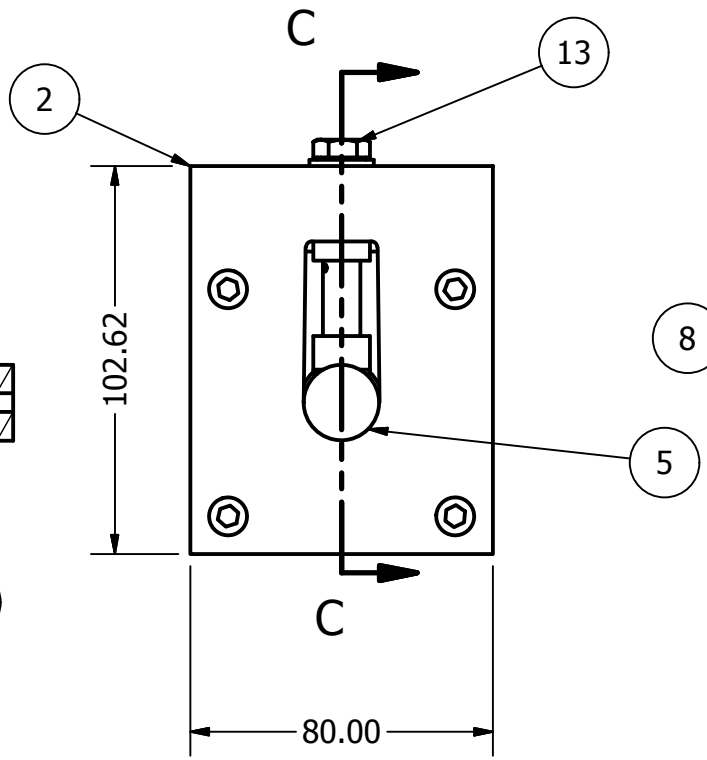

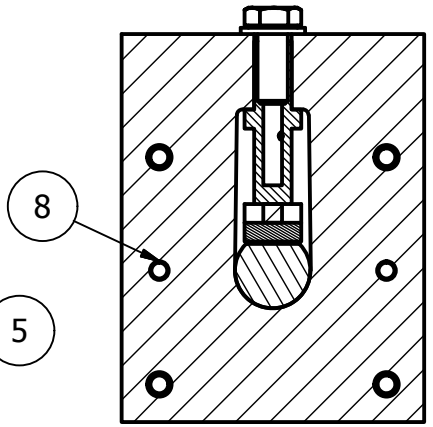

SECTION E-E
SCALE 1:2

Parts List		
ITEM	QTY	PART NUMBER
1	1	loadcell
2	1	MonolythicLoadFrame
3	1	MonolythicMountingPlate
4	1	Compression test specimen
5	1	wedgebar2500
6	1	MLFPatformCompactCGSpecimen
8	2	BS 1804-2 - 5 x 20
9	4	ISO 4762 - M6 x 30
10	1	BS 4320 - M8 (Form A)
13	1	AS 1110 - M8 x 20

University of Cape Town

Department of mechanical engineering

Title: MLF Assembly

Size	Tolerance		Drawing number
A4	U.O.S 0.05mm		
Scale:1:1	Sheet:1		Drawing by Melchior Stander

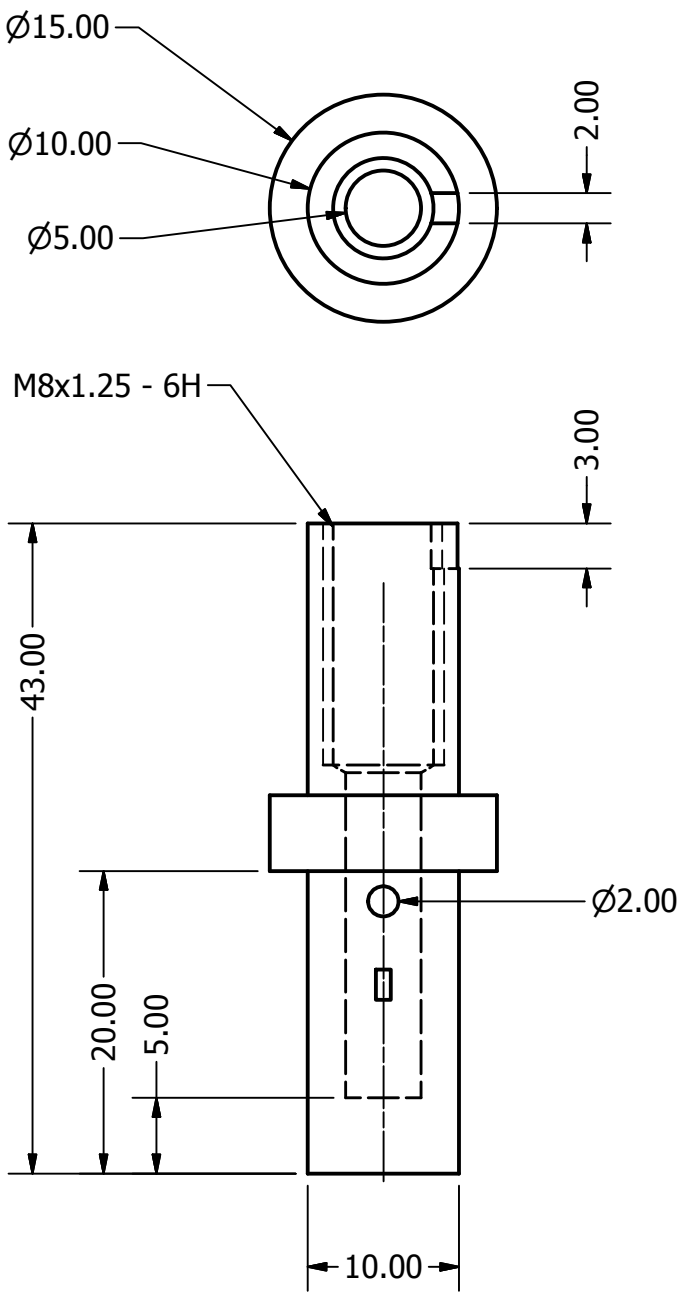

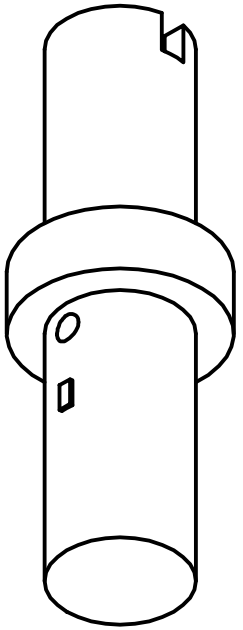

Material: Stainless steel		QUANTITY: 1
University of Cape Town Department of mechanical engineering		
Title Load cell		
Size A4	Tolerance U.O.S 0.05mm	Drawing number
Scale: 2:1	Sheet: 1	Drawing by Melchior Stander

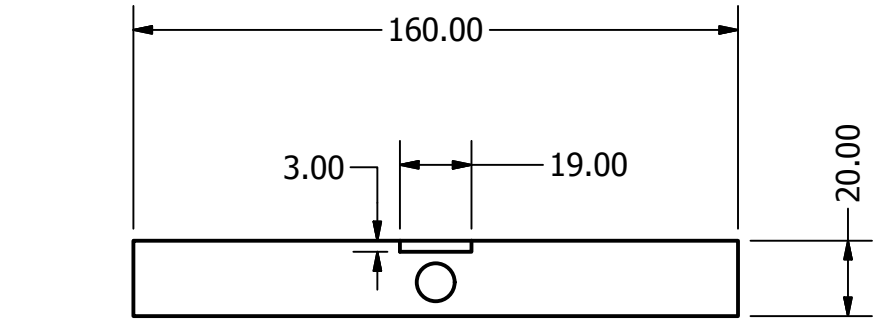

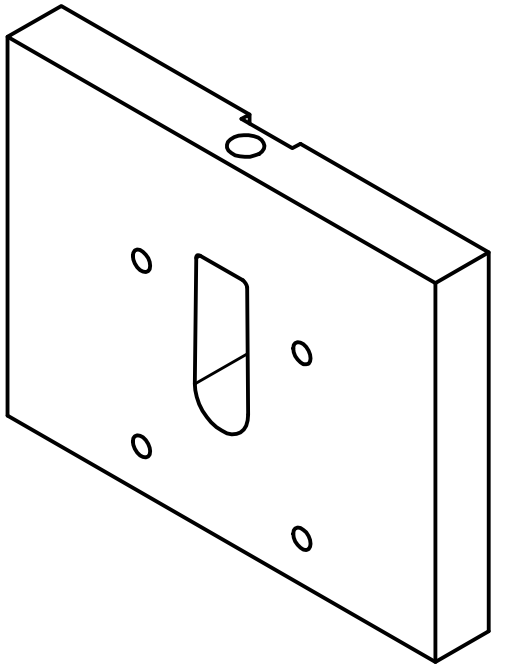

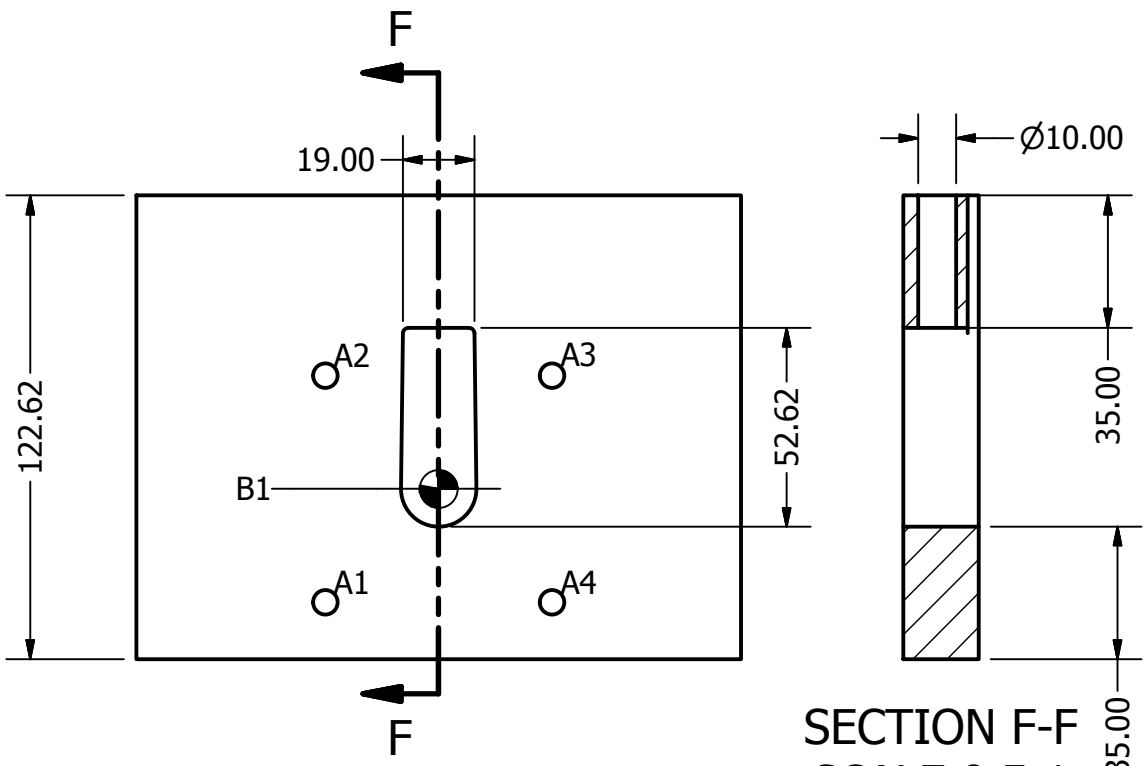

SECTION F-F
SCALE 0.5:1

Hole Table			
HOLE	XDIM	YDIM	DESCRIPTION
A1	-30.00	-30.00	Ø6.50 THRU
A2	-30.00	30.00	Ø6.50 THRU
A3	30.00	30.00	Ø6.50 THRU
A4	30.00	-30.00	Ø6.50 THRU
B1	.00	.00	-

Material: Cast Iron			QUANTITY:1
University of Cape Town Department of mechanical engineering			
Title Monolithic load frame			
Size A4	Tolerance U.O.S 0.05mm		Drawing number
Scale:2:1	Sheet:1		Drawing by Melchior Stander

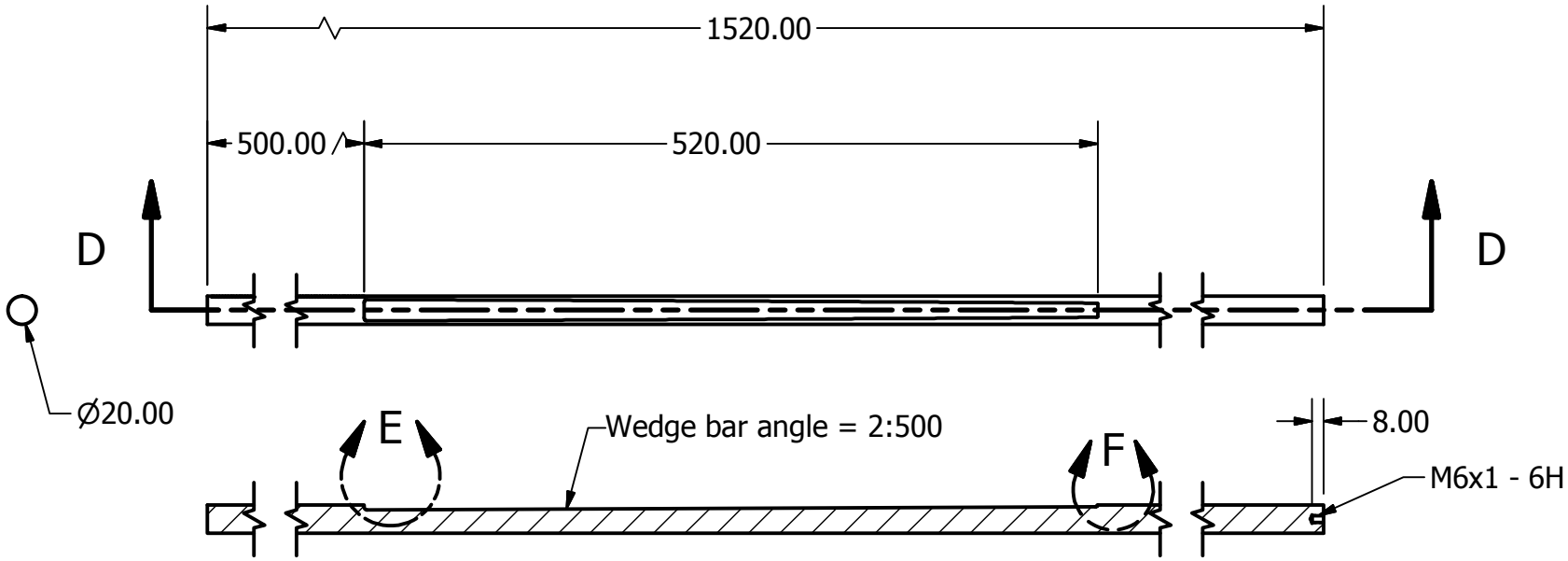

SECTION D-D

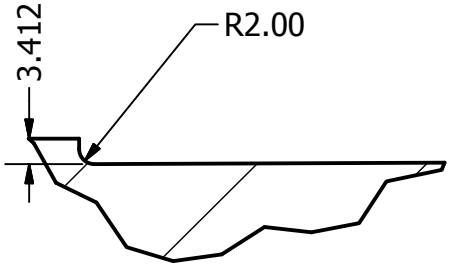

DETAIL E

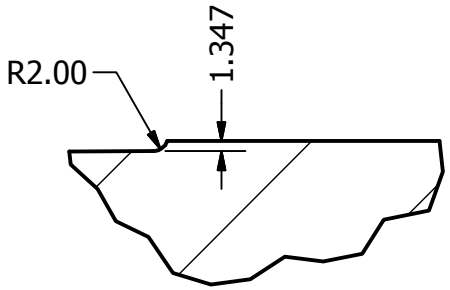

DETAIL F

Material: Silver Steel			QUANTITY:1
University of Cape Town Department of mechanical engineering			
Title: Wedge bar (2:500)			
Size A4	Tolerance U.O.S 0.05mm		Drawing number W002
Scale:0.2:1	Sheet:1		Drawing by Melchior Stander

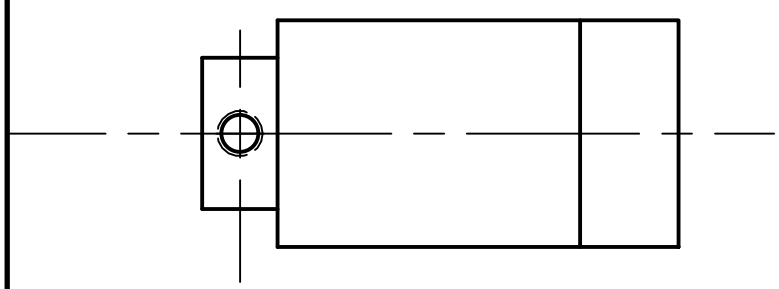

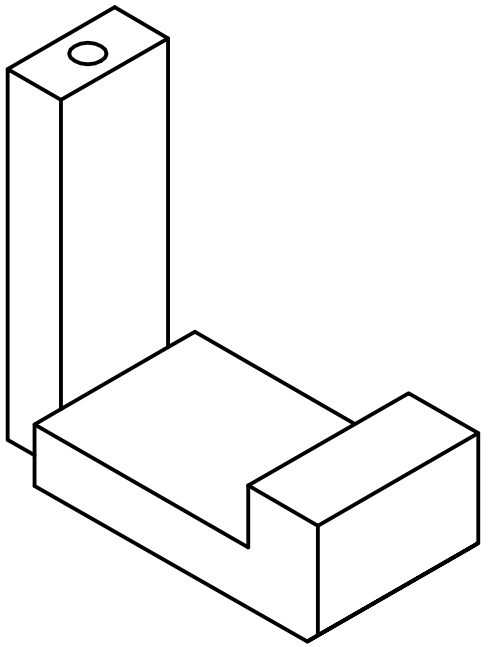

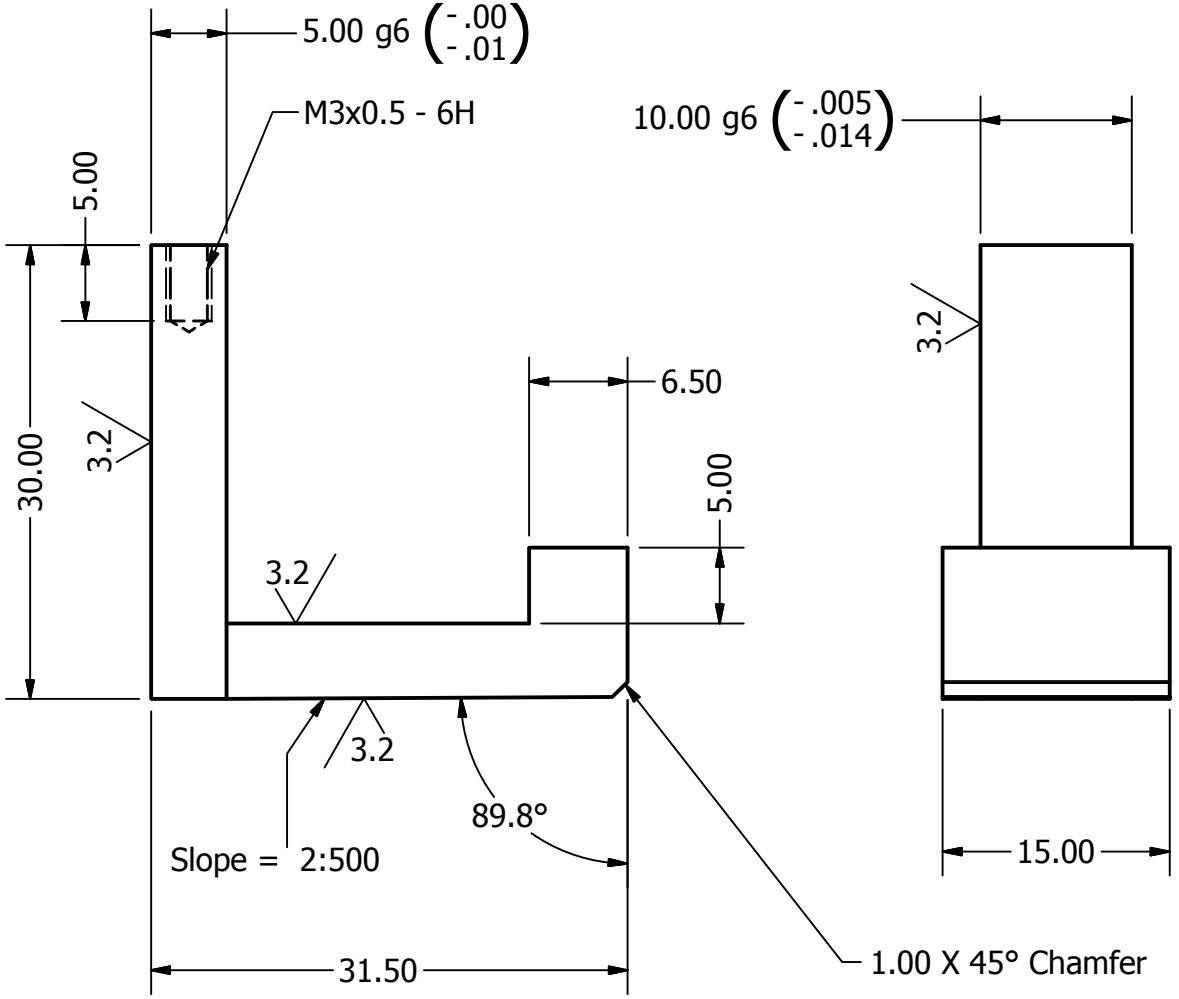

Material: Guage Plate		QUANTITY: 1
University of Cape Town Department of mechanical engineering		
Title Monolythic loading platform		
Size A4	Tolerance U.O.S 0.05mm	Drawing number
Scale: 2:1	Sheet: 1	Drawing by Melchior Stander

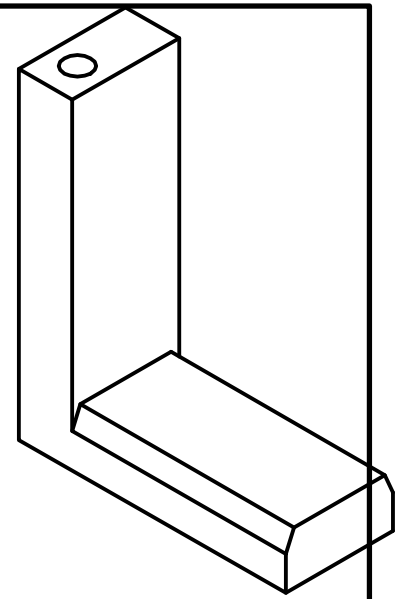

5.00 g6 $\left(^{-.00}_{-.01}\right)$

30.00

5.00 $^{+.01}_{-.01}$

89.77°

Angle = 1:500

10.00 g6 $\left(^{-.005}_{-.014}\right)$

To be a sliding fit with the mounting plate supplied

.75

67.0°

10.00

25.00

Material: Silver Steel		QUANTITY: 1
University of Cape Town Department of mechanical engineering		
Title Loading platform (1:500) (5mm specimen)		
Size A4	Tolerance U.O.S 0.05mm	Drawing number LP150050
Scale: 1:1	Sheet: 1	Drawing by Melchior Stander

PRODUCED BY AN AUTODESK EDUCATIONAL PRODUCT
PRODUCED BY AN AUTODESK EDUCATIONAL PRODUCT
PRODUCED BY AN AUTODESK EDUCATIONAL PRODUCT

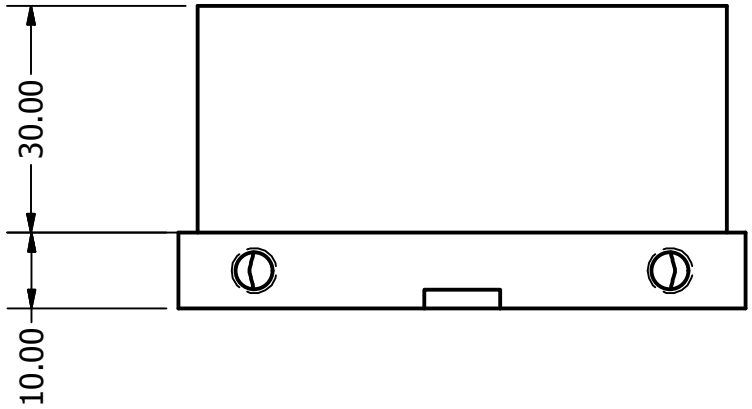

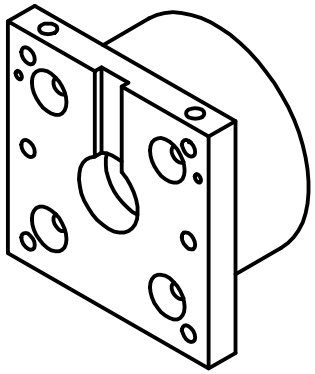

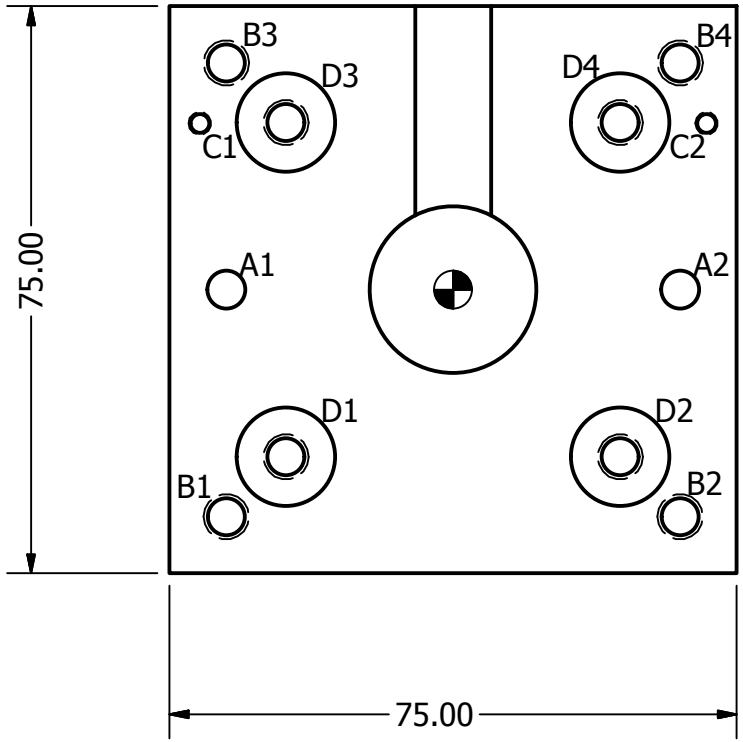

Hole Table			
HOLE	XDIM	YDIM	DESCRIPTION
A1	-30.00	.00	⌀5.00 ↧ 7.00
A2	30.00	.00	⌀5.00 ↧ 7.00
B1	-30.00	-30.00	M6x1 - 6H
B2	30.00	-30.00	M6x1 - 6H
B3	-30.00	30.00	M6x1 - 6H
B4	30.00	30.00	M6x1 - 6H
C1	-33.50	22.00	M3x0.5 - 6H
C2	33.50	22.00	M3x0.5 - 6H
D1	-22.10	-22.10	M6x1 - 6H ↧ 5.95 ⌵ ⌀13.00 X 90.0☐
D2	22.10	-22.10	M6x1 - 6H ↧ 5.95 ⌵ ⌀13.00 X 90.0☐
D3	-22.10	22.10	M6x1 - 6H ↧ 5.95 ⌵ ⌀13.00 X 90.0☐
D4	22.10	22.10	M6x1 - 6H ↧ 5.95 ⌵ ⌀13.00 X 90.0☐

Material: Steel	QUANTITY:1
University of Cape Town Department of mechanical engineering	
Title: Back Plate	
Size A4 / Tolerance U.O.S 0.05mm / Drawing number	
Scale:1:1 / Sheet:1	Drawing by Melchior Stander

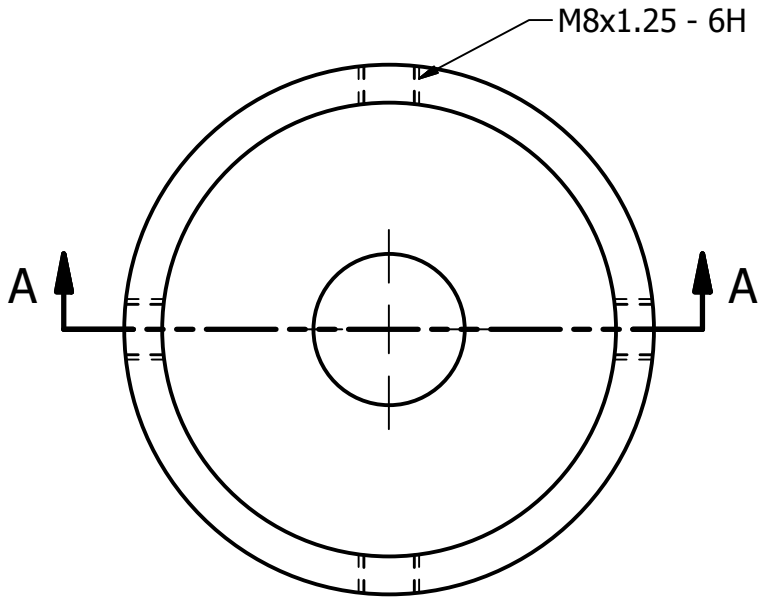

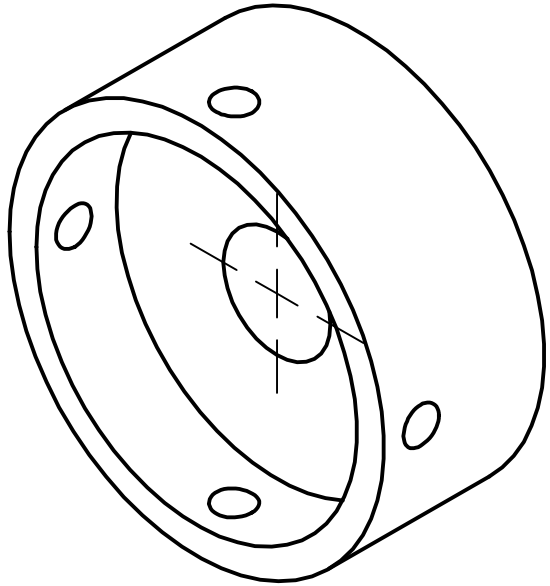

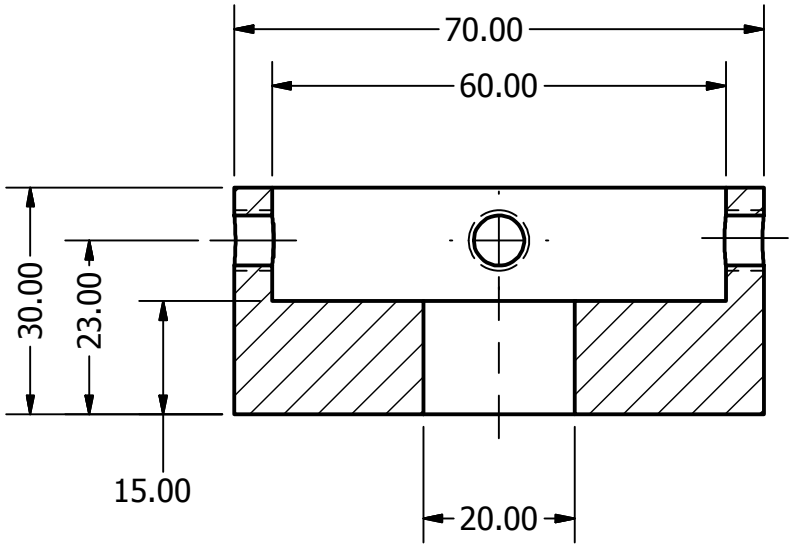

SECTION A-A

Material: HTPE Plastic		QUANTITY:1
University of Cape Town Department of mechanical engineering		
Title Barrel End Cap		
Size A4	Tolerance U.O.S 0.05mm	Drawing number
Scale:1:1	Sheet:1	Drawing by Melchior Stander

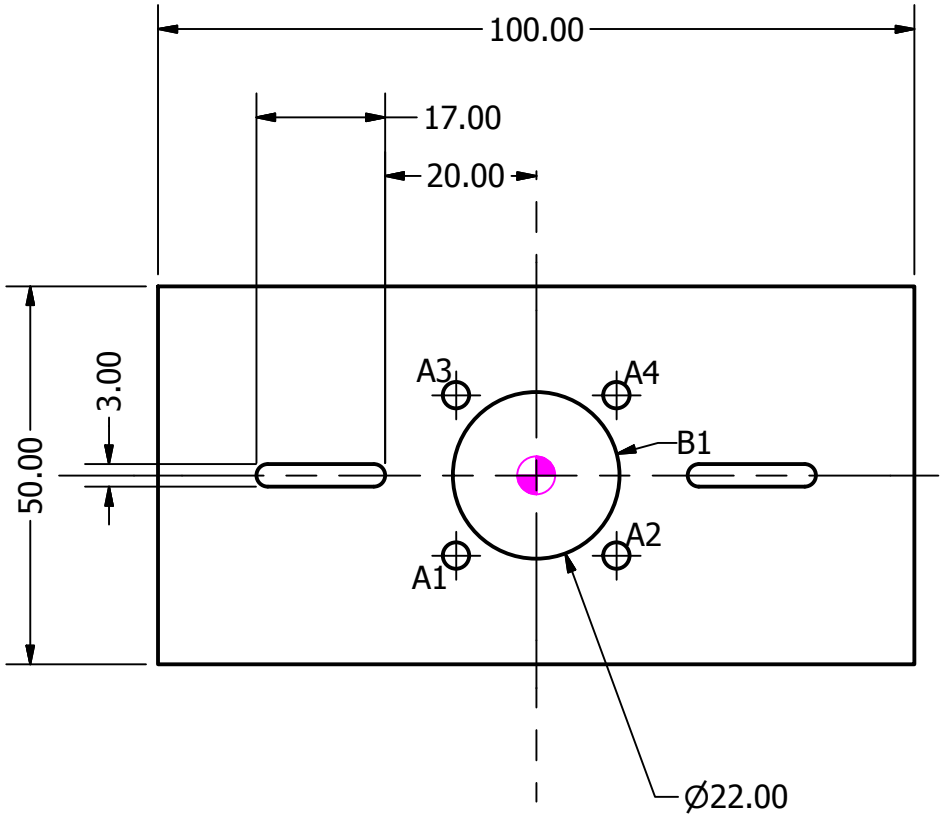

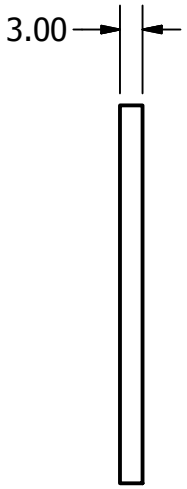

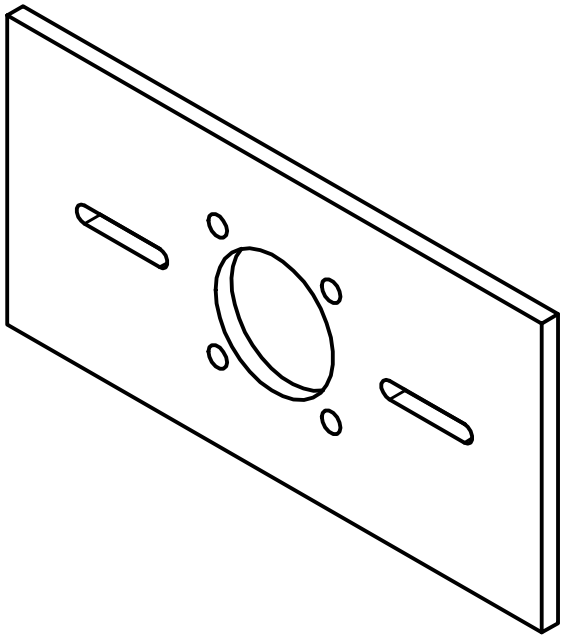

HOLE TABLE			
HOLE	XDIM	YDIM	HOLE DIAMETER
A1	-10.61	-10.61	3.50
A2	10.61	-10.61	3.50
A3	-10.61	10.61	3.50
A4	10.61	10.61	3.50
B1	.00	.00	22.00

Holes A1-A4, on a Ø30 mm circle concentric with hole B1.

Material:	QUANTITY: 1

University of Cape Town

Department of mechanical engineering

Title: ROS Holder

Size	Tolerance	Date	Drawing number
A4	U.O.S 0.05mm	27/05/2010	
Scale:		Sheet: 1	Drawing by: Melchior Stander

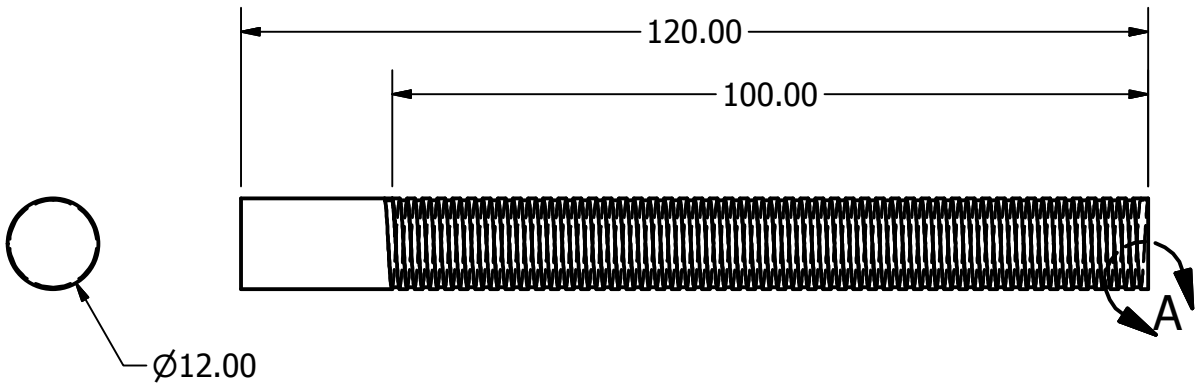

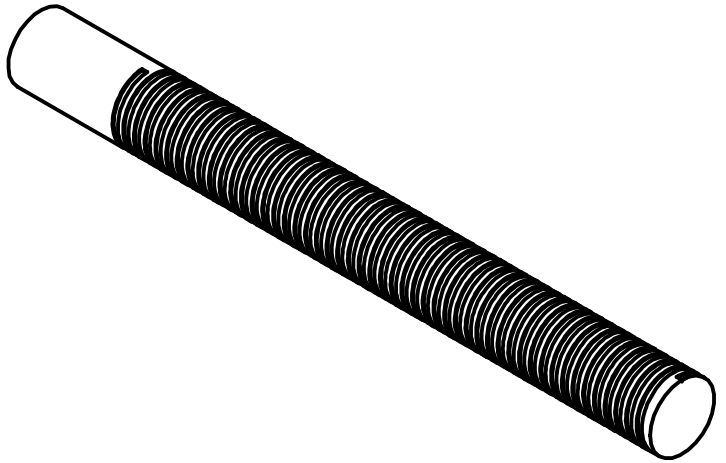

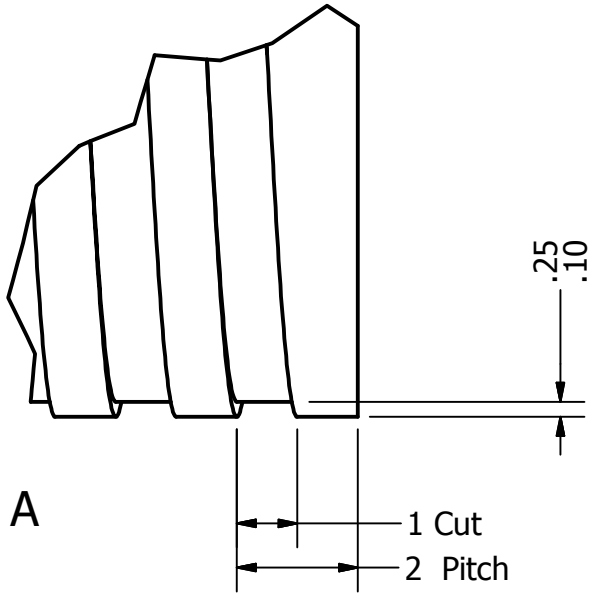

DETAIL A

The profile of the cutter is not critical but it is desiarable that the depth of the tread be as shallow as posible.

Thread specifications

Pitch	% Cut	% Cut
4	50%	75%
3	50%	75%
2	50%	75%
1	50%	75%

Material: Silver steel	QUANTITY:8

University of Cape Town

Department of mechanical engineering

Title: Threaded Bars

Size	Tolerance		Drawing number
A4	U.O.S 0.05mm		b001

Scale:1:1	Sheet:1	Drawing by Melchior Stander

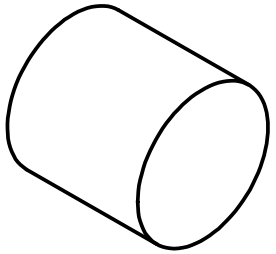

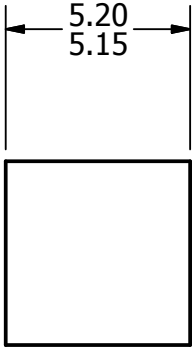

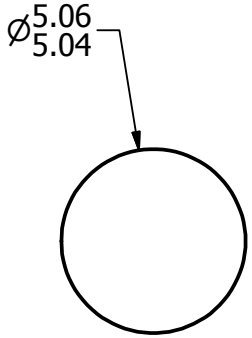

Mild steel	30
99.9% pure aluminium	30
99.9% pure copper	30
Material:	QUANTITY:

University of Cape Town

Department of mechanical engineering

Title: Compression test specimen

Size	Tolerance		Drawing number
A4	U.O.S 0.05mm		001
Scale:5:1	Sheet:1		Drawing by Melchior Stander

Appendix H

Ethics Form

EBE Faculty: Assessment of Ethics in Research Projects (Rev2)

Any person planning to undertake research in the Faculty of Engineering and the Built Environment at the University of Cape Town is required to complete this form before collecting or analysing data. When completed it should be submitted to the supervisor (where applicable) and from there to the Head of Department. If any of the questions below have been answered YES, and the applicant is NOT a fourth year student, the Head should forward this form for approval by the Faculty EIR committee: submit to Ms Zulpha Geyer (Zulpha.Geyer@uct.ac.za; Chem Eng Building, Ph 021 650 4791). **NB: A copy of this signed form must be included with the thesis/dissertation/report when it is submitted for examination**

This form must only be completed once the most recent revision EBE EiR Handbook has been read.

Name of Principal Researcher/Student: Department: Mechanical Engineering

Preferred email address of the applicant: MelchiorS@PatersonCooke.com

If a Student: Degree: MSC Mechanical Engineering Supervisor: T Cloete

If a Research Contract indicate source of funding/sponsorship:

Research Project Title: Development of an Intermediate Strain Rate Compression Testing Machine

Overview of ethics issues in your research project:

Question 1: Is there a possibility that your research could cause harm to a third party (i.e. a person not involved in your project)?	YES	NO X
Question 2: Is your research making use of human subjects as sources of data? If your answer is YES, please complete Addendum 2.	YES	NO X
Question 3: Does your research involve the participation of or provision of services to communities? If your answer is YES, please complete Addendum 3.	YES	NO X
Question 4: If your research is sponsored, is there any potential for conflicts of interest? If your answer is YES, please complete Addendum 4.	YES	NO X

If you have answered YES to any of the above questions, please append a copy of your research proposal, as well as any interview schedules or questionnaires (Addendum 1) and please complete further addenda as appropriate. Ensure that you refer to the EiR Handbook to assist you in completing the documentation requirements for this form.

I hereby undertake to carry out my research in such a way that

- there is no apparent legal objection to the nature or the method of research; and
- the research will not compromise staff or students or the other responsibilities of the University;
- the stated objective will be achieved, and the findings will have a high degree of validity;
- limitations and alternative interpretations will be considered;
- the findings could be subject to peer review and publicly available; and
- I will comply with the conventions of copyright and avoid any practice that would constitute plagiarism.

Signed by:

		Date
Principal Researcher/Student:		2014/01/29

This application is approved by:

Supervisor (if applicable):	T Cloete	2014/01/29
HOD (or delegated nominee): *Final authority for all assessments with NO to all questions and for all undergraduate research.*		2014/01/29
Chair : Faculty EIR Committee For applicants other than undergraduate students who have answered YES to any of the above questions.		